INTEGRATED FUEL PERFORMANCE AND THERMAL-HYDRAULIC SUB-CHANNEL MODELS FOR ANALYSIS OF SODIUM FAST REACTORS

By
Joseph William Fricano

M.S., Nuclear Science and Engineering (2009)
Massachusetts Institute of Technology

B.S., Nuclear Engineering (2007)
Rensselaer Polytechnic Institute

B.S., Physics (2007)
Rensselaer Polytechnic Institute

SUBMITTED TO THE DEPARTMENT OF NUCLEAR SCIENCE AND ENGINEERING
IN PARTIAL FULFILLMENT OF THE REQUIREMENTS FOR THE DEGREE OF

DOCTOR OF PHILOSOPHY IN NUCLEAR SCIENCE AND ENGINEERING
AT THE
MASSACHUSETTS INSTITUTE OF TECHNOLOGY

February 2012

Author:_____
Joseph William Fricano
Department of Nuclear Science and Engineering
February 2012

Certified by:_____
Prof. Jacopo Buongiorno
Associate Professor of Nuclear Science and Engineering, MIT
Thesis Supervisor

Certified by:_____
Dr. Pavel Hejzlar
Reactor Core Design Lead, TerraPower
Thesis Reader

Accepted by:_____
Prof. Mujid Kazimi
TEPCO Professor of Nuclear Engineering, MIT
Chair, Department Committee on Graduate Students

INTEGRATED FUEL PERFORMANCE AND THERMAL-HYDRAULIC SUB-CHANNEL MODELS FOR ANALYSIS OF SODIUM FAST REACTORS

By
Joseph William Fricano

Submitted to the Department of Nuclear Science and Engineering January 18, 2012
in partial fulfillment of the requirements for the degree of

DOCTOR OF PHILOSOPHY IN NUCLEAR SCIENCE AND ENGINEERING

Abstract

Sodium Fast Reactors (SFR) show promise as an effective way to produce clean safe nuclear power while properly managing the fuel cycle. Accurate computer modeling is an important step in the design and eventual licensing of SFRs. The objective of this work was to couple a model for metal fuel performance to a sub-channel analysis code to more precisely predict critical phenomena that could lead to pin failure for steady-state and transient scenarios. The fuel code that was used is the recently developed and benchmarked FEAST-METAL code. The sub-channel analysis code that was selected is COBRA-IV-I. This code was updated with current correlations for sodium for pressure drop, mixing, and heat transfer. The new code, COBRA-IV-I-MIT was then validated with experimental data from the Oak Ridge National Laboratory (ORNL) 19-Pin Bundle, the Toshiba 37-Pin Bundle, and the Westinghouse Advanced Reactors Division (WARD) 61-Pin Bundle.

Important topics that were addressed for coupling the codes include the following. The importance of azimuthal effects in the fuel pin: FEAST only evaluates the fuel in two-dimensions, assuming azimuthal symmetry; however, coupling to COBRA produces an azimuthal temperature distribution. The acceptability of assuming a two-dimensional fuel rod with an average temperature was examined. Furthermore, how the fuel pin evolves over time affects the assembly geometry. How well a two-dimensional fuel rod allows for an accurate description of the changing assembly geometry was also considered. Related to this was how the evolution of the assembly geometry affects its thermal hydraulic behavior, which determined the exact form of coupling between the codes.

Ultimately one-way coupling was selected with azimuthal temperature averaging around the fuel pin. The codes were coupled using a wrapper, the COBRA And FEAST Executer (CAFE), written in the Python programming language. Data from EBR-II was used to confirm

and verify CAFE. It was found that the number of axial nodes used in FEAST can have a large effect on the result. Finally FEAST was used to parametrically study three different pin designs: driver fuel, radial blanket, and tight pitch breed and burn fuel. This study provides data for pin expected life in assembly design.

Thesis Supervisor: Jacopo Buongiorno
Associate Professor of Nuclear Science and Engineering, MIT

Thesis Reader: Dr. Pavel Hejzlar
Reactor Core Design Lead, TerraPower

Acknowledgments

This work was made possible through the financial support of TerraPower.

I am grateful and fortunate to have had the help and support of many great people through the course of my education and while writing my thesis, without whom I never would have made it. I would like to thank all my friends, family, and teachers who have helped, taught, and guided me throughout the years, specifically I would like to thank:

My advisor, Professor Jacopo Buongiorno, who patiently directed me for the last three years and always made sure I was moving in the right direction. Without him I could have been stuck as a graduate student for many more years.

My Thesis Reader, Dr. Pavel Hejzlar, who provided insightful and relevant feedback.

Paul Romano and Rachel Morton, who generously assisted me with vast their computer knowledge and coding wisdom.

And finally my parents, Joseph and Barbara Fricano, who made everything possible, and instilled in me the value of a good education.

Table of Contents

List of Figures

List of Tables

Chapter 1. Introduction

1.1. Motivation

As the twenty-first century progresses the demand for inexpensive carbon free energy will continue to rise. With seemingly no viable alternatives, nuclear power will likely be a key supplier of that increasing power demand (1). Currently most operating nuclear power plants in the world are Light Water Reactors (LWR); however, innovative reactor designs with improved safety and performance features look promising for future deployment. Six advanced reactor concepts have been proposed as Generation IV reactors (2).

One of these six designs, the Sodium Fast Reactor (SFR), has gained considerable traction. Prominent American SFR designs such as the S-PRISM (a GE Hitachi SFR design) (3)(4)(5)(6) and the Traveling Wave Reactor (TWR, a TerraPower reactor design) (7)(8)(9) exist with increasing promise of one day being constructed. There is already experience with construction and operation of experimental and prototype SFRs in many countries. A partial listing is shown in Table 1-1, for a complete listing of SFR designs consult the International

Atomic Energy Agency (IAEA) Fast Reactor Database (10). Finally, the SFR has been shown as a technically viable way of closing the nuclear fuel cycle (2).

An important hurdle that must be overcome for all novel design concepts for nuclear applications is verification of safe and successful operation. One way of accomplishing this is through the use of computer simulation. Codes based on first principles and previously developed correlations can be benchmarked with previous data from experimental reactors, and then applied to new reactor designs.

This work focused on the modeling of two facets of SFRs, fuel performance and thermal hydraulics, and the coupling of these models to provide a better description of the behavior of each. The main purpose of this work was to couple a thermal hydraulic model and a fuel performance model together. This allows for the ability to predict and model both phenomena more accurately because feedback effects between the two are accounted for better with a coupled model. A more detailed discussion of all the objectives of this work occurs in Section 1.3.

Table 1-1- List of countries with SFR experience and some of the corresponding reactors in those countries, for a more complete list consult the IAEA database (10).

Country	Reactor
America	Experimental Breeder Reactor-II (EBR-II) (11)
	Fast Flux Test Facility (FFTF) (12)
China	China Experimental Fast Reactor (CEFR) (13)
France	Phenix (14)
	SuperPhenix (15)
India	Fast Breeder Test Reactor (FBTR) (16)
	Prototype Fast Breeder Reactor (PFBR) (17)
Japan	JOYO (18)
	Monju (19)
Russia	BOR-60 (20)
	BN-600 (21)

1.2. Background

1.2.1. Sodium Fast Reactors

The major distinguishing features of an SFR from other reactor types are listed in its name. An SFR uses liquid sodium as a coolant and operates with a fast neutron spectrum. Beyond these two defining properties, SFRs can take on a number of different incarnations. An example of variety in SFRs at very high-level design is the reactor configuration, which can be of the loop or pool type (22). Table 1-2 below lists some basic design ranges from Generation IV SFRs.

The design features of the SFR imbue it with varied functionality and engineering challenges. For example, the SFR design can support a conversion ratio that allows it to be run as either a breeder or burner reactor. The sodium coolant offers increased heat removal capability due to its high thermal conductivity, and is minimally corrosive to steel; however, it is highly reactive with water and air. Furthermore the use of sodium coolant allows SFRs to be operated at near-atmospheric pressure.

Table 1-2- Design parameters for Generation IV SFR designs (2).

Reactor parameter	Reference Value
Outlet Temperature	510-550°
Pressure	Near Atmospheric
Power Rating	1000-5000 MWth
Fuel	Oxide, metal, carbide or nitride alloy
Cladding Material	Ferritic-Martensitic or low swelling Austenitic alloys
Average Burnup	100-200 GWD/MTHM
Conversion Ratio	0.25-1.30
Average Power Density	350 MWth/m^3

One thing that remains constant in SFR design is the general assembly design. SFR cores, like LWR cores, are broken up into units called assemblies. SFR assemblies are arrays of fuel pins, often wrapped with spacer wires for stability, through which the sodium coolant flows.

While the fuel pin is a constant in SFRs, the fuel material used inside of them can vary. Listed in Table 1-2 are many of the possible options for SFR fuel. The two options that are most common for SFR designs are oxide and metal fuel. While oxide fuel is appealing due to the large amount of operating experience in LWRs and good chemical stability with the cladding material, metal fuel is the focus of this thesis. Metal fuel has myriad advantages and disadvantages as a fuel type. Table 1-3 shows a comparison of the properties of the two fuel types. Notably, metal fuel has a higher heavy-metal density and thermal conductivity, which is desirable. Furthermore, properly designed metal fuel experiences low Fuel Clad Mechanical Interaction (FCMI) however it interacts chemically with the clad (23). A major disadvantage of metal fuel is its low melting point which would be even lower without Zirconium, which is alloyed into the fuel. Figure 1-1 shows the phase diagram for a Plutonium-Uranium system, while the melting temperature is high for systems with primarily uranium, the eutectic melting temperature is close to only 900 K (24).

For a considerably more detailed description on Sodium Fast Reactors consult Tang et al. (22).

Table 1-3-Comparison of properties of uranium oxide fuel (25) to metallic alloy fuel (23).

Property	U-Pu-10Zr	UO_2
Theoretical Density at room temperature (kg/m^3)	15.8×10^3	10.97×10^3
Heavy Metal Density (kg/m^3)	14.22×10^3	9.67×10^3
Melting point (°C)	1080	2800
Thermal conductivity average 200-1000 °C (W/m°C)	15	3.6
Specific heat at 100 °C (J/kg°C)	80	247

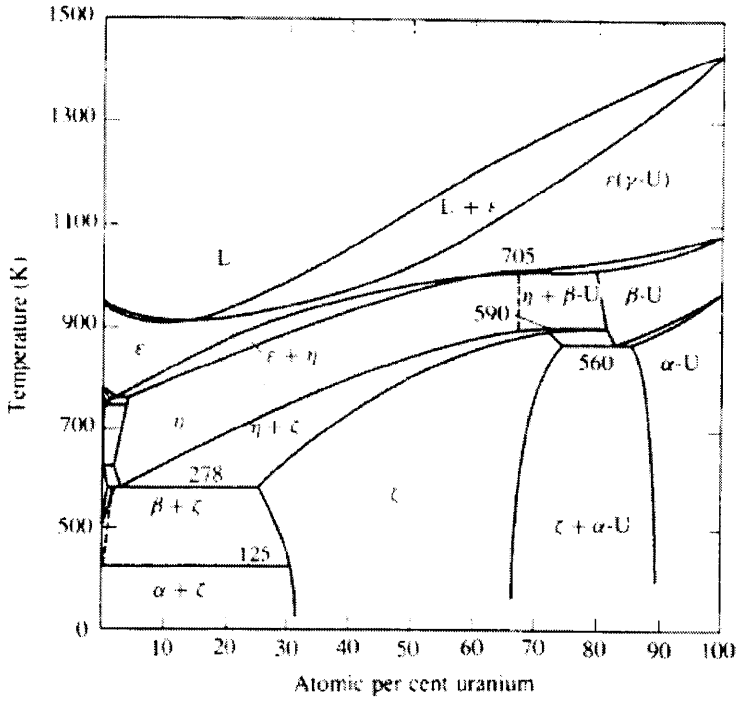

Figure 1-1- Phase diagram for Plutonium-Uranium system (24).

1.2.2. Sub-Channel Analysis

The method that was used in this work for the thermal hydraulic modeling of SFRs is sub-channel analysis. The basic principal behind sub-channel analysis is standardizing the porous body control volume equations for a well defined layout (26). The porous body approach treats a system by dividing it up into regions and assigning values to properties based on volume averages for that region. The well defined layout for sub-channel analysis is fluid flowing in connected channels, which are the conditions of a nuclear fuel assembly. As such, sub-channel analysis is an effective way to examine the fluid behavior of a nuclear fuel assembly.

There are various ways to assign exact sub-channel geometry to an assembly; the method used in this work will be coolant centered channels. For a hexagonal assembly this divides the assembly into many small triangles with their vertices being at the center of each fuel rod. This is shown for a small 19-pin assembly in Figure 1-2.

In addition to the many regular triangular sub-channels that are formed there are some non-triangular shaped channels at the edges of the assembly. These channels are called edge and corner sub-channels and are illustrated in Figure 1-2. The regularly shaped triangular sub-channels are referred to as interior sub-channels. While the true shape of the sub-channels is triangular, the solid fuel rods eliminate some of the free area where fluid can flow, resulting in the flow area for the channel.

For SFR assemblies there is an additional geometric feature that is not shown in Figure 1-2. A wire is wrapped around each fuel rod to give rigidity to the assembly and to promote cross flow, which is discussed below. To fully define the assembly cross-sectional geometry for sub-channel analysis the geometric parameters listed in Table 1-4 are needed (this does not include values needed to be defined in the axial direction).

In addition to dividing the cross-section of the assembly into cells, the assembly is nodalized axially as well. The length of a node axially is generally on the order of a few centimeters. The fully nodalized assembly is completely broken down into small control volumes each of which communicates with surrounding control volumes based on conservation equations.

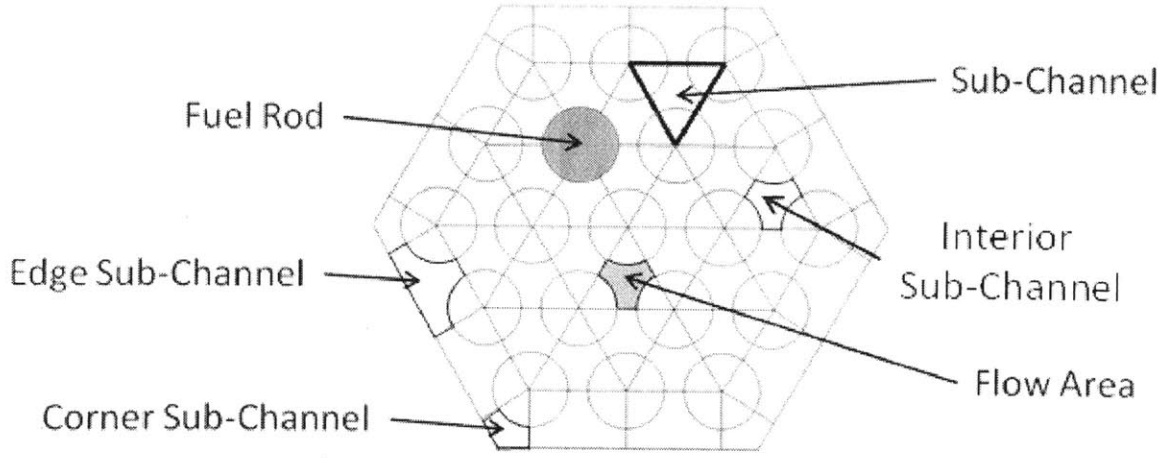

Figure 1-2- Cross-sectional view of a 19-pin SFR fuel assembly with the channel centered geometry definitions for sub-channel analysis overlaid.

Table 1-4- Range of typical geometric values for SFR assemblies.

Geometric Parameter	Range of Sample Values
Number of Fuel Rods	7-271
Fuel Rod Diameter	.584-1.32cm
Fuel Rod Pitch or Pitch to Diameter Ratio	1.082-1.24 (p to d ratio)
Inner Flat to Flat Distance	Dependent on number of fuel rods
Wire Wrap Diameter	.094-.142cm

The single phase conservation equations for a sub-channel j can be written as follows (for a derivation up to this point refer to Nuclear Systems II: Elements of Thermal Hydraulic Design by Todreas and Kazimi (26)). Please note the notation presented here is slightly different from the book to match the notation used in Chapter 2 which presents the equations employed in the sub-channel code selected. The notable differences are that x is used for the axial direction and the subscript j denotes the current sub-channel, while the book uses z and i for these purposes.

Continuity

$$A_{fj}\frac{\delta}{\delta t}\langle\rho_j\rangle + \frac{\Delta \dot{m}_j}{\Delta x} = -\sum_{i=1}^{I} W_{ji} \qquad 1\text{-}1$$

Energy

$$A_{fj}\frac{\delta}{\delta t}\left[\langle\rho h\rangle_j\right] + \frac{\Delta}{\Delta x}\left[\dot{m}_j h_j\right] = \langle q_j{}'\rangle_{rb} - \sum_{i=1}^{I} W_{ji}^{*H}\left[h_j - h_i\right] - \sum_{i=1}^{I} W_{ji}\{h^*\} + A_{fj}\langle\frac{Dp_j}{Dt}\rangle \qquad 1\text{-}2$$

Axial Momentum

$$\frac{\delta}{\delta t}\langle\dot{m}_j\rangle + \sum_{i=1}^{I} W_{ji}\{v_x^*\} + \frac{\Delta\left(\dot{m}_j v_{xj}\right)}{\Delta x} = -A_{fj}\langle\rho\rangle g_x - A_{fj}\frac{\Delta\{p\}}{\Delta x} - \sum_{i=1}^{I} W_{ji}^{*M}\left(v_{xj} - v_{xi}\right) - \left\{\frac{F_{jx}}{\Delta x}\right\} \qquad 1\text{-}3$$

Transverse Momentum

$$\frac{\delta}{\delta t}(W_{ji}) + \frac{\Delta}{\Delta z'}(W_{ji}\{v_z\}) + \frac{\Delta}{\Delta x}(W_{ji}\{v_x\}) = -\left(s_{ji}^{y}\frac{\Delta}{\Delta z'}\{p\}\right) - \left\{\frac{F_{jz}}{\Delta z'\Delta x}\right\} \qquad 1\text{-}4$$

Where the variables are defined as:

A_f	Flow area
F	Form loss coefficient
h	Enthalpy
I	Number of adjacent sub-channels
$\dot{m}$	Mass flow rate
p	Pressure
ρ	Density
q´	Linear heat rate
s	Gap distance between fuel rods
v	Velocity
W	Mass transverse flow rate
W^M	Momentum transverse flow rate
W^H	Energy transverse flow rate

And the sub/superscripts mean:

j	The sub-channel

i	An adjacent sub-channel
j,i	Between sub-channel j and i
x	In the x (axial) direction
y	In the y direction
z	In the z direction
*	Effective amount transported by diversion cross-flow rate
′	Previous axial level

The first of the four equations, the continuity equation, conserves the total amount of mass in the cell, in the units of mass per unit length. It consists of three terms in total. The first term represents the change of the mass in the cell with time.

$$A_{fj}\frac{\delta}{\delta t}\langle\rho_j\rangle \qquad 1\text{-}5$$

The second term is the mass that enters the cell in the axial direction. This is the mass that flows into the cell from the previous cell (or perhaps in some harsh transients with flow reversal from the next cell).

$$\frac{\Delta\dot{m}_j}{\Delta x} \qquad 1\text{-}6$$

The final term is the crossflows from the adjacent cells.

$$-\sum_{i=1}^{I} W_{ji} \qquad 1\text{-}7$$

In a similar way the other equations track the momentum and energy for the cells, the purpose of each term is explained in Table 1-5. A sub-channel analysis code uses these equations along with closure relations (for mixing, pressure drop, and heat transfer), to model the fluid behavior.

An alternative method to sub-channel analysis that was considered for application in this work is Computational Fluid Dynamics (CFD). CFD is capable of obtaining much finer resolutions than sub-channel analysis methods because it divides the volume up in to a much finer mesh. This increased accuracy comes at the price of computational efficiency. Sub-channel analysis is capable of modeling much larger domains of both time and space than CFD (27). For the purpose of coupling a fluid model to a fuel model many design iterations will be necessary for assemblies with long run times (on the order of years), thus sub-channel analysis was the chosen approach. This is not to say that CFD has no place in the future of this work. A possible way to provide ever better models for certain phenomena may be to explore them with CFD when experiments are too costly or difficult.

Table 1-5 – A breakdown of the Energy and Momentum equations used in sub-channel analysis by terms with descriptions of each term.

Equation	Terms and Description						
Energy	$A_{fj}\frac{\delta}{\delta t}[\langle\rho h\rangle_j]$	$\frac{\Delta}{\Delta x}[\dot{m}_j h_j]$	$\langle q_j{}'\rangle_{rb}$	$\sum_{i=1}^{I} W_{ji}^{*H}[h_j - h_i]$	$\sum_{i=1}^{I} W_{ji}\{h^*\}$	$A_{fj}\langle\frac{Dp_j}{Dt}\rangle$	
	Change in energy with time	Axial transport of energy	Linear heat generation rate	Energy transferred from adjacent cells	Energy carried by mass exchange from adjacent cells	Energy change from change in pressure	
Axial Momentum	$\frac{\delta}{\delta t}\langle\dot{m}_j\rangle$	$\sum_{i=1}^{I} W_{ji}\{v_x^*\}$	$\frac{\Delta(\dot{m}_j v_{xj})}{\Delta x}$	$-A_{fj}\langle\rho\rangle g_x$	$A_{fj}\frac{\Delta\{p\}}{\Delta x}$	$\sum_{i=1}^{I} W_{ji}^{*M}(v_{xj} - v_{xi})$	$\left\{\frac{F_{jx}}{\Delta x}\right\}$
	Change in axial momentum with time	Axial momentum carried by mass exchange from adjacent cells	Axial transport of momentum	Momentum loss from gravity	Momentum loss from pressure drop	Axial momentum transferred from adjacent cells	Momentum lost to form loss
Transverse Momentum	$\frac{\delta}{\delta t}(W_{ji})$	$\frac{\Delta}{\Delta z'}(W_{ji}\{v_z\})$	$\frac{\Delta}{\Delta x}(W_{ji}\{v_x\})$	$-\left(s_{ji}^{y}\frac{\Delta}{\Delta z'}\{p\}\right)$	$\left\{\frac{F_{jz}}{\Delta z'\Delta x}\right\}$		
	Change in transverse momentum with time	Momentum carried from the previous level	Momentum carried from adjacent cells	Momentum loss from pressure drop	Momentum lost to form loss		

1.2.3. FEAST

The tool that will be used in this work to model the fuel performance of SFRs is the Fuel Engineering And Structural Tool (FEAST) (23)(28)(29). Two versions of FEAST were developed, FEAST-METAL and FEAST-OXIDE. Since the interest of this work is metal fuel FEAST-METAL is the version employed and will hence forth be referred to as just FEAST for brevity.

FEAST was developed to fully model a metal fuel pin, which includes the fuel, the sodium bond, the clad, and the fission gas plenum. FEAST nodalizes the fuel pin in the radial and the axial direction, while assuming there is symmetry in the azimuthal direction. The axial direction supports up to 20 nodes, while the radial direction can have up to 8. The radial nodes must be split between the fuel and the clad; the recommended split is to use 6 fuel nodes and 2 clad nodes (23). This is shown in Figure 1-3.

FEAST was written in Fortran-90. FEAST employs several different modules and couples them using an explicit numerical solution algorithm. The modules in FEAST are (23):

1) Fission gas release and swelling
2) Fuel chemistry restructuring
3) Temperature distribution
4) Fuel clad chemical interaction
5) Fuel and clad mechanical analysis
6) Transient creep-fracture in the clad

These models allow FEAST to analyze a fuel pin for both steady-state and transient conditions and predict critical phenomena that could lead to pin failure.

The required inputs to run FEAST include the pin geometry, the fuel composition, and the complete history of the pin. The history of the pin includes the power, flux fission rate, and

clad temperature or coolant temperature and heat transfer coefficient as functions of time. FEAST has been benchmarked with the currently available metal fuel data from EBR-II and has proven accurate (23)(28)(29).

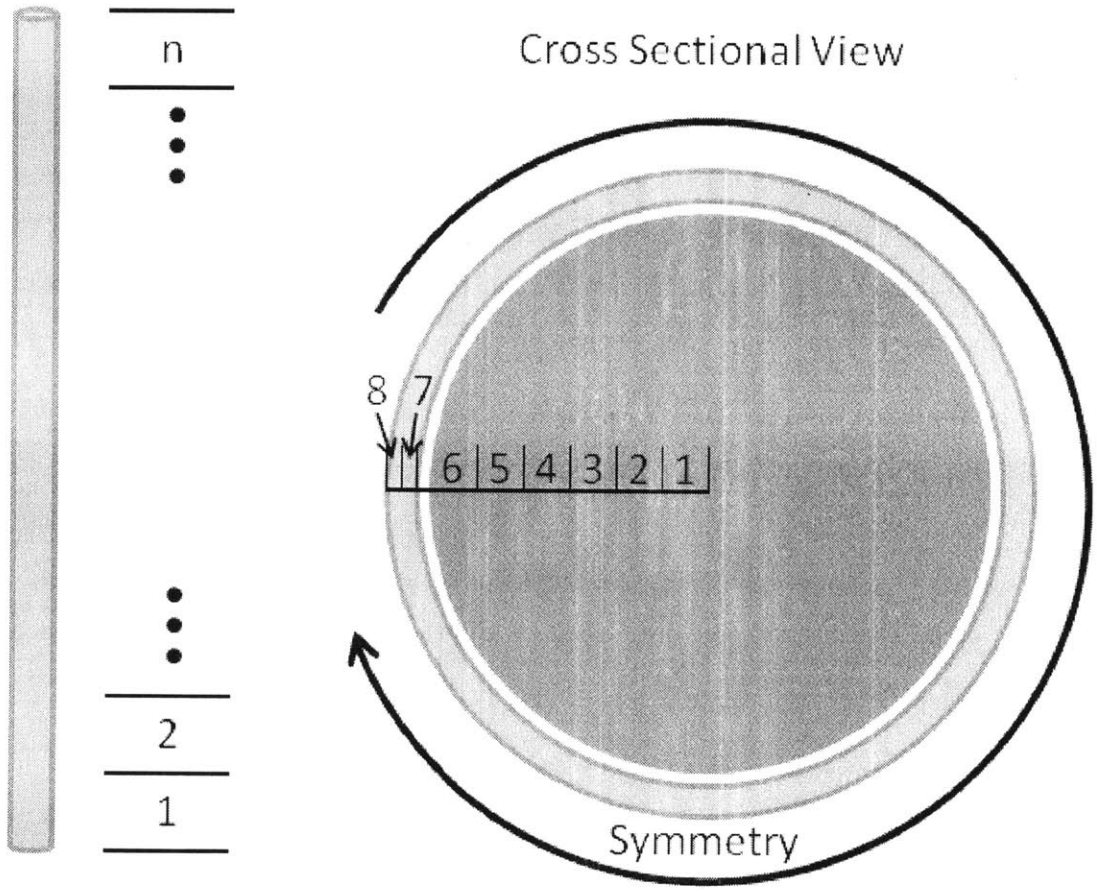

Figure 1-3- Diagram of the nodalization employed by FEAST, the fuel rod is divided in to nodes along the axial direction (left) and the radial direction while being assumed azimuthally symmetric (right).

1.3. Objectives

The over-arching objective of this work was to produce a coupled model for thermal hydraulic and fuel performance for SFRs. Fuel performance is highly sensitive to coolant temperature; the accuracy of predictions made by any fuel performance model will be only as good as the coolant information used. Any user wishing to employ a fuel performance model has to make some assumptions about the thermal hydraulic behavior of the coolant. The information usually available is the coolant inlet temperature and the pin linear power, along with either the coolant mass flow rate or outlet temperature. The latter two could apply either to the pin specifically or to the assembly. Without the coupling of a sub-channel analysis code, a simple one-dimensional energy balance must be assumed for the coolant. Peaking factors can be introduced to increase accuracy; however, phenomena like mixing can never be captured with a simple model.

Figure 1-4 shows the difference between the axial temperature distributions between COBRA (the sub-channel analysis code ultimately selected for this work) and the simple coolant model used in FEAST for a sample pin. The difference is as much as 10 °C at some axial locations. Differences such as this can produce major discrepancies in predicted performance, which is described in Section 5.1.

Further value of coupling a fuel performance model to a thermal hydraulic model, like sub-channel analysis, is the ability to examine multiple pins from an assembly as the coolant behavior of the entire assembly is given by such a model. While peaking factors can often be used to approximate the coolant conditions for a hot fuel pin, predicting the coolant behavior for pins in the periphery of the assembly is not as straightforward.

The coupling of the two models was broken down into three sub-objectives. Firstly a suitable model for the thermal hydraulics was needed. At the start of the project the fuel model, FEAST, was already in hand, however this was not the case for the coolant model. Second, the two models needed to be coupled together. Finally, the coupled model needed to be tested and applied. The outline below shows these objectives with sub-tasks listed.

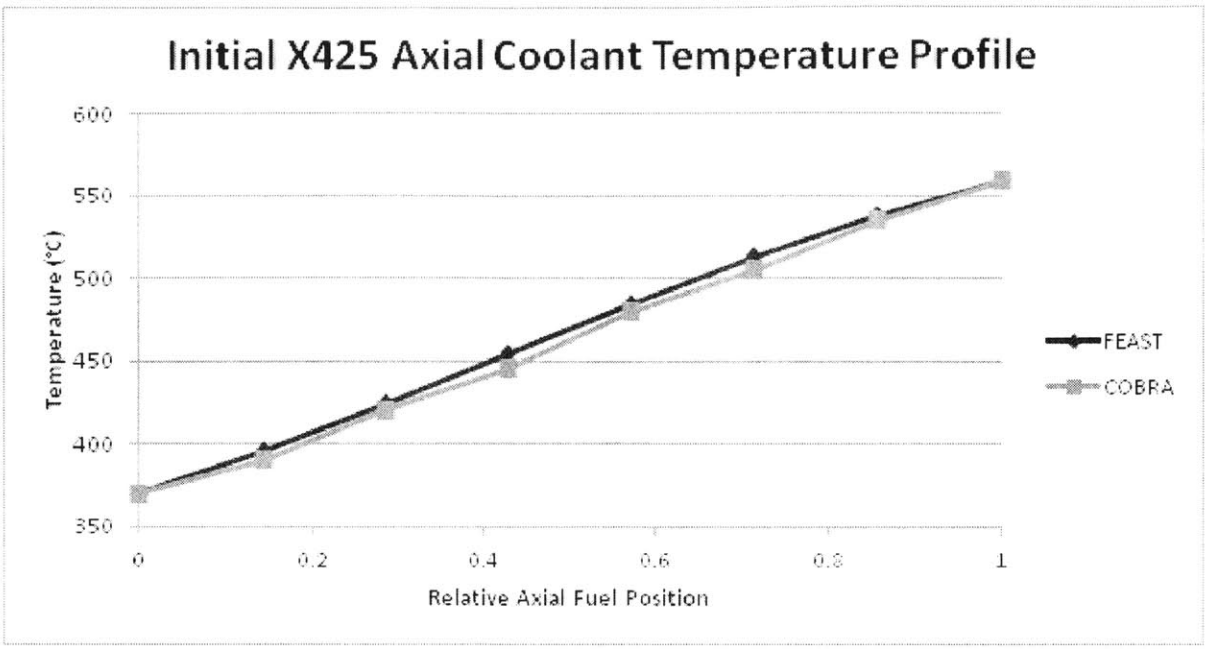

Figure 1-4- Comparison of the axial coolant temperature profile produced by the models in FEAST and COBRA, taken from Figure 5-4 in Section 5.1 where a more thorough discussion of its context can be found.

I) *Obtaining a suitable sub-channel analysis code (Chapters 2 and 3)*

1) Several sub-channel analysis codes existed as potential candidates for coupling, the first task was to select an appropriate one for use and evaluate it. (Section 2.1 and 2.2)

2) After the sub-channel code was selected, evaluating the current features of the code and adding/improving the missing/desired parts was next. Specifically, constitutive relations for heat transfer, pressure drop, and flow mixing needed to be examined to ensure they were capturing the operating domain of interest with a reasonable accuracy. (Section 2.3)

3) Benchmarking and validation was the final step for preparing the sub-channel analysis model. Sources for validation of the sub-channel code were previous experiments, for example the ORNL 19-pin test bundle. (Chapter 3)

II) *Coupling of the fuel and sub-channel codes (Chapter 4)*

4) After completing the development of an up-to-date sub-channel analysis code, it was coupled with FEAST. The method of coupling was such that there is only one input file and execution to produce results (no intermediate formatting or commands were needed by the user). However at the same time each code was preserved in a way that independent development of each can be carried out and easily adapted to the coupled version. (Section 4.4)

5) One challenge to coupling the codes was the effect of azimuthal variations of the clad temperature on the fuel performance. FEAST is a two dimensional code examining only the axial and radial directions of the fuel, while sub-channel analysis provided the coolant behavior around the fuel rod. This effect was studied to determine its importance and how to address it when coupling. (Section 4.2)

6) In implementation of coupling the codes, the question of computational efficiency of the communication between the two codes was addressed. This point was important to ensure that the coupled program runs in a reasonable amount of time. Because of the stiffness of the fuel governing equations, FEAST has to be run with fairly short time steps (on the order of tens of seconds), even at steady-state. On the other hand, the thermal-hydraulic behavior of the assembly at steady-state evolves over periods of days, weeks, or months. A further extension of this problem was determining what directions between the codes information was passed. As described above, the evolution of coolant behavior affects the fuel performance, however the evolution of the fuel, to a lesser degree, affects the coolant behavior. It was necessary to

determine if the magnitude of this effect was great enough to warrant two-way communication between the codes, which would significantly affect the overall computational efficiency. (Section 4.1 and 4.3)

III) *Validation and application (Chapter 5)*

7) Ideal benchmarking of the coupled code would look at data consisting of fuel performance results from multiple pins from an assembly with known operating conditions. Unfortunately data sets such as this could not be found in the literature. Since benchmarking and validation of the combined code was still required, more creative means were necessary. The combined model was compared to experimental data and FEAST results for fuel pins to examine its validity. (Sections 5.1 and 5.2)

8) The completed model allows the examination of any pin from an assembly. It was necessary to determine how the performance of pins in cooler regions of the assembly compared to that of the hot pin. (Section 5.3)

9) The ability to examine the fuel performance of any pin in the assembly can allow for better design, but beyond the hot pin it is not obvious which pins need to be examined to ensure the postulated thermal limits are met. Assemblies can consist of up to 271 pins, which would be a rather daunting number of pins to examine. A parametric study was conducted to determine fuel pin limits based on different geometry and operating conditions, with a goal of determining a set of guidelines for what pins to examine when looking at an assembly. (Section 5.4)

Chapter 2. Sub-Channel Code Selection and Upgrade

2.1. Code Selection

Selecting the sub-channel analysis method is the first step to choosing the code to use for modeling the thermal-hydraulics for the coupling. The pros of using an existing sub-channel analysis code were weighed against writing a new code. Writing a new code had many enticing benefits. A new code could be tailored to do specifically what is required; the solution scheme could be designed with its intended use in mind. Furthermore, the code would be modern and understood because there would be no need to decipher sparsely commented codes written in archaic programming languages. However, the time investment required to prepare a code from scratch was considered too steep if a code already existed that contained most of the features required. Considering the vast field of choices that already existed, dozens of sub-channel analysis codes (e.g. VIPRE, COBRA, and SLTHEN) and many more codes that can be used as sub-channel analysis codes (e.g. RELAP), it was likely a suitable code could be found.

Important criteria were identified, and then cross-referenced with the available codes so the best choice could be made.

2.1.1. Criteria

The complexity and features of sub-channel analysis codes can vary greatly depending on their intended application. It was necessary to choose a code that was suited for the purposes of examining sodium fuel assemblies with an emphasis on coupling to fuel behavior. The following criteria were deemed important features for the code to have:

-Can handle sodium as the fluid: This is an obvious criterion however many sub-channel analysis codes are written for water as the fluid. While it was possible that such a code could be selected and adapted for this purpose it would have involved considerable changes to the code.

-Supports hexagonal geometry with wire wrap: Most sodium fuel assemblies are packed into a hexagonal geometry because it allows tighter packing, and have wire wraps to promote mixing. The code must be able to handle this geometry.

-Capable of both steady-state and transient analysis: Time scales of these different modes of operation can be vastly different, possibly requiring different solution schemes and correlations. Both modes of analysis were desired.

-Contains a transverse momentum equation: The transverse momentum equation helps describe the transfer between cells radially. Some codes implement correlations in place of this equation. Eliminating unnecessary correlations means a more physical model and requires less benchmarking.

-Employs up to date correlations: Many sub-channel codes were written decades ago, and as such many experiments have since been conducted that have added to the empirical data available for places where correlations are necessary. Out of date correlations were the easiest of the above criteria to overlook as new correlations could be implemented without major changes to the code.

While these five requirements provided a good description for what the code should be there was an additional requirement that superseded them. Any potential code must have an available source code. Even an ideal sub-channel analysis code for this purpose required access to the source in order to couple it to FEAST.

2.1.2. Sub-Channel Analysis Options

Below is a listing of existing sub-channel analysis codes, this list is not exhaustive due to the sheer number of variations on codes that exist.

ASFRE	Japanese sub-channel analysis code that is used for fast breeder reactors (30).
COBRA	Code commissioned originally by the Atomic Energy Commission (AEC). Later versions, which included support for sodium reactors were developed at Pacific Northwest Laboratory (31)(32)(33).
MATRA LMR	Korean code for liquid metal reactors based on MATRA which was in turn based on COBRA. MATRA LMR improves COBRA in structure, capabilities and new models (34).
RELAP	Not traditionally a sub-channel analysis code however which can be used as one (35).
SABRE	A British line of codes originally developed for the treatment of blockages in sodium assemblies. The code was improved on many times with different versions adding capabilities for transient and boiling calculations (36).
SLTHEN	Code based on SuperEnergy, sharing many of the same benefits and drawbacks (37).

SuperEnergy	Code developed at MIT, its predecessor was the ENERGY code. In this code the energy and momentum equations are decoupled allowing for less computational time at the cost of more correlations (38).
VIPRE	Code based on COBRA for water only (39).

Many of the codes on this list were quickly eliminated for one reason or another. VIPRE is a sub-channel analysis code used for water, the amount of work to change it for use with sodium was not worthwhile considering different evolutions of its predecessor (COBRA) were designed specifically for sodium reactors. Many foreign codes are very similar to American codes but much harder to obtain (ASFRE, CADET, SABRE). Other codes like RELAP can be used in a non-conventional way as a sub-channel analysis code; however, it requires the use of a very large number of junctions, which makes setting up the input file very cumbersome (35). Table 2-1 below contains a pared down list of the most promising codes, with their most current versions listed, and the important criteria that they do or do not satisfy.

The final code listed, COBRA-IV-I satisfied the most important column, availability, and almost every other requirement. The only other code readily available was SuperEnergy2 and that lacked many capabilities. COBRA-IV-I did have some drawbacks, the main one being its age, the IV-I version is from 1976, which evolved from codes written 10 years before that. Nonetheless it was the best choice.

Table 2-1- Comparison of possible sub-channel analysis codes considered for use based on properties deemed necessary for the chosen code.

Code	Hexagonal Geometry	Transient Analysis	Transverse Momentum Equation	Available	Current Correlations
SuperEnergy2	Limited number of rings	No	No	Yes	No
SABRE4	Yes	Yes	Yes	No	No
MATRA LMR	Yes	Yes	Yes	No	Yes
SLTHEN	Limited number of rings	No	No	No	Yes
COBRA-IV-I	Yes	Yes	Yes	Yes	No

2.2. COBRA-IV-I

2.2.1. Code Structure and Initial Changes

Initial changes were made to the COBRA code so it could be compiled and run on modern machines. The code was designed to be run on ancient computers such as a CDC-7600, a CRAY, or an IBM360. The language used for the code was Fortran IV, the version developed in 1961 predecessor to Fortran 66. Due to the premium on computer memory 45 years ago, an additional program, called SPECSET accompanied COBRA to resize arrays based on the size of the problem. These common blocks were inserted into the code with the "include" statement, however maximum sizes for arrays must still be set before the executable is compiled.

Table 2-2 shows what variables are sized by this program along with the reasonable values used to compile the program that should allow for most assemblies to be run without recompiling. If it is desired to run an assembly that does not fit these characteristics the code can be recompiled.

A second additional program also accompanies COBRA called GEOM. GEOM creates geometry files that are needed to run COBRA using simple geometry inputs. A wrapper program was designed to run both GEOM and COBRA. This program makes entering the input and running both programs easier and more efficient.

COBRA itself is composed of many sub-routines ranging from ones as simple as HCOOL, a sub-routine used to determine heat transfer coefficients, to more complicated ones like SCHEME and XSCHEM. These two routines are of particular importance because they perform the steady-state implicit and transient explicit solutions, respectively. A description of all the sub-routines can be found in (31). Figure 2-1 shows the diagrams for SCHEME and XSCHEME, while Figure 2-2 shows the overall flow diagram for the program, and where SCHEME and XSCHEME fit in.

Table 2-2-Listing of arrays that must be sized with the program SPECSET before COBRA can be compiled. Values given are those used to compile so most SFR assembly geometries can be examined.

Parameter Name	Description	Maximum value for current version
MP	Cards in property, axial heat flux, and forcing function tables	601
MC	Sub-channels	546
MG	Sub-channel gap connections	816
ML	Axial locations for gap and area variation	10
MX	Axial nodes plus one	451
MN	Fuel collocation points plus three	6
MT	Fuel types	4
MR	Fuel rods	271
ME	Same as MX	451
MZ	Axial locations for grid spacers	12
MK	Number of grid spacer types	5
MA	Sub-channels that can have area variation	42
MW	Wall connections	24
MY	Axial fuel type divisions	5
MO	Array width	5
MI	Connections to a channel	24
MS	Gaps that can have gap spacing variation	60

The implicit solution scheme uses a lumped parameter finite difference method to solve the conservation equations (Equations 1-1 through 1-4 in Section 1.2.2). The final formulation for these equations is shown in Equations 2-1 through 2-4 (31).

Continuity

$$A_j \frac{(\rho_j - \bar{\rho}_j)}{\Delta t} + \frac{m_j - m_{j-1}}{\Delta x} = -[DC]^T W_j \qquad 2\text{-}1$$

The matrix operators [DC] and $[DC]^T$ are the finite difference and summing operators, respectively. A bar over a variable denotes the previous time quantity.

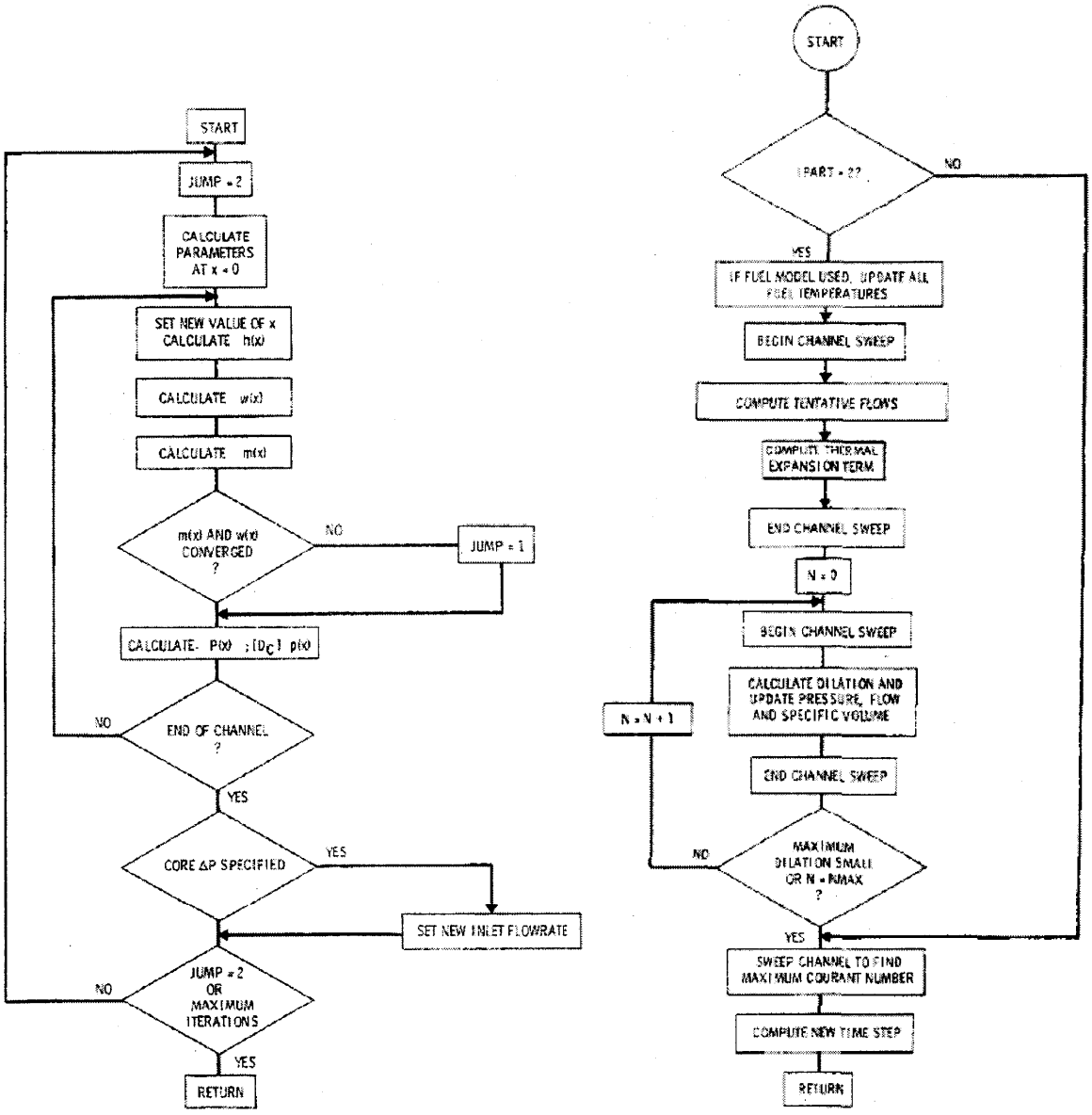

Figure 2-1- Flow diagrams showing the calculation procedure used in SCHEME and XSCHEM, the sub-routines used by COBRA-IV-I to calculate the implicit and explicit solution schemes (31).

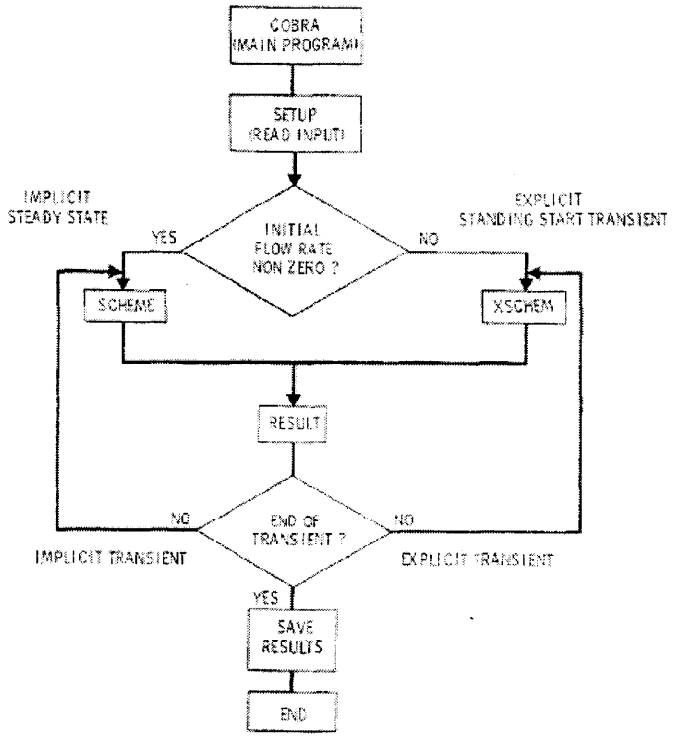

Figure 2-2- Flow diagram for the main COBRA routine (31).

Energy

$$\frac{A'\bar{\rho}(h_j - \bar{h}_j)}{\Delta t} + \frac{m_{j-1}(h_j - h_{j-1})}{\Delta x} = q' - \left[[DC]^T h_j^* W_j + [DC]^T W'[DC]h_j - h_j[DC]^T W_j\right] + Q_A + [DC]^T c[DC]_j^T + [DW]^T U_w(T_{wj} - T_j) \quad 2\text{-}2$$

In this equation U represents the overall heat transfer coefficient, the subscript w denotes wall, c is the thermal conduction coefficient, and the operator $[DW]^T$ is similar to $[DC]^T$ but orders by wall connection rather than sub-channel. These appear in terms that were not in the original energy Equation 1-2, as they were either assumed negligible (radial conduction) or not accounted for (wall heat transfer). Additionally, the term Q_A is new and accounts for axial

conduction. The set of bracketed terms at the end of the first line of the equation are equivalent to the two summations in Equation 1-2, having slightly different definitions of crossflow rate adds the additional complexity.

Axial Momentum

$$\frac{m_j - \bar{m}_j}{\Delta t} + [DC]^t u_j^* w_j + \left(\frac{m_j u_j - m_{j-1} u_{j-1}}{\Delta x}\right) = -gA'\rho\cos(\theta) - \frac{A' g\left(P_j - P_{j-1}\right)}{\Delta x} - [DC]^T w'[DC]u_j - K_L m_j^2 \qquad 2\text{-}3$$

The terms in this equation match up one to one with Equation 1-3, the only differences being that u is used for velocity in place of v and the cos(θ) term accounts for the possibility of a non-vertical geometry. The last term is the loss due to friction.

Transverse Momentum

$$\frac{w_j - \bar{w}_j}{\Delta t} + \left(\frac{u_j^* w_j - u_{j-1}^* w_{j-1}}{\Delta x}\right) + \frac{s}{l} c_j w_j = \frac{s}{l}[DC]P_{j-1} - \frac{s}{l}[S][DC]^T w_j^2 \frac{\cos\theta}{\rho^* s^2} \qquad 2\text{-}4$$

The second and third terms in Equation 1-4 are combined into the second term in the equation above; this can be done because the control volume is selected so that no lateral flow exists across transverse surfaces. For this same reason Δx' can be written as *l*, the characteristic gap length. The new term on the left hand side of the equation is a conduction term, while the terms of the left match up to Equation 1-4 as pressure drop and friction loss terms. The new operator that appears, [S], is a summing operator similar to [DC].

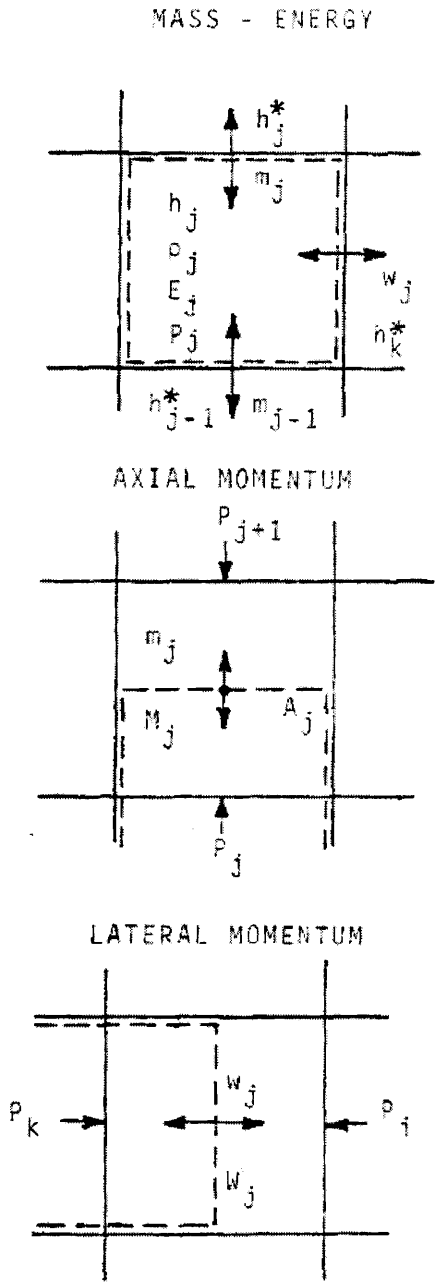

Figure 2-3- Computational cells used for the explicit energy equations. Dashed lines show the boundaries of the Mass-Energy Cells (31).

The explicit solution scheme is a pressure-velocity solution method with an implicit energy equation. It uses Equations 2-5 through 2-8, whose computational cells are shown in Figure 2-3 (31).

Continuity (Implicit)

$$A\Delta x\frac{\delta\rho}{\delta t}+[DC]^T w_j^{n+1}\Delta x+m_j^{n+1}-m_{j-1}^{n+1}=E_j^{n+1} \qquad 2\text{-}5$$

Energy (Implicit)

$$A\Delta x\frac{\delta\rho h}{\delta t}+[DC]^T h_k^* w_j^{n+1}\Delta x+m_j^{n+1}h_j^*-m_{j-1}^{n+1}h_{j-1}^*=Q_j \qquad 2\text{-}6$$

Axial Momentum (Implicit)

$$m_j^{n+1}=m_j^n-\Delta tM_j-A\frac{\Delta t}{\Delta x}g\left(P_{j+1}^{n+1}-P_j^{n+1}\right) \qquad 2\text{-}7$$

Transverse Momentum (Implicit)

$$w_j^{n+1}=w_j^n-\Delta tW_j-\frac{s}{l}g\Delta t[DC]P_j^{n+1} \qquad 2\text{-}8$$

The superscript n refers to the time step. The terms Q, M, and W are lumped explicit terms for energy,

axial flow, and transverse flow, respectively. The term E in the continuity equation represents volume dilation or volumetric error which is to be corrected by pressure adjustment in the solution. Using Equation 2-9 which, relates density to enthalpy, with Equations 2-5 and 2-6, Equation 2-10 can be derived for E_j (31).

$$\rho = \rho(h, P^*) \tag{2-9}$$

$$E_j' = m_j^{n+1} v_j^* - m_{j-1}^{n+1} v_{j-1}^* + \Delta x [DC]^T w_j^{n+1} v_k^* - \Delta x \frac{\delta v}{\delta h} Q - \Delta x A' \frac{\delta v}{\delta h} \rho_j^n \frac{\delta P}{\delta t} \tag{2-10}$$

By further substituting Equations 2-6 and 2-7 into Equation 2-10 a pressure correction equation is formed. The derivate of the pressure correction equation is (31):

$$\frac{\delta E_j'}{\delta P_j} = g \frac{\Delta x}{\Delta t} A \left[v_j^* + v_{j-1}^* + \frac{\Delta x^2}{A} \frac{s}{l} [DC]^T v_k^* [DC] \right] \tag{2-11}$$

The explicit solution proceeds by first calculating the flows in the momentum equations (Equations 2-7and 2-8) using an initial guess or pervious cycle result for pressure. The cell volume error and other quantities are now calculated with pressures and flows from the first calculation. The amount of pressure change for the cycle is calculated with Equations 2-9 and 2-11 through the equation below (31).

$$\delta P_j = \frac{-E_j'}{\frac{\delta E}{\delta P}} \tag{2-12}$$

This change is used to calculate the other incremental changes to complete the cycle. The solution is complete when E_j' falls below a set threshold (31).

In addition to these fundamental equations several constitutive relationships are needed. COBRA-IV-I contained many cutting edge correlations from its time; however since then there have been many developments. Before any tinkering was done with these relations a few analyses were done to examine the validity of the code as is.

2.2.2. Reference Case

The first analysis conducted was a reference case to benchmark how well the code performed without making any changes to it. The Oak Ridge National Laboratory (ORNL) 19-pin test assembly was chosen as the reference case because it was a common test case for other codes and because it contained data for both high and low flow cases (where different flow and mixing effects are dominant) (40)(41). Table 2-3 shows the input parameters used in COBRA to do the calculations.

The parameters are broken up into three groups. The first group is the geometric parameters that were discussed earlier, the values needed to fully define the sub-channel geometry. The second group is the system conditions which detail the specific operating conditions of the experiment or simulation preformed. The final group is the calculation parameters, which are values that COBRA needs as inputs but are not physical like the previous two groups.

Several sources of data have been published from other codes that have also run these cases. These include data sets from RELAP (35), MATRA-LMR, SABRE4 and SLTHEN (34). However, in most cases the data was published in the form of a plot, thus obtaining values introduced a certain amount of error to the values above what they previously contained.

Both cases were plotted with the initial result and comparisons to other codes and the data from the experiment, as shown in Figure 2-4. The X-axis on these plots is sub-channel number. The sub-channels to plot were chosen to show the behavior of the coolant across the assembly. Figure 2-5 shows the numbering of sub-channels for a 19-pin assembly. The values on X-axis of Figure 2-5 make a path across the assembly.

Table 2-3- Input parameters for the ORNL 19-pin test assembly to run COBRA for both high and low flow cases.

	Input Parameter	ORNL
Geometry	Number of Pins	19
	Rod Diameter (mm)	5.84
	Rod Pitch (mm)	7.26
	Wire Wrap Diameter (mm)	1.42
	Wire Wrap Pitch (m)	0.3048
	Duct inside flat to flat distance (m)	0.0341
	Total Length (m)	1.016
	Heated Length (m)	0.5334
	Lower Unheated(m)	0.4064
System Conditions	Pressure (atm)	1
	Inlet Temperature (°C)	315
	Inlet Mass Flow (kg/s)	3.0378 / 0.04087 (high / low)
	Average Rod Power (W)	16975 / 263 (high / low)
	Axial Power Distribution (max/avg)	Uniform
	Radial Power Distribution	Uniform
Calculation Parameters	Wire Pitch Fraction (δ)	0.0417
	Turbulent Mixing Factor (β)	0.01
	Number of Axial Nodes	80

The Y-axis shows the value of the temperature of each cell at the end of the heated length in relative temperature. Relative temperature is defined by Equation 2-13.

$$T_{j,rel} = \frac{T_{j,x} - T_{in}}{T_{out,avg} - T_{in}} \qquad 2\text{-}13$$

Where the variables are defined as:

$T_{j,rel}$ The relative temperature for a sub-channel j

$T_{j,x}$ The coolant temperature of sub-channel j, at the location x where the relative temperature is calculated, usually the the outlet or end of heated length

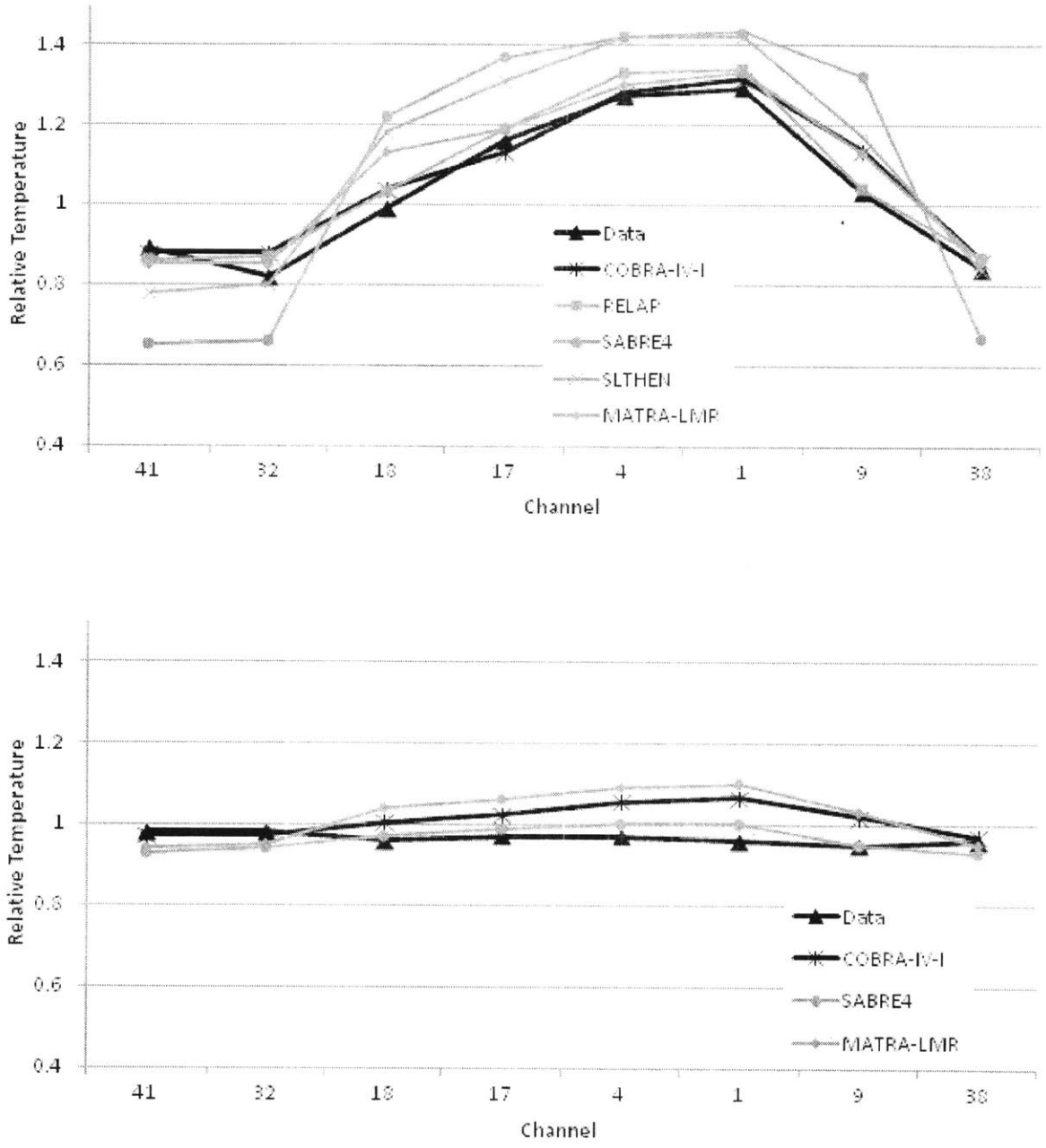

Figure 2-4- Comparison of the performance of COBRA-IV-I and other sub-channel codes with the experimental data for the ORNL test assembly for the high flow case (top) and the low flow case (bottom).

$T_{out,avg}$ The bundle average coolant outlet temperature

T_{in} The coolant inlet temperature

The relative temperature of a channel is a unitless measurement; it is the ratio of the temperature rise of the channel divided by the bundle average temperature rise. It is a convenient way to measure temperature and is commonly used in the literature; however, caution must be exercised when employing it because it is easy to disguise errors. It is better suited for determining if the shape of the temperature profile is correct, saying little about the magnitude of the temperature rise. In this way it lives up to its name as it is good for determining the performance of the code for each channel relative to the others but not absolutely.

The high flow case shows good agreement of the data with COBRA, MATRA, and RELAP. SABRE and SLTHEN show higher temperatures in the interior of the assembly and lower temperatures on the periphery, which is caused by a greater fraction of the flow going through the peripheral sub-channels. The high flow case shows that the correlations are working well for this set of operating conditions.

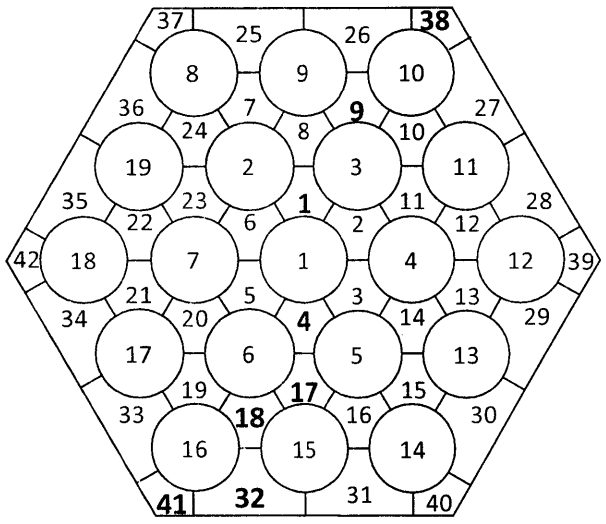

Figure 2-5- Rod and sub-channel numbering for a 19-pin assembly with the cells bolded that correspond to the temperature profile of Figure 2.5.

The low flow case shows different behavior. The first thing of note is that every data point from the experiment is below 1.00. However, with the definition of relative temperature this is impossible; a weighted flow average of all the sub-channels relative temperature should yield unity. While every channel is not plotted on this graph, the center channels are, which are expected to be the hottest because the power distribution across the assembly is uniform. It stands to reason if the center channels are not even 1.00 then no other channel will be, making it impossible for all the channels to average out properly.

The reason the experimental data is like this can be explained in many ways. The first is measurement error; error in measurement accuracy for the various instruments used in the experiment does not exceed 1% with the exception of flow measurement, 5% (42). So it is unlikely this phenomenon was caused solely by measurement error. The second is the way the relative temperature was calculated in the experiment; the temperature used for the bundle average was not a true bundle average outlet temperature. It was not calculated with the mass flow and power or by flow averaging the temperature of every channel, but rather measured downstream from the heated length with a single thermocouple (40). A third affect that could cause this phenomenon would be improperly calculating the bundle average outlet temperature by neglecting heat losses through the walls of the bundle. This effect does not apply here because the bundle average temperature was not calculated, but will be important when the phenomenon of all data points being below one appears again in Section 3.2.3.

A plausible simple assumption that can be used when observing this phenomenon is that the temperature profile across the assembly is approximately flat around unity. Comparing the values of the actual outlet temperatures for the ORNL low flow case examined supports this assumption; the outlet temperatures range from 783.6 °F to 785.9 °F (42), a difference of just 2.3 °F or just over one degree Celsius. As a final comment on this effect, while visible in this case due to the nature of the data this error will be a part of all data sets even when not as obvious-the high flow case for example does not look abnormal. Matching experimental data within 5% is a reasonable goal for the code, much beyond that cannot be resolved.

The COBRA result does not match the low flow case well, neither does the MATRA result. SABRE is the only one of the three to match the data well. This indicates that the correlations for this regime need examination, as will be done in Section 2.4.

2.2.3. Sensitivity Analysis of and Convergence of COBRA

The second analysis performed was to examine the transient capabilities of the code. A parametric study looked at how both time step size and axial nodalization affected the code performance for two separate accident scenarios for a generic assembly. The two accident scenarios are an Unprotected Transient Over Power (UTOP) and Unprotected Loss Of Flow (ULOF).

The input parameters for the sample assembly are listed in Table 2-4. The details of the transient cases are shown in Figure 2-6 and Figure 2-7. The implicit solution scheme was used.

Table 2-4- Input parameters for a sample test assembly to run COBRA for a sensitivity analysis for time step and node length.

	Input Parameter	Sample Assembly
Geometry	Number of Pins	271
	Rod Diameter (mm)	8.8
	Rod Pitch (mm)	9.85
	Wire Wrap Diameter (mm)	1.05
	Wire Wrap Pitch (m)	0.5
	Duct inside flat to flat distance (m)	0.165
	Total Length (m)	4.5
	Heated Length (m)	2.5
	Lower Unheated Length (m)	0
System Conditions	Pressure (atm)	1
	Inlet Temperature (°C)	360
	Inlet Mass Flow (kg/s)	49.2
	Average Rod Power (W)	38773
	Axial Power Distribution (max/avg)	Cos 1.57
	Radial Power Distribution	Uniform
Calculation Parameters	Wire Pitch Fraction (δ)	Based on axial nodes
	Turbulent Mixing Factor (β)	0.01
	Number of Axial Nodes	varied

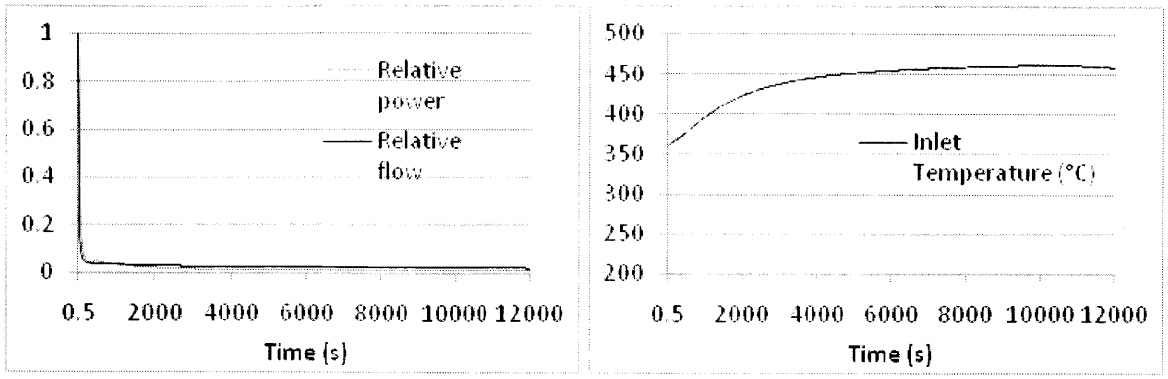

Figure 2-6- Relative power and flow and inlet temperature for the ULOF transient as a function of time.

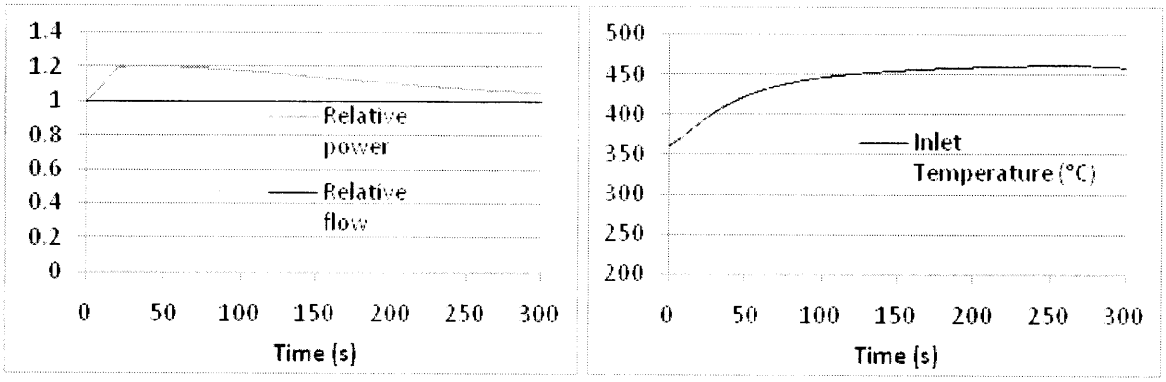

Figure 2-7- Relative power and flow and inlet temperature for the UTOP transient as a function of time.

The purpose of this analysis was twofold: to determine what reasonable node lengths were and what time steps were practical for running the code with the implicit transient solution (time step is set by the Courant limit for the explicit solution as described Section 4.1.2). This was done by running various time steps and node lengths and determining how they affected the time it took to run the code and the answer that it produced. For the purpose of determining the validity of each result, it was compared to the result with the finest step for an error calculation. The error calculation was performed simply with Equation 2-14.

$$Error = \frac{|x_{n,i} - x_{m,i}|}{x_{n,i}} \qquad 2\text{-}14$$

The Root Mean Square (RMS) difference of the data can be also calculated and used to determine the order of convergence. The formula for calculating the RMS difference is shown in Equation 2-15 below.

$$RMS = \sqrt{\frac{1}{j}\sum_{i=1}^{j}(x_{n,i} - x_{m,i})^2} \qquad 2\text{-}15$$

In these equations j is the number of data points being compared and $x_{n,i}$ and $x_{m,i}$ are the corresponding data points at time i. For the purposes of calculating error $x_{n,i}$ was taken as the finest nodalization for the given case. With this definition the finest nodalization has identically 0 error.

Error was calculated for coolant temperature for both transients at several axial locations and pressure drop for each channel type (interior, edge, and corner). The errors for the various locations were of similar magnitude. The results presented below are for the outlet of the assembly.

Table 2-5 shows the matrix of cases that were examined. For each transient both axial node length and time step were varied, while one was examined the other was held constant. Limits on sizes and lengths that could be examined were determined by various factors. The maximum number of time steps was 100,000. If the time step or node length was too course the code would fail to converge. The combinations examined represented the range of available nodalizations.

The run time for the calculation is approximately linear with both nodalizations, as can be seen by the similar values in the run time per nodes columns of Table 2-5. The run time per axial node is significantly greater for the ULOF then the UTOP because there are more time

nodes for the ULOF. All cases were run on the same computer with a Pentium 4 3.6 GHz processor.

Figure 2-8 through Figure 2-11 show the error for the hot channel outlet temperature, as defined by Equation 2-14 plotted as a function time. The larger node steps display greater error than the smaller node steps as would be expected. The large initial error for Figure 2-9 is the result of the the conditions of the ULOF transient changing so quickly initially, as can be seen on Figure 2-6. The error for all the nodalizations stays mostly constant over time, with the time nodalizations being slightly more variable than the axial ones.

Table 2-5- Node lengths and time steps examined for the parametric study, and a comparison their of the run times. The number of time steps is the length of the transient divided by the time step size.

	Axial Node Size (cm)	Number of Axial Nodes	Time Step Size (s)	Number of time steps	Run Time (s)	Run Time Per Axial Node (s)	Run Time Per Time Node (s)
ULOF	2	219	5	2400	2974	13.58	
	4	109	2	6000	2681		0.45
	4	109	5	2400	1030	9.45	0.43
	4	109	10	1200	681		0.57
	6	73	5	2400	786	10.77	
UTOP	2	219	0.33	900	750	3.42	
	4	109	0.1	3000	986		0.33
	4	109	0.33	900	310	2.84	0.34
	4	109	1	300	124		0.41
	8	55	0.33	900	198	3.60	

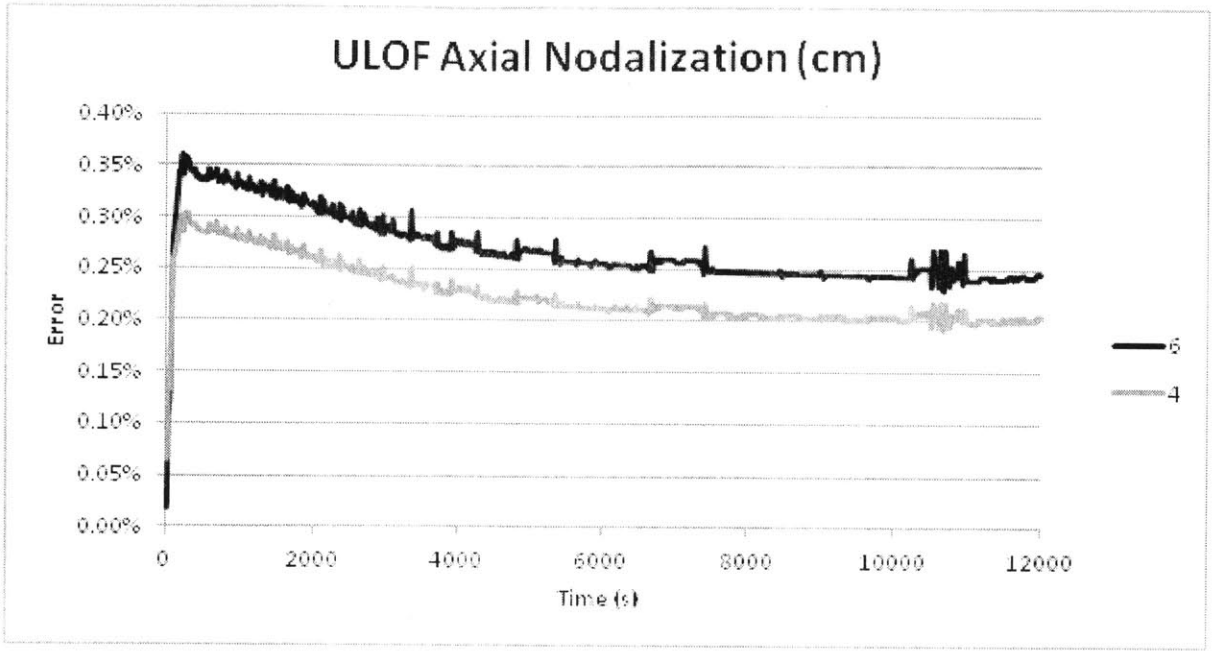

Figure 2-8- Error in the hot channel temperature rise for the ULOF for 4 and 6 cm node lengths relative to a 2 cm node length.

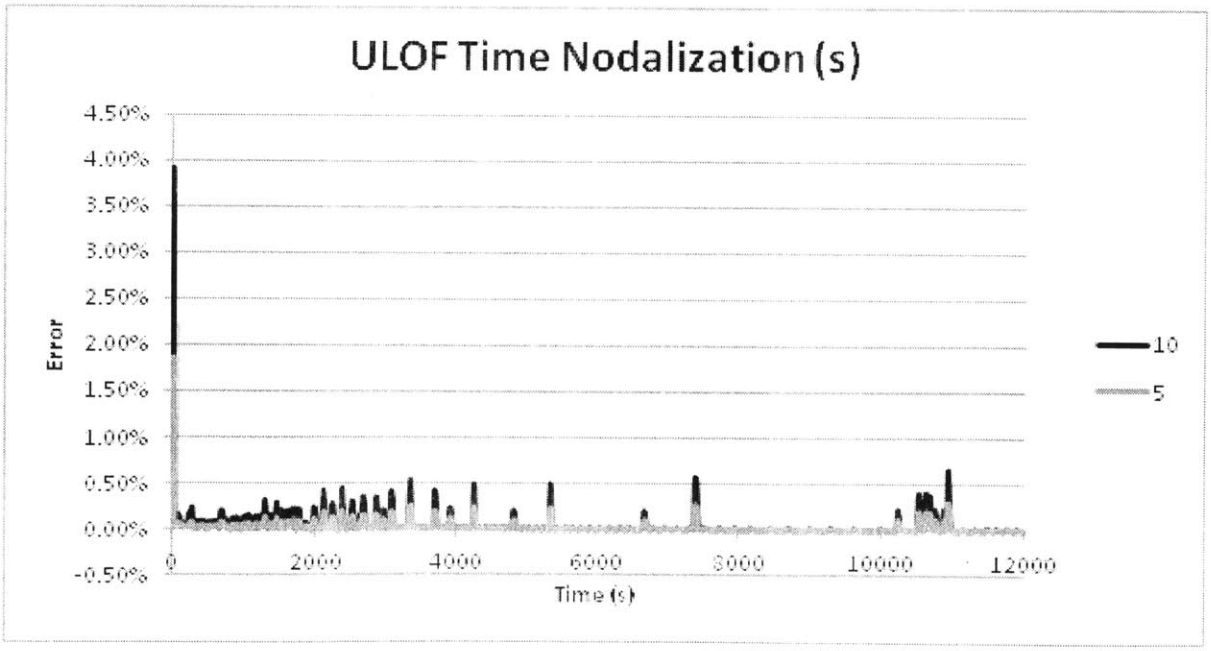

Figure 2-9- Error in the hot channel temperature rise for the ULOF for 5 and 10 second node lengths relative to a 2 second node length.

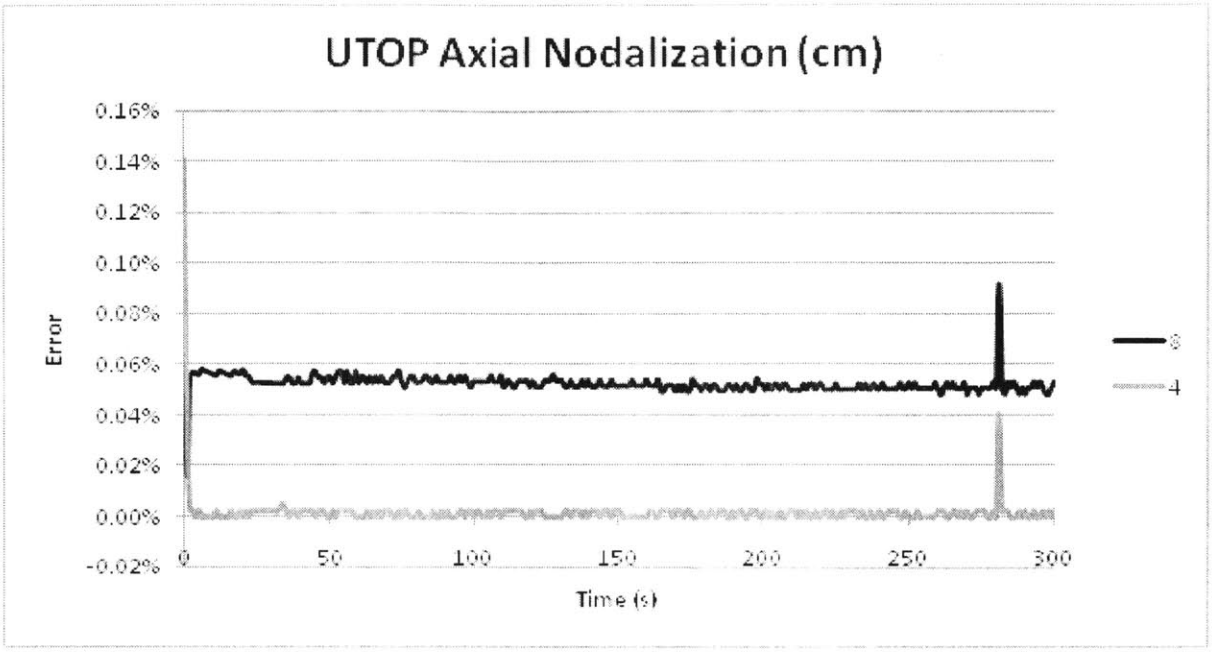

Figure 2-10- Error in the hot channel temperature rise for the UTOP for 4 and 8 cm node lengths relative to a 2 cm node length.

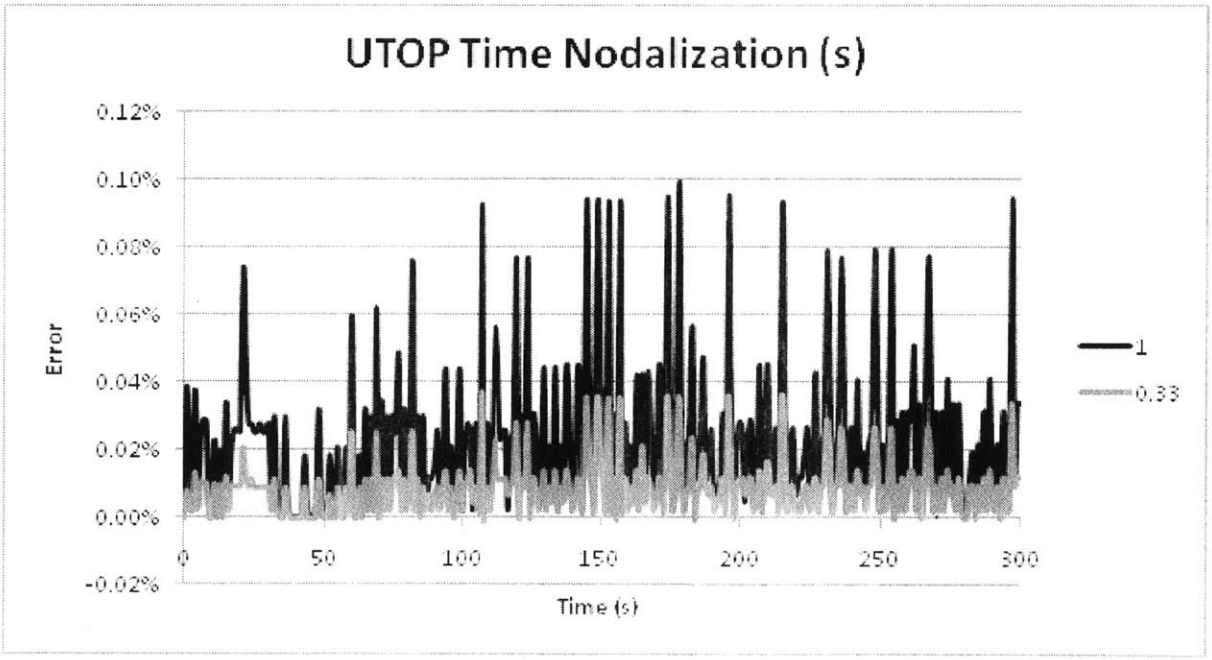

Figure 2-11- Error in the hot channel temperature rise for the UTOP for 0.33 and 1 second node lengths relative to a 0.1 second node length.

The results of the RMS analysis for all three channel types for both temperature rise and pressure drop are shown in Table 2-6. The RMS difference for the pressure drop is very small for all cases, even the axial UTOP analysis which has channel errors of near 0.5 kPa because the bundle pressure drop is hundreds of kPa.

The temperature rise data for the axial nodalizations shows little to no order. There is not a monotonic convergence based on node size. This can be seen on Figure 2-12, which is a plot of the node length data plotted on a log-log scale. On the order of 1 °C of variation occurs for the corner and edge channels as the axial node size is changed in both transients, again though this only a small fraction of the total temperature rise, which is over 200 °C for the duration of the transients.

The data converges much better based on time step; with order of approximately 1 (the regression value is .92). Figure 2-13 shows the data on a log-log plot, the linear convergence can be seen clearly.

Table 2-6- RMS data for temperature rise and pressure drop for a ULOF and UTOP simulated with COBRA.

				Root Mean Square Difference					
				Temperature Rise (°C)			Pressure Drop (kPa)		
	x_n	x_m	x_n-x_m	Interior Channel	Edge Channel	Corner Channel	Interior Channel	Edge Channel	Corner Channel
Time ULOF	2 s	5 s	3 s	0.31	0.22	0.22	0.01	0.01	0.01
	5 s	10 s	5 s	0.35	0.42	0.26	0.01	0.01	0.01
	2 s	10 s	8 s	0.66	0.58	0.47	0.01	0.01	0.01
Axial ULOF	2 cm	4 cm	2 cm	0.44	1.34	1.42	0.03	0.04	0.03
	4 cm	6 cm	2 cm	0.09	0.25	0.45	0.00	0.01	0.01
	2 cm	6 cm	4 cm	0.53	1.12	1.00	0.03	0.04	0.05
Time UTOP	0.1 s	0.33 s	0.23 s	0.03	0.02	0.02	0.01	0.01	0.01
	0.33 s	1 s	0.67 s	0.05	0.04	0.04	0.01	0.01	0.01
	0.1 s	1 s	0.9 s	0.07	0.06	0.06	0.02	0.02	0.02
Axial UTOP	2 cm	4 cm	2 cm	0.02	1.95	1.34	0.16	0.19	0.17
	4 cm	8 cm	4 cm	0.13	1.23	0.72	0.41	0.06	0.37
	2 cm	8 cm	6 cm	0.12	0.73	0.62	0.47	0.21	0.28

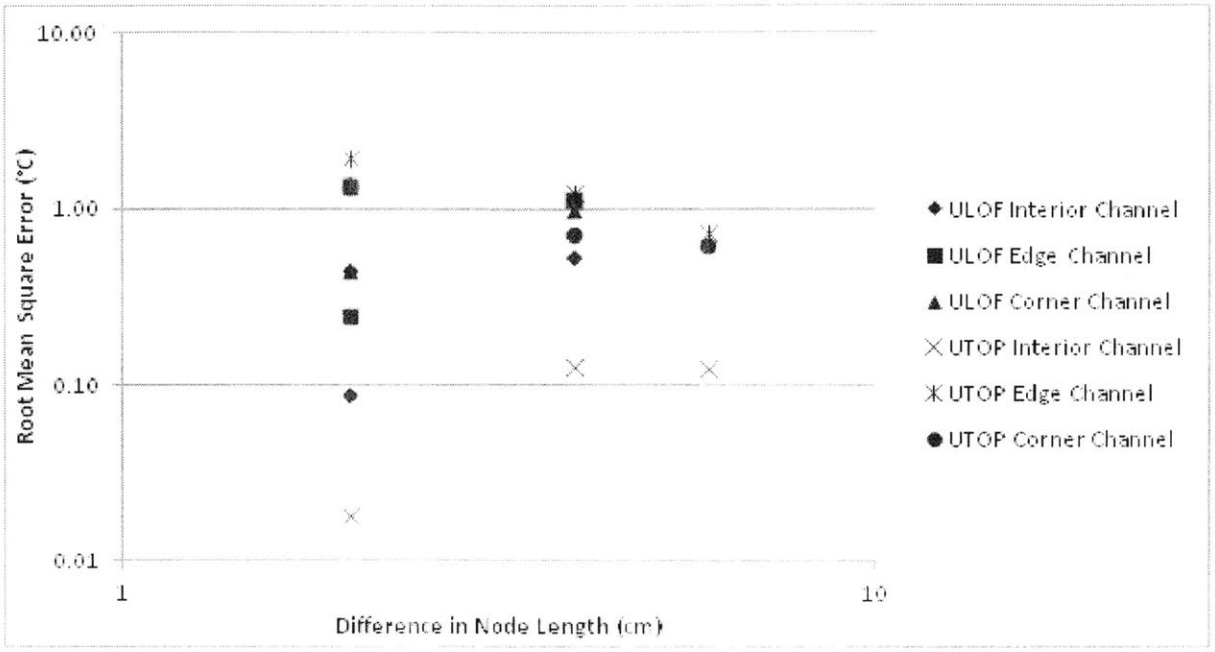

Figure 2-12- Root Mean Square difference of temperature rise for COBRA axial node length for two transients plotted on a log-log scale.

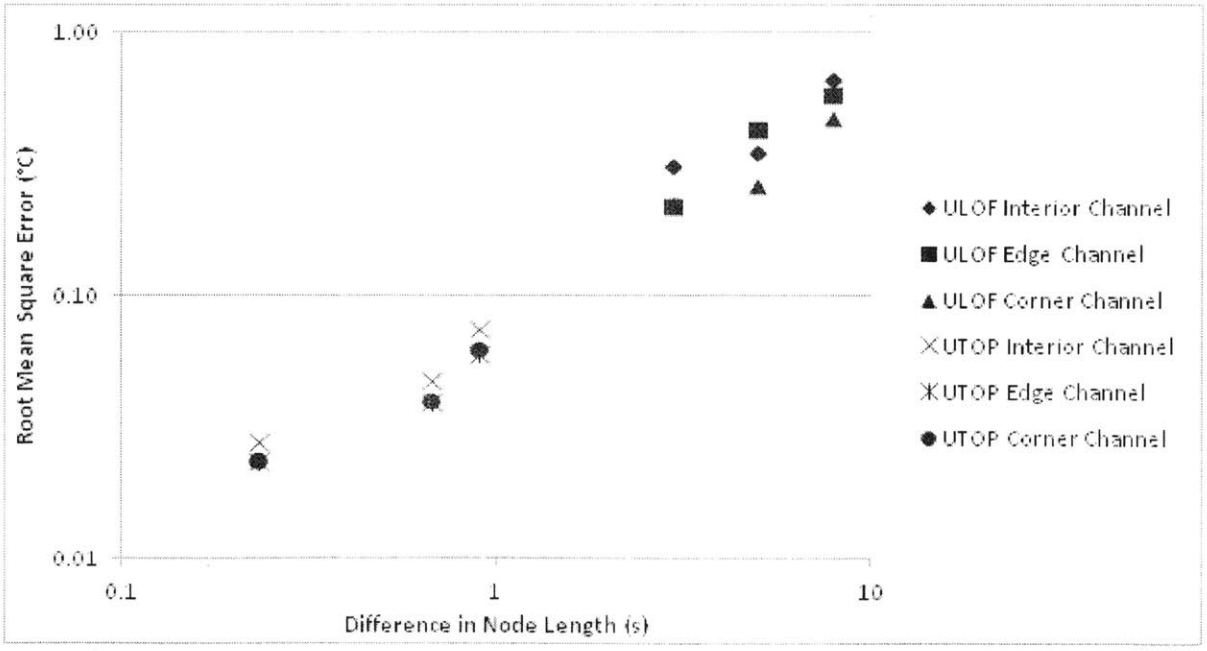

Figure 2-13- Root Mean Square difference of temperature rise for COBRA time node length for two transients plotted on a log-log scale.

The conclusions drawn from this analysis were that COBRA node lengths can be varied without adversely affecting the results. Furthermore, the time to run COBRA is proportional to both the number of axial and time nodes. Because COBRA runs steady cases very quickly, on the order of tens of seconds, a fine axial node mesh should always be used. For transients the time step should be determined based on the length of the transient, how rapid changes to the operating conditions occur, and the computational power available.

2.3. Correlations Update

The initial analysis of COBRA-IV-I showed it to be very capable for examining SFR assemblies; however, there was room for improvement, especially for low flow situations. Each of the areas in the code where empirical correlations were used (pressure drop, mixing, and heat transfer) were closely reviewed. Then a literature review was conducted to survey advancements made in these areas. New correlations were implemented in each area. As new correlations were implemented they were benchmarked individually against the reference case, the ORNL bundle (the details of this case can be found in section 2.3.2 Table 2-3)

2.3.1. Pressure Drop

In COBRA pressure drop is calculated from friction factor in the usual way using Equation 2-16.

$$\Delta P = f \frac{L}{D_e} \frac{\rho v^2}{2} \qquad 2\text{-}16$$

Where f is friction factor, L is length, D_e is equivalent diameter, ρ is density, and v is velocity. The existing correlation, in COBRA-IV-I for friction factor, has the form of Equation 2-17. This equation includes three constants, A, B, and C, which the user is to specify and the Reynolds Number, Re. The COBRA manual recommends values of 0.316, -0.25, and 0 for these constants, corresponding to the Blasius approximation for friction factor (43). This is for a smooth case however, not taking into account pressure drop from the wire wrap.

$$f = A \times Re^{B} + C \qquad 2\text{-}17$$

Novendstern (44) proposed a correction factor to account for the additional pressure loss due to wire wrap, Equation 2-18.

$$M = \left(\frac{1.034}{(P/D)^{0.124}} + \frac{29.7 \left(\frac{P}{D}\right)^{6.94} (Re)^{0.086}}{(H/D)^{2.239}} \right)^{0.885} \qquad 2\text{-}18$$

Where P is the rod pitch and H is the wire wrap pitch. Novendstern's factor was added to the code as an option for the user to choose. Both the original COBRA model and the Novendstern model share a limitation: they do not account for difference in pressure drop that result from channel type (interior, edge, or corner). Cheng and Todreas developed a set of correlations, fitted with experimental data, which provide a friction factor correlation for each channel type (45)(46). These were also implemented into the code as an option. When using the Cheng and Todreas model for pressure drop, it is necessary to also use their model for forced mixing, which will be described below in Section 2.3.2, to obtain accurate results.

The Cheng and Todreas model assumes that the pressure loss comes from the sum of the friction loss from the fuel and the drag loss on the wire. The friction loss on the fuel for an interior channel is defined similar to the friction loss in a tube

$$e_f = f'\left(\frac{P_w'}{P_w}\right)\left(\frac{L}{De}\frac{\rho V^2}{2}\right) \qquad 2\text{-}19$$

The extra term that would not appear in a pressure drop equation for a smooth channel or tube is the ratio of bare wetted perimeter, P_w', for the channel divided by the wire-wrapped wetted perimeter, P_w. Note that Cheng and Todreas use axially averaged values for wire-wrapped geometric parameters, not local ones. The friction factor f' is defined based on the flow type

$$f' = C_f'/Re^m$$
$$m = \begin{matrix} 1\, for\ laminar \\ .18\, for\ turblent \end{matrix} \qquad 2\text{-}20$$

C_f' is a function of the pitch to diameter ratio

$$C_f' = a + b_1(P/D - 1) + b_2(P/D - 1)^2 \qquad 2\text{-}21$$

Where a, b_1, and b_2 are constants (different for laminar and turbulent flow) and can be found in Table 2-7 (45). For transition flow the friction factor is found from

$$f_{tr} = f_L(1 - \psi)^\gamma + f_T\psi^\gamma \qquad 2\text{-}22$$

Where ψ is an intermittency factor defined as

$$\psi = \frac{\log Re - \log Re_L}{\log Re_T - \log Re_L} \qquad 2\text{-}23$$

Table 2-7- Coefficients used for the Cheng and Todreas bare rod correlation for calculating C_f' in Equation 2-21 (45).

Flow Regime	Subchannel	1.0<P/D<1.1			1.1<P/D<1.5		
		a	b1	b2	a	b1	b2
Laminar	Interior	26.00	888.2	-3334.	62.91	216.9	-190.2
	Edge	26.18	554.5	-1480.	44.40	256.7	-267.6
	Corner	26.98	1636	-10050	87.26	38.59	-55.12
Turbulent	Interior	0.09378	1.398	-8.664	0.1458	0.03632	-0.03333
	Edge	0.09377	0.8732	-3.341	0.1430	0.04199	-0.04428
	Corner	0.1004	1.625	-11.85	0.1499	0.006706	-0.00957

and γ is an exponent fitted from data and has a value of 1/3. The drag force caused by the wire is defined as

$$e_d = 3\left(\frac{L}{H}\right)\left(\frac{A_{r1}}{A_1'}\right)C_d\left(\frac{\rho V^2}{2}\right) \qquad 2\text{-}24$$

where C_d is an empirical constant

$$C_d = \frac{W_d}{Re_1^m}\left(\frac{D_w}{De_1}\right)^m \qquad 2\text{-}25$$

and W_d is the wire drag constant defined as

$$W_d = [29.5 - 140(D_w/D) + 401(D_w/D)^2](H/D)^{-0.85} \qquad 2\text{-}26$$

for turbulent and laminar flow. The total pressure drop is the sum of these two losses.

$$e = e_f + e_d = \left[f' \left(\frac{P'_w}{P_w} \right) + C_d \left(\frac{De}{H} \right) \left(\frac{3A_{r1}}{A'_1} \right) \right] \left(\frac{L}{De} \frac{\rho V^2}{2} \right) \quad \text{2-27}$$

The effective friction factor for the total pressure drop can now be written as Equation 2-28.

$$f = \frac{1}{Re^m} \left[f' \left(\frac{P'_w}{P_w} \right) + W_d \left(\frac{De}{H} \right) \left(\frac{3A_{r1}}{A'_1} \right) \left(\frac{De}{D_w} \right)^m \right] \quad \text{2-28}$$

For the bare rod case this simplifies down to give the friction energy loss only, as would be expected. The pressure losses for edge and corner channels are derived in a similar fashion, as described by Cheng and Todreas (45).

The Cheng and Todreas correlations were the most recent and the most comprehensive set of correlations found in the literature for pressure drop in hexagonal wire wrapped assemblies. Chun and Seo (47) carried out an analysis on many pressure drop correlations. It included those developed by Rehme (48) and by Engel (49), which are not included in the code along with Novendstern's and Cheng and Todreas' correlation. The conclusion recommended Cheng and Todreas' correlation for use in sub-channel analysis for all flow regions.

Figure 2-14 shows the ORNL 19-pin high flow test plotted for each of these three correlations. The extra effect of the Novendstern factor is negligible; however, both this correlation and Blasius' match the data well. The Cheng and Todreas correlation predicts slightly higher peaking.

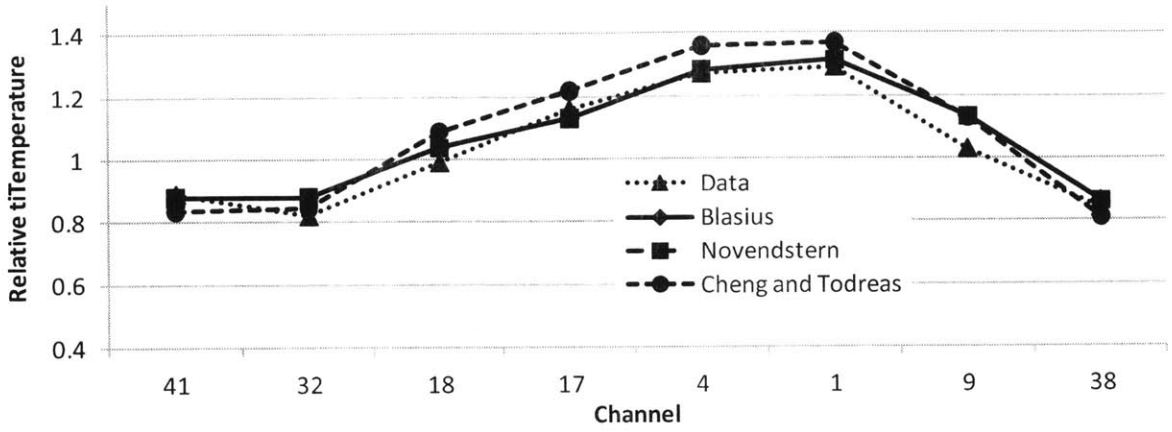

Figure 2-14- Comparison of new pressure drop correlations added to COBRA with the data and the old correlations for the high flow case.

2.3.2. Mixing

Mixing is the most complex phenomena modeled empirically, referring to mass, momentum and energy transfer across sub-channels boundaries radially. The many mixing terms, represented as W in the constitutive equations, are made up of an amalgam of different types of mixing. Some forms of mixing are accounted for by the transverse momentum equation and flow redistribution, while others require empirical model, radial conduction, and forced mixing.

Conduction mixing is a form of mixing where only energy is exchanged across the cell boundaries. COBRA has Equation 2-29 built in as an option for radial fluid conduction mixing.

$$W_p = k\frac{c}{l} * (T_i - T_j) * \kappa \qquad 2\text{-}29$$

This equation has the same form as suggested by Ro and Todreas (50). Here k is thermal conductivity of the fluid, c is the gap spacing, l is the channel centroid to centroid distance, and T

is the temperature of the channel. The two sources differ in their recommendation for the factor κ, the conduction shape factor (referred to as G_k in the COBRA literature). COBRA suggests a constant value of 0.5 for the factor while Ro and Todreas propose Equation 2-26 for it.

$$\kappa = 0.66\left(\frac{P}{D}\right)\left(\frac{c}{D}\right)^{-0.3} \qquad 2\text{-}30$$

For the geometry of the ORNL 19-pin test assembly the value of κ is 1.24 using Equation 2-30, significantly higher than the value recommended by COBRA. Furthermore Ro and Todreas propose an additional factor to account for conduction that takes place through the fuel rods.

$$R = 0.45\left(\frac{k_{rod}}{k_{Na}}\right)^{0.38}\left(\frac{P}{D}\right)^{-1.04}\left(\frac{c}{D}\right)^{-0.684} \qquad 2\text{-}31$$

This value for the ORNL geometry is 1.28. The combined effect of the two factors from the Ro and Todreas correlations yields five times more conduction mixing than COBRA recommends. The effect of this increase is shown in Figure 2-15. The high flow ORNL case is barely affected by the increased conduction mixing, as would be expected. The low flow case however is significantly smoothed out, as it should be. The conduction increase from the Ro and Todreas correlations accurately describes the low flow behavior without over-predicting the mixing or distorting the high flow predictions.

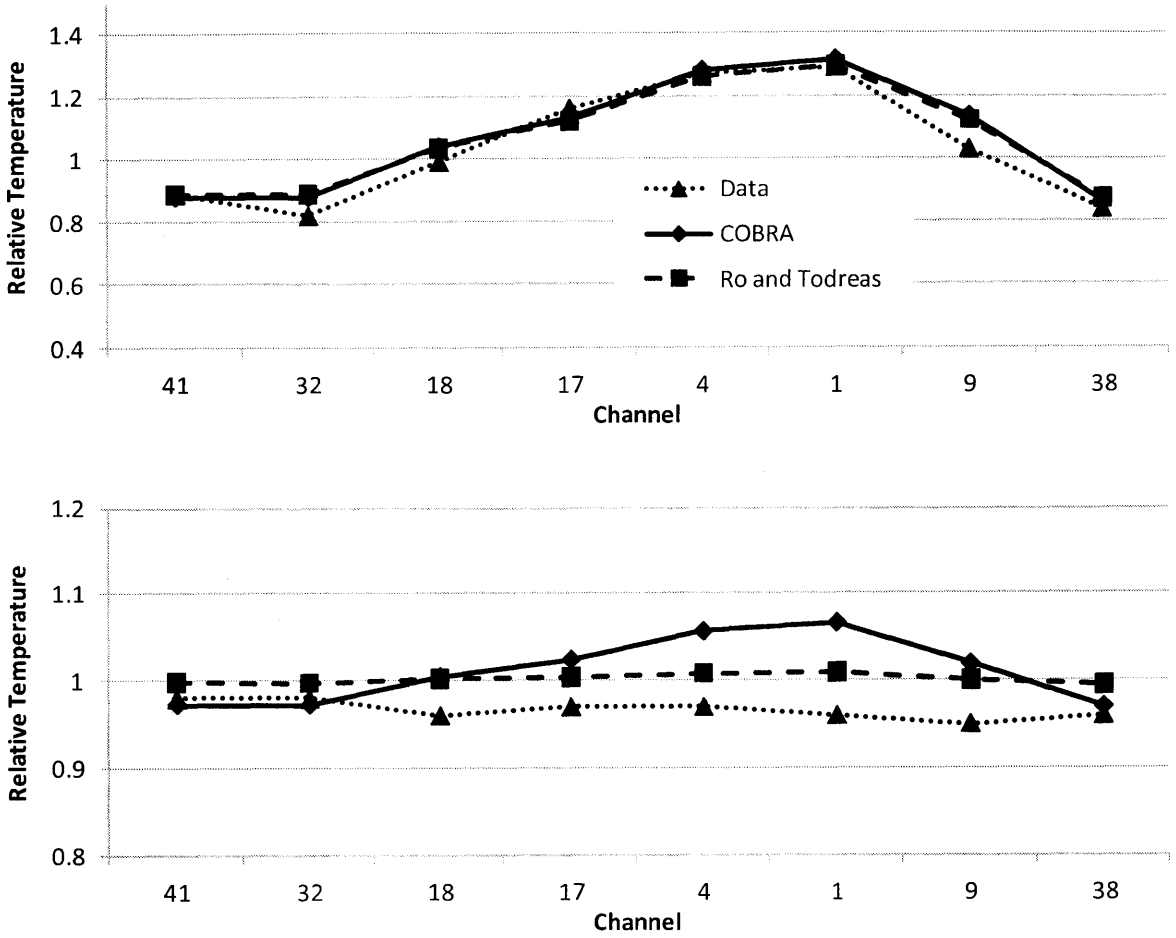

Figure 2-15- Comparison of new radial conduction correlations added to COBRA with the data and the old correlations for both the high and low flow cases.

Forced mixing is further divided into two types: wire-wrap sweeping and turbulent mixing. Wire-wrap sweeping describes mixing due to the transverse velocity of the fluid resulting from wires in the sub-channel that make an angle with the axial direction. Two similar descriptions of this effect exist, one in COBRA and another by Cheng and Todreas (45). Both models assume the transverse velocity will be proportional to the axial velocity (V), the ratio of the area of the wire to the subchannel (A_w/A') and the tangent of the angle made between the wire and the vertical axis.

$$V_T \propto V\left(\frac{A_r}{A'}\right)^{1/2} \tan\theta \qquad 2\text{-}32$$

From this, Equations 2-33 and 2-34 follow as the equations used to calculate the wire wrap mixing parameter, for interior ($\varepsilon_{1\eta}$*) and edge channels (C_{1L}). Interior mixing is mixing between an interior channel and any other channel, edge mixing is between two edge channels only. In the model included with COBRA C_m and C_s are set to one.

$$\varepsilon_{1\eta}^{*} = C_m\left(\frac{A_{r1}}{A_1'}\right)^{1/2} \tan\theta \qquad 2\text{-}33$$

$$C_{1L} = C_s\left(\frac{A_{r1}}{A_1'}\right)^{1/2} \tan\theta \qquad 2\text{-}34$$

Cheng and Todreas introduce the equations below to calculate C_m and C_s. Although the COBRA and Cheng and Todreas models are similar, each should be used only with its corresponding description of pressure drop to obtain consistent results.

Turbulent Flow

$$C_{mT} = .14\left(\frac{c}{D}\right)^{-0.5} \qquad 2\text{-}35$$

$$C_{sT} = .75\left(\frac{H}{D}\right)^{0.3} \qquad 2\text{-}36$$

Laminar Flow

$$C_{mL} = .077\left(\frac{c}{D}\right)^{-0.5} \qquad 2\text{-}37$$

$$C_{sL} = .413\left(\frac{H}{D}\right)^{0.3} \quad 2\text{-}38$$

Where c is gap between the rods, D is the rod diameter, and H is the wire wrap pitch.

Turbulent mixing is the result of turbulent motion of the fluid causing it to transverse sub-channel boundaries. COBRA offers several options for turbulent mixing correlations; the simplest one is Equation 2-39, where β is the turbulent mixing factor and G the mass flux.

$$W_k = \beta\, c\, \bar{G} \quad 2\text{-}39$$

COBRA recommends a constant value of 0.01 for the turbulent mixing factor β. Many correlations exist to calculate β. One such correlation was developed by Rehme, shown in Equation 2-40 (51), where the variable D_h denotes hydraulic diameter of the cell.

$$\beta = 0.00525\left(\frac{D}{l}\right)\left(\frac{D_h}{c}\right)Re^{-0.1} \quad 2\text{-}40$$

The advantage of using a correlation for β in place of a constant is to account for the local conditions of the sub-channel of interest. A representative value of β calculated for the ORNL 19-pin test assembly is 0.008. The impact of such a small difference is negligible, as shown in Figure 2-16. In fact the general effect of turbulent mixing is so small (less than 10% of total mixing) that in many cases it can be ignored because in SFR fuel assemblies forced mixing driven by the wire wrap dominates (45).

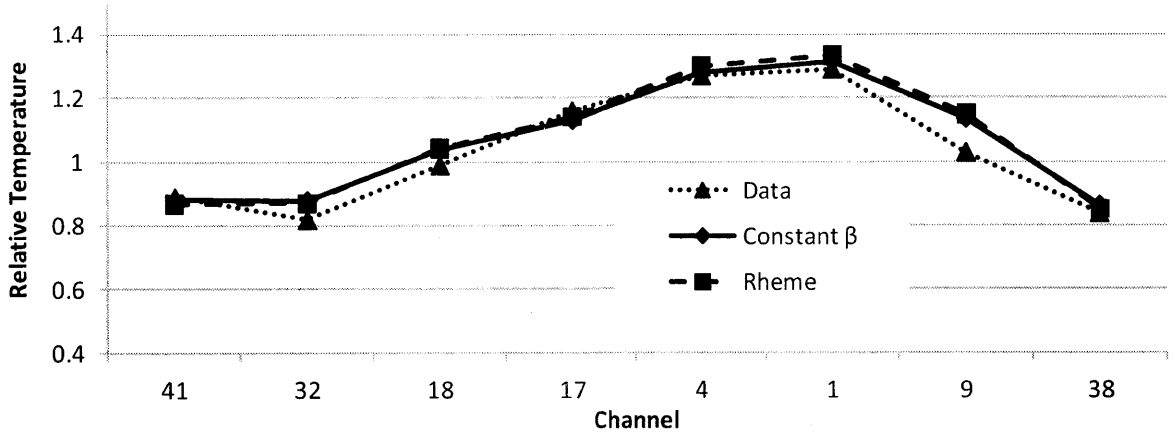

Figure 2-16- Comparison of new turbulent mixing correlation added to COBRA with the data and the old correlation.

2.3.3. Heat Transfer

The heat transfer coefficient is not needed for the actual sub-channel calculations for the coolant; it is used only when calculating clad and fuel temperatures. The heat transfer correlation in COBRA is Equation 2-41, with Pr being the Prandlt number.

$$h = \left(\frac{k}{D_h}\right)(A1 \cdot Re^{A2} Pr^{A3} + A4) \qquad 2\text{-}41$$

The recommended values for the constants A1 through A4 in this equation are 0.023, 0.8, 0.4, and 0.0, respectively. This gives the Dittus-Boelter equation (25). This equation is for nonmetallic fluids however. To obtain the general form of the equation for metallic fluids A2 and A3 can be set equal. As an alternative to the above form for a heat transfer correlation, Equation 2-42 was added as an option. This correlation comes from a recent review of relevant data and correlations for liquid metal tube bundles conducted by Mikityuk (52), it was selected because it is fit to the complete set of data available.

$$h = \left(\frac{k}{D_h}\right)\left(1 - e^{-3.8\left(\frac{P}{D}-1\right)}\right)(Pe^{0.77} + 250) \qquad 2\text{-}42$$

Here Pe is the Peclet number, which is the product of the Reynolds and Prandlt numbers.

2.3.4. Results of New Correlations

Figure 2-17 shows a comparison of the results of the original code versus the updated code for the ORNL test bundle. The equations used for this and all further analysis in the updated code, COBRA-IV-I-MIT, are listed in Table 2-8.

COBRA-IV-I-MIT, while performing slightly poorer for the high flow case, increases the accuracy of the low flow case significantly. Furthermore error in both cases is on the conservative side, predicting slightly higher temperatures. The ORNL cases represent only a small portion of possible conditions. Chapter 3 reviews many more cases to thoroughly benchmark the code.

Table 2-8- Recommended correlations to use for the various phenomena that require empirical models in COBRA.

Phenomena	COBRA-IV-I Correlation	COBRA-IV-I-MIT recommendation
Pressure Drop	Blasius	Cheng and Todreas
Wire-Wrap Sweeping	COBRA model	Cheng and Todreas
Turbulent Mixing	Constant β	Constant β
Fluid Radial Conduction Mixing	Constant κ	Ro and Todreas
Rod Radial Conduction Mixing	None	Ro and Todreas
Heat Transfer Coefficient	Dittus-Boelter	Mikityuk

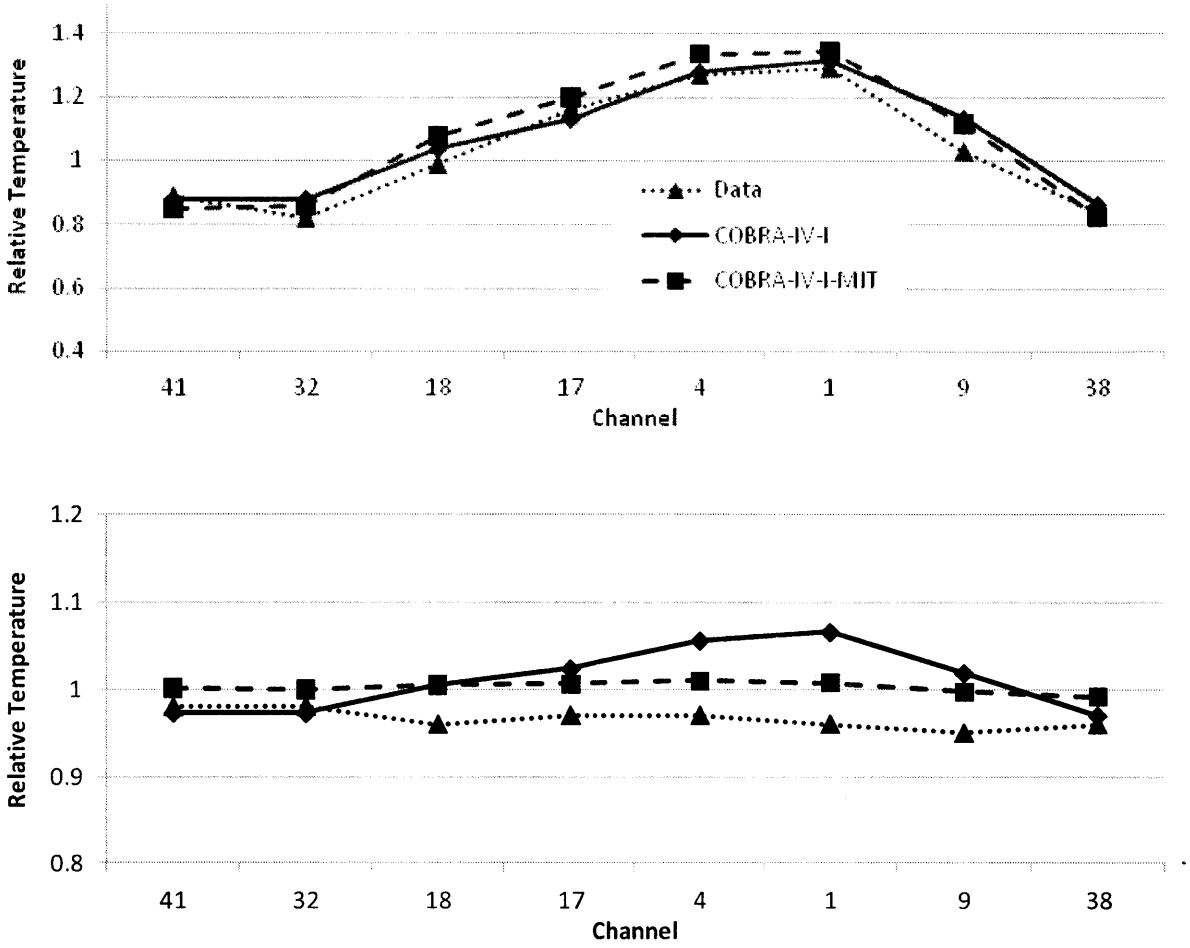

Figure 2-17- Comparison of how COBRA-IV-I performs with the original correlations it contained versus the new correlations that are recommended in Table 2-8 for the high flow case (top) and the low flow case (bottom) of the ORNL 19-pin reference case.

Chapter 3. COBRA-IV-I-MIT Benchmarks and Validation

3.1. Range of Operating Conditions

Through the course of normal and transient operation SFRs can encounter a wide range of operating conditions. When further taking into account different geometries, like driver fuel geometry versus blanket geometry, and novel reactor designs the matrix of different possible input conditions for the new sub-channel analysis code is quite extensive. To determine the effectiveness of the tool for each range a methodical approach was needed. Different parameters of interest and their corresponding ranges are listed in Table 3-1. The table is divided into two groups of parameters, geometric parameters are listed first and operating parameters are listed second. This is not an exhaustive list of every single code input that could affect behavior; however it does cover all the major inputs that characterize designs.

Table 3-1- Necessary ranges for parameters for thorough benchmarking of the updated version of COBRA.

Parameter	Regions of Interest
Bundle Size	Up to 271 pins
Pitch to Diameter Ratio	Fuel and Blanket
Convection Type	Natural, Mixed, Forced
Flow Type	Laminar, Transition, Turbulent
Power Skews	Various

This list of parameters is not a unique choice, but rather a convenient one. For example, convection and flow type, could be replaced with flow rate, linear power, and some geometric parameters. This would describe the conditions equally well, but is more complicated. Thus the above set was chosen because it is concise.

What is of particular interest for varying operating conditions is how the importance of the physical phenomena described by the empirical correlations varies. The most complicated empirical phenomena modeled is mixing; Ro and Todreas (50) produced a convenient way to visualize how this is affected by varying parameters. Figure 3-1 shows two different plots with the relative importance of mixing phenomena. The x-axis captures the effects of the flow regime using the Reynolds number defined in Equation 3-1, while the y-axis captures the effects of the convection heat transfer regime using the Grashof number defined in Equation 3-2. Each plot is for a different pitch to diameter ratio, one being representative of a driver fuel region, the other of a blanket region.

$$Re = \frac{\rho D_h v}{\mu} \qquad 3\text{-}1$$

$$Gr_{\Delta T} = \frac{g\beta^* \left[\frac{\Delta T_b}{L}\right] D_{hb}^4}{(\mu/\rho)^2} \qquad 3\text{-}2$$

Where the variables are defined as:

β^* Volumetric expansion coefficient

D_h Hydraulic diameter

D_{hb} Bundle averaged hydraulic diameter

g acceleration due to gravity

ρ Density

ΔT_b Change in bulk Temperature

v velocity

μ viscosity

Figure 3-1 shows how varying either flow regime, convection regime, or geometry (pitch to diameter ratio) can change which types of mixing are most prominent, and in turn which correlations are dominating. It also provides a convenient way to do benchmarking, as thorough benchmarking will use assemblies operated with conditions that cover all important regions of the plot. Each of the different bundles that were used for benchmarking are discussed in the next section, and their coverage of different possible operating conditions in the following section.

3.2. Test Bundles and Designs Used as Benchmarks

Three experimental bundles of different sizes were used as the primary benchmarks for COBRA-IV-I-MIT, and one code to code comparison was done. The experimental benchmarks include the ORNL 19-pin bundle (40)(41), the Westinghouse Advanced Reactors Division (WARD) 61-pin bundle (53), and the Toshiba 37-pin bundle (54) while the code to code

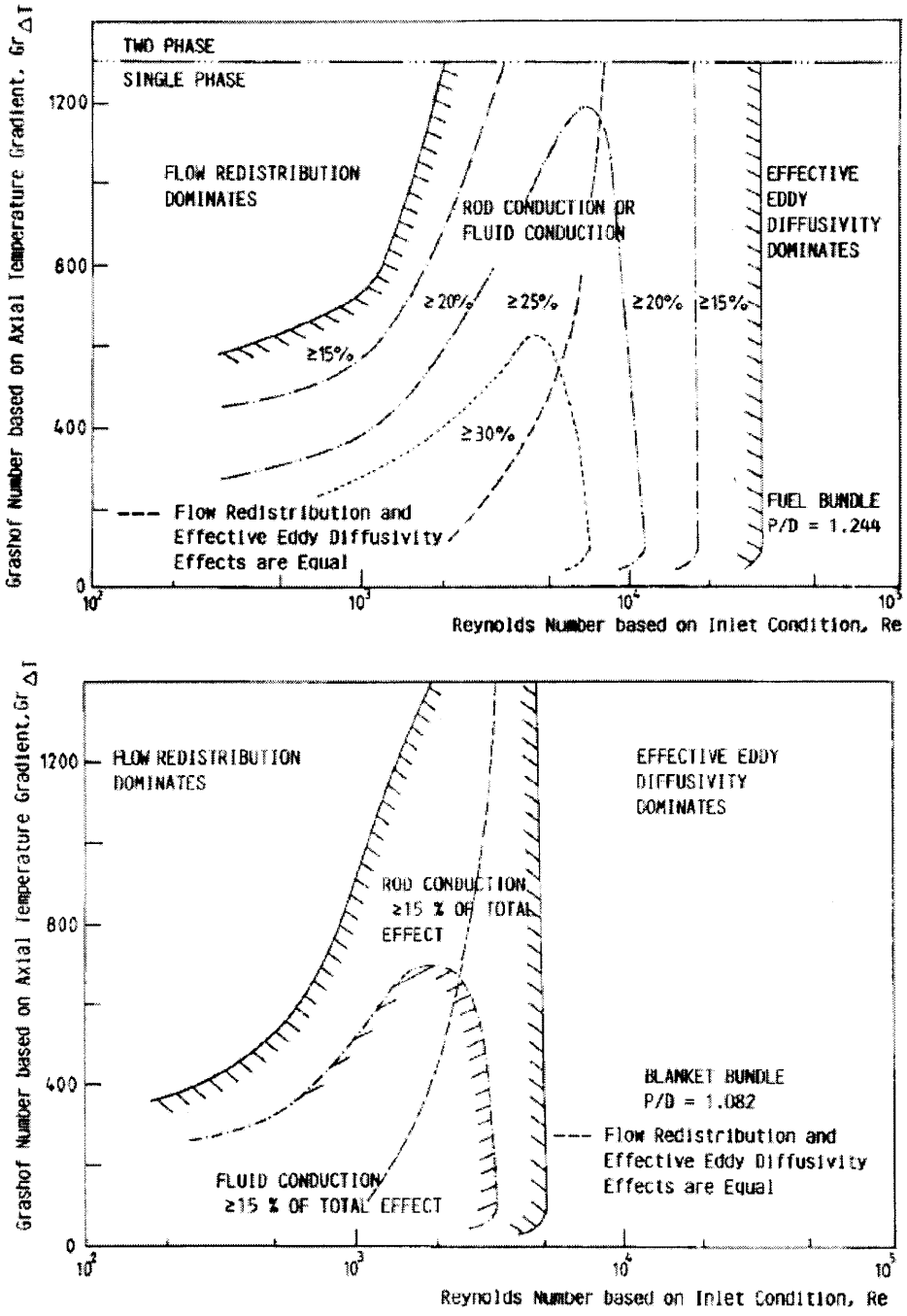

Figure 3-1- Plots showing the relative importance of different mixing effects based on the flow and convections conditions. The importance of the different effects changes based on the pitch to diameter ratio of the bundle, the P/D ratios shown here are representative of fuel (top) and blanket (bottom) regions (50).

comparison was done for a 271-pin bundle from the Korea Advanced Liquid Metal Reactor (KALIMER) 150 MWe pool reactor design (34). Table 3-2 shows the input data for each of these runs, note the data for the ORNL bundle is reiterated from Table 2-4 for comparison purposes.

Table 3-2- A comparison of the input data for COBRA for each of the cases used to benchmark the code.

	Input Parameter	ORNL	WARD	Toshiba	KALIMER
Geometry	Number of Pins	19	61	37	271
	Rod Diameter (mm)	5.84	13.2	6.5	7.67
	Rod Pitch (mm)	7.26	14.216	7.865	8.95
	Wire Wrap Diameter (mm)	1.42	0.94	1.32	1.2
	Wire Wrap Pitch (m)	0.3048	0.1016	0.307	0.2085
	Duct inside flat to flat distance (m)	0.0341	0.114	0.0773	0.1498
	Total Length (m)	1.016	2.65	3.043	3.163
	Heated Length (m)	0.5334	1.143	0.930	1.0
	Lower Unheated(m)	0.4064	0.2413	0.3986	0
System Conditions	Pressure (atm)	1	1	1	1
	Inlet Temperature (°C)	315	318	Varied*	386.2
	Inlet Mass Flow (kg/s)	Varied	Varied	Varied	21.6
	Average Rod Power (W)	Varied	Varied	Varied	14800
	Axial Power Distribution (max/avg)	Uniform	Cosine 1.4	Cosine 1.21	Uniform
	Radial Power Distribution	Uniform	Varied	Varied	Uniform
Calculation Parameters	Wire Pitch Fraction (δ)	0.0417	0.1249	0.0417	0.0607
	Turbulent Mixing Factor (β)	0.01	0.01	0.01	0.01
	Number of Axial Nodes	80	209	240	250

*parameters listed as "varied" can be found preceding the result presented, Table 2-4 for the ORNL bundle, Table 3-3 for the Toshiba bundle, and Table 3-4 for the WARD bundle.

3.2.1. ORNL 19-Pin Bundle

The smallest of the bundles used for benchmarking has only 3 rings totaling 19-pins. This bundle was the first chronologically out of those uncovered from the literature. Located at the Oak Ridge National Laboratory the bundle was part of the Fuel Failure Mockup (FFM), a large high-temperature facility built to test fuel rods for liquid metal reactors. Figure 3-2 shows a schematic of the bundle and the test section, while a thorough description of the FFM can be found in Fontana et al. (40).

This bundle was not only used for benchmarking the final results of the update, but each correlation added as described in the previous chapter. This assembly was chosen for benchmarking each correlation because it had two distinct operating conditions and many other codes used it as a benchmark (34)(35) allowing extensive code to code comparison. The results of this assembly versus COBRA-IV-I-MIT are detailed in Chapter 2 in Section 2.4.4.

3.2.2. Toshiba 37-Pin Bundle

One ring larger than the ORNL bundle is the Toshiba Bundle, a 37-pin bundle operated by the Toshiba Corporation Nuclear Engineering Laboratory in Japan in the 1980s (54). Figure 3-3 shows a schematic of the test section and the bundle. The bundle is divided into three regions that can each be operated at different power levels, providing for the ability to examine power skews across the bundle. Three different power skews were examined: 1:1, 1.4:1, and 1.96:1. For each case three different sets of operating conditions were examined corresponding to different flow and convection regimes. The specific operating conditions for each case are listed in Table 3-3.

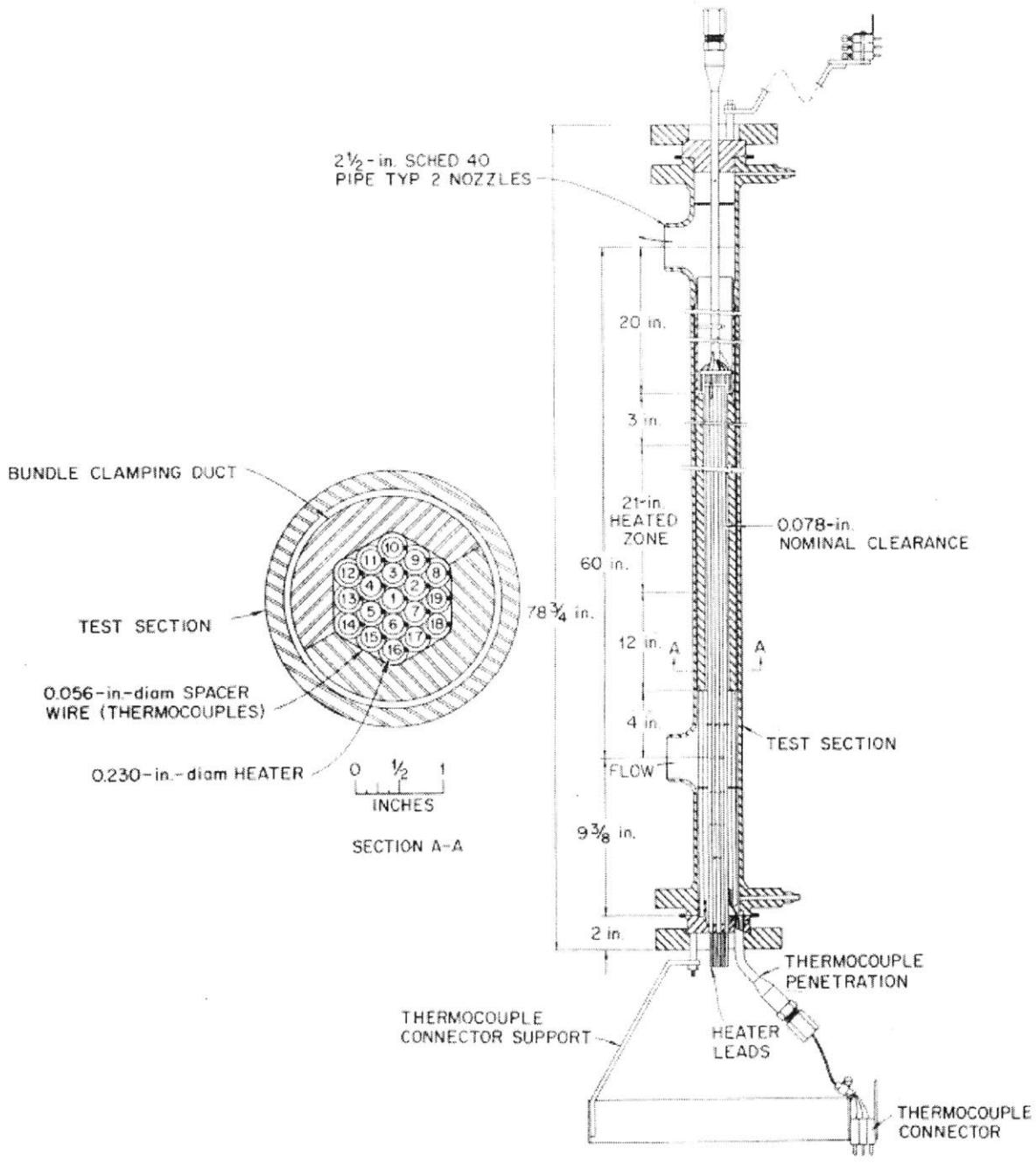

Figure 3-2- A schematic of the test section for the ORNL 19-pin bundle (40).

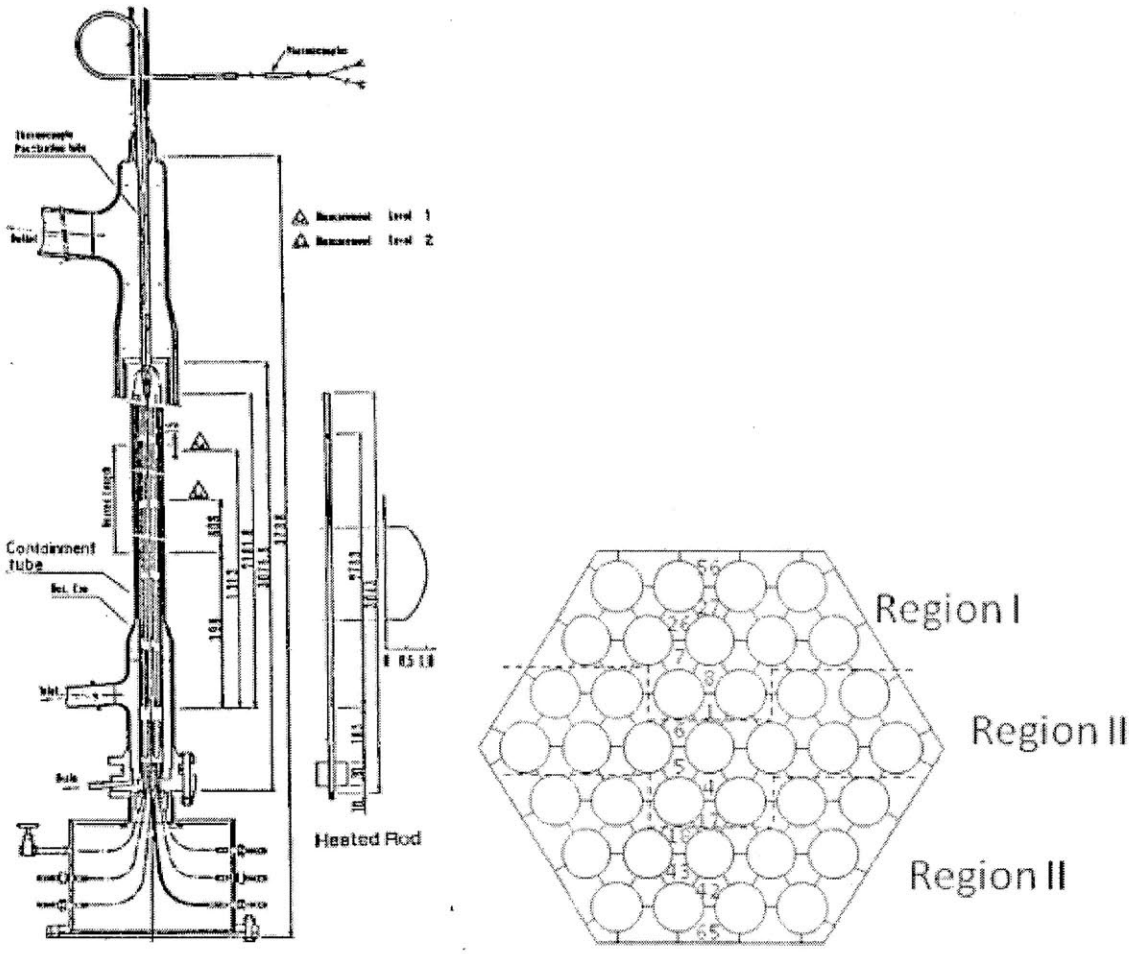

Figure 3-3- A schematic of the test section for the Toshiba 37-pin bundle and the three regions that the bundle was divided into which could be operated at different power levels (54).

The results of the runs can be seen graphically in Figure 3-4 to Figure 3-6. Each figure corresponds to one of the power skews, with the three different sets of operating conditions plotted together. A visual inspection of the plots shows that agreement is best with the flat power profile and decreases as the skew increases. A quantitative analysis of this is conducted in Section 3.3.2.

Table 3-3- Operating conditions used in the different experiments of the Toshiba bundle used for benchmarks. The run number corresponds to the number from the source (54). Many values are listed in the units for COBRA input.

Run	Power Skew	Inlet Temp. [F]	Bundle Average Outlet Temp. [F]	Reynolds Number	Mass Flux [Mlbs/ft^2-hr]	Power [kW]	Heat Flux [Mbtu/ft^2-hr]	Grashoff Number
B37P02	1:1	412.00	465.55	13024	1.0825	53.58	0.024170	56
C37P06	1:1	398.30	578.45	3022	0.2512	41.02	0.018504	204
E37P13	1:1	403.52	613.83	851	0.0707	13.40	0.006045	238
E37P17	1.4:1	409.10	488.01	8177	0.7359	53.82	0.024278	82
F37P20	1.4:1	400.28	648.84	2971	0.2406	53.82	0.024278	303
F37P27	1.4:1	400.10	677.32	1712	0.1309	32.56	0.014688	357
G37P22	1.96:1	402.44	484.20	8020	0.7218	54.57	0.024616	85
G37P25	1.96:1	398.66	651.29	2971	0.2406	54.57	0.024616	309
L37P43	1.96:1	401.18	751.42	1487	0.1097	34.13	0.015396	451

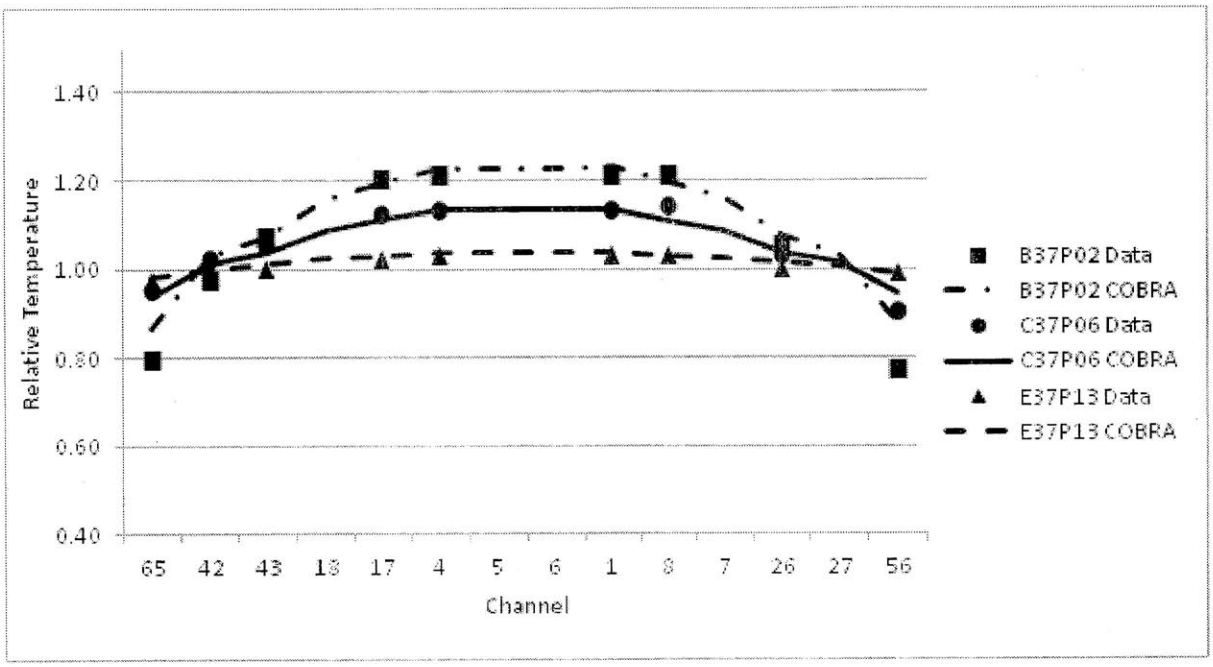

Figure 3-4- Benchmark for the Toshiba case with a 1:1 power skew across the bundle.

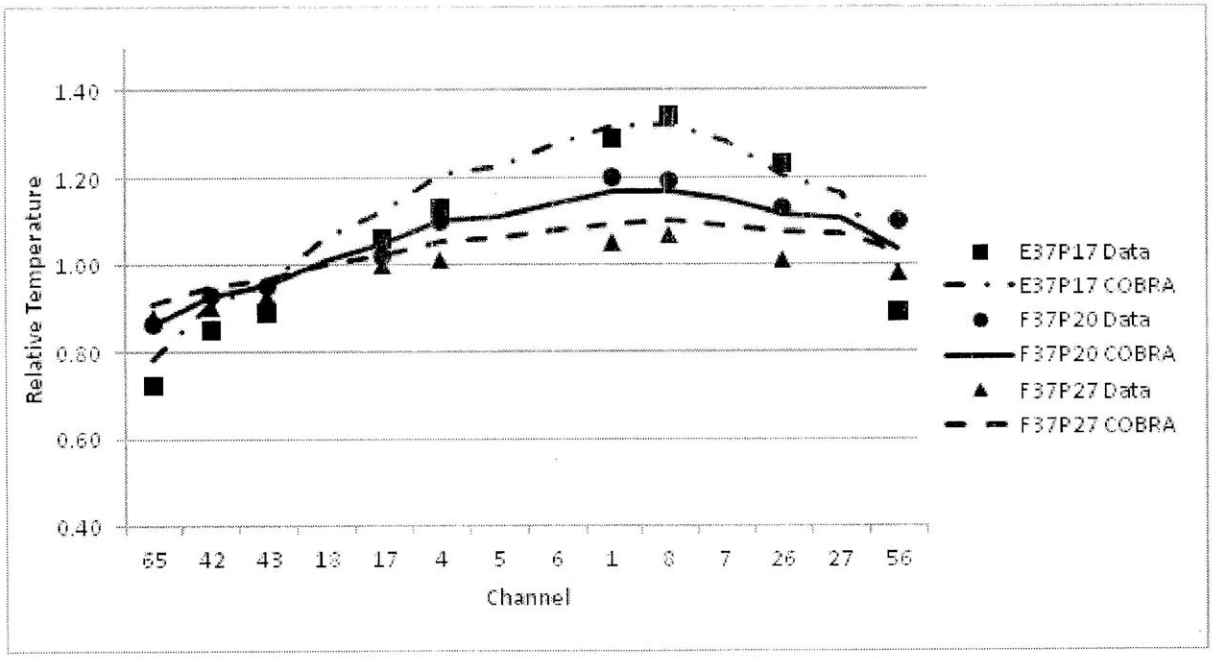

Figure 3-5- Benchmark for the Toshiba case with a 1.4:1 power skew across the bundle.

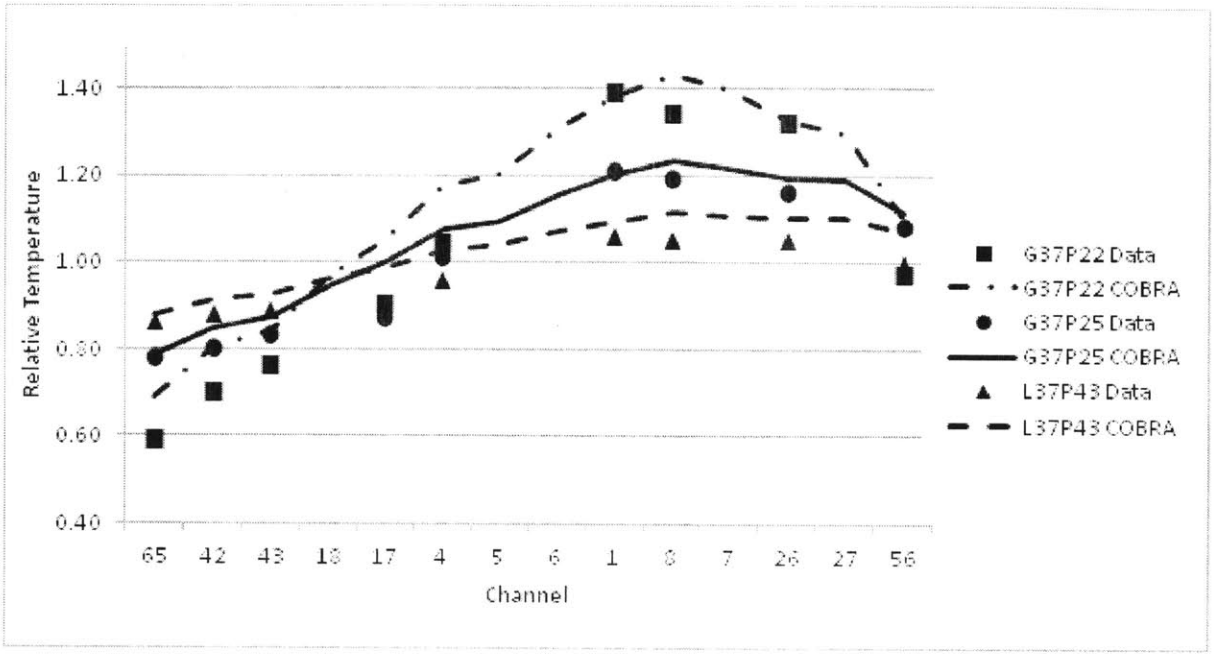

Figure 3-6- Benchmark for the Toshiba case with a 1.96:1 power skew across the bundle.

3.2.3. WARD 61-Pin Bundle

The largest of the experimental data sets to benchmark with was the WARD bundle totaling 5 rings 61-pins. The test section can be seen diagramed in Figure 3-7. Measurements were taken for this bundle at a number of different axial locations. Comparisons were made to the middle of the heated length, the end of the heated length and downstream from the heated length. This gave more and different comparisons from previous benchmarks where data was only compared at the end of the heated length. Also shown in Figure 3-7, each row of the assembly could be operated at a different power level, providing for even more control over power skews than the Toshiba Bundle.

Four or five different operating conditions for the WARD bundle were examined for three different power skews: a flat skew, a U-shaped skew with 1.5:1:1.5 profile and an extreme skew with a 2.8:1 profile. The details of each of these runs can be seen in Table 3-4.

The results of each of the runs are compared to the COBRA-IV-I-MIT predictions in Figure 3-8 to Figure 3-14. Similar to the Toshiba runs, better agreement is found for the flat power distribution as opposed to the skewed distributions. For some of the low flow cases, downstream from the heated length the same phenomena is observed as was discussed for the ORNL low flow case, where every experimental data point for the run is below 1.00 in relative temperature. The bundle average outlet temperature in the experiment was calculated with the flow rate and assembly power (53). A plausible explanation of why the relative temperatures at the end of the assembly all fall below 1.0 is that heat is lost through the assembly duct, which was not reflected in the energy balance calculating the average outlet temperature. It should be noted too that the middle of heated length produces relative temperatures between 0.4 and 0.6. Even though the measurements are being taken at the middle of heated length the definition of relative temperature does not change. The temperature rise to that point is still compared to the bundle averaged temperature rise, and thus values in the vicinity of 0.5 for middle of heated length are expected.

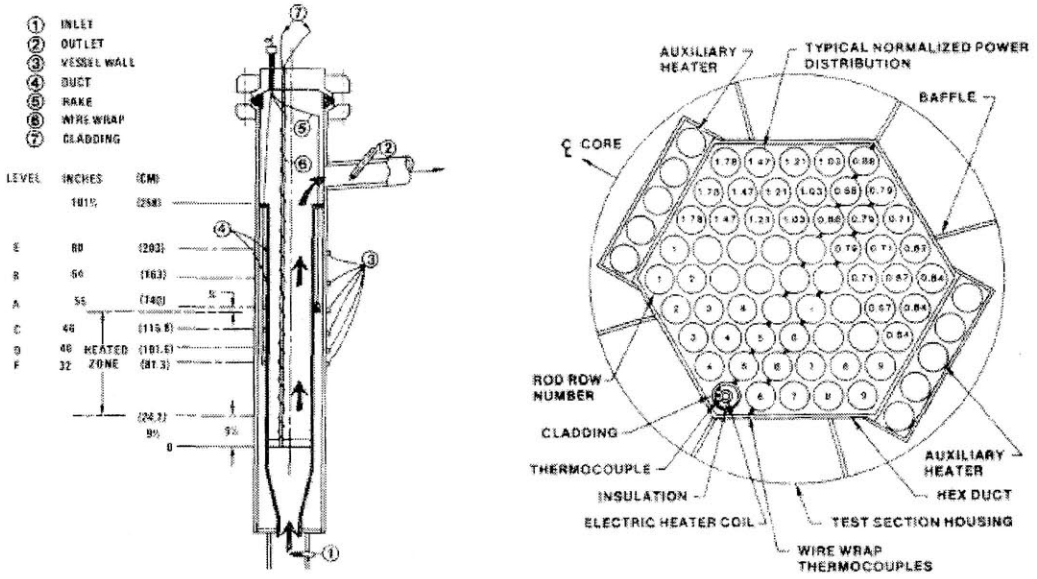

Figure 3-7- Schematic of the WARD test section and the power break down across the bundle. Each row can be operated at a different power level to achieve different power skews across the assembly (53).

Table 3-4- Operating conditions used in the different experiments of the WARD bundle used for benchmarks. The run number corresponds to the number from the source (53) with the exception of those denoted with an "*" which lacked a number and are designated with run numbers 1-6 to distinguish between them for this work. Many values are listed in the units for COBRA input.

Run	Power Skew	Inlet Temp. [F]	Bundle Average Outlet Temp. [F]	Reynolds Number	Mass Flux [Mlbs/ft^2-hr]	Power [kW]	Heat Flux [Mbtu/ft^2-hr]	Grashoff Number
1*	1:1	605.2	797.83	13000	0.8326	440	0.04830	289
224	1:1	605.2	792.46	7900	0.5059	260	0.02854	291
218	1:1	605.2	800.63	3800	0.2433	130	0.01427	279
2*	1:1	605.2	798.73	1000	0.0640	34	0.00373	287
3*	1.5:1:1.5	605.2	824.77	11500	0.7965	440	0.04830	343
4*	1.5:1:1.5	605.2	820.24	4400	0.2818	165	0.01811	343
5*	1.5:1:1.5	605.2	835.03	1100	0.0704	44	0.00483	321
6*	1.5:1:1.5	605.2	835.46	550	0.0352	22	0.00241	327
313	2.8:1	605.2	798.00	13000	0.8326	440	0.04830	287
223	2.8:1	605.2	798.61	7900	0.5059	260	0.02854	289
221	2.8:1	605.2	800.03	3800	0.2433	130	0.01427	290
231	2.8:1	605.2	798.86	1000	0.0640	43	0.00373	279
229	2.8:1	605.2	799.37	500	0.0320	17	0.00186	287

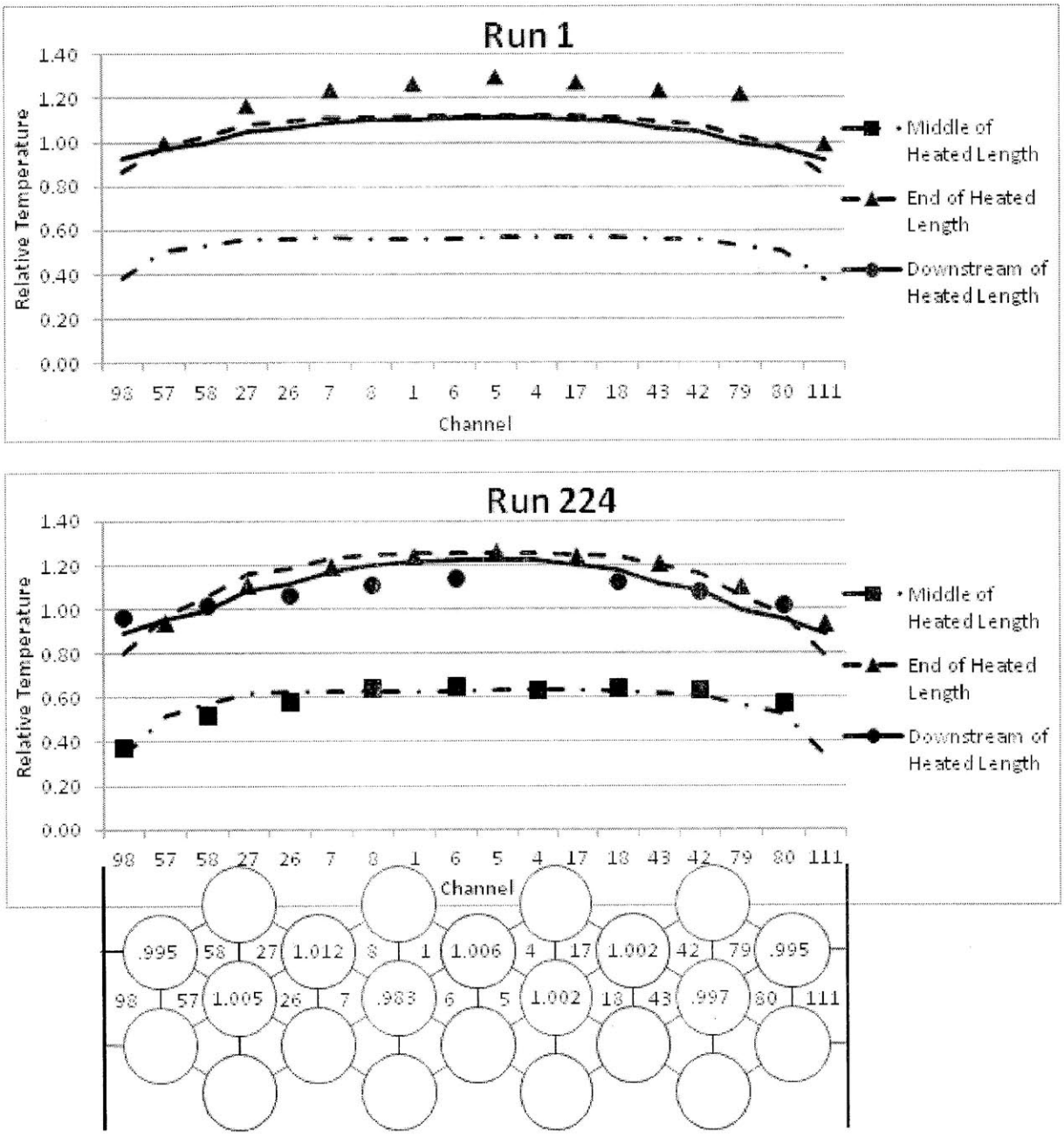

Figure 3-8- The two higher power benchmarks for the WARD case with a 1:1 power skew (top, middle), and the schematic section of the assembly showing the power skew (bottom). The data points downstream and at the middle of the heated length were not reported in the source for run 1.

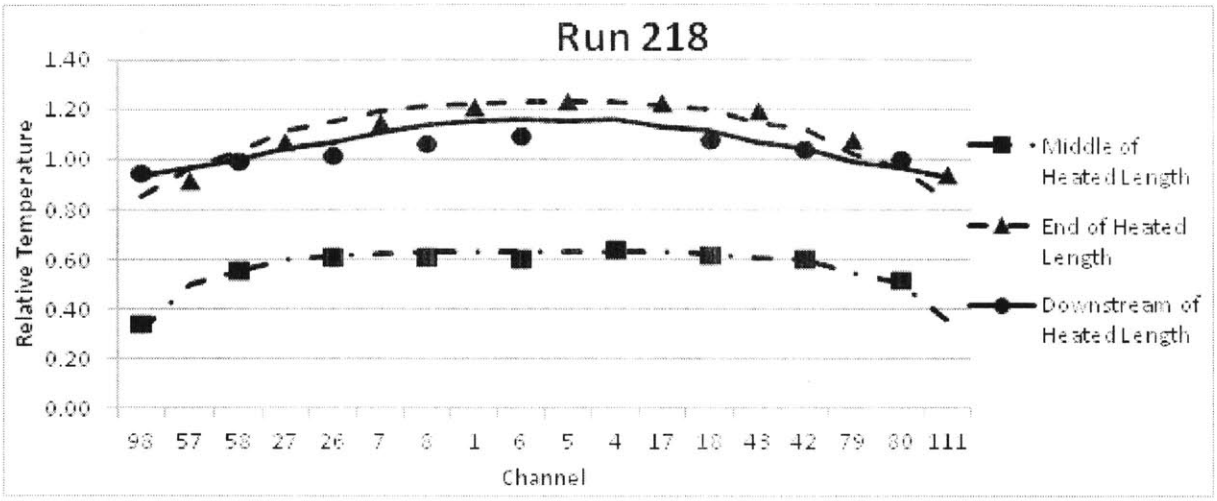

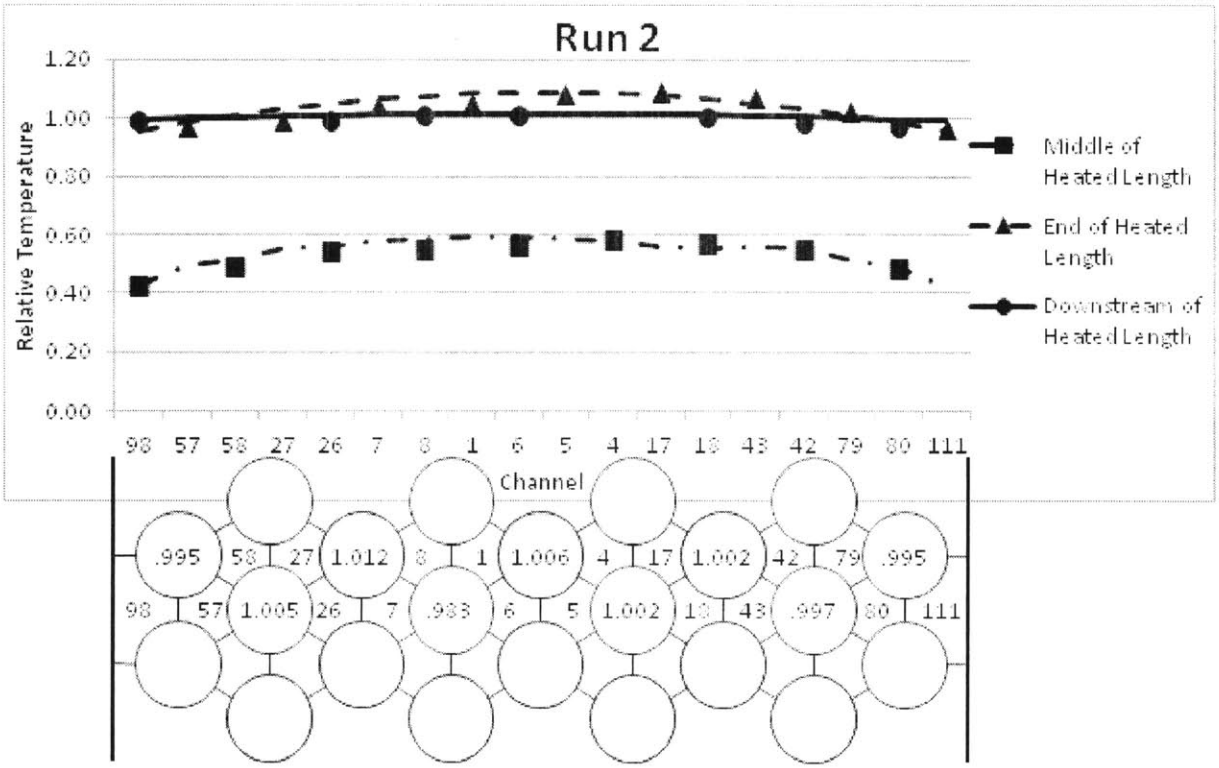

Figure 3-9- The two lower power benchmarks for the WARD case with a 1:1 power skew (top, middle), and the schematic section of the assembly showing the power skew (bottom).

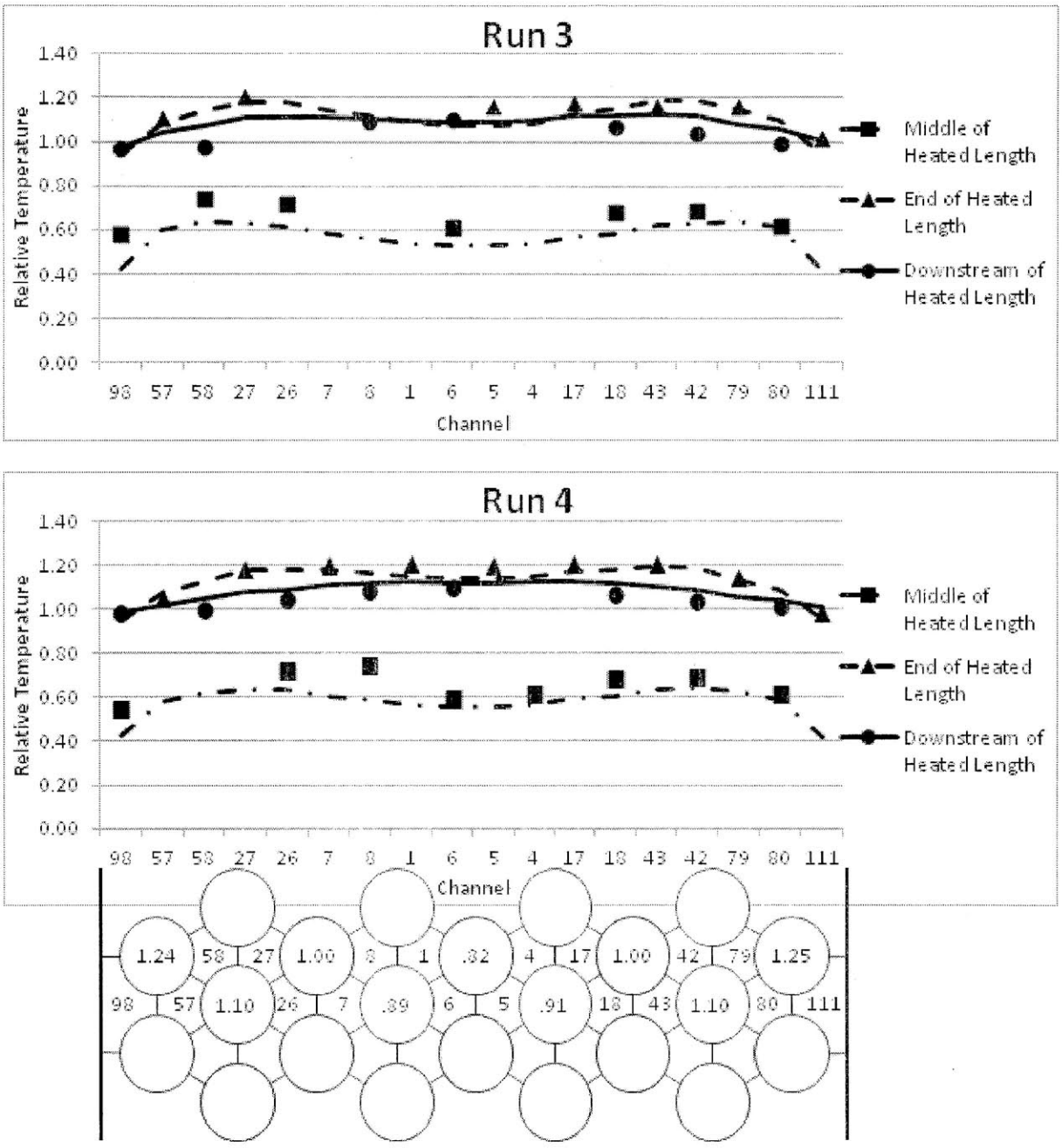

Figure 3-10- The two higher power benchmarks for the WARD case with a 1.5:1:1.5 power skew (top, middle), and the schematic section of the assembly showing the power skew (bottom).

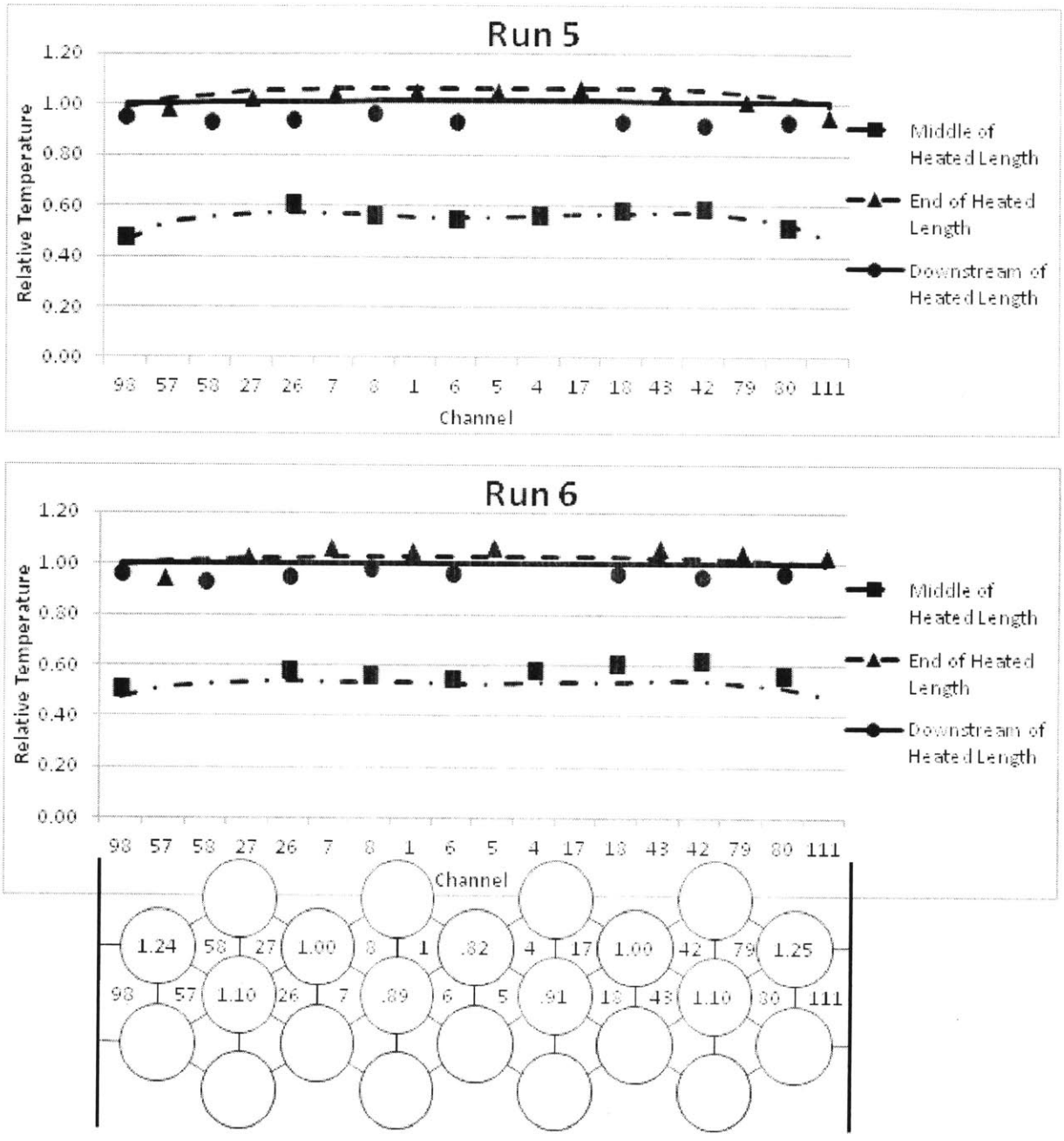

Figure 3-11- The two lower power benchmarks for the WARD case with a 1.5:1:1.5 power skew (top, middle), and the schematic section of the assembly showing the power skew (bottom).

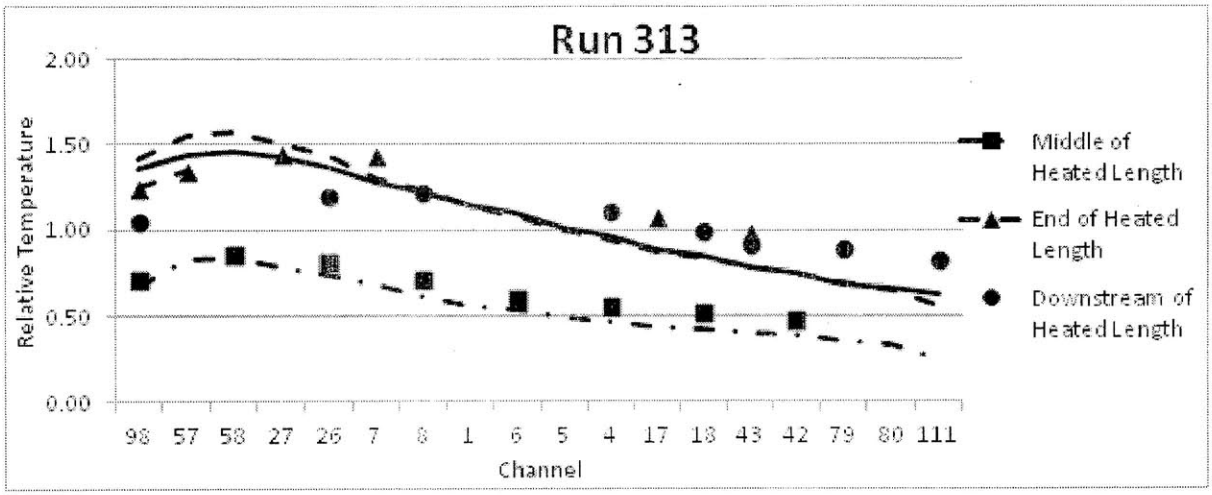

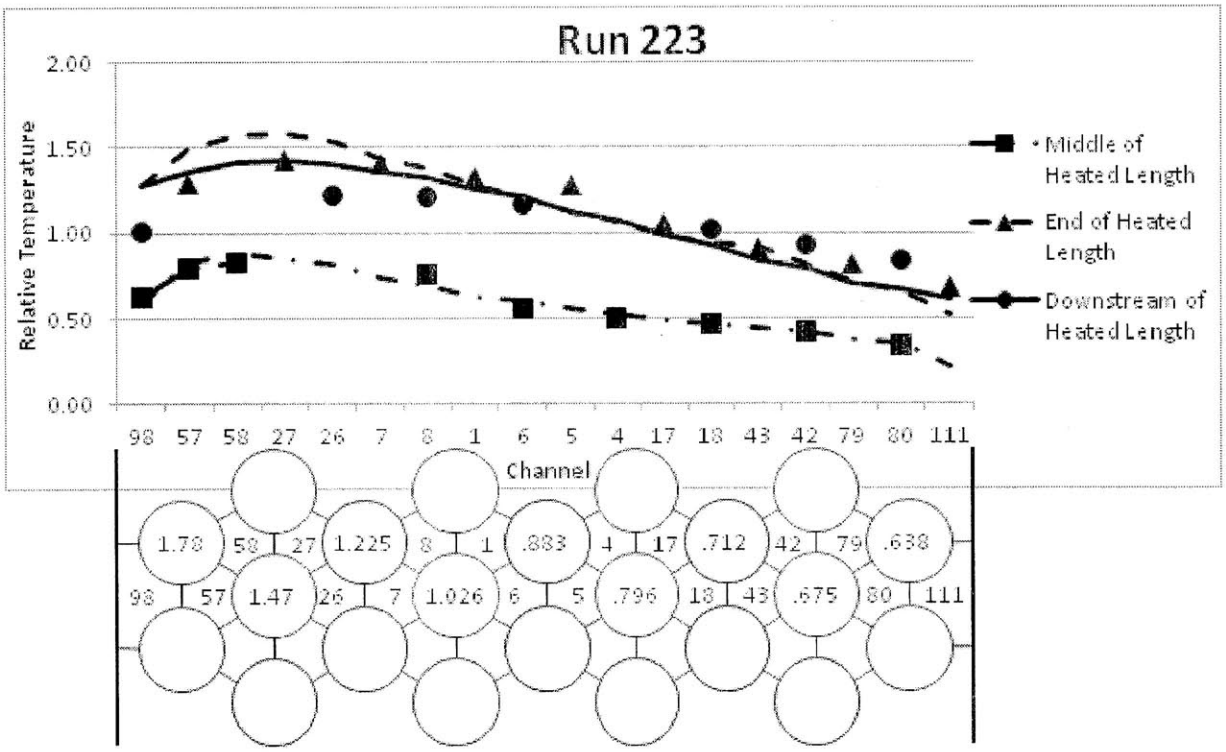

Figure 3-12- The two higher power benchmarks for the WARD case with a 2.8:1 power skew (top, middle), and the schematic section of the assembly showing the power skew (bottom).

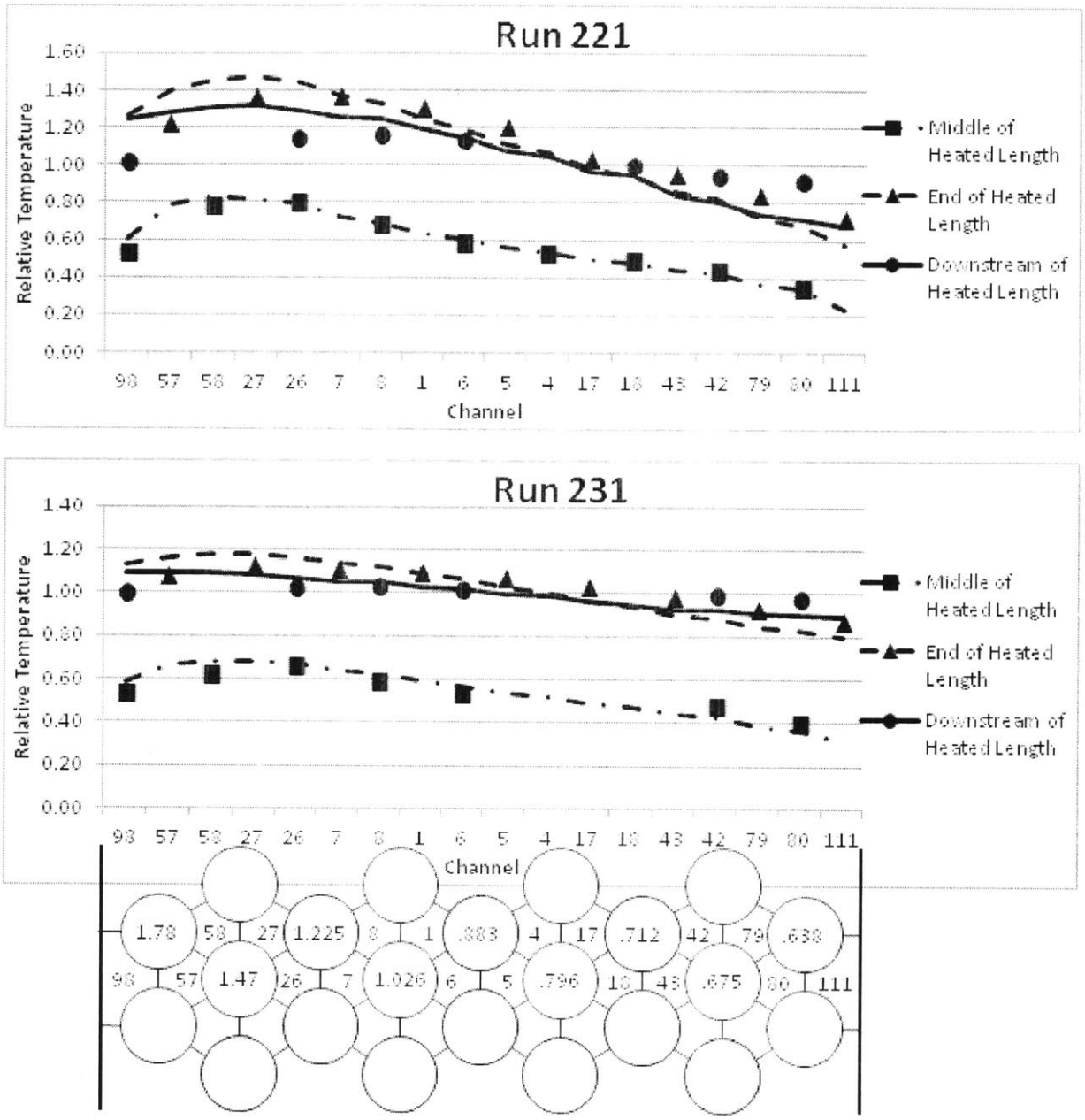

Figure 3-13- The two lower power benchmarks for the WARD case with a 2.8:1 power skew (top, middle), and the schematic section of the assembly showing the power skew (bottom).

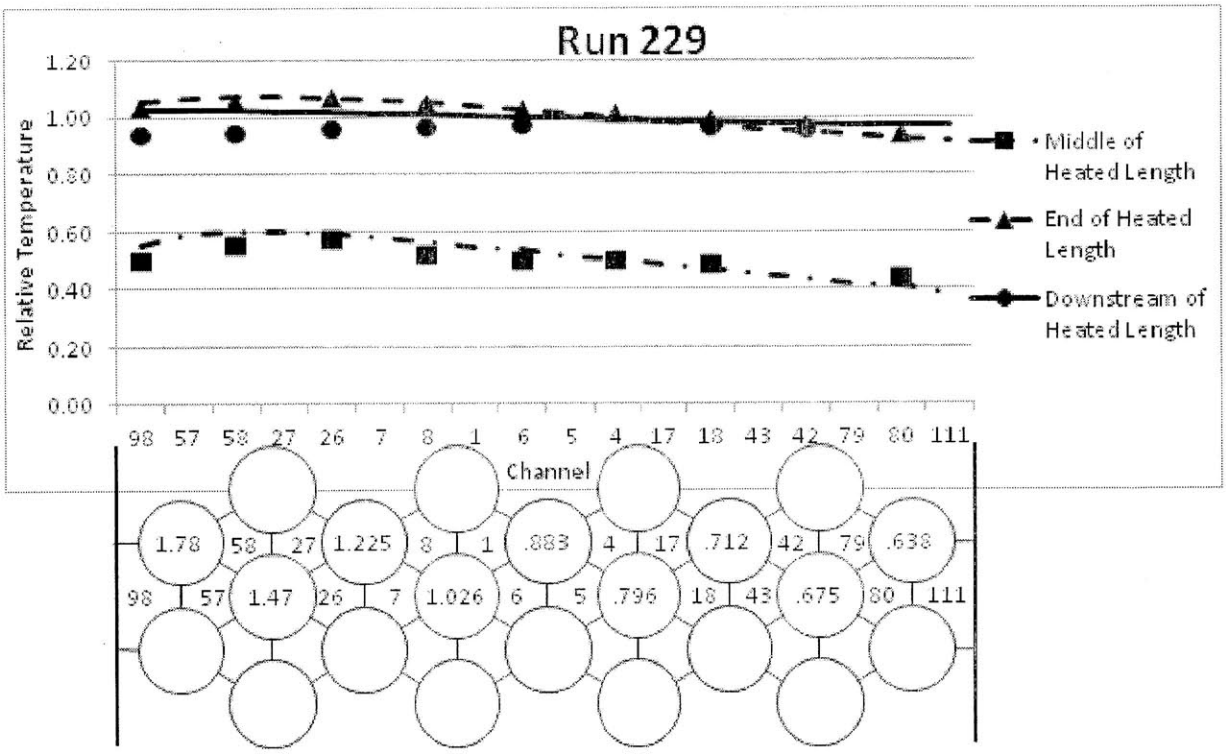

Figure 3-14- The lowest power benchmark for the WARD case with a 2.8:1 power skew (top), and the schematic section of the assembly showing the power skew (bottom).

In addition to benchmarks across the bundle the WARD case also provides the opportunity to do an axial benchmark because of the numerous axial levels temperature measurements were taken at. Figure 3-15 shows such an axial benchmark for a 2.8:1 power skew case, Run 223. Three channels are examined for this case. All three channels show good agreement for the heated length of the channels, up to axial location A. After A the best agreement is found for channel 1, a central sub-channel. The channels closer to the periphery predict a higher temperature than is measured; a behavior that has shown up consistently in benchmarks for highly skewed cases. This could suggest that the Cheng and Todreas correlation is underpredicting the effect of swirl flow around the outside of the assembly.

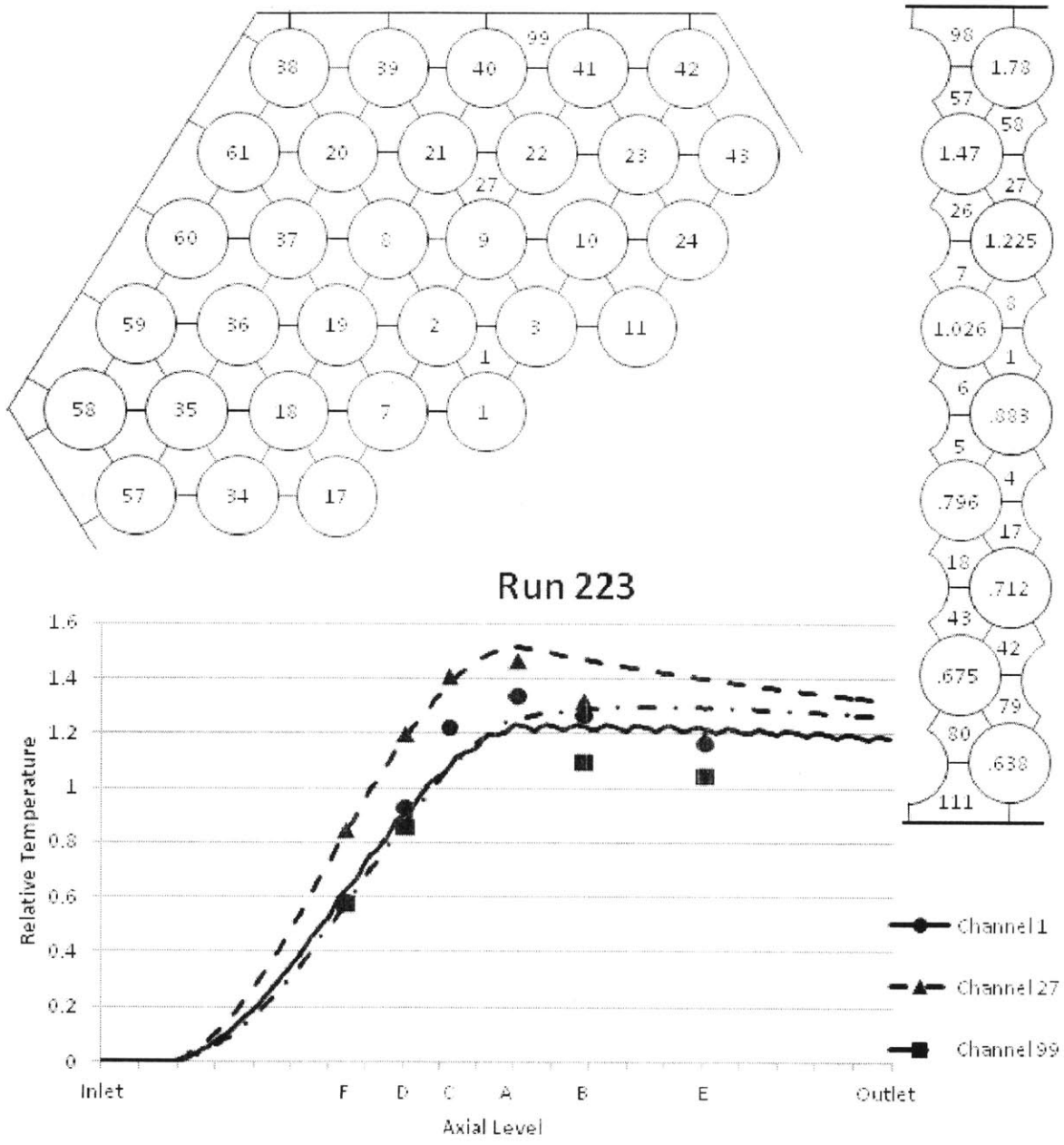

Figure 3-15- Axial benchmark for the WARD case with a 2.8:1 power skew, shown in the assembly slice in the top right. The rows in the partial assembly have the power level of the corresponding row in the assembly slice. The channels of the three benchmarks are shown on the partial assembly.

3.2.4. KALIMER 271-Pin Design

This is not a benchmark against experimental data like all the previous examples in this section but rather a code to code comparison. A code to code comparison, while not as meaningful as an actual experimental benchmark was deemed necessary so COBRA-IV-I-MIT could be tested for large assemblies. Actual experimental data for benchmarks was limited to bundles sizes of 61-pins. Realistic assemblies for commercial SFRs could be as large as 271 pins. The KALIMER design provided an opportunity to do this testing as Kim et al. published the results of MATRA-LMR, SABRE4, and SLTHEN for the analysis of this reactor (34). The comparison was done for a fuel interior assembly, the details of which can be found previously in Table 3-2. The results of the comparison are shown in Figure 3-16.

Note that this plot is of actual temperature rather than relative temperature. The plot shows good agreement between COBRA-IV-I, COBRA-IV-I-MIT, and SLTHEN. MATRA appears to predict a slightly higher temperature uniformly, but matches the shape of the other three codes. Having either a slightly higher input power or slightly lower mass flux would cause a shift like this, and thus the shift is not overly concerning. SABRE4 has a notably higher peak, likely caused by shifting more coolant flow to the periphery of the assembly, an actual disagreement with the other four codes.

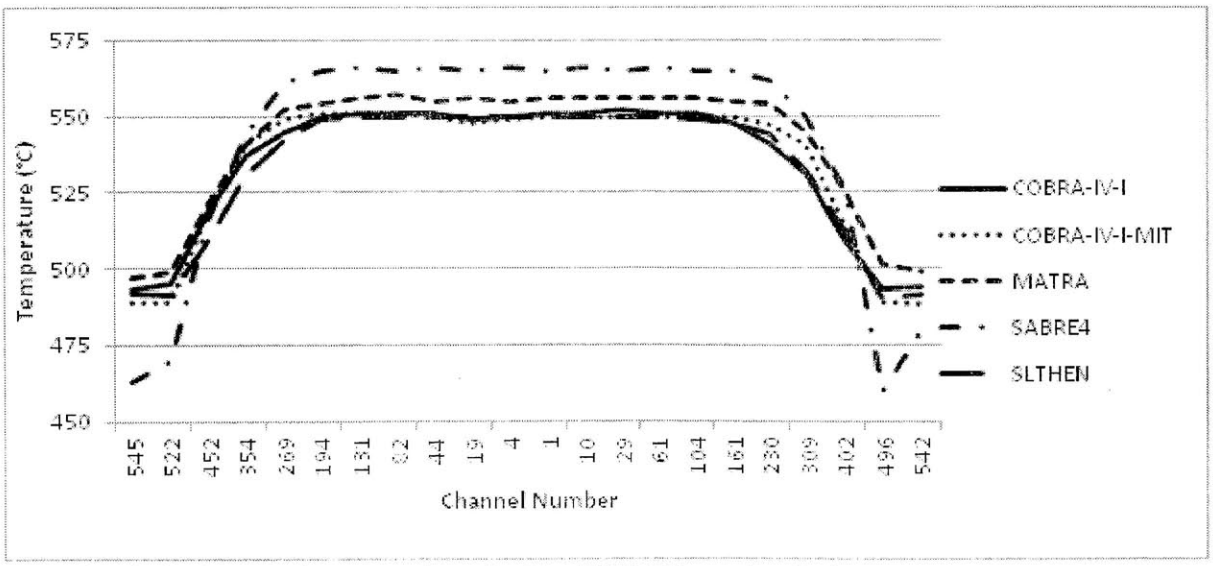

Figure 3-16- Code to code comparison for the KALIMER reactor design.

3.3. Quantitative Analysis of Benchmarks

In the previous section numerous plots were presented comparing the results from experimental studies to COBRA-IV-I-MIT predictions for those data sets. For each of the comparisons the agreement appears acceptable based on visual inspection. This section will rigorously test the agreement of the code with the experimental data through quantitative analysis of the benchmarks.

3.3.1. Coverage of Operating Range

Determining if some of the desired ranges are covered by the benchmarks is simple. Pitch to diameter ratio, bundle size, and power skew were covered by examining cases that contained that feature. The flow and convection regimes on the other hand are more complicated to determine if the benchmarks were exhaustive, as they interact in complex ways with each other and the other parameters. To ensure that there is satisfactory coverage of all the desired conditions the plots presented in Figure 3-1 are referred to. By populating these plots with data points for each benchmark an inspection will determine if all important regions are covered, as shown in Figure 3-17.

Figure 3-17 contains a populated plot for both a tight pitch, typical of a blanket region, and a looser pitch that would normally be associated with a driver fuel region. Both plots are divided into three different regions of importance for benchmarking purposes. The line down the middle of each plot splits them into two regions: one dominated by flow redistribution, important for low flow conditions, and the other dominated by eddy redistribution and forced mixing, important at high flow conditions. The third region of importance is conduction mixing which contributes most significantly at intermediate or transitional flows when there are low thermal rises across the assembly. The plots suggest that the most important regions of the map were covered.

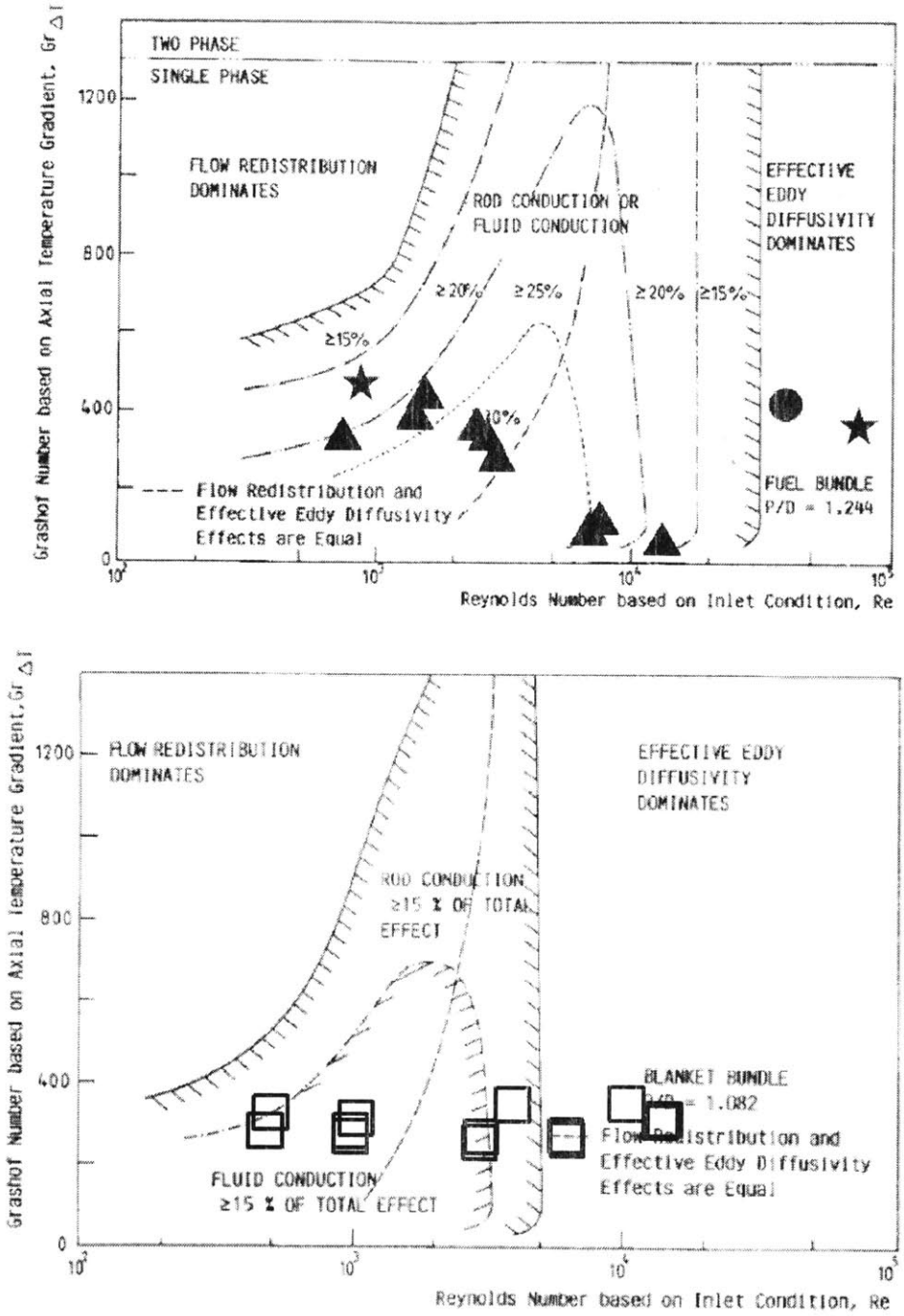

Figure 3-17- Plots from Figure 3-1, which now contain points designating the conditions for the different benchmarks and comparisons (50). The symbols correspond to the following benchmarks: Star=ORNL, Triangle=Toshiba, Square=WARD, Circle=KALIMER.

3.3.2. Average Error for each Case

Table 3-5 shows the average error from the data for each benchmark. Average error for a case is calculated as shown in Formula 3-3.

$$Average\ Error = \sum^{n} |T_{rel\_n\_predicted} - T_{rel\_n\_measured}|/n \qquad 3\text{-}3$$

Where the sum is over each sub-channel in the bundle for which there was a measured data point and T_{rel} is defined in Equation 2-13. Table 3-5 presents the error by geometry and power skew.

Note that the flatter power skews performed better than the more pronounced skews of 2.8:1 and 2:1. The extreme skews were expected to have higher error because the power is concentrated at the edge of the assembly; however, the energy loss through the duct of the assemblies was not modeled with COBRA. This was tested and confirmed and is discussed in section 3.3.3.

Another trend that holds for all the assemblies is that the error decreases for each geometry and skew from the higher power cases to the lower power cases. This trend is also expected because the relative temperature varies more in higher power cases; it is easier to predict a case that falls between .9 and 1.1 with low error than it is one that ranges from .7 to 1.3.

Of the flat and conservatively skewed cases only one shows an error greater than 6%. This case is the WARD 1 which has an error of 13.3%. A look back at a Figure 3-8 shows that the code predicts values lower than are reported experimentally. However a closer look at the experimental data shows that the lowest measured values are approximately 1.0. This is the reverse phenomena as has been observed for some of the low flow measurements. The bundle averaged relative temperature based on the data shown here would be greater than 1.0, a contradiction to the definition of relative temperature. So in all likelihood the measured relative temperatures should be shifted down closer to the prediction.

Table 3-5- The average error for each of the benchmarks as calculated by Equation 3-3. The error is shown for each specific case, and the average for each of the runs of similar geometry and skew.

Benchmark Case		Average Error of Relative Temperature [%]			
Assembly	Case		Level (of heated length)		
			Middle	End	Downstream
ORNL		4.5			
	High Flow			5.4	
	Low Flow			3.6	
Toshiba 1:1		1.9			
	B37P02			3.6	
	C37P06			1.5	
	E37P13			0.6	
Toshiba 1.4:1		3.9			
	E37P17			5.7	
	F37P20			1.9	
	F37P27			4.2	
Toshiba 2:1		6.3			
	G37P22			9.0	
	G37P25			4.6	
	L37P43			2.3	
WARD 1:1		3.9			
	1		-	13.3	-
	224		2.5	3.9	5.5
	218		1.2	3.9	3.5
	2		1.7	2.1	1.2
WARD 1.5:1:1.5		4.5			
	3		8.7	4.5	4.7
	4		6.1	2.4	3.8
	5		1.4	2.1	73
	6		4.9	3.3	435
WARD 2.8:1		8.2			
	313		7.3	15.8	16.2
	223		10.9	10.2	14.4
	221		2.3	9.0	12.6
	231		4.2	5.6	5.1
	229		3.1	1.4	4.5

For the other cases the magnitude of the error is reasonable (around or less than 5%) and almost always on the conservative side. The temperature rise for each of the cases used in the benchmarks above is on the order of 100 °C or less in some cases. This means the actual error between the code and the measurement is generally less than 5 °C for cases that have 5% or less error.

Figure 3-18 shows a cumulative distribution function for the relative error for all of the data points which were compared to COBRA predictions, a set of roughly 400. 62% of the COBRA predictions fall within 5%, 87% fall within 10%, and 98.5% fall within 20% of the relative temperature rise of the data. The range between 10% and 20% is largely populated by comparisons between the highly skewed cases.

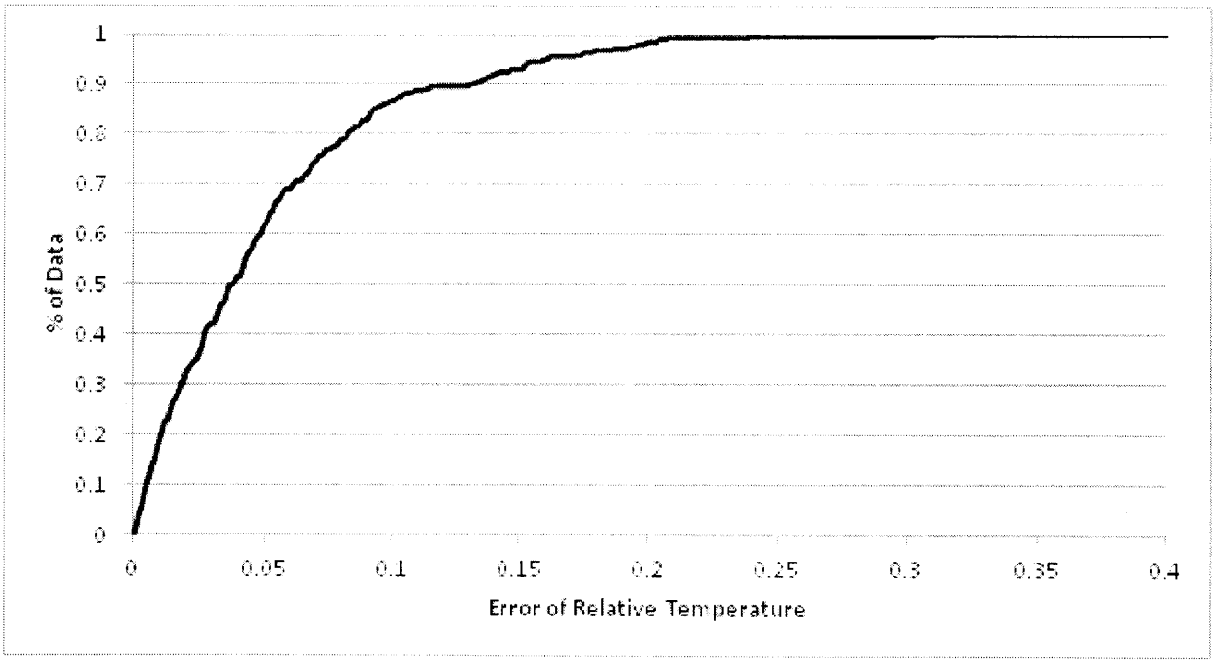

Figure 3-18- Cumulative distribution function of the error between the COBRA predictions and the data for the WARD, Toshiba, and ORNL bundles.

Determination of the reasonable amount of error is closely tied to what the experimental errors are for the experiments that were used for the benchmarks. The temperature data was drawn from thermocouples which would indicate the measurement error should be low. The

literature indicates that the measurement error for these experiments is 2 °C (54). Error greater than this is likely introduced in the calculation of relative temperature (which is the way the data is presented). Evidence supporting this has occurred many times when looking at data sets for low flow cases when each of the data points across the assembly has a relative temperature at the outlet of less than 1.0 (or high flow cases where it is greater than 1.0 in one case). In some cases the experimental data is converted into relative temperature using a measured temperature for the bundle average outlet as opposed to a calculated one. The temperature is measured downstream from the heated length so it is assumed to be near the bundle average; however, in order for the low flow cases to be lower than 1.0 across the assembly, the measured value must be a few degrees higher actual bundle average. In another case the bundle average temperature is calculated but it is not stated if heat loss through the duct is accounted for, again likely causing this temperature to be a few degrees higher than the true bundle average outlet.

A second source of error from the data comes from the way it was presented in the literature. The data is presented in the sources in the form of plots. A sample plot is shown in Figure 3-19. In order to do a quantitative comparison of the data it must be converted from points on the plot back into values. The error involved in this process is related to the resolution of the plots, which in many cases was very low. While impossible to accurately quantify all the sources of error, 5% seems an acceptable level of error.

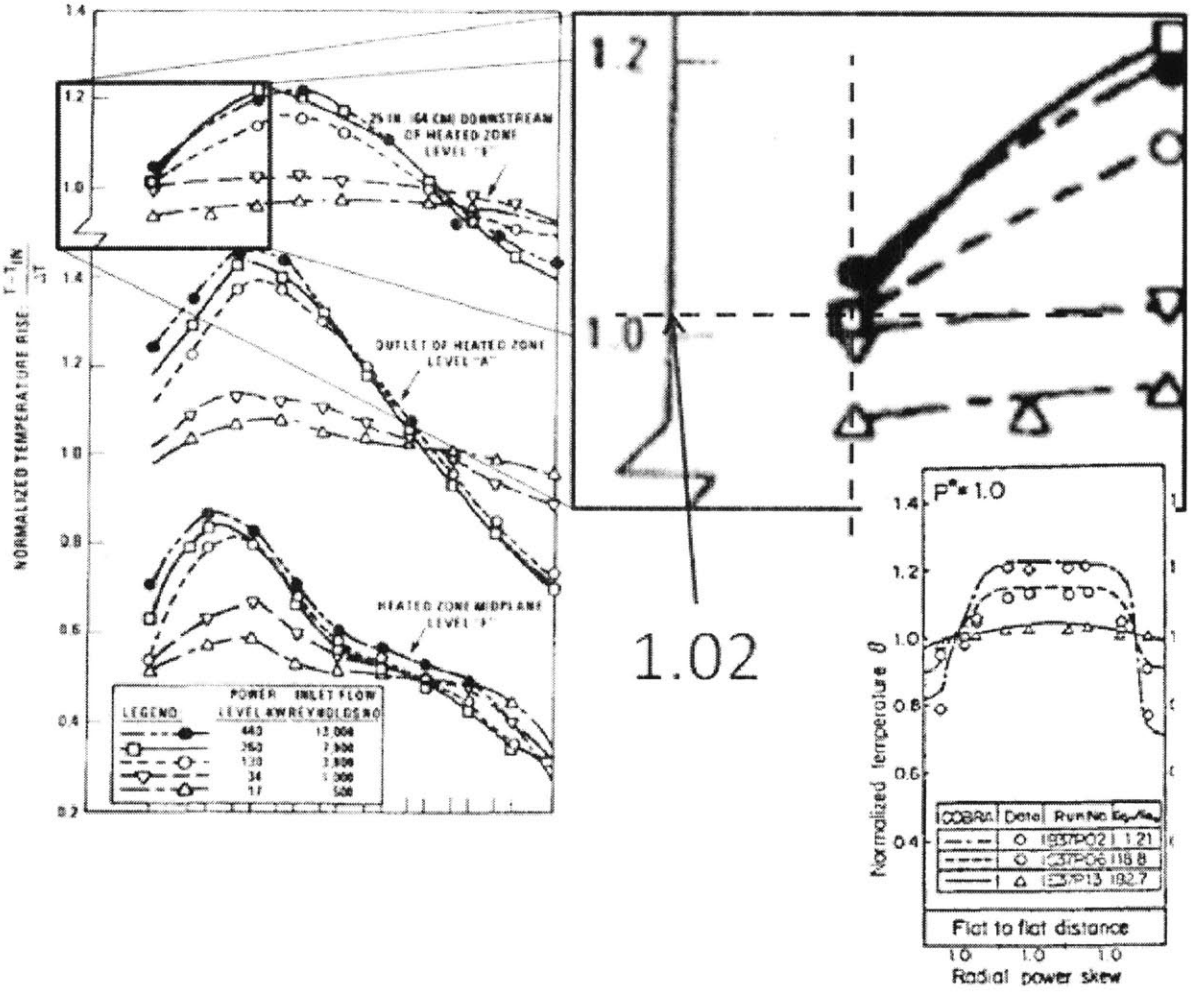

Figure 3-19- Plots of the experimental data for the WARD assembly (53) (left) and the Toshiba assembly (54) (bottom right); the magnified area shows how data points are converted to numbers.

3.3.1. Effect of Conduction Losses Due to Wall

The quantitative analysis in the previous section showed that the highly skewed cases varied the most between experimental data and COBRA-IV-I-MIT predictions. One reason for this is because heat loss through the walls of the bundle has not been modeled thus far. To determine if heat loss through the walls does account for the extra error in the skewed cases the

Toshiba assemblies were run with heat loss. These assemblies were chosen for this purpose because the source gave an estimate of the power lost through the duct (54).

Heat loss is more important for skewed cases than flat cases because the power is concentrated more closely to one wall and thus heat is not lost uniformly. The experimental set up for the Toshiba case is such that the bundle is installed in a containment tube in a hexagonal can that is filled with sodium, with many horizontal baffle plates to limit heat loss from convection. The estimated radial heat loss is 2.5% of total bundle power (54).

Heat loss was modeled in COBRA by adding an additional sub-channel to the Toshiba assembly that was connected through wall conduction only to each edge and corner sub-channel. Because wall geometry and properties of the actual assembly were not known, the wall was set up so that approximately 2.5% of the total power was lost to the new sub-channel.

Figure 3-20 to Figure 3-22 show the new predictions for the Toshiba cases with radial heat loss through the wall. All three Toshiba assembles were rerun, even the flat case which had low disagreement with the data. This is to ensure that the correction helps the skewed case without negatively affecting the flat case, as would be expected if it was a more accurate model of the actual experiment. Compared to the previous plots for the Toshiba case (Figure 3-4 to Figure 3-6) the new predictions match the data better, this can be seen particularly near the edges of the assembly. The data is presented quantitatively in Table 3-6.

The results confirm that the additional error for highly skewed cases may plausibly be the result of radial heat loss. Average error of the relative temperature was reduced for both skewed cases, bringing each below 5% error. The flat case was relatively unaffected, going from 1.93% error to 2.20% error, a negligible rise considering the errors already discussed. Of further note is only one individual case is now above 5% error, G37P22. However, referring to Table 3-3 the temperature rise for this assembly is only 82° F or 46 °C. Thus, converting relative error to real error results in only a few degrees of discrepancy.

$$Real\ Error = Relative\ Error * \Delta T_{bundle} = .077 * 46°C = 3.5°C \qquad 3\text{-}4$$

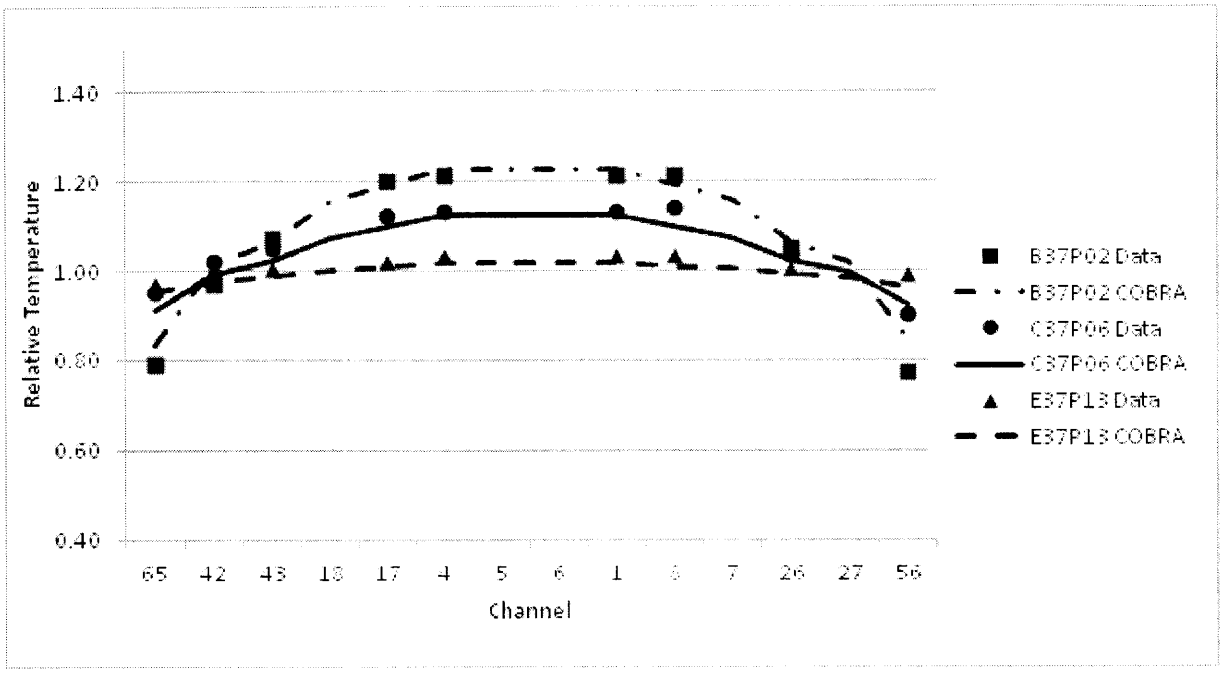

Figure 3-20- Benchmark for the Toshiba case with a 1:1 power skew across the bundle corrected for heat loss through the wall of the assembly.

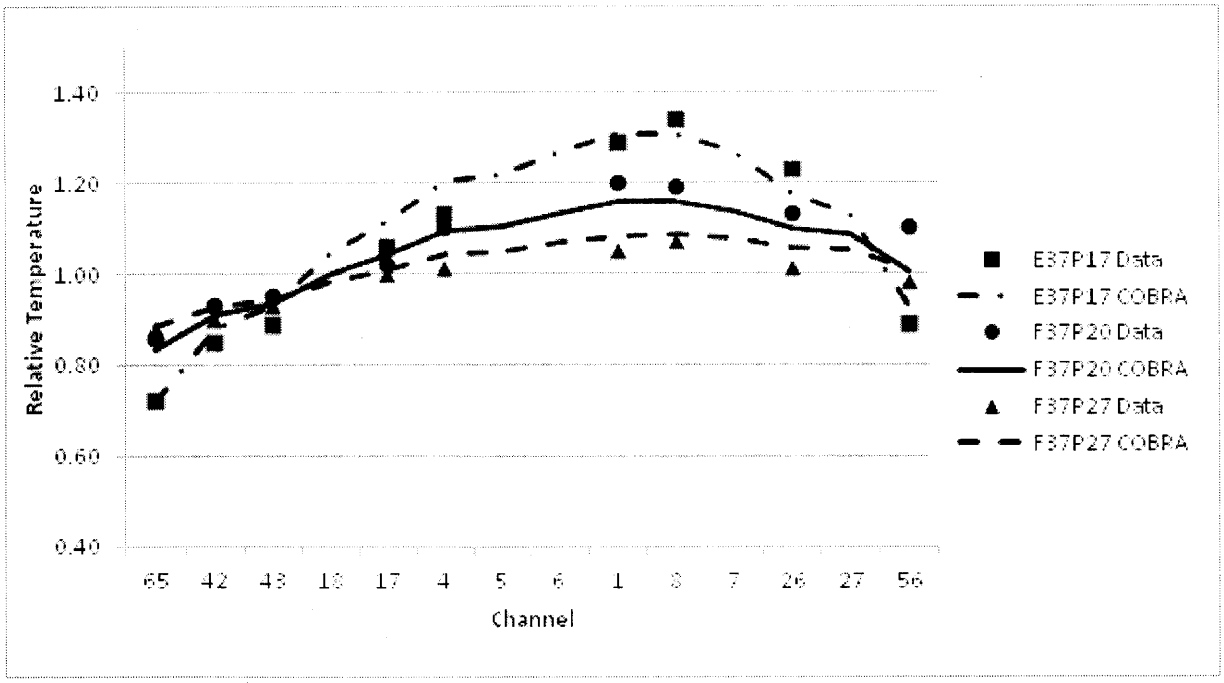

Figure 3-21- Benchmark for the Toshiba case with a 1.4:1 power skew across the bundle corrected for heat loss through the wall of the assembly.

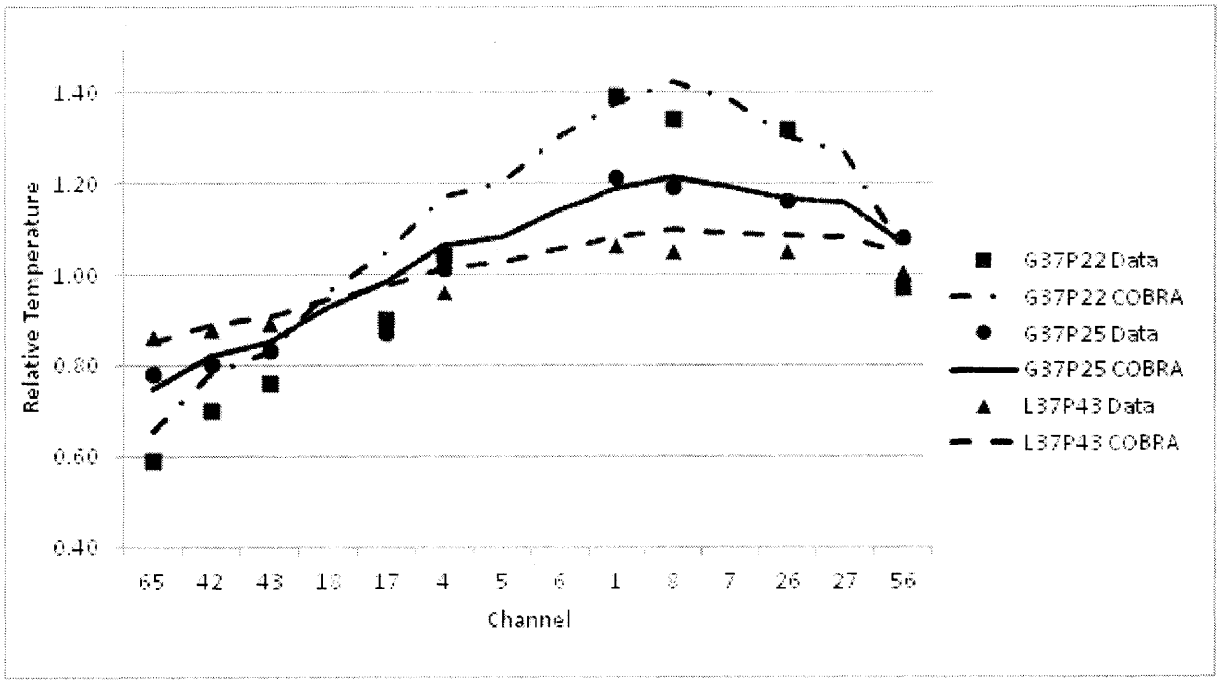

Figure 3-22- Benchmark for the Toshiba case with a 1.96:1 power skew across the bundle corrected for heat loss through the wall of the assembly.

Table 3-6- The average error for each of the Toshiba benchmarks as calculated by Equation 3-3 with radial heat loss through the wall taken into account.

Benchmark Case		Average Error of Relative Temperature [%]	
		No Wall Heat Loss	~2.5% Wall Heat Loss
Toshiba 1:1		1.93%	2.20%
	B37P02	3.65%	2.73%
	C37P06	1.52%	2.14%
	E37P13	0.62%	1.72%
Toshiba 1.4:1		3.95%	3.11%
	E37P17	5.71%	3.82%
	F37P20	1.89%	3.19%
	F37P27	4.23%	2.31%
Toshiba 2:1		6.31%	4.81%
	G37P22	9.05%	7.70%
	G37P25	4.64%	3.36%
	L37P43	5.25%	3.39%

An error of 3.5 °C is good agreement as the experiment specifically notes 2 °C error, which is compounded by the relative temperature calculation done for the experiment and the data conversion to numbers from plots.

Figure 3-23 shows an updated cumulative distribution function of the relative error for the 72 data points in the Toshiba Case. The distribution has shifted to the left from Figure 3-18: now 79% of the COBRA predictions fall within 5%, 96% fall within 10%, and 100% fall within 15% of the relative temperature rise of the data. Proper modeling of heat loss in the experimental setup allows COBRA-IV-I-MIT to accurately model skewed bundles.

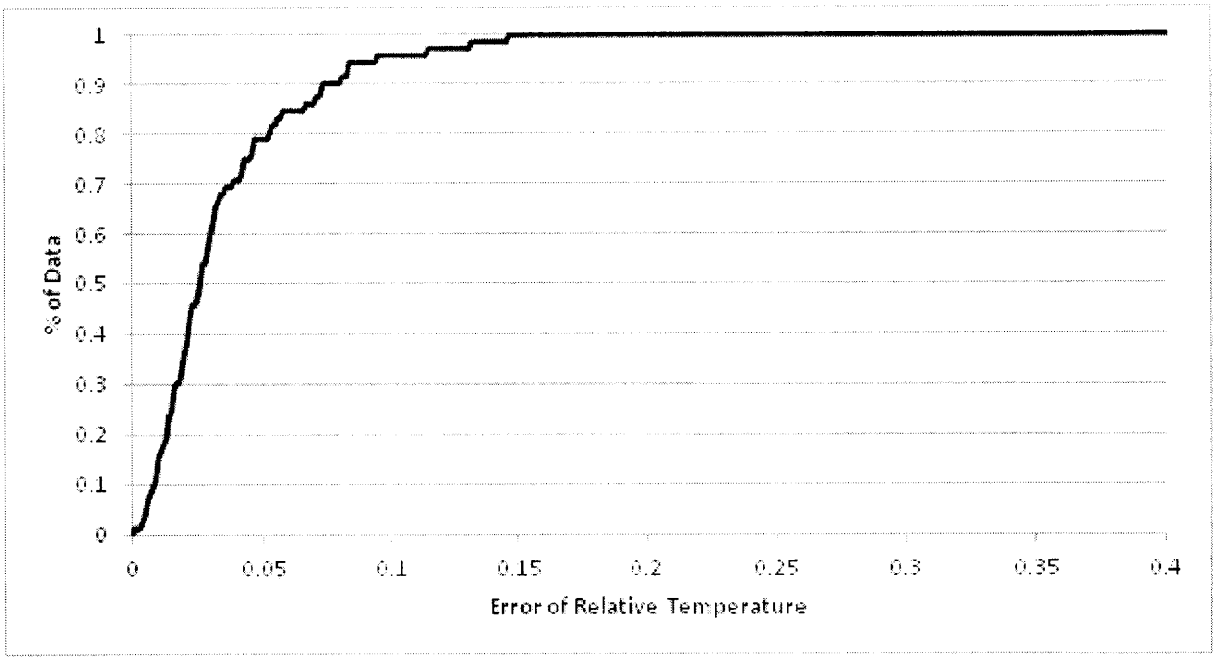

Figure 3-23- Cumulative distribution function of the error between the COBRA predictions including heat loss though the duct for the Toshiba bundle.

3.4. Pressure Drop Benchmark

The focus of the benchmarking thus far in this chapter has been on predicting the temperature rise of the channels; this is because data sets were available for comparison. No data sets for pressure drop could be found for sodium bundles in the literature. The pressure drop correlations are not specific to sodium, however all the changes and updates to the code have focused specifically on sodium thus far; it is unclear how well the code would perform with water.

However, unlike temperature rise which is dependent on many correlations, the pressure drop across the assembly is dependent mainly on the correlation used to find the friction factor. Section 2.3.1 discusses the newly implemented correlation into COBRA, the Cheng and Todreas Correlation. The Cheng and Todreas correlation was benchmarked against data (45)(46). A hand calculation using this correlation can be compared to COBRA results to ensure it was properly implemented into the code, to give confidence that COBRA is correctly predicting the pressure drops of assemblies.

This was done for the ORNL assembly, which has a high and low flow case, the operating conditions for these cases can be found in Table 2-3 or Table 3-2. The formulas used in the hand calculation are as follows.

$$\Delta P_{total} = \Delta P_{acceleration} + \Delta P_{gravity} + \Delta P_{friction} \quad 3\text{-}5$$

$$\Delta P_{acceleration} = G^2 * \left(\frac{1}{\rho_{out}} - \frac{1}{\rho_{in}}\right) \quad 3\text{-}6$$

$$\Delta P_{gravity} = \rho g l \quad 3\text{-}7$$

$$\Delta P_{friction} = f_{bundle} \frac{G^2 l}{2\rho D_e} \qquad 3\text{-}8$$

Where the variables are defined as:

D_e Equivalent diameter

f Friction factor calculated with the Cheng and Todreas Correlation

g Acceleration due to gravity

G Mass flux

L Bundle length

ρ Density

ΔP Pressure drop

All state properties were taken at the assembly midplane temperature in the calculation. This will introduce a small discrepancy with COBRA. The equations in Section 2.3.1 are used to calculate the friction factor for a single sub-channel. The comparison was made for the bundle average pressure drop. The bundle average pressure drop is calculated with Equation 3-9.

$$f_{bundle} = \frac{D_{eb}}{Re^m}\left(\sum_{i=1}^{3} S_i \left(\frac{D_{ei}}{D_{eb}}\right)^{m/(2-m)} \left(\frac{C_{fi}}{D_{ei}}\right)^{1/(m-2)}\right)^{m-2} \qquad 3\text{-}9$$

Where the variables are defined as:

Re Reynolds number

C_{fi} Bare rod friction constant, Equation 2-21

m 0.18 for turbulent flow, 1 for laminar flow

i Channel type, interior, edge and corner

b Bundle

S Total cross sectional area of channel type, Equation 3-10

$$S_i = \frac{N_i A_i}{A_b} \qquad 3\text{-}10$$

Where A is the cross sectional area of the channel or bundle and N is the number of channels. The results of the calculations are shown in Table 3-7. COBRA only reports total pressure drop, so the constituent pressure drops could not be compared. The agreement between the total pressure drops is good as expected.

Table 3-7- Comparison of pressure drop calculated by hand and with COBRA for the ORNL assembly. All values are in kPa.

		High Flow	Low Flow
Hand Calculation	Acceleration	1.15	0.00024
	Gravity	8.69	8.69
	Friction	145.43	0.10
	Total	154.12	8.79
COBRA	Total	150.58	8.82

3.5. Benchmark Conclusions

For three different experimental data sets and one code to code comparison covering an extensive set of operating conditions COBRA-IV-I-MIT can predict the sodium relative temperature rise with less than 5% average error. This level of accuracy is satisfactory considering the method used, sub-channel analysis, and the various errors related to the experimental data.

One method for further validation of this code and sub-channel methods in general would be the use of CFD to generate data sets for benchmarking. This would provide the ability to benchmark any geometry or conditions. CFD would even allow benchmarks to be carried out on transient conditions, which currently there are no data sets for.

A word of caution about the current sub-channel code validation: there is a relatively small set of experimental data for benchmarking a sub-channel code such as this for sodium. Unfortunately these data sets were also the only data available to those who developed the correlations for the codes. Therefore, it is not entirely surprising that COBRA-IV-I-MIT and the other codes adopting similar correlations predict all the data sets well since they use correlations that are based off those same data sets.

With the update and benchmark of COBRA-IV-I-MIT completed, Chapter 4 begins the examination of the coupling of the sub-channel model to the fuel-performance model.

Chapter 4. Coupling COBRA-IV-I-MIT to FEAST

4.1. Geometry and Time Scale

Due to the nature of the physical phenomena modeled by each code, they use different time scales and geometries. Coupling of the codes requires that these are reconciled so that information can be properly passed between the two. Time scale considerations must be taken into account for both steady-state operation and for transients.

4.1.1. Steady-State Operation

COBRA can be run for steady-state operation or for transients. For steady-state operation the code analyzes the assembly for a set of unchanging conditions. Thus to represent a steady-state assembly that is operated for a length of time with changes to the power and flow, COBRA

would have to be run many times, once for each time the conditions changed. Figure 4-1 shows an example of the power and outlet temperature history from an EBR-II subassembly, X447 (23)(55). For this case COBRA would have to be run 11 times to capture each of the different power levels of the steady-state operation. In a sense the steady-state operation of COBRA is length independent, that is to say a single run of COBRA would capture a one day steady-state operation as well as a one year operation as long as none of the inputs (power, geometry, flow) change. Because of this, the computational time to run COBRA for steady-state examinations is very low.

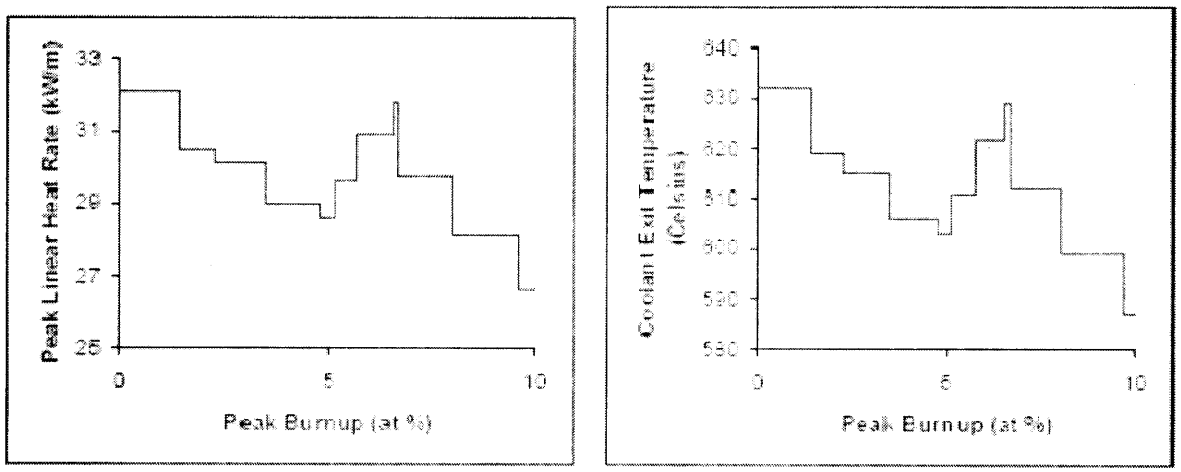

Figure 4-1 – Plots showing a power and outlet temperature history for fuel rod DP04 from assembly X447 from EBR-II (23). This is an example of what a steady-state power history could look like.

Conversely for FEAST there would only be one run to simulate this power history for a pin. The nature of modeling fuel performance is different than thermal hydraulics modeling; the length of time to run a steady-state history will be proportional to the length of the history for fuel performance modeling. The thermal hydraulic behavior only changes minimally while the power level of an assembly is constant, but the fuel is always evolving. So while COBRA must only be run once at each power level to generate a description of the assembly, and in effect, a table of inputs for FEAST, FEAST must be run with a very fine time scale. As will be discussed in Section 4.3 below thermal hydraulic behavior can be affected by the fuel evolution, as fuel swelling will cause geometry changes. Even so these changes are very slow in time scale, months to years for normal operation, and will not require COBRA to be run with significantly

higher frequency. The recommended time step for FEAST steady-state runs is 10 seconds (23). In comparison the length of fuel operation is on the order of years or even on the order of decades for some breed and burn reactor designs. This results in very long computational time for FEAST steady-state runs.

4.1.2. Transient Operation

The transient operation for both codes calls for a much finer time scale. The time scale required for COBRA depends on the solution algorithm used. The implicit solution scheme allows for the user to set the time step by setting the total length of the transient and the number of time steps during the transient. If the explicit scheme is used, the time step length for COBRA is determined by the Courant limit defined in Equation 4-1 below (31).

$$FCOUR = \frac{v * \Delta T}{\Delta X} \qquad 4\text{-}1$$

Where FCOUR is the courrant limit, v is the velocity, ΔT is the time step and ΔX is the axial node length. COBRA recommends a default value for the courrant limit of 0.5. Resulting time step sizes for COBRA are generally quite small. For example, with a node size of 2 cm and a velocity of 4 m/s the resulting time step is 0.0025 s.

For FEAST the transient time step is defined by the user. The recommended maximum time step length is 0.005 seconds (23). Having similar time steps between COBRA and FEAST for transients allows for the FEAST transient file (specifically the tables with the power, coolant, etc., inputs) to be generated with any desired fineness-although in most cases it will not need to be near the order of the time step.

It should be noted for FEAST that transient operation can begin at any set time during a steady-state run. This leaves open the possibility to operate the code for many years with the steady-state time step of 10 seconds before the transient occurs calling for the much finer time step only when needed.

4.1.3. Geometry

A general description of sub-channel analysis geometry can be found in Section 1.2.2. The geometry of COBRA is three dimensional, generally with a fine mesh axially but limited to one node per sub-channel radially. Nonetheless each fuel rod is adjacent to 5 or 6 sub-channels, depending on location in the assembly (interior or edge), and thus there are multiple coolant temperatures for each rod.

In Section 1.2.3, the background of the geometry of FEAST is discussed, the important take away, for the concerns of coupling, is that FEAST is a two-dimensional code. Each rod is nodalized axially and radially outwards, however azimuthal symmetry is assumed. This presents a challenge for coupling: which temperature and heat transfer coefficient are given by COBRA to FEAST? This problem is illustrated by Figure 4-2.

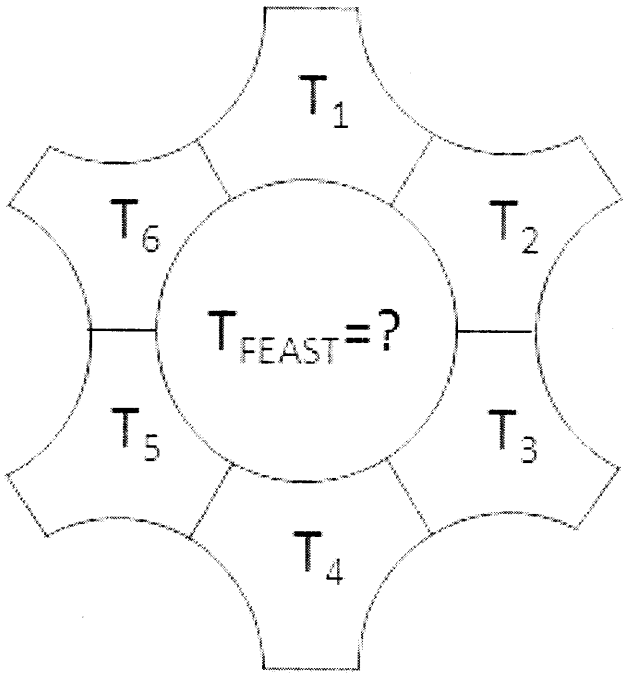

Figure 4-2- A schematic of a fuel pin and its surrounding sub-channels. Each channel has a different temperature and heat transfer coefficient.

One way to handle this problem would be to modify FEAST so it could accommodate for a third dimension. This however would make the code computationally very heavy. Another solution would be to run the rod in FEAST for each temperature. This would eliminate making any changes to FEAST, but would still be very inefficient computationally and any information regarding effects caused specifically by azimuthal variations would be lost. The simplest way to resolve this geometric difference would be to pass the coolant average temperature to FEAST. This would be the most efficient way to handle the problem; however there would be a large loss of information. The next section discusses the acceptability of this approximate approach.

4.2. Sensitivity Analysis of Azimuthal Temperature Distribution

The purpose of this analysis is to determine if the model of two dimensional fuel rods is acceptable given that the coolant temperature distribution around the clad is not uniform. The approach adopted to accomplish this was to employ a finite-difference heat conduction analysis code, HEATING7 (56). The code was used to model the temperature distribution in fuel rods that arose from forcing functions applied to the outside of the clad. Forcing functions were determined based off of literature review, and were chosen to represent bounding scenarios of azimuthal variation.

The temperature distribution of the fuel rod that was calculated was then fed to ADINA, which is finite element analysis software (57)(58). ADINA was used to calculate the stresses generated by the azimuthal temperature variation. Stress calculations were checked by hand for consistency and then compared to other stresses which occur in the fuel cladding.

4.2.1. Azimuthal Temperature Profile

Various azimuthal temperature distributions were considered. These temperature distributions were tested for representative EBR-II and S-PRISM pin geometries. These geometries and other proprieties used can be found in Table 4-1. Variations on these base conditions to test for sensitivity included the following:

-Fuel Radius- Expanded to clad inner radius to simulate fuel that has already been in the core for a length of time.

-Clad Conductivity- 22 W/m-K for clad conductivity was chosen as a representative value for ferritic-martensitic and austenitic steel at 500 °C (59)(60), variations on this, both slight (16 W/m-K) and severe (1 W/m-K and 100 W/m-K) were examined to see the bounding effects of clad conductivity on the temperature distribution.

-Heat Transfer Coefficient- This property is dependent on numerous different values, 195 kW/m^2-K was calculated for a standard set of conditions. This value was varied in both directions by 50% (from 97.5 to 292.5 kW/m^2-K) to account for a wide range of values that could result from different operating conditions.

-Linear Power- In addition to 40 kW/m, a value of 30 kW/m was tested.

The forcing function used to model azimuthal variation around the pin was a sinusoidal function that altered the heat transfer coefficient to give a desired outer clad temperature distribution. Heat transfer coefficient was altered instead of coolant temperature due the program used for the modeling-it was just as effective as varying the coolant temperature as it achieved the desired outer clad temperature distribution.

Two different magnitudes of forcing functions were used. A severe function that simulated a temperature swing of about 15 °C around the pin was used to represent pins near the periphery of the assembly, where the temperature change from channel to channel is greatest. The second function simulated a temperature swing of only a few degrees, which describes the conditions in the center of an assembly where the variation from channel to channel is minimal.

Table 4-1- Nominal values of the geometric and thermal properties used to test the effect of azimuthally varying temperature functions on the clad.

Geometric Properties			Thermal Properties	
	EBR-II	S-PRISM		
Fuel Radius	2.16 mm	2.739 mm	Fuel Conductivity	16 W/m-K
Clad Inner	2.539 mm	3.161 mm	Sodium Conductivity	60 W/m-K
Clad Outer	2.92 mm	3.72 mm	Clad Conductivity	22 W/m-K
Pitch to	1.19	1.26	Linear Power	40 kW/m
Diameter Ratio			Heat Transfer Coefficient	195 kW/m^2-K

The magnitudes of the functions were chosen based on the sub-channel analysis results for the various assemblies presented in Chapter 3.

Figure 4-3 shows the results of each of the two forcing functions for the base conditions of EBR-II. For the case of the slight function the azimuthal temperature distribution is almost negligible, varying from average by at most a degree for the clad and much less than that for the fuel. For the more severe case there is a larger variation for the clad, however it is still only elevated by about 8 °C over the average clad temperature. This latter case will generally occur in the periphery of the assembly where the coolant temperature is low. In both cases the temperature distributions are very gradual, so are not likely to cause large thermal stresses. Each of the variations of the base conditions discussed above yield similar results to the plots shown.

Review of the literature showed that the most severe azimuthal distributions are not caused by variations from sub-channel to sub-channel but from clad contact with wire-wraps, with the exception of very tight pitches to be discussed below (61). Even though upon onset this study desired to look at variations from channel to channel, ultimately the most important part of the analysis is to capture the bounding case that causes the most variation. The two-dimensional rod assumption is blind to whether it is affected by sub-channel variation or clad hot-spot variation.

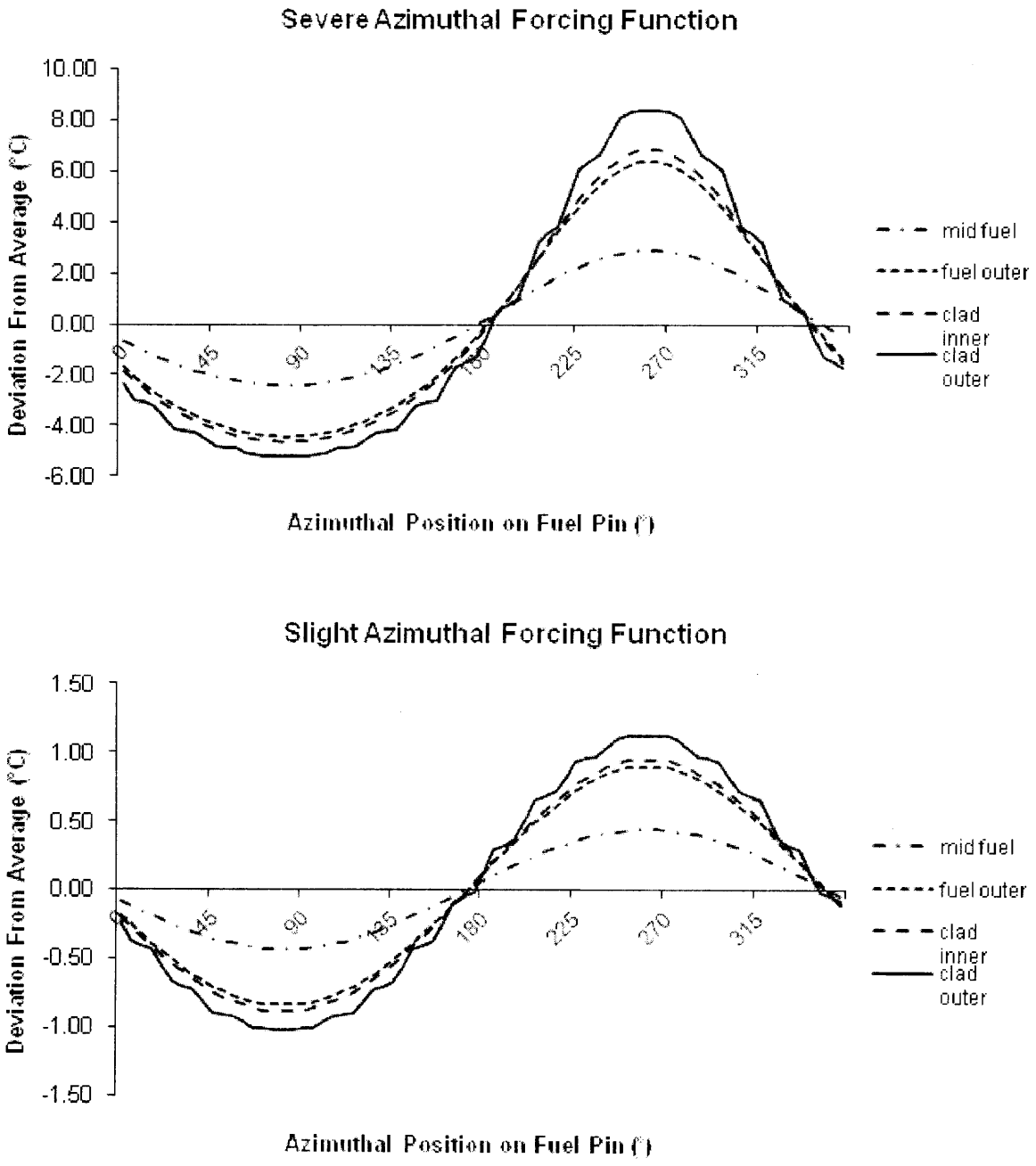

Figure 4-3- Resulting temperature distributions for two different azimuthal forcing functions at different radial locations.

The bounding case for local clad temperature peaking due to wire wrapping occurs when a single wire wrap is simultaneously touching two rods at the same time, as illustrated in Figure 4-4. Due to symmetry this situation can be modeled by looking at only a quarter of a single rod, shown in Figure 4-5.

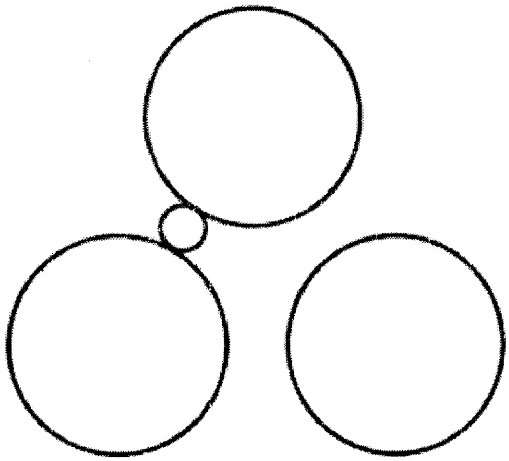

Figure 4-4 – Cross-sectional view of three fuel rods and the wire wrap. At this axially location the wire wrap is touching two rods at the same time.

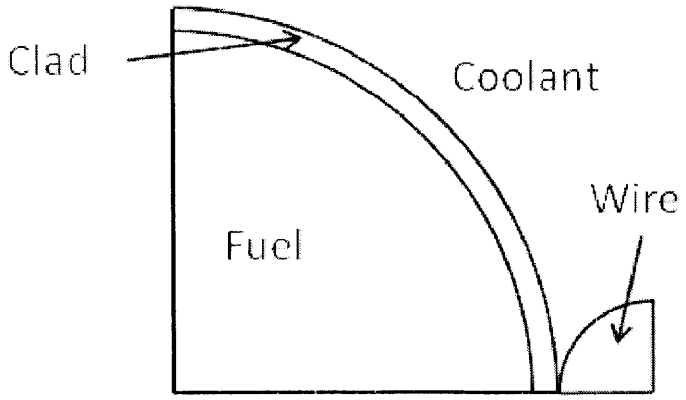

Figure 4-5 – Symmetry allows the situation in Figure 4-4 to be modeled with a quarter of one fuel rod, as shown here.

Due to geometry limitations a simplification to the model was made. It was not possible to use radial coordinates with two different origins, thus the wire could not be modeled as a

quarter circle but rather was modeled as a slice of an arc, as shown in Figure 4-6. This assumption is conservative, so the resulting temperature distribution will be more severe than what actually occurs, and this will still be a bounding case.

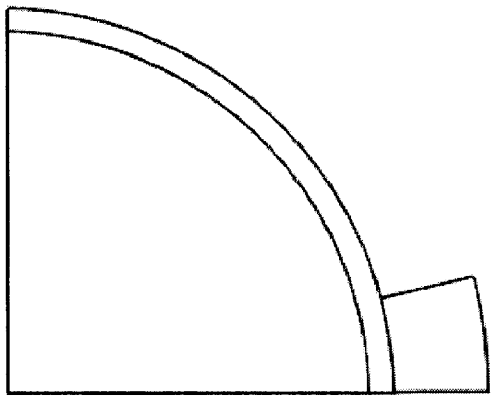

Figure 4-6 – Approximation of Figure 4-5 where all the shapes are drawn based on radial coordinates with the same origin.

The resulting outer clad temperature distribution for the wire wrap peaking can be found in Figure 4-7 for the S-PRISM geometry with a wire wrap diameter of 1.422 mm. This shows that the clad contact effect only has a significant effect on the clad temperature; the fuel temperature only differs a few degrees off the average. The importance of the large temperature spike in the clad is that this effect will be prevalent throughout the assembly; thus the pins in the hottest central regions will suffer equally as the cooler pins located near the edge.

To verify this result a comparison to models in the literature was made. The work of Chuang et al provides an opportunity for comparison as a similar situation is modeled (61). The geometry for this case is shown in Figure 4-8. Compared to Figure 4-6 the geometry is very similar for modeling the wire wrap.

Chuang introduces a dimensionless temperature for looking at peaking. The dimensionless temperature is defined as the difference of the local azimuthal temperature and the bulk coolant temperature divided by the difference of mean azimuthal temperature and the bulk coolant temperature, shown in Equation 4-2.

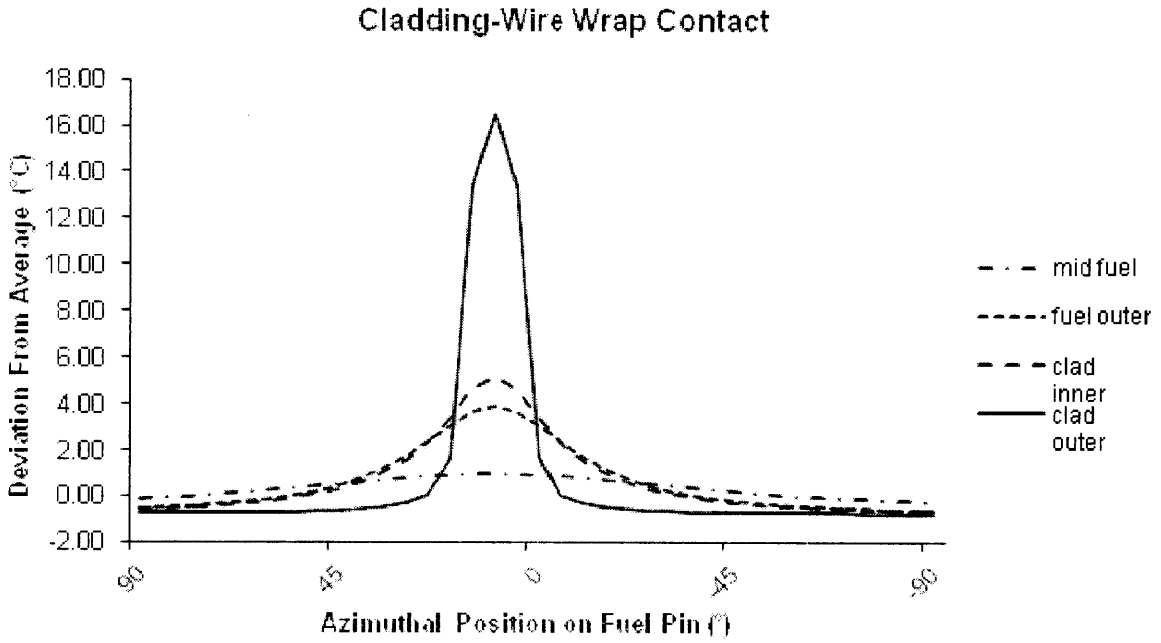

Figure 4-7 – Temperature distribution produced by wire wrap peaking when testing the S-PRISM geometry and conditions with HEATING7.

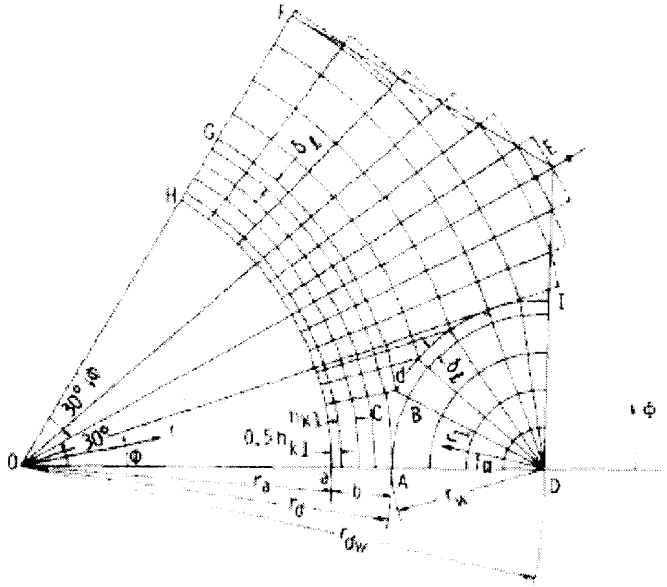

Figure 4-8 – Mesh from the Chung et al. to test wire wrap peaking (61).

$$T = \frac{T_{clad,\varphi} - T_{bulk\_coolant}}{T_{clad,average} - T_{bulk\_coolant}} \qquad 4\text{-}2$$

The dimensionless temperature is an effective hot spot factor, which is independent of heat flux (61). Figure 4-9 shows Chuang's results, which is based on the EBR-II geometry.

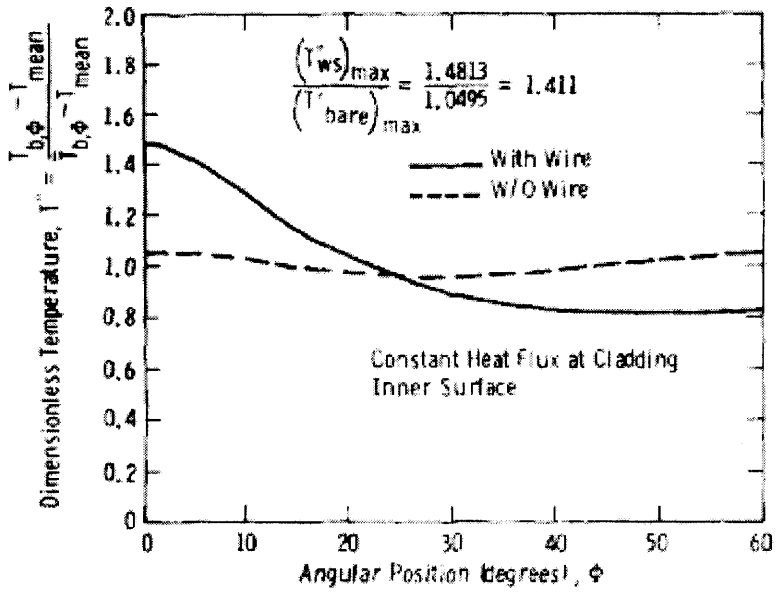

Figure 4-9 – Results obtained by Chung et al. for azimuthal peaking with and without a wire wrap (61).

Figure 4-10 shows the results of the model presented in this paper converted into dimensionless temperature. While Figure 4-9 and Figure 4-10 are for different geometries the driving geometric parameter for this analysis is pitch to diameter ratio, which is 1.256 for the EBR-II geometry and 1.19 for S-PRISM geometry, so similar results are expected. The results match well for the wire wrapped case. The results of the unwrapped case are similar in the magnitude of the variation however take on a different shape. For Chuang's result the temperature dips at 30° as compared to a (very slight) steady drop in Figure 4-10. The reason for this comes from a difference in the effect that is modeled for the bare rod case. Chuang is looking at differences caused over a single channel, based off of distance to nearest pin, as the

model in this thesis is concerned with differences from channel to channel. The effect of just the wire wrap can be isolated in Chuang's case by dividing the hot spot factor with the wire by the one without it, as shown in Figure 4-9. The factor is already isolated for this work because the wire wrap model does not include the forcing functions applied to get variations from sub-channel to sub-channel.

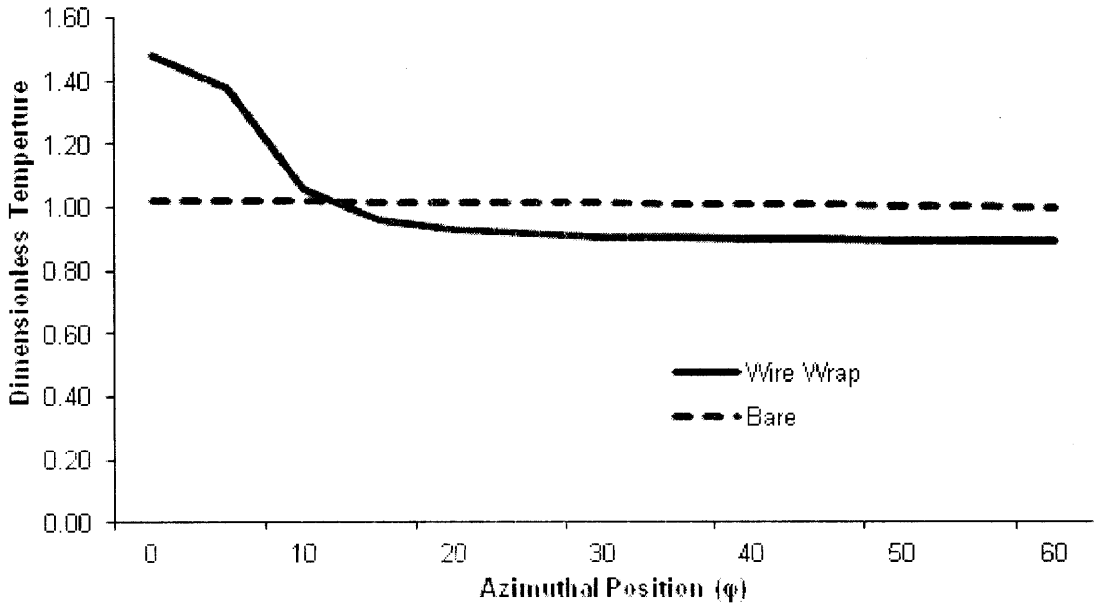

Figure 4-10 – Results from HEATING7 for the S-PRISM design converted into dimensionless temperature.

Now a finite element analysis can be conducted with confidence in the thermal model for the bounding case, wire wrap azimuthal peaking, which is done in the next section. It should be noted that hot spot peaking factors on bare rods caused by the pitch of the assembly were not covered by the model in this thesis as it is not captured by sub-channel analysis due to the nature of the method (each channel having a single temperature). As can be seen in Figure 4-9 the effect is negligible in cases where pitch to diameter ratio is high, as it is seen in this plot (1.257) (61). However, as the pitch becomes tighter the importance of this factor increases surpassing the peaking due to wire wraps at approximatly 1.10. Figure 4-11 shows a plot of the bare factor

(F_B) and the wire wrapped factor (F_W) for a large range of pitch to diameter ratios (F_{WS} is the combined factor). For bare rod cases with very tight pitches the most important azimuthal effect is missed entirely by the sub-channel model. The analysis in the next section will still provide a good estimate of the importance of azimuthal effects because the total peaking factor is largely independent of pitch to diameter ratio.

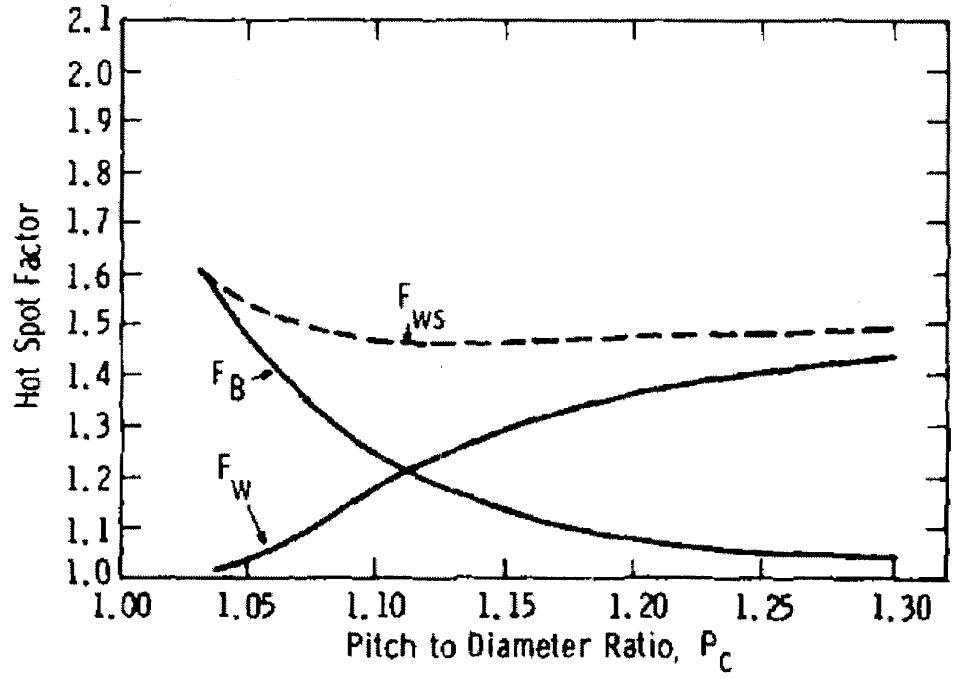

Figure 4-11- Plot for Chuang et al. showing the hot spot factor caused by the wire and the bundle pitch as a function of the pitch to diameter ratio (61).

4.2.2. Finite Element Analysis

Determining the stresses caused in the clad by the temperature distribution produced by the wire wrap required a finite element analysis to handle the complexity of the distribution. While thermal strains will also be caused by an azimuthal temperature distribution, additional

thermal strains for a temperature change on the order of 10 °C will be very small. Thus stresses are focused on primarily in this section while strains are covered in Section 4.2.3. In addition to the thermal strains caused by azimuthal temperature peaking there will be additional creep strain (both irradiation and thermal), which is significant but not well suited for examination by finite element analysis.

An analytical solution can be found for the simple case of determining the stresses produced in the clad from a purely radial temperature gradient across it. The solution for the plain stress case, where σ_z=0, starts with an equilibrium of the stresses:

$$\frac{d\sigma_r}{dr} + \frac{\sigma_r + \sigma_\theta}{r} = 0 \qquad 4\text{-}3$$

The strains are defined as:

$$\varepsilon_r = \frac{du}{dr} \qquad 4\text{-}4$$

$$\varepsilon_\theta = \frac{u}{r} \qquad 4\text{-}5$$

And therefore,

$$\frac{d\varepsilon_\theta}{dr} + \frac{\varepsilon_\theta - \varepsilon_r}{r} = 0 \qquad 4\text{-}6$$

Hooke's law provides the following two relations:

$$\varepsilon_r = \frac{1}{E}(\sigma_r - \nu\sigma_\theta) + \alpha T \qquad 4\text{-}7$$

$$\varepsilon_\theta = \frac{1}{E}(\sigma_\theta - \nu\sigma_r) + \alpha T \qquad 4\text{-}8$$

Equations 4-3 to 4-8 can be combined into the following differential equation:

$$r\frac{d^2\sigma_r}{dr^2} + 3\frac{d\sigma_r}{dr} = -E\alpha\frac{dT}{dr} \qquad 4\text{-}9$$

The heat conduction equation for a cylindrical shell with no internal generation is:

$$-\frac{dT}{dr} = \frac{T_a - T_b}{\ln(\frac{b}{a})}\frac{1}{r} \qquad 4\text{-}10$$

Substituting Equation 4-10 into 4-9 yields:

$$r\frac{d^2\sigma_r}{dr^2} + 3\frac{d\sigma_r}{dr} = -E\alpha\frac{T_a - T_b}{\ln(\frac{b}{a})}\frac{1}{r} \qquad 4\text{-}11$$

Using the boundary conditions $\sigma_r(a) = \sigma_r(b) = 0$, the differential equation can be solved for $\sigma_r(r)$ as follows and $\sigma_\theta(r)$ can be obtained from Equation 4-11.

$$\sigma_r(r) = \frac{E\alpha(T_a - T_b)}{2}\left[\frac{\ln(\frac{r}{a})}{\ln(\frac{b}{a})} - \frac{\frac{1}{a^2} - \frac{1}{r^2}}{\frac{1}{a^2} - \frac{1}{b^2}}\right] \qquad 4\text{-}12$$

$$\sigma_\theta(r) = \frac{E\alpha(T_a - T_b)}{2}\left[\frac{1 + \ln(\frac{r}{a})}{\ln(\frac{b}{a})} - \frac{\frac{1}{a^2} + \frac{1}{r^2}}{\frac{1}{a^2} - \frac{1}{b^2}}\right] \qquad 4\text{-}13$$

Where the variables are defined as:

a: Inner radius

α: Linear coefficient of thermal expansion

b: Outer radius

E: Young's Modulus

ε: Strain

r: Radial direction

σ: Stress

T: Temperature

θ: Azimuthal direction

ν: Poisson's Ratio

Figure 4-12 shows the results from ADINA for the thermal and pressure stresses for a fuel rod. The plot also shows the analytical stress for the temperature gradient. All stresses are effective stresses as defined by ADINA:

$$\sigma = \sqrt{\sigma_r^2 + \sigma_\theta^2 + \sigma_z^2} \qquad 4\text{-}14$$

Note this is a different definition than the Von Mesis Stress which is typically used to define effective stress. The values used for the geometry were the S-PRISM rod geometry values listed in Table 4-1. The material properties used were those for HT9 (23), and the values can be found in Table 4-2.

Table 4-2 – Material Properties of HT9

Young's Modulus	$1.62*10^{11}$ MPa
Poisson's Ratio	0.2935
Linear Coefficient of Thermal Expansion	$1.19*10^{-5}$ (1/K)

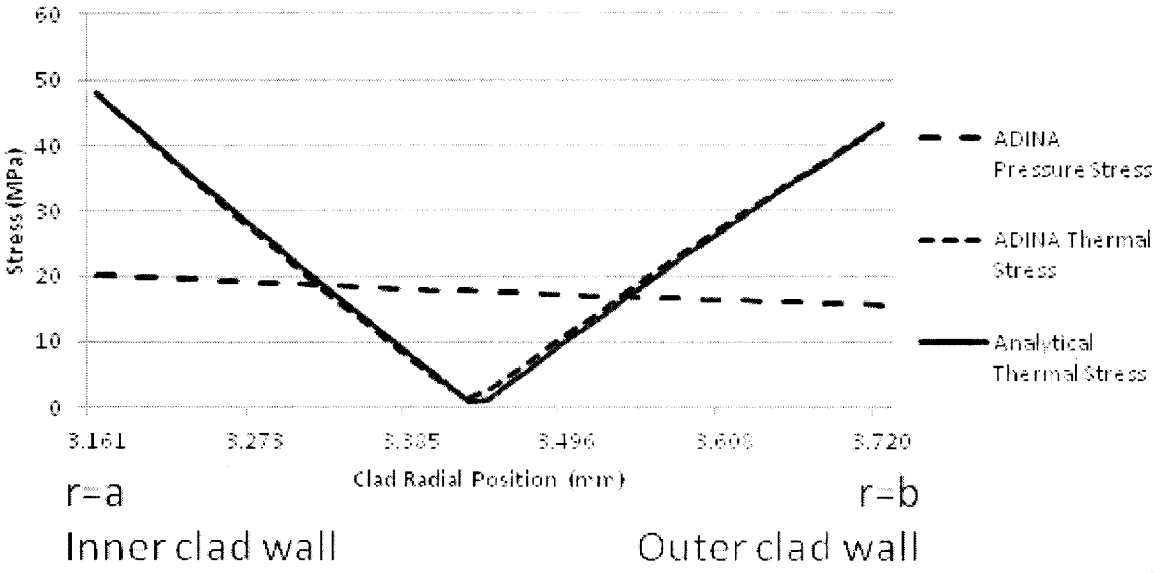

Figure 4-12 – ADINA results for effective thermal and pressure stresses on the fuel cladding for a typical S-PRISM rod. Also shown is the analytical solution for the thermal stress of the same case.

The analytical solution and the ADINA result match for the thermal stresses. A check on the pressure stress calculated by ADINA can be accomplished with the formulas for the stress of a thin walled cylinder (62):

$$\sigma_\theta = P_i \frac{b}{b-a} \tag{4-15}$$

$$\sigma_z = P_i \frac{b}{2(b-a)} \tag{4-16}$$

$$\sigma_r = \frac{P_i - P_o}{2} \tag{4-17}$$

where P_i is the pressure in the rod, which is assumed to be 3 MPa and P_o is the external pressure, assumed to be atmospheric. Therefore the effective pressure stress is:

$$\sigma_P = \sqrt{\left(3MPa\,\frac{3.72}{3.72-3.161}\right)^2 + \left(3MPa\,\frac{3.72}{2(3.72-3.161)}\right)^2 + \left(\frac{3MPa-.1MPa}{2}\right)^2} \qquad 4\text{-}18$$

$$= 22.36\ MPa$$

The value of 22.36 MPa calculated with Equation 4-18 with a thin shell approximation matches the ADINA result reasonably. ADINA was compared to the analytical results for this simple case as a check to ensure the code would properly model the fuel rod, as an accurate solution for the bounding case cannot be obtained analytically.

Analyzing the S-PRISM geometry with the wire touching, and temperature distribution shown in Figure 4-13 with ADINA produces the results shown in Figure 4-14. The additional stresses caused by the imposed bounding temperature distribution are on the order of hundreds of KPa while the total stress on the inside or outside clad is between 40 and 50 MPa. This is a rather negligible contribution of additional stress generated from the bounding scenario.

Even though a perfect analytical description of the bounding case cannot be solved for by hand, a conservative solution can be obtained by making some assumptions. First, the geometry is assumed to be that as is represented in Figure 4-15. There are two clad regions, region A, covered by the wire is at one temperature, while region B, uncovered is at a lower temperature. The area covered by the wire is a small angular amount, denoted as 2β. Further assumptions are:

- The strains and stresses considered are membrane strains and stresses, i.e., averaged over the thickness of the shell.

- The shell is unconstrained in the z-direction (plain stress case), σ_z=0

- There is no temperature gradient in the radial direction and no pressure, σ_r=0

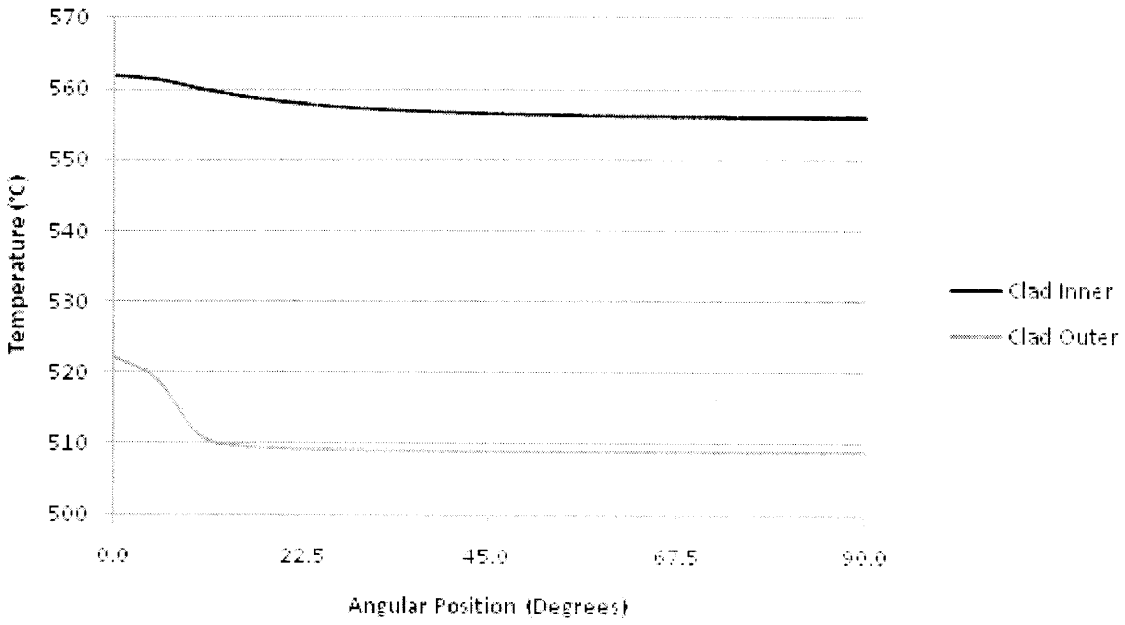

Figure 4-13 – Angular temperature profile used to test the stress profile in ADINA.

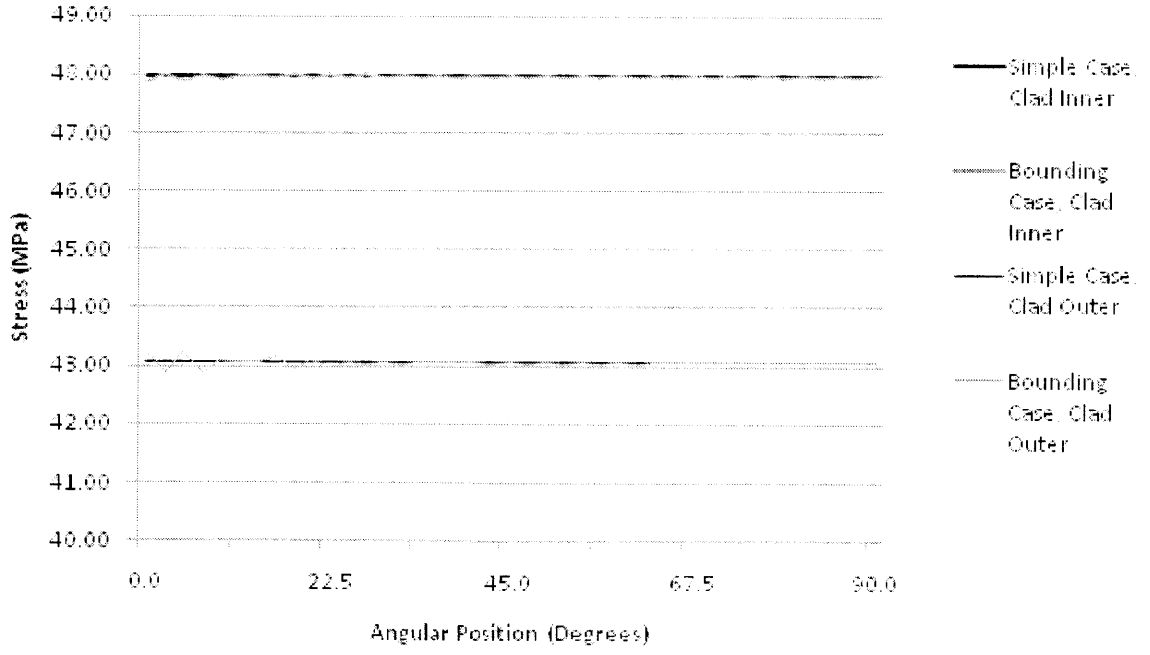

Figure 4-14 – Resulting stress profile for the inner and outer clad for the simple case, where there is azimuthal asymmetry, and the bounding case which uses the azimuthal profile from Figure 4-13.

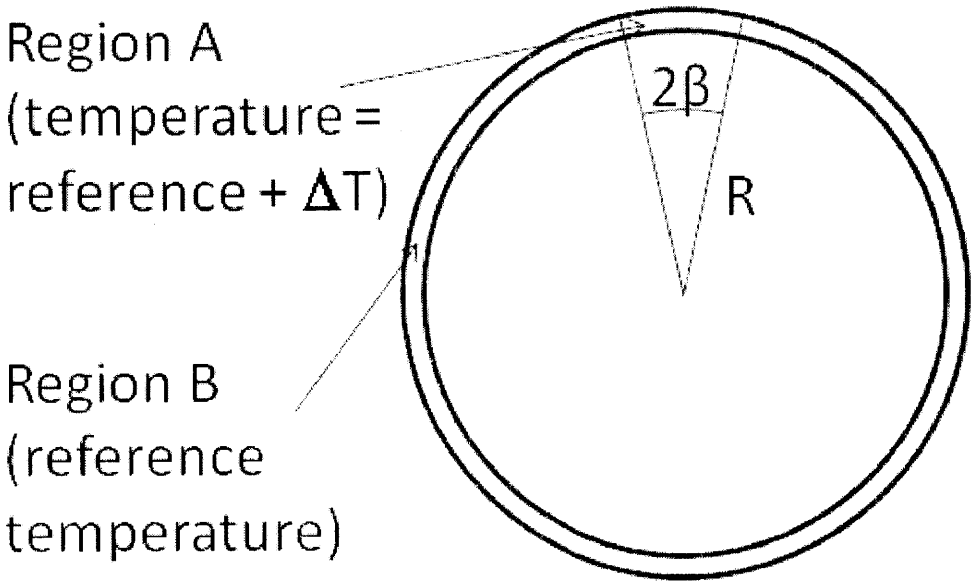

Figure 4-15- Diagram of a simple geometry that can be used to solve analytically for an azimuthally varying temperature function.

The azimuthal strain can be defined as follows, for zone A and zone B, respectively.

$$\varepsilon_{\theta A} = \frac{1}{E}\sigma_{\theta A} + \alpha\Delta T \qquad 4\text{-}19$$

$$\varepsilon_{\theta B} = \frac{1}{E}\sigma_{\theta B} \qquad 4\text{-}20$$

Imposing the conservative assumption that the shell circumference is fixed gives the equation below.

$$\varepsilon_{\theta A} 2\beta R + \varepsilon_{\theta B}(2\pi - 2\beta)R = 0 \qquad 4\text{-}21$$

Using these three equations and noting that the continuity of the stresses at the interface gives the boundary condition $\sigma_{\theta A} = \sigma_{\theta B}$ yields Equation 4-22.

$$\sigma_\theta = -E\alpha\Delta T\frac{\beta}{\pi} \qquad 4\text{-}22$$

Examining this equation, if the entire shell is at the lower reference temperature then $\beta=0$ and there is no stress, as would be expected. Also, if the entire shell is at an elevated temperature, then $\beta=\pi$ and the stress is a maximum, this too is as expected because of the assumption of a fixed circumference. The assumption of a fixed shell circumference is indeed conservative for this case because a fuel rod is allowed to expand during operation. A more rigorous treatment of this would give a non-zero σ_r because of the assumption of fixed circumference; however, the error induced would be quite small, on the order of:

$$\left(1-\frac{\nu}{2}\frac{t}{R}\right)\sigma_\theta \qquad 4\text{-}23$$

For the case of a typical fuel rod, this is about a 2% contribution. If the shell were constrained in the z-direction, there would be an additional factor of (1-ν) in the denominator increasing σ_θ, however this would be an unnecessary additional conservative assumption because the fuel rods are not constrained axially.

Examining Figure 4-13 shows that the temperature is elevated for about 20° or $\pi/9$ radians of the circumference, using this value for β, and 12 °C for ΔT also shown on that figure, a value can be calculated for σ_θ:

$$\sigma_\theta = -E\alpha\Delta T\frac{\beta}{\pi} = 162\ GPa * 1.19 * 10^{-5}\frac{1}{K} * 12\ K * \frac{\pi/9}{\pi} = 2.57\ MPa \qquad 4\text{-}24$$

This conservatively-estimated value is about an order of magnitude greater than what was calculated by ADINA, however very low compared to the thermal stresses induced by the radial temperature gradient.

In summary, this examination has shown that localized azimuthal peaking on a fuel rod is on the order of 10-20 °C. In rods of large pitch-to-diameter ratio, this peaking is mainly due to contact with the wire wrap, while in rods of tight pitch-to-diameter ratio it is due mostly to lower coolant flow in the rod-to-rod gap resulting in a lower local heat transfer coefficient. Neither of these effects can be modeled effectively through sub-channel analysis; however the effect is only severe at the outer surface of the clad and quickly falls off in the interior of the clad due to high thermal conductivity.

The additional stresses produced by azimuthal temperature peaking are small compared to the total stress on the fuel rod cladding, on the order of 1%. In light of this a two-dimensional fuel model is acceptable for coupling to the sub-channel analysis, but peaking affects still need to be considered and are discussed in the next section.

4.2.3. Clad Hot Spot Creep Strain

As can be seen in Figure 4-3 and Figure 4-7 the azimuthal temperature distributions in the fuel are minor (on the order of degrees), thus neglecting azimuthal temperature peaking phenomena occurring in the fuel or at the fuel-clad interface is acceptable. In the previous section it was shown that thermally induced stress in the clad from azimuthal affects is negligible. The only remaining phenomena left that could be affected by a non-uniform temperature profile around the pin is clad creep strain. Because creep strain is highly dependent on temperature, temperature peaking in the clad on the order of 10 °C will have an effect and cannot be neglected.

To account for the hot spot effect, clad creep strains and cumulative damage fraction (CDF) must be calculated with the clad at an elevated temperature. The stress on the inner wall of clad will remain unchanged because the temperature peaking does not affect the fuel clad mechanical interaction or the plenum pressure. An extra option was added to FEAST to allow

the user to enter a hot spot peaking temperature change, at which additional calculations will be made for the clad thermal creep strain, irradiation creep strain, and CDF. A sample case with representative EBR-II conditions was run with a hot spot peaking temperature change of 10 °C. The results showed that the peak thermal creep strain increased from 0.63% for the normal calculation to 1.31% when the 10 °C increase in temperature was considered, and similarly the peak CDF increased from 0.95% to 2.78%. The peak irradiation creep strain was unaffected.

While this additional calculation in FEAST provides the user with an estimate of the strains that will result from hot spot temperatures it should be used with caution. The strains are calculated in addition to the stress-strain calculations in FEAST and are external to it, they do not feedback into the calculation (this is impossible to do with FEAST because it is one-dimensional.) Furthermore, as will be discussed in the next section, the stress and strains in each pin in an assembly are coupled through contact with the wire wraps. The location at which the peak strains will likely be occurring will be the site of contact with the wire wraps (the cause of the temperature peaking), which will generate additional stress on the clad. Ultimately a three-dimensional full assembly model would be needed to accurately calculate the creep strains in the fuel pin caused by azimuthal temperature variation.

4.3. Iterative Coupling Considerations

Before coupling the codes, the structure of the coupling needed to be determined. The two options considered were a one way flow of information from COBRA to FEAST, or an iterative process of updating COBRA with information from FEAST. The two methods of coupling are shown schematically in Figure 4-16. In both methods inputs, such as power and geometry, are fed to both codes. Also common to both methods COBRA feeds FEAST the coolant temperature and heat transfer information. The iterative method features a loop where FEAST passes geometry changes back to COBRA. This section examines the advantages and

disadvantages of both approaches and gives the reasoning for the choice made to go with a one-way structure.

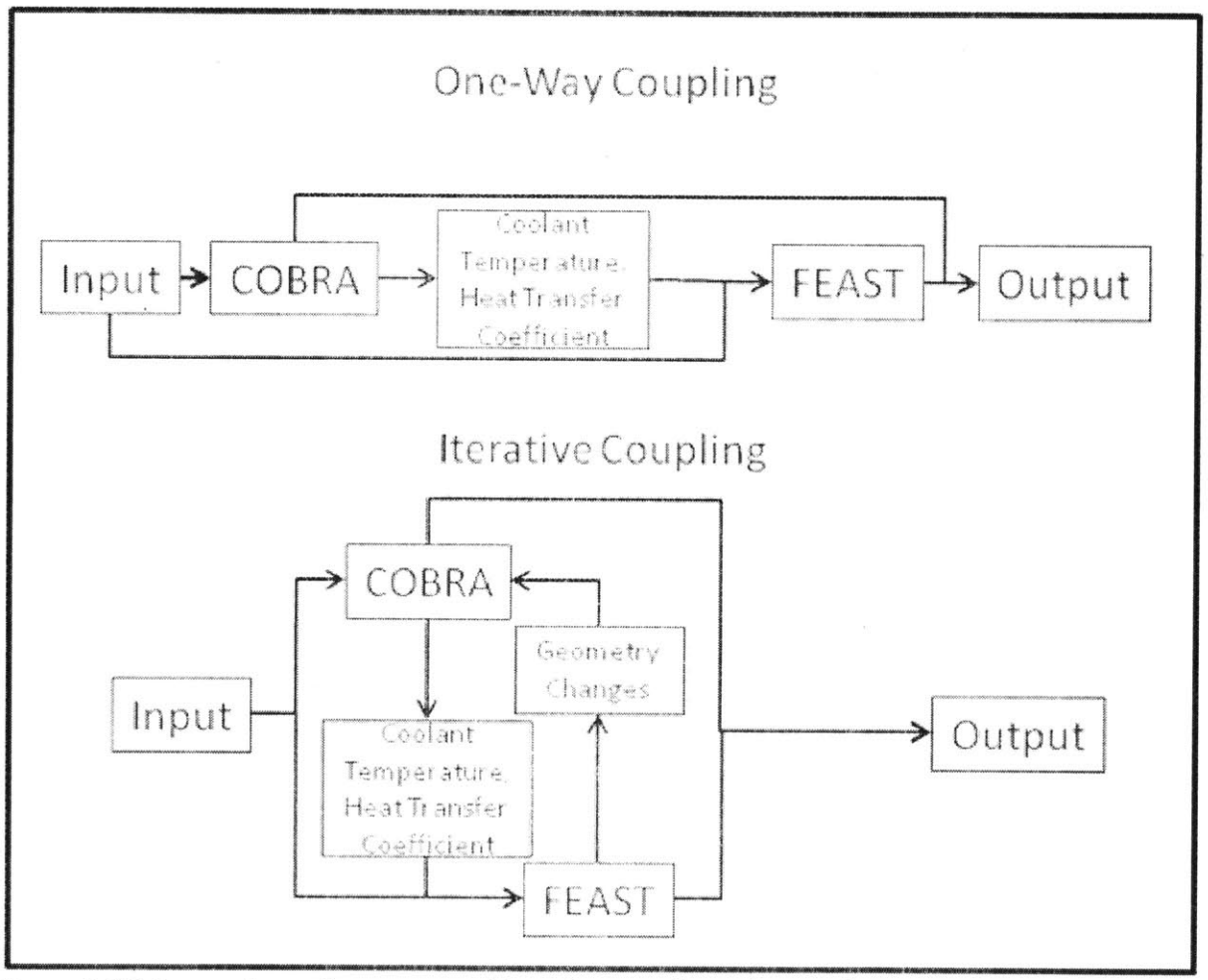

Figure 4-16-Comparison of one-way and iterative coupling schemes for COBRA and FEAST.

4.3.1. Advantages and Disadvantages

The advantage of going with an iteratively coupled model is that it can more accurately represent actual assembly operation. The coolant behavior is affected by the geometry of the assembly. As the fuel pins evolve over time they swell, changing the geometry of the assembly.

A coupled model will capture the evolution of the assembly geometry as it affects the thermal hydraulic analysis and in turn the fuel performance.

The disadvantage to a coupled model is the computational time. FEAST is a computationally intensive code. On systems with a good amount of memory (2 GB RAM is enough) it is limited by processor speed. For example, when compiled with optimizations using the Compaq Visual Fortran compiler version 6.6 (63) and a processor speed of 2.93 GHz the code takes about one hour to run one year of simulation for a pin. FEAST is not parallelized, so multiple cores do not give any significant speed increase. For a 217-pin assembly that is run for only three years it would take roughly 650 processor-hours to simulate every pin. In its purest form an iterative code would need to run every pin to know how the geometry is evolving, as each pin will behave differently based on its location in the assembly. Adding even just one feedback step to create and iterative code requires large amount of time, computing power, or both. The situation becomes even more problematic for different reactor designs, like breed and burn reactors that run on 20 year or greater cycles.

Certain assumptions can be made that would reduce the computational time for an iterative scheme. Instead of running each pin in FEAST to determine the changes in assembly geometry, a sampling could be taken, one pin from each ring for example, or an interior, edge, and corner pin. The geometry changes could then be applied to each similar pin. This would provide for a compromise allowing for feedback between the two codes while not being prohibitively expensive computationally.

4.3.2. Impact

With possible coupling schemes in mind it was first worth looking at the impact of how much of an effect implementing an iterative scheme would have. This was accomplished by simulating reference geometry in COBRA and then modifying the geometry based on changes that would occur during normal operation.

The reference geometry taken was the S-PRISM geometry (4). This was chosen because it is a large assembly, 271 pins, with sufficient literature information detailing operating

conditions. The reference geometry and input conditions for COBRA are listed in Table 4-3. Note pressure drop is listed in this table where flow rate was listed in previous chapters. Holding pressure drop constant is more meaningful when talking about changing geometry as the overall core pressure drop will remain the same.

Table 4-3- Reference conditions for running COBRA with an S-PRISM geometry.

	Input Parameter	S-PRISM
Geometry	Number of Pins	271
	Rod Diameter (mm)	7.44
	Rod Pitch (mm)	8.86
	Wire Wrap Diameter (mm)	1.42
	Wire Wrap Pitch (m)	0.2032
	Duct inside flat to flat distance (m)	0.149
	Total Length (m)	4.070
	Heated Length (m)	1.016
	Lower Unheated(m)	1.117
System Conditions	Pressure (atm)	1
	Inlet Temperature (°C)	371
	Pressure Drop (MPa)	.25
	Average Rod Power (W)	20875
	Axial Power Distribution (max/avg)	Chopped Cosine 1.12
	Radial Power Distribution	Uniform
Calculation Parameters	Wire Pitch Fraction (δ)	0.1252
	Turbulent Mixing Factor (β)	0.01
	Number of Axial Nodes	160

The exact geometric evolution of an SFR assembly during its operating life is a very complex process. Ohmae et al. have tried to model the evolution of assemblies with spacer grids (64). For a wire wrapped assembly the pin clad and duct walls swell from thermal and irradiation creep and thermal expansion. After a point the pins and the duct become coupled and further growth of the fuel pins will cause additional duct swelling or impingement on the wire wraps. A proper description of this evolution would require a three-dimensional code to model the mechanical behavior of the assembly, however this is beyond the scope this work. Several

approximations of the assembly swelling behavior are examined that could feasibly be implemented into an iterative version of the coupled COBRA-FEAST code.

A value of 3% pin swelling was chosen for pin diametral growth as clad embrittlement and pin failure often occur before this point (23)(65). While it may be possible to extend pin life past 3% diametral growth if it is dominated by irradiation creep strain, 3% is a reasonable value for the purposes of this examination.

The first case examined was changing the pin diameter only, increasing it by 3%. Every other value was held constant. The result of this case shows a substantial temperature increase for the entire assembly, as seen in Figure 4-17. This is expected because the flow area is significantly decreased as the channels are smaller, so for a constant pressure drop there will be less flow which leads to higher temperatures.

This case is largely unphysical; a change of pin diameter will have other indirect changes to the assembly. To bring the model closer to reality the pin to diameter ratio must also increase. Figure 4-18 shows schematically why the pin to diameter ratio must also change. While in a real assembly there will be some squishing of the wire wraps for this analysis it was assumed they did not change geometry. The assembly walls also need to swell to accommodate the pin swelling, however assembly swelling will not be of the same magnitude as pin swelling. While the pins were enlarged 3% the assembly flat to flat distance was only increased by 1.5%. The value of 1.5% was used because it was the minimum assembly swelling that permitted sufficient flow through the corner channels for COBRA to converge. The results of this case are shown in Figure 4-19.

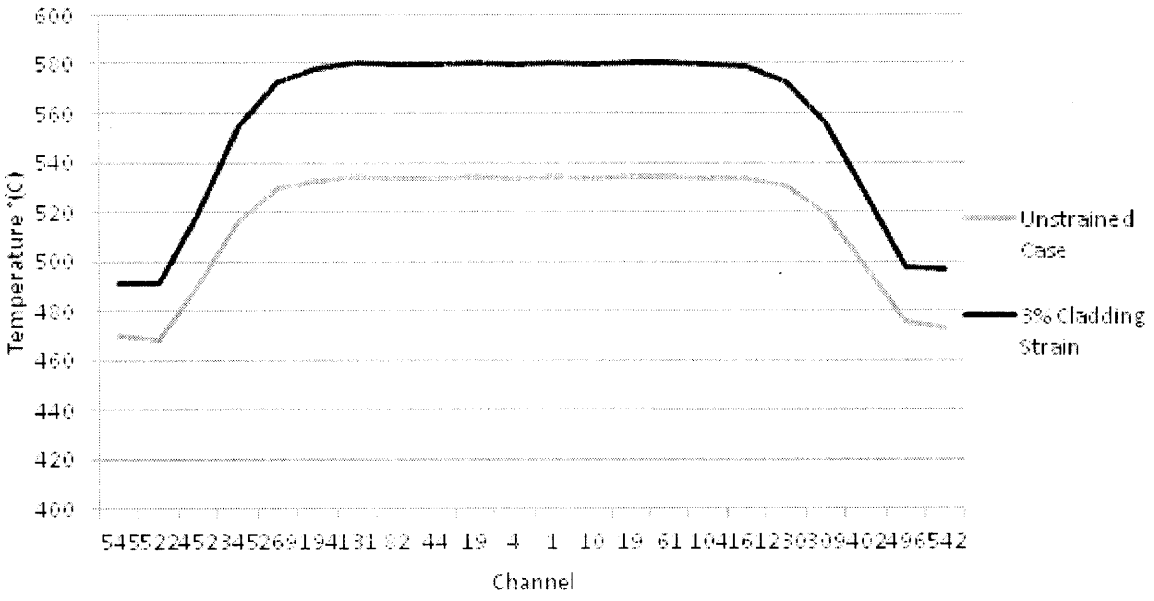

Figure 4-17 – Assembly temperature distributions for S-PRISM geometry with unstrained fuel rods versus rods with 3% strain, where the growth simply crushes the wire wrap.

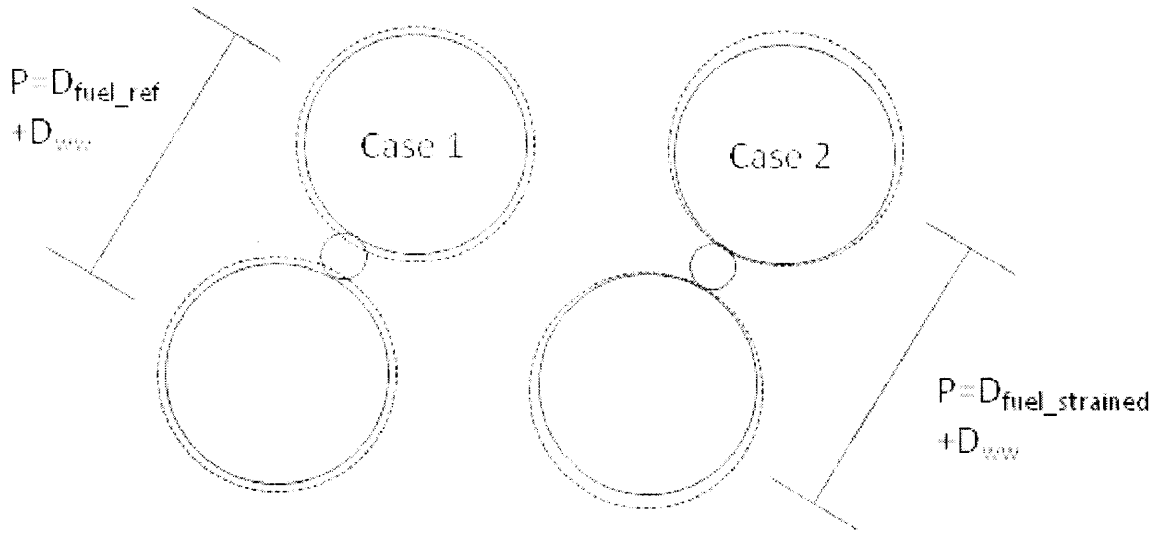

Figure 4-18 – Diagram showing why the pitch of the assembly increases when the pin diameter does. If the pitch does not increase then the wire-wraps are "crushed." In reality there will be some wire wrap impingement and some pitch to diameter ratio growth.

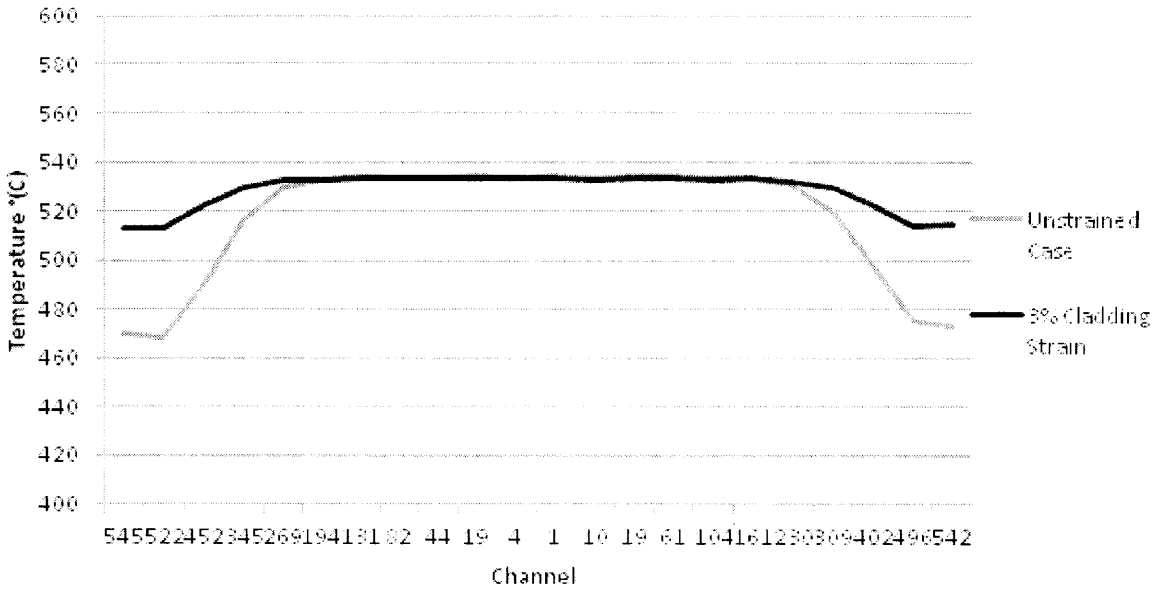

Figure 4-19 - Assembly temperature distributions for S-PRISM geometry with unstrained fuel rods versus rods with 3% strain and 1.5% swelling of the assembly flat to flat distance.

For this case the interior sub-channels have the same outlet temperature as the reference case. The edge and corner channels are significantly higher than the reference case but still below the interior channels. Considering the changes to geometry the overall flow area of the interior channels is actually increased. The larger pitch has more of an effect increasing the area than the increased diameter does detracting from it. This explains the lack of difference, or even slight decrease for the interior channels. The exterior fuel rods see less flow, because the rod swelling is more dominant than the slight increase in assembly flat to flat distance, and hence the temperature rises on the outer channels are much higher. The overall effect of this swelling was to flatten the temperature distribution of the assembly, and while it did not cause the peak temperature to increase there were significant changes to the coolant distribution that would indicate that COBRA needs information for FEAST for geometry evolution.

However there was still one more consideration that was not properly represented, which was that swelling is a function of axial location along the rod. In the previous cases the rod was assumed to swell uniformly along its entire length, all 4 meters. In reality only the portion of the rod that has fuel will swell significantly, and the swelling will be relative to the power level and temperature at each axial location. A third case was run where the swelling only occurred at

axial levels where there was fuel, and was tapered so that the 3% swelling would occur at the fuel mid-plane. This is shown in Figure 4-20.

The results of Case 3 are shown in Figure 4-21 below. The figure shows that the temperature distribution is almost the same as the reference case. With this case it looks as though the geometry feedback is not as important as the earlier cases indicated. While being the closest representation to the swelled geometry of any of the cases considered, this was still an approximation of the situation. Also consider that 3% strain is a limit, meaning that if it is reached it would be at the end of life for the fuel. The vast majority of the life of the assembly would be at much less strain than this, reducing the importance of strain feedback to COBRA.

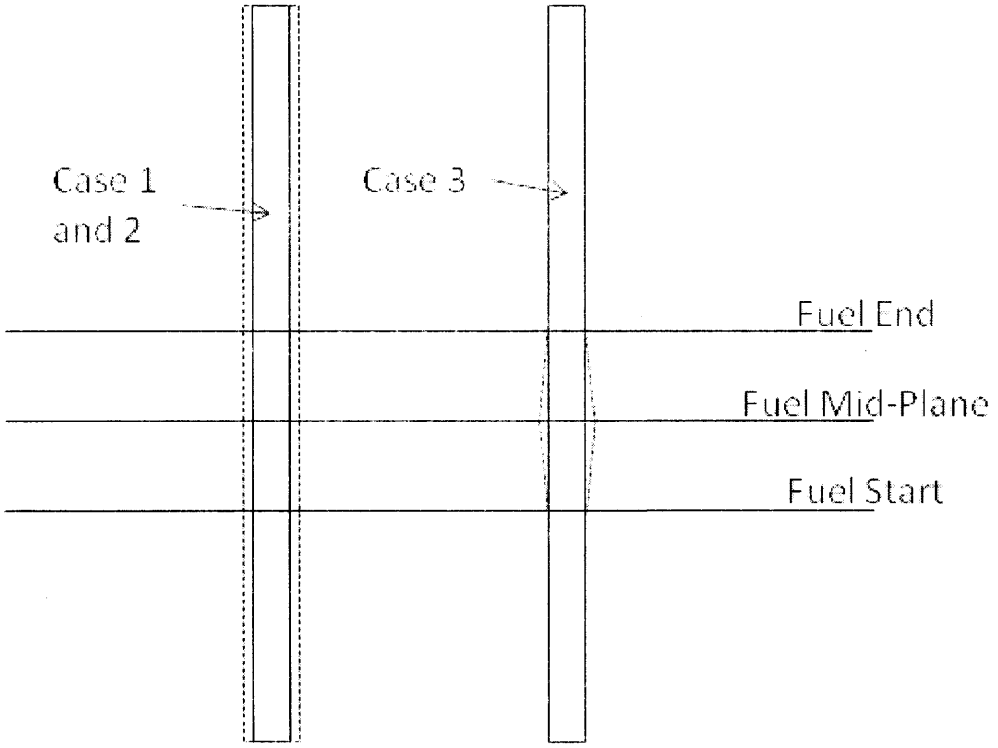

Figure 4-20 – Diagram showing the difference in swelling profiles axially for the cases modeled to test the effects of swelling on assembly coolant behavior.

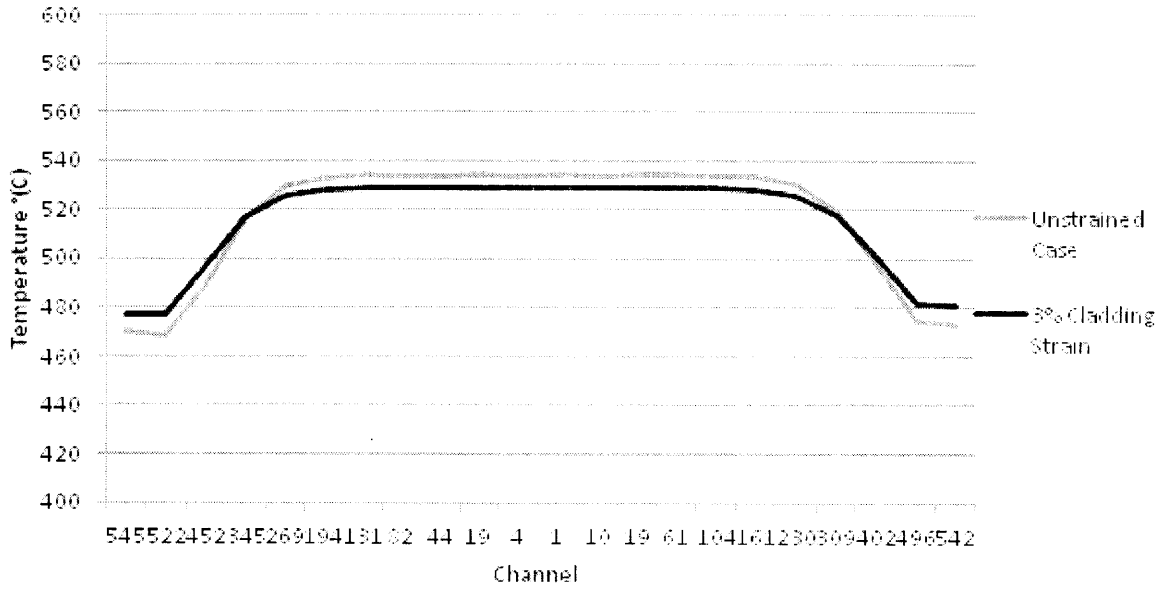

Figure 4-21 – Assembly temperature distributions for S-PRISM geometry with unstrained fuel rods versus rods with 3% strain, where the swelling only occurs in the active fuel region axially.

4.3.3. Conclusions

Considering the large amount of computational expense, added complexity to the coupled code, inability to know the correct geometric evolution of the assembly, and the overall impact of geometry changes on COBRA it was determined that an iterative coupling scheme was not necessary. Swelling, or other geometry changes, can be handled just as effectively by entering approximate conditions into COBRA if desired. For example, the general swelling behavior of the fuel rods is known based on burnup, the geometry can be appropriately altered at each time step that COBRA is executed. This will be explained in more detail in Section 4.4.3. Future work on iterative coupling would be facilitated by a three-dimensional mechanical model of the assembly.

4.4. CAFE: COBRA And FEAST Executer

The coupled code was written with a modular approach. Rather that integrate the two codes into one, the source and executable files were left separate. The advantage of this approach is that if improvements are made to each code independently it will be much easier to reconcile these improvements with the coupled approach. Leaving the two codes independent required a third code for the coupling. This third code is a parent code to the other two, it formats input and output files for COBRA and FEAST and calls them based on the user's settings. It is called COBRA And FEAST Executer or CAFE. While both COBRA and FEAST are written in FORTRAN, CAFE is written in Python.

4.4.1. Python Coding Language

Python (66) was an ideal candidate language for writing CAFE because its functionality meshed well with the tasks that CAFE had to accomplish. Unlike COBRA and FEAST there was no need for a language that had strong science and engineering roots to complete strenuous numerical problems like FORTRAN. The main features deemed necessary for CAFE are as follows:

- A user friendly interface

-Easy formatting and parsing of text documents for constructing input and output files

-The ability to call other codes and spawn new processes

-A clear and straight-forward source file that can be easily modified

These match very well with the strengths of Python.

Python is a dynamic programming language in some ways similar to Tcl, Perl, Ruby, Scheme and Java. It features a "very clear, readable syntax...intuitive object orientation... [and] extensive standard libraries and third party modules for virtually every task" (67). Furthermore Python is an open source code that is easy to learn and has an avid developer and user community.

Python translates into the previous bullet points in the following way:

-A user friendly interface: a module for Python was employed that allowed interfacing with a Microsoft Excel spreadsheet. This provided a happy compromise between using data files that are text documents that are often dense and confusing versus developing a graphical user interface that would have taken considerable time.

-Easy formatting and parsing of text documents for constructing input and output files: Python excels at handling text data. Python can read an entire text document into a vector of lines. These lines can then be parsed by characters. This allows for the very specific formatting to be accomplished as is required for the input files.

-The ability to call other codes and spawn new processes: Python can call executables as subroutines.

-A clear and straight forward source file that can be easily modified: Python does not require very strict formatting when coding. In most cases the code reads like a description of what is being done, without any comments.

Below is an excerpt of the CAFE code to show the Python language:

```
1     if inopts.cell('C5').value=='Yes': #run the GEOM program
2           gtemplate = open('geomtemplate.dat','r') #open the template
3           print "updating and running GEOM"
4
5           gline=gtemplate.readlines() #read the lines of the template file
            into a list
6           gtemplate.close()
7           k=0         #current line
8
```

```
9           gopts=master.get_sheet_by_name('GEOM Input') #get sheet
            containing the GEOM options
10
11          #Edit the lines one by one where the master input allows for
            choices
12
13          #Using GEOM option 2 the following formats Card 3
14          k+=2
15          gline[k]=(gline[k][:5]+str(float(gopts.cell('E4').value))[0:5].
            rjust(5,)+
16          str(float(gopts.cell('C5').value))[0:5].rjust(5,)+
17          str(float(gopts.cell('E6').value))[0:5].rjust(5,)+ gline[k][20:])
18
19          #Using GEOM option 3 the following formats the Card 7
20          k+=2
21          gline[k]=(str(int(gopts.cell('C8').value))[0:5].rjust(5,)+
22          str(float(gopts.cell('E4').value))[0:5].rjust(5,)+gline[k]
            [10:30]+
23          str(float(gopts.cell('C10').value))[0:5].rjust(5,)+gline[k][35:])
24
25          if gopts.cell('C9').value=='Counterclockwise':
26                gline[k]=gline[k][:20]+'    0'+gline[k][25:]
27
28          if gopts.cell('C11').value=='No':
29                gline[k]=gline[k][:35]+'    0'+gline[k][40:]
30
31          #Write data to GEOM input file
32          geomin = open('geom.dat','w')
33          for x in gline:
34                geomin.write(x)
35
36          geomin.close()

37          #Call GEOM
38          subprocess.call('geom.exe <geom.dat', shell='true')
```

This segment of code handles the formatting for the GEOM program. All the text in grey are comments and do not affect the execution of the code. The first line checks if GEOM is being executed in this instance of CAFE, this process does not run if the input option (found in cell C5 of the input options worksheet of the input spreadsheet) is not selected. Lines 2-7 initialize the code by opening the template file, reading it into a vector of lines, closing the template file, and seting a counter to 0. Line 9 accesses the geometry input worksheet, shown in Figure 4-22.

	A	B	C	D	E	F	G
1							
2							
3							
4		What is the rod diameter?	0.73	cm	0.287402	in	
5		What is the rod pitch to diameter ratio?	1.19				
6		What is the flat to flat internal duct dimension?	14	cm	5.511811	in	
7							
8		What is the number of rods in the bundle?	217				
9		What is the wire wrap direction?	Counterclockwise				
10		What is the pitch fraction for forcing cross flow?	0.0633	(recommended-node length/wire wrap pitch)			
11		Include corner subchannels?	Yes				
12							
13		The number of subchannels is:	438				
14		The number of gaps is:	654				
15							

Figure 4-22 – Sample input for the GEOM portion of CAFE, the portion of the code in the excerpt above.

Lines 13 through 17 of the code format the 3rd card (GEOM refers to lines as cards) of the input file. Lines 19 through 34 format the 7th card, (which appears two lines below the third 3rd card on the input file for this style of GEOM input). Finally lines 32 through 37 open and write the GEOM input file, geom.dat and line 38 calls the GEOM executable.

The template file that this code works on is shown in Figure 4-23.

```
    1 GEOM SETUP


1 11
          1.000    1    1   60          1
```

Figure 4-23- Template that CAFE uses to create a GEOM input file.

All the values on the template are options set by GEOM that would only in rare cases need to be altered. The resulting input file the code produces using the template is shown in Figure 4-24.

```
     1 GEOM SETUP

      0.287 1.195.511
1 11
  2170.2871.000     1     0    600.063     1
```

Figure 4-24 – Resulting input file created by CAFE with the template and input above.

The version of Python used is 2.6 (68). The library for reading and writing Microsoft Excel files that was used is OpenPyXL (69). This software and extensive documentation are available at python.org.

4.4.2. CAFE Code Interface, Input and Output

As discussed above, CAFE employs the OpenPyXL package that allows it to interface with a Microsoft Excel spreadsheet. A user interface has been created for CAFE from a Microsoft Excel spreadsheet that includes all the input options needed to run CAFE, and all the more common input options for COBRA and FEAST.

The input workbook consists of several different worksheets, each containing a grouping of input options. The worksheets are as follows:

-Input Options- These are the necessary inputs and options for the CAFE code itself. These inputs range from options about which portions of the code to run to nodalization data for FEAST and COBRA necessary to create input files.

-GEOM Input- These are inputs for the GEOM program, the program which creates the geometry files for COBRA.

-COBRA Input- These are the inputs for COBRA.

-COBRA Tables- This worksheet contains relative heat flux tables for COBRA which allows COBRA to simulate different power levels when creating a set of FEAST input files.

-FEAST Input- These are the inputs for FEAST.

The inputs for the various codes do not cover every possible set of inputs for COBRA and FEAST. Values that do not often change are not handled by CAFE, for example coolant properties. If the user wished to alter the coolant properties, to change from sodium to lead, he would need to access the COBRA input files directly. This can be done in two ways. First, CAFE assembles the input files for FEAST and COBRA from template files that contain a full set of standard inputs. Any changes made to the template file will be reflected in any future CAFE runs. So in the example above all the sodium properties could be changed to lead properties in the COBRA template. The second way to handle this is to bypass the input file construction by CAFE altogether. This is an option in the input options worksheet. If the bypass is toggled on then the user must provide the name of a COBRA input file for each FEAST time step he wishes to run and the name of a FEAST master input file. The interface does not support the construction of COBRA transient input files at this time. If a transient is part of the simulation the COBRA input file for that transient must be assembled by the user and the name of that file supplied to CAFE.

Figure 4-25 shows a portion of the CAFE interface file. The worksheet shown here is the COBRA Input worksheet. Column A lists the card or variable the input corresponds to in the COBRA manual. Column B prompts the user for the input to be entered in Column C. For cases where there are a set number of possible inputs, such as correlations to choose from, or yes/no options a drop down bar will appear when selecting column C with a list of options This can be seen in cell C8 in Figure 4-25, which shows a drop down menu of possible heat transfer correlation options.. Answering some questions will require the user to go to a place in the workbook to fill out other cells. When this is the case a cell will be highlighted in green with this instruction. In the figure below cell row 11 prompts the user for how many entries there will be in the axial flux table. After entering this number row 12 instructs the user to head to the <Cobra Tables> workbook to fill out this table. Numbers entered that have associated units with

them will have a drop down menu appear in column D. The input units used in column C should be selected from this menu, and the value will automatically be converted into the correct units for COBRA and displayed in Column E. This can be seen in row 20; a value of 20.32 cm is entered for the wire wrap pitch, which is converted into 8 in. Finally all cells that require attention will be highlighted in red when an input is required but not present. In Figure 4-25, cell C21 shows this, as the user has yet to enter a value for the outer rod diameter of the pins, the file cannot be run until this is done.

One of the major benefits of the CAFE interface beyond the friendly format that Microsoft Excel provides is the simplification of the number of input files required. To run COBRA or FEAST without CAFE each would need up to a dozen input files depending on the specifics of the run.

The output from CAFE is all the resulting output files from COBRA and FEAST. The code does not do any processing of the output files, nor does it alter them in any way. Both codes have a useful output format so changes to it were not necessary. Output improvements would be better served through changes in COBRA and FEAST, if that was desired.

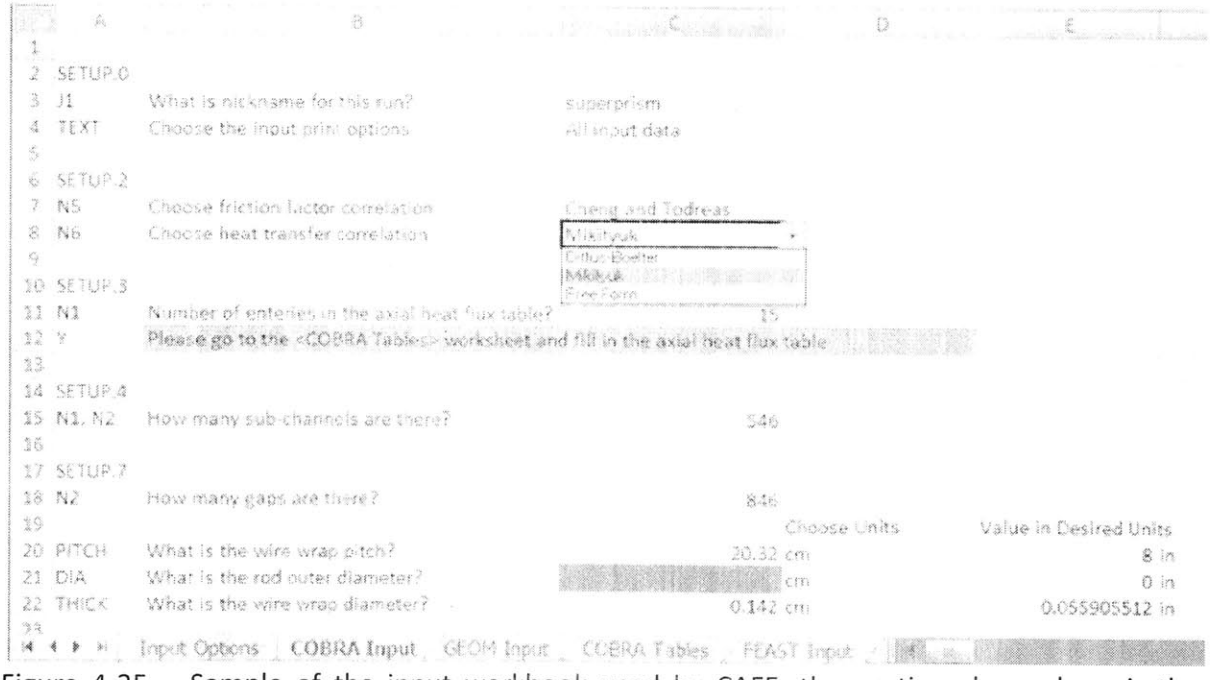

Figure 4-25 – Sample of the input workbook used by CAFE, the portion shown here is the COBRA Input options.

4.4.3. CAFE Code Processes

In Section 4.3 it was shown that a once through process for CAFE would be the most efficient while still accurately predicting the fuel and coolant behavior. The overall flow diagram for the procedure used in CAFE is shown in Figure 4-26. The figure shows that the program proceeds linearly through the steps. Step by step the code works as follows:

1) Update Geometry-This step is flagged by cell C4 of the input options worksheet. It toggles whether or not to run GEOM, which is the program that sets up the geometry for COBRA.
2) Update COBRA Input Files- This step is controlled by cell C7 of the input options worksheet. The user must choose between using the COBRA templates and data from the COBRA Input tab or if they wish to supply already complete formatted COBRA input files by name. If new input files are generated they are saved so the user can go back and modify them for future use if desired.
3) Run COBRA- This is the only step which cannot be turned off. CAFE will run COBRA a number of times determined by the number of FEAST time steps. FEAST time steps are set by the user and should be based on when the steady-state assembly conditions change. For example, a change in power level or flow rate should call for a new COBRA run. COBRA will run an additional time if there is a transient.
4) Format FEAST Data Files- This option is toggled on and off by cell C11 in the input options worksheet. It determines if a new set of input files for FEAST is generated based on the COBRA runs.
5) Run FEAST- The flag for running FEAST is cell C17 of the input options worksheet. FEAST will be executed a number of times equal to the number of pins that are to be examined.

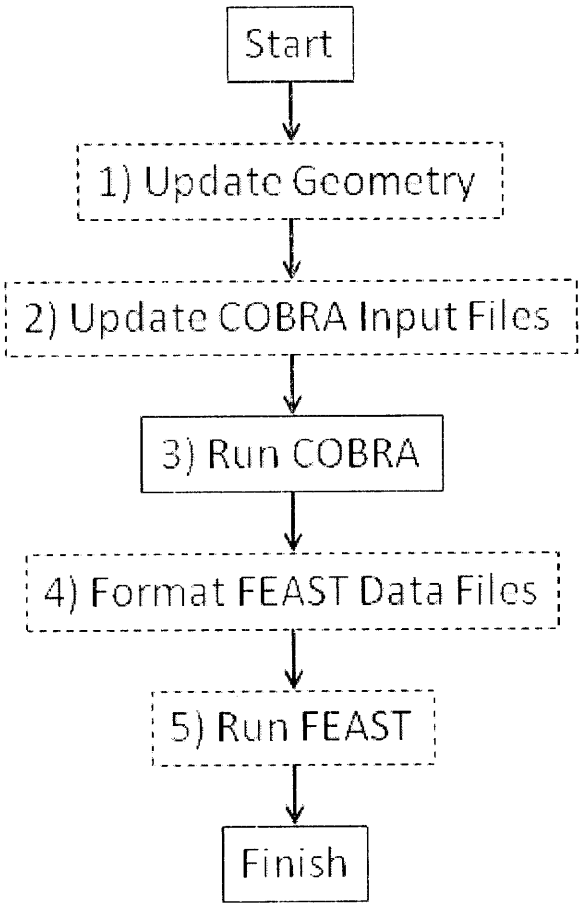

Figure 4-26- Process flow chart for CAFÉ.

Of the steps above most are straight-forward in the way they run. Steps 3 and 4 are the exceptions to this. Generating the input files for FEAST is the most complex portion of CAFE. This process is diagramed in Figure 4-27 below. The flow chart contains a box, all the steps in the box are incorporated into COBRA and all the steps outside the box are handled by CAFE. There are two different processes that COBRA does, either running a steady-state or transient case, or printing a temporary file that contains all the data required for FEAST input files (temporary files are in addition to the normal COBRA output files). The logic in CAFE controls COBRA, parses the data, and then formats and prints the FEAST data files. The process below shows that a transient must always be run after the last time step of COBRA; this does not mean that the transient must occur at the end of simulation. While all the other time steps must occur

in order, FEAST has an input that specifies when the transient starts. The transient data files for FEAST are completely separate from the steady-state files.

The current construction of CAFE allows for great flexibility in running different sets of options. Above the case was discussed where the user would want to change the geometry of the assemblies over time based on known swelling effects. This is easily accomplished by running CAFE steps one, two, and three. This would give the COBRA data for each time step with the assembly geometry constant, and the corresponding formatted COBRA input files. Then the axial geometry table can be added to the input files that are desired to simulate swelling or other geometric changes. Then CAFE can be run with steps three, four, and five and the swelling effects on COBRA will be passed to FEAST. The user can now compare the effect that the geometry changes had on the new and old COBRA output files.

This concludes the discussion of the coupling; the next chapter explores the validation and uses of the coupled code.

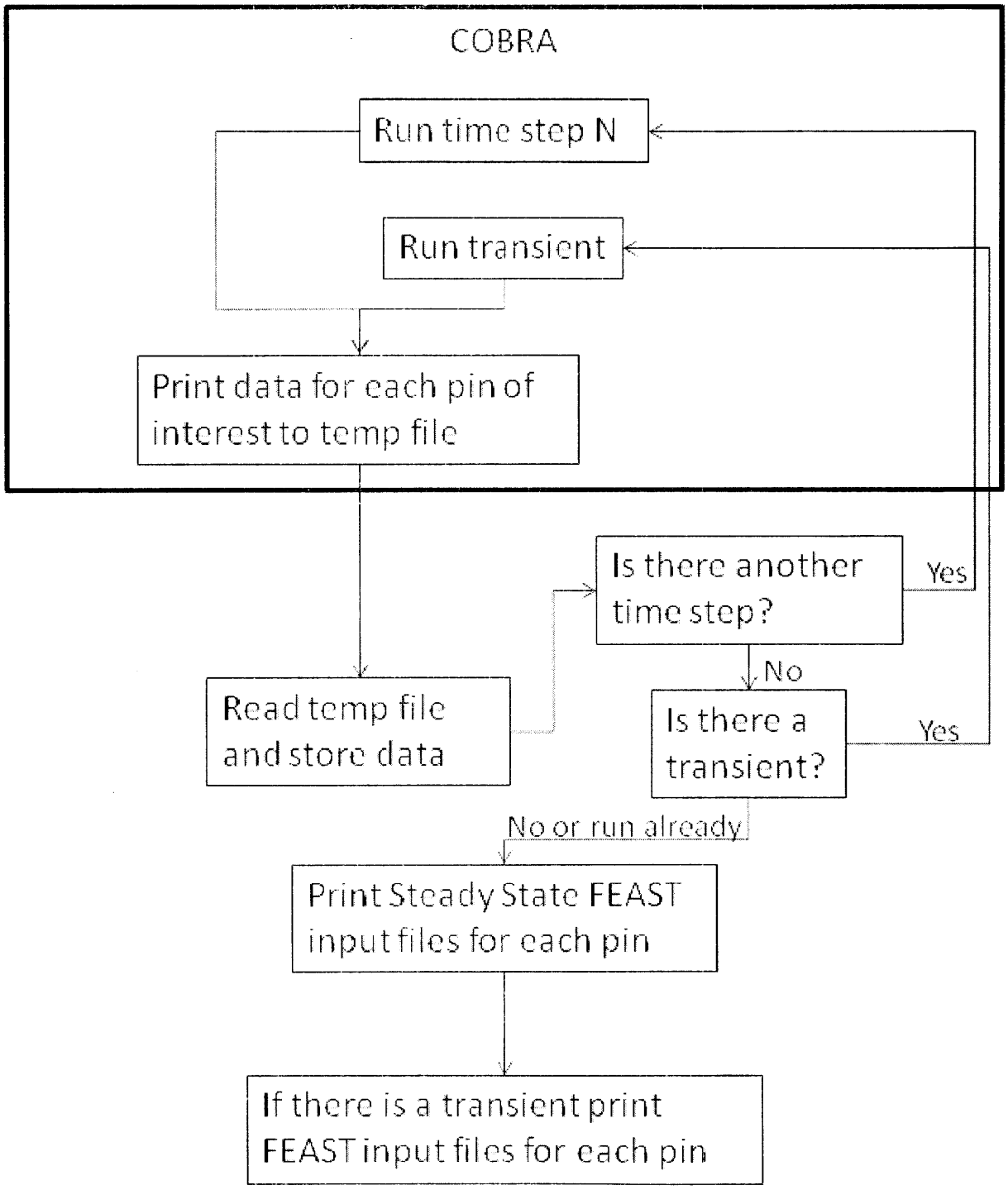

Figure 4-27 – Flow diagram for the portion of CAFE that runs COBRA and creates the input files for FEAST.

Chapter 5. Validation and Application of CAFE

5.1. CAFE Benchmark

While COBRA and FEAST have been benchmarked thoroughly independently (Chapter 3 and Reference (23)(28)), a benchmark of the combined performance is desirable. A rigorous benchmark for CAFE would require a full set of assembly operating conditions along with fuel performance data from multiple pins from that assembly. Unfortunately a complete set of data such as this could not be found in the literature. The nearest complete sets of data found are from assemblies from the EBR-II reactor. One such assembly is X425 from EBR-II. The data available for this assembly includes:

-The pin geometry (23)(70)

-The assembly geometry for a 61-pin array (71)

-The assumed coolant outlet temperature history and power history for the hot pin (23), shown in Figure 5-1 and Figure 5-2.

The only data missing necessary to make a COBRA model for this assembly was a flow history. However this could be determined from the power and peak channel outlet temperature. The data used for the COBRA model is found in Table 5-1. The data used to model the fuel rods in FEAST is found in Table 5-2. Figure 5-3 shows the burnup for the assembly as a function of time.

Table 5-1- COBRA input data used to model the EBR-II X425 assembly.

	Input Parameter	Sample Assembly
Geometry	Number of Pins	61
	Rod Diameter (mm)	5.84
	Rod Pitch (mm)	6.91
	Wire Wrap Diameter (mm)	1.07
	Wire Wrap Pitch (m)	0.15
	Duct inside flat to flat distance (m)	0.0582
	Total Length (m)	0.75
	Heated Length (m)	0.343
	Lower Unheated Length (m)	0.03
System Conditions	Pressure (atm)	1
	Inlet Temperature (°C)	370
	Inlet Mass Flow (kg/s)	5.81
	Peak Linear Power (kW/m)	40
	Axial Power Distribution (max/avg)	Chopped Cos 1.48
	Radial Power Distribution	Uniform
Calculation Parameters	Wire Pitch Fraction (δ)	0.0938
	Turbulent Mixing Factor (β)	0.01
	Number of Axial Nodes	50

Table 5-2- FEAST input data used to model the hot fuel pin from EBR-II X425 assembly.

	Input Parameter	Sample Assembly
Geometry	Clad Outer Radius (mm)	2.92
	Clad Inner Radius (mm)	2.539
	Fuel Outer Radius (mm)	2.16
	Wire Wrap Radius (mm)	0.535
	Plenum to Fuel Ratio	1.0
	Axial Node Length	0.049
Fuel Conditions	Zr weight fraction	10
	Pu weight fraction	19
	Initial Fill Gas Pressure (kPa)	84
Calculation Parameters	Time Periods in Rod History	50
	Number of Axial Nodes	7
	Time Step (seconds)	10
	Flux Conversion Factor	5.02

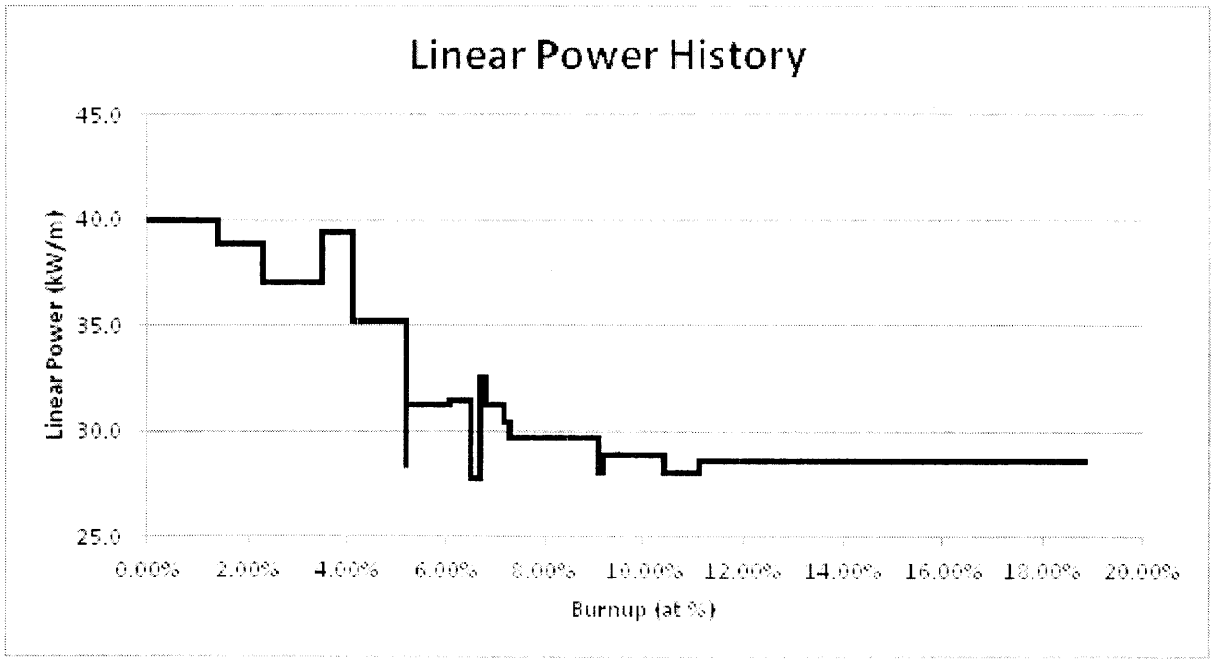

Figure 5-1- Power history for the EBR-II X425 assembly.

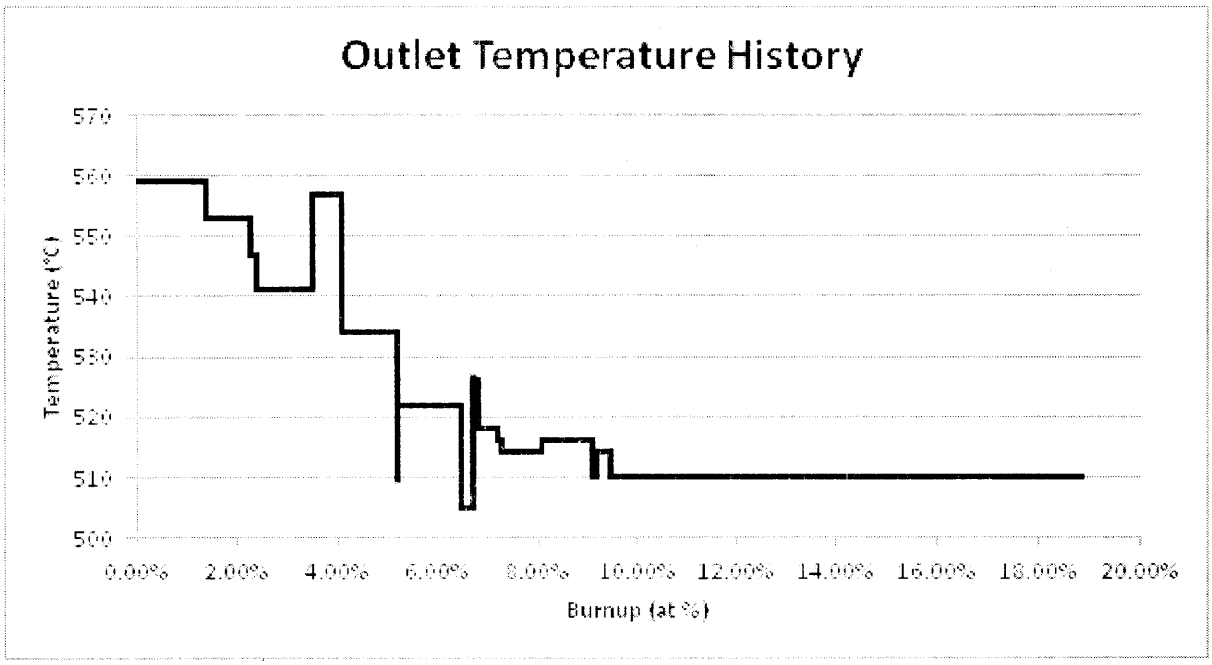

Figure 5-2- Outlet temperature history for the EBR-II X425 assembly.

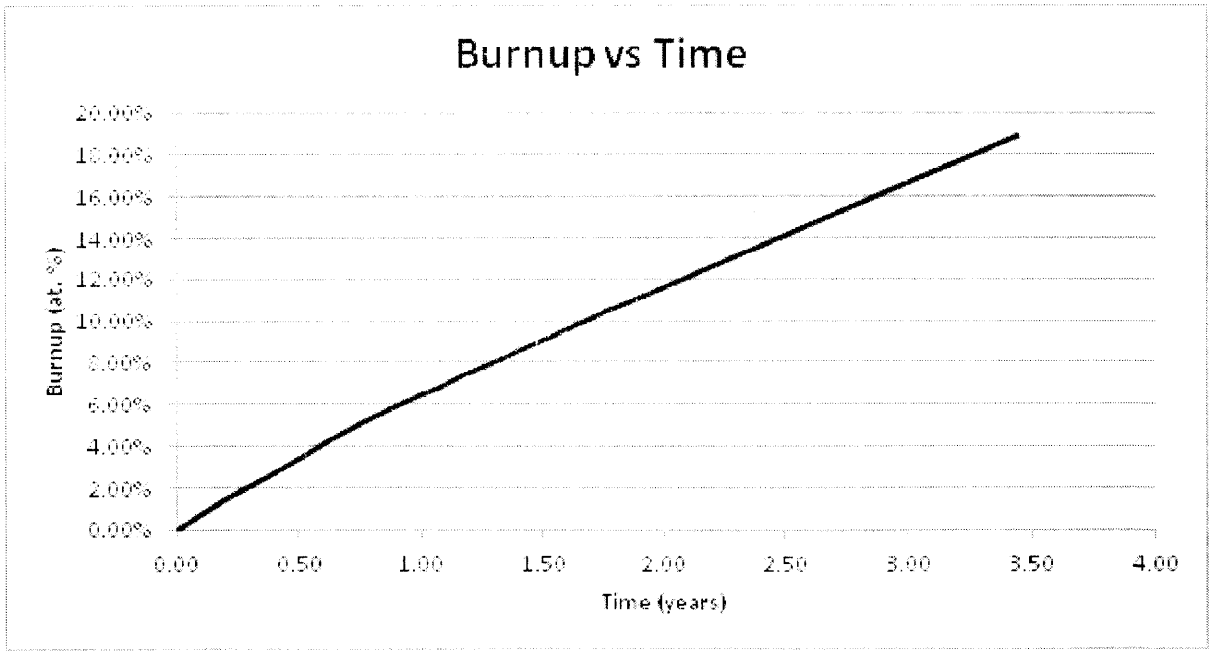

Figure 5-3-Burnup versus time history for EBR-II X425 assembly, the slope changes at points corresponding to changes in power for the assembly.

So with enough data to make COBRA and FEAST models for the X425 assembly, a CAFE model of this assembly was constructed and analyzed. The hot pin was benchmarked against the data and compared to the previous FEAST results. Peak clad strain for each case is shown below in Table 5-3.

Table 5-3- Comparison of peak clad strain data in at. % between the experiment, FEAST only results and CAFE results.

Peak Burnup (at. %)	Experimental data	FEAST	CAFE
10.4	.25	.22	.21
15.8	.98	1.0	.80
18.9	2.0	2.23	1.52

The CAFE results are significantly under-predicting the experimental data, and of greater concern the FEAST data, with which good agreement is expected. The discrepancy is due to the way the power profile and the nodalization of both codes are handled. In both cases (FEAST only and CAFE) FEAST is run with 7 axial nodes. This means the power profile can only have 7 different values. COBRA on the other hand has a much finer axial nodalization and has a much smoother power distribution. The two power distributions are shown in Figure 5-4 below. When COBRA passes data to FEAST it takes the average power over the section of the FEAST node. Both distributions conserve the total power of the pin. However a difference still results because of the calculation of the coolant temperatures. CAFE is using COBRA to calculate coolant temperatures, so it employs the smooth power distribution in the sub-channel analysis model. When FEAST is used alone, it uses the discrete power distribution in a simple energy balance model, not accounting for mixing. The difference in these two methods produces a different axial coolant temperature distribution, as shown in Figure 5-5.

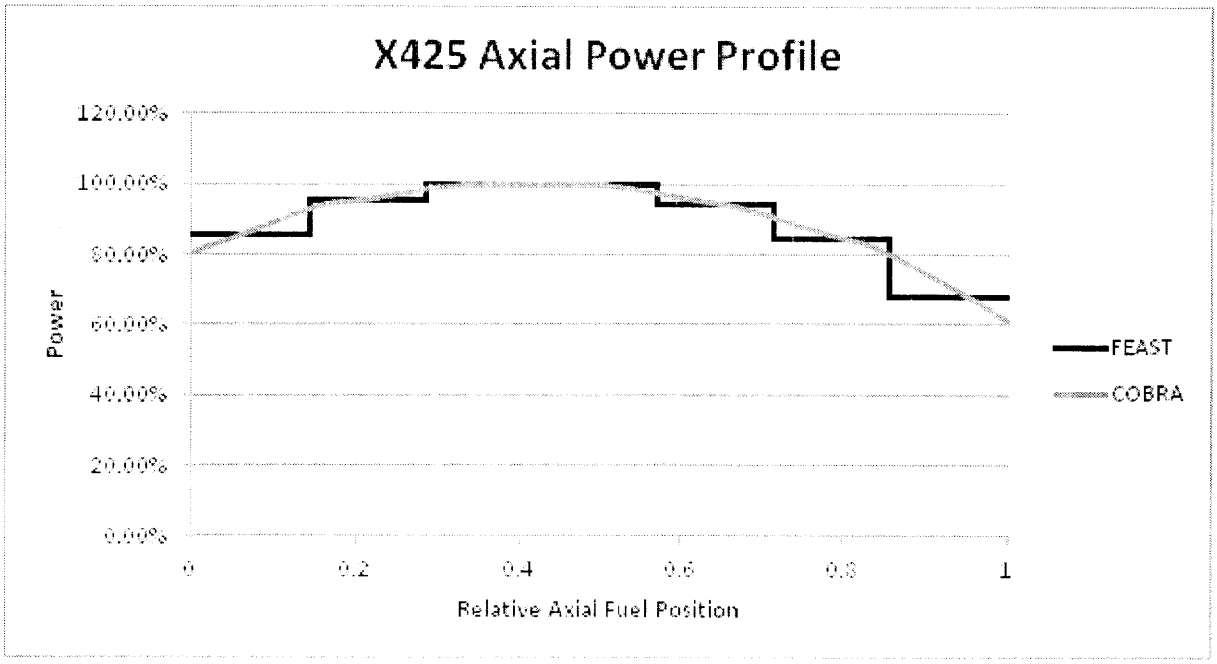

Figure 5-4- Comparison of the axial power profile input between FEAST and COBRA.

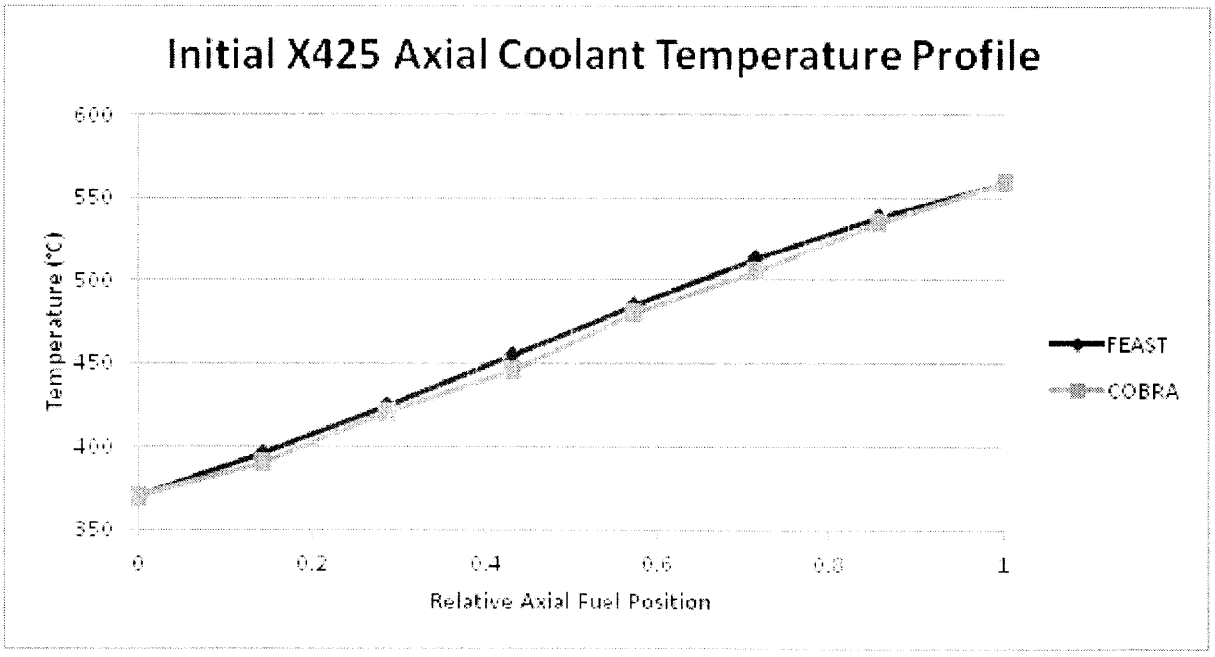

Figure 5-5- Comparison of the axial coolant temperature profile produced by the models in FEAST and COBRA.

The difference in the two distributions is slight, but very important nonetheless. To understand why a change of temperature on the order of 10 °C at the axial mid-plane of the fuel has such an effect on the clad strain the mechanism of the clad strain must be considered. The temperatures at this portion of the clad are low enough that thermal creep strain is negligible, thus irradiation creep strain is responsible for the total strain. The formula for irradiation creep strain rate is (23):

$$\varepsilon = B * \sigma^{1.3} * \varphi \qquad 5\text{-}1$$

Where B is a function of temperature, σ is the equivalent stress, and φ is the flux. The power level is the same for both cases, thus the flux is the same. The form of B is such that a change in temperature on the order of a few degrees will have little effect. That means any difference from creep strain rate must result primarily from the stress on the cladd. A difference in coolant temperature affects both the cladd and coolant temperature. The fuel temperature in this range will have a large effect on the FCMI stress that is placed on the clad because the temperature affects the stiffness of the fuel.

In reality the temperature distribution along the fuel will be continuous, so FEAST is only sampling a certain number of temperatures along the fuel rod, and misses anything that happens between those nodes. In the above example, the clad peak strain is 125% greater (1.0% versus 0.8%) for the FEAST only version than CAFE because the data passed to FEAST in CAFE happens to "miss" a temperature where FCMI is the most important. There are two ways to reconcile this difference. One way would be to force the temperature distribution CAFE passes to FEAST to be equal to the one FEAST calculates. This however would defeat the purpose of using CAFE in the first place. The second way would be to increase the number of axial nodes FEAST uses which will make it less likely that important temperatures are missed. The results of this solution are shown in Table 5-4 below.

Table 5-4- Comparison of peak clad strain data in at. % between the experiment, FEAST only results and CAFE results with two different numbers of axial nodes.

Peak Burnup (at. %)	Experimental data	FEAST	CAFE 7 nodes	CAFE 13 nodes
10.4	.25	.22	.21	.23
15.8	.98	1.0	.80	1.03
18.9	2.0	2.23	1.52	1.80

The results of running CAFE with more FEAST nodes matched up to the previous FEAST data and the experimental data better. For each of the three burnups, the agreement of CAFE is better with both the experimental data and FEAST. The only major discrepancy between FEAST alone and CAFE is the strain at 18.9% burnup. No matter how fine of nodalization is used there may be some differences between FEAST alone and CAFE. This is because even though the clad temperature is continuous along the rod and any specific temperature can be sampled by increasing the nodalization, it does not guarantee that properties like heat transfer coefficient and power will be the same for FEAST and CAFE at that specific location on the pin.

Up until this point only the peak axial clad strain has been considered. Figure 5-6 through Figure 5-8 shows the clad strain as a function of axial position for 15.8% burnup for the various cases considered. Figure 5-6 shows a comparison between the standalone version of FEAST and the data. Figure 5-7 and Figure 5-8 show the CAFE results for 7 and 13 nodes, respectively, against the experimental data. These plots indicate the experimental error with dashed lines. All three cases predict the data with reasonable accuracy. CAFE with 7 nodes matches the shape of the data the best, but under predicts its magnitude. CAFE with 13 nodes predicts the shape of the data well, and predicts the peak extremely well in magnitude and location.

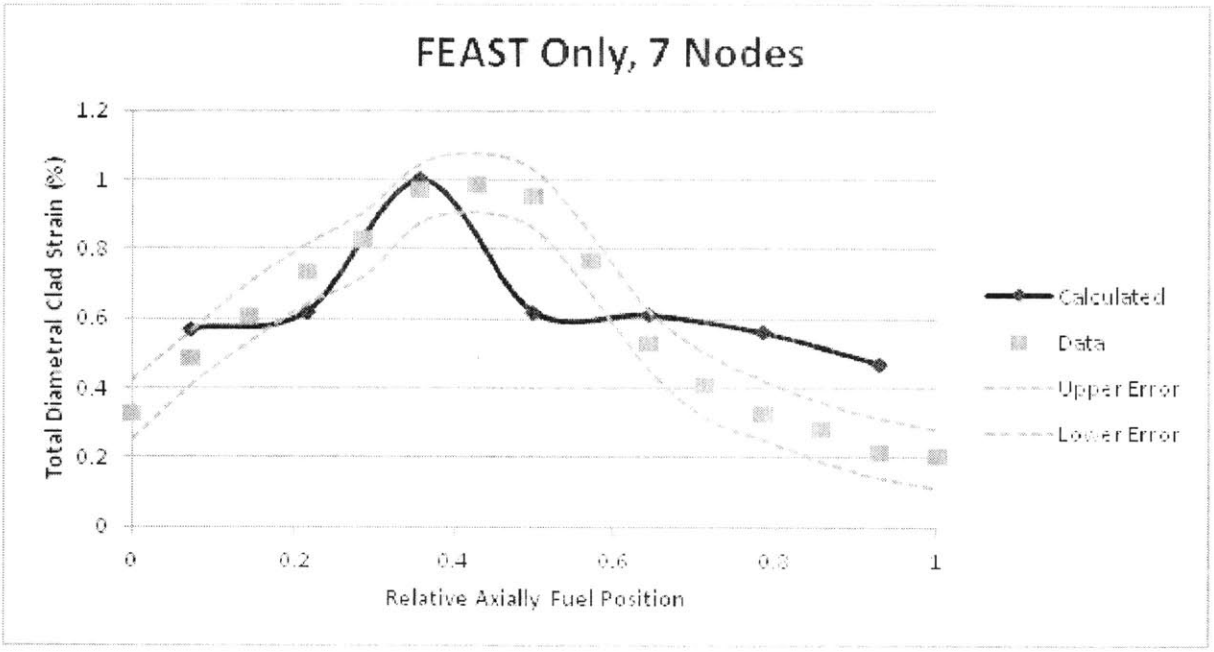

Figure 5-6- Axial clad strain profile produced with FEAST using 7 axial nodes for the EBR-II X425 hot fuel pin (23).

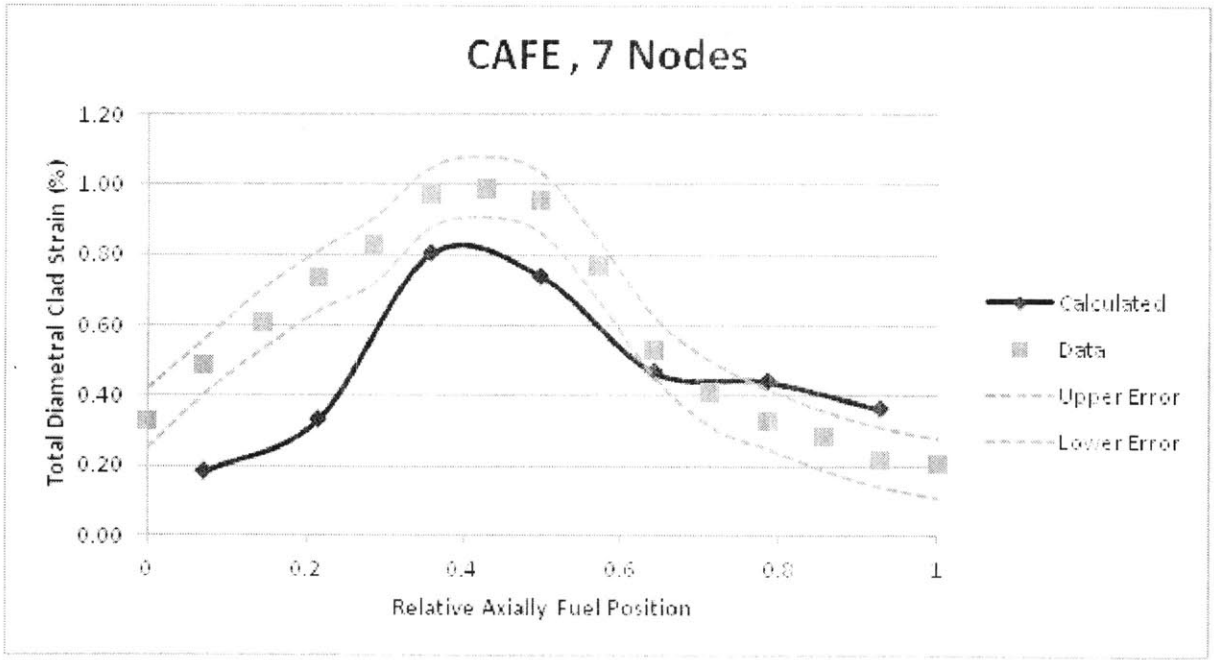

Figure 5-7- Axial clad strain profile produced with CAFE using 7 axial FEAST nodes for the EBR-II X425 hot fuel pin.

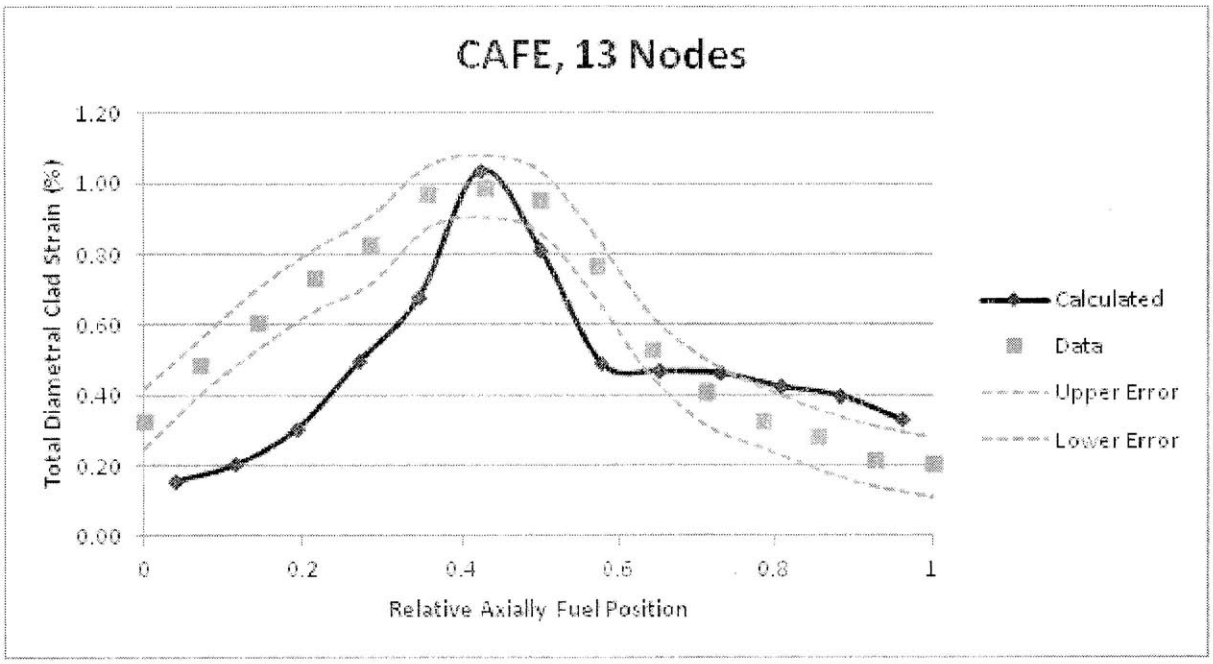

Figure 5-8- Axial clad strain profile produced with CAFE using 13 axial FEAST nodes for the EBR-II X425 hot fuel pin.

Clad strain data was the only set of data specifically available for the X425 assembly. Fuel rods of similar type operated under similar conditions have clad wastage reported that is on the order of 20 microns (72). This compares well with Figure 5-9 which shows peak clad wastage as a function of burnup. Similarly, fission gas release data from the X425 model can be benchmarked against fission gas release data from similar rods with the same fuel composition (73), as shown in Figure 5-10.

For both of these cases the nodalization has little effect on the result. The number of nodes should have the greatest effect on properties that are highly temperature dependent that do not occur at the peak temperature. This will mainly include FCMI and effects that are dependent on it such as irradiation creep strain.

With these benchmarks it is clear that CAFE is predicting fuel behavior with at least the level of accuracy of FEAST. To see further benchmarks of FEAST consult references (23) and (28).

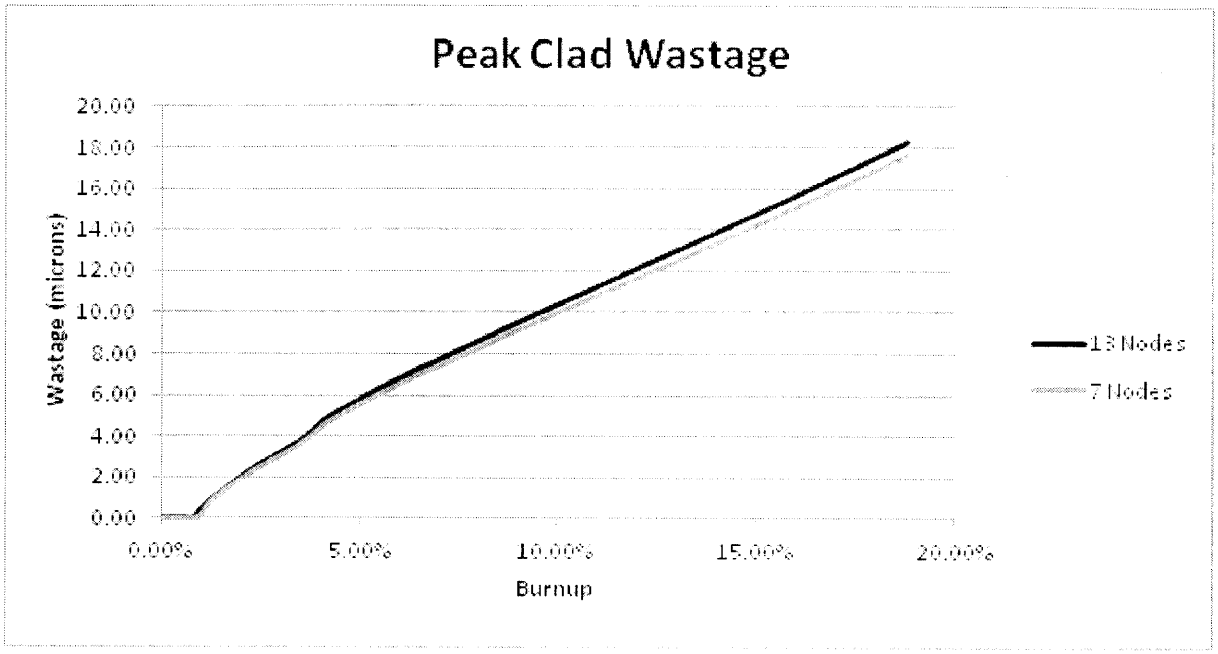

Figure 5-9 – Peak clad wastage history predicted by CAFE.

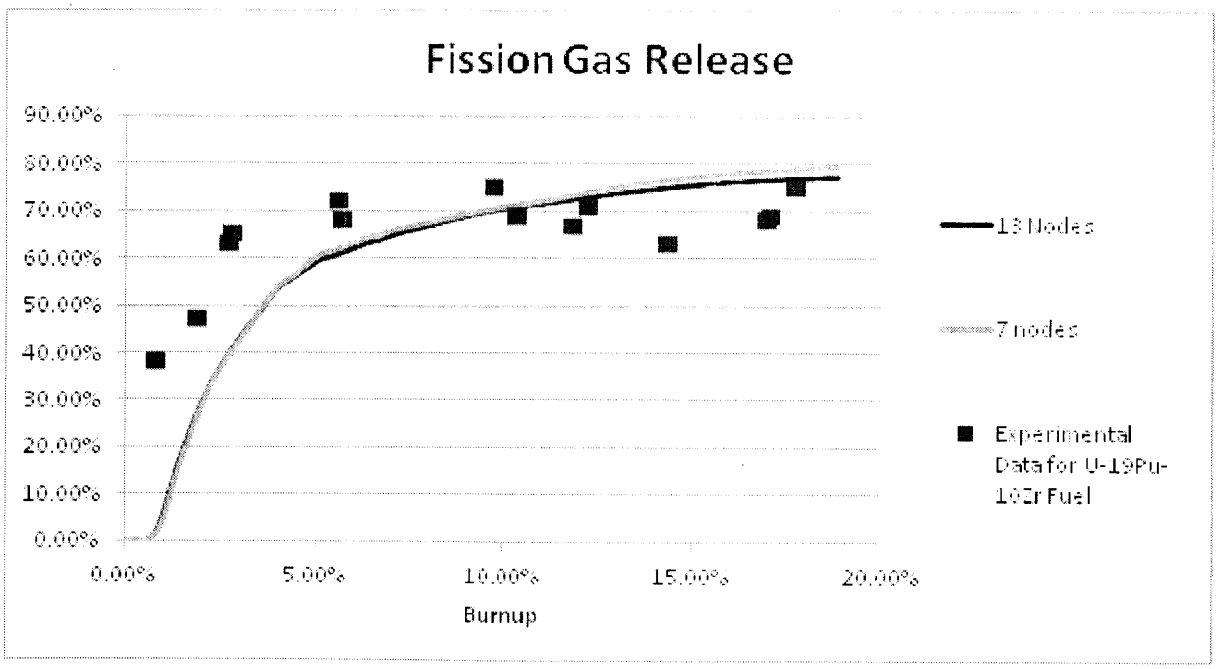

Figure 5-10- Fission gas release history predicted by CAFE.

5.2. CAFE Verification

In light of the results regarding axial nodalization in the previous section, it was deemed important to test the sensitivity of FEAST to axial nodalization and ensure that the solution convergence was achieved as the number of nodes was increased. To examine this, an assembly with geometry and conditions based on the S-PRISM design was employed. The switch in geometry from EBR-II in the previous section to S-PRISM was done because the active fuel length is much longer for the latter design, around a meter for S-PRISM and only a third of that for EBR-II. The CAFE input data for the S-PRISM design is shown below in Table 5-5 and Table 5-6.

Table 5-5- COBRA input data used to model an S-PRISM driver fuel assembly.

	Input Parameter	Sample Assembly
Geometry	Number of Pins	271
	Rod Diameter (mm)	7.44
	Rod Pitch (mm)	8.86
	Wire Wrap Diameter (mm)	1.42
	Wire Wrap Pitch (m)	.203
	Duct inside flat to flat distance (m)	.149
	Total Length (m)	4.070
	Heated Length (m)	1.016
	Lower Unheated Length (m)	1.017
System Conditions	Pressure (atm)	1
	Inlet Temperature (°C)	371
	Inlet Mass Flow (kg/s)	24.09
	Peak Linear Power (kW/m)	19
	Axial Power Distribution (max/avg)	Chopped Cosine 1.41
	Radial Power Distribution	Uniform
Calculation Parameters	Wire Pitch Fraction (δ)	0.1252
	Turbulent Mixing Factor (β)	.01
	Number of Axial Nodes	160

Table 5-6- FEAST input data used to model S-PRISM driver fuel pins.

	Input Parameter	Sample Assembly
Geometry	Clad Outer Radius (mm)	3.72
	Clad Inner Radius (mm)	3.16
	Fuel Outer Radius (mm)	2.74
	Wire Wrap Radius (mm)	0.711
	Plenum to Fuel Ratio	2.0
	Axial Node Length	.145
Fuel Conditions	Zr weight fraction	10
	Pu weight fraction	19
	Initial Fill Gas Pressure (kPa)	84
Calculation Parameters	Time Periods in Rod History	2
	Number of Axial Nodes	varied
	Time Step (seconds)	10
	Flux Conversion Factor	5.0

The number of axial nodes is varied only for FEAST and not for COBRA. The effect of axial nodalization on COBRA was examined previously in Section 2.2.3, with the conclusion that the COBRA nodes should be set as small as allowable by the code (1-2 cm generally), as computational time is not an issue for steady-state runs. FEAST examinations have been previously made on the effect of radial nodalization (23), but none for the axial direction.

Cases were examined for 5, 7, 10, 14, and 20 axial nodes. Table 5-7 shows the corresponding node sizes for each of these nodalizations, along with the peak clad temperature calculated by FEAST.

Table 5-7- Number and size of FEAST nodes compared with the peak clad temperature predicted by FEAST.

Number of Nodes	Node Size (m)	Peak Clad Temperature (°C)
5	0.203	548.66
7	0.145	552.21
10	0.1015	555.79
14	0.0725	557.45
20	0.05075	559.15

A comparison of the performance with different numbers of nodes is shown in Figure 5-11. This figure shows the end of life total clad strain axial profile. The profile is plotted for 14 nodes and 20 nodes, while the data points for 5, 7, and 10 nodes are shown for comparison. As the number of nodes increase the data sets converge on one another. The coarsest nodalization, 5 nodes only, completely misses the behavior at the bottom of the fuel rod where the strain is negative. The finest nodalization of 20 nodes predicts a localized peak in clad strain near the bottom of the rod. While the peak appears completely unphysical it is predicted by FEAST and corresponds to a localized peak in FCMI that FEAST predicts to occur at this point, perhaps due to the increased stiffness of the fuel and higher retention of fission gas due to this location being at the bottom of the rod and having a lower fuel temperature.

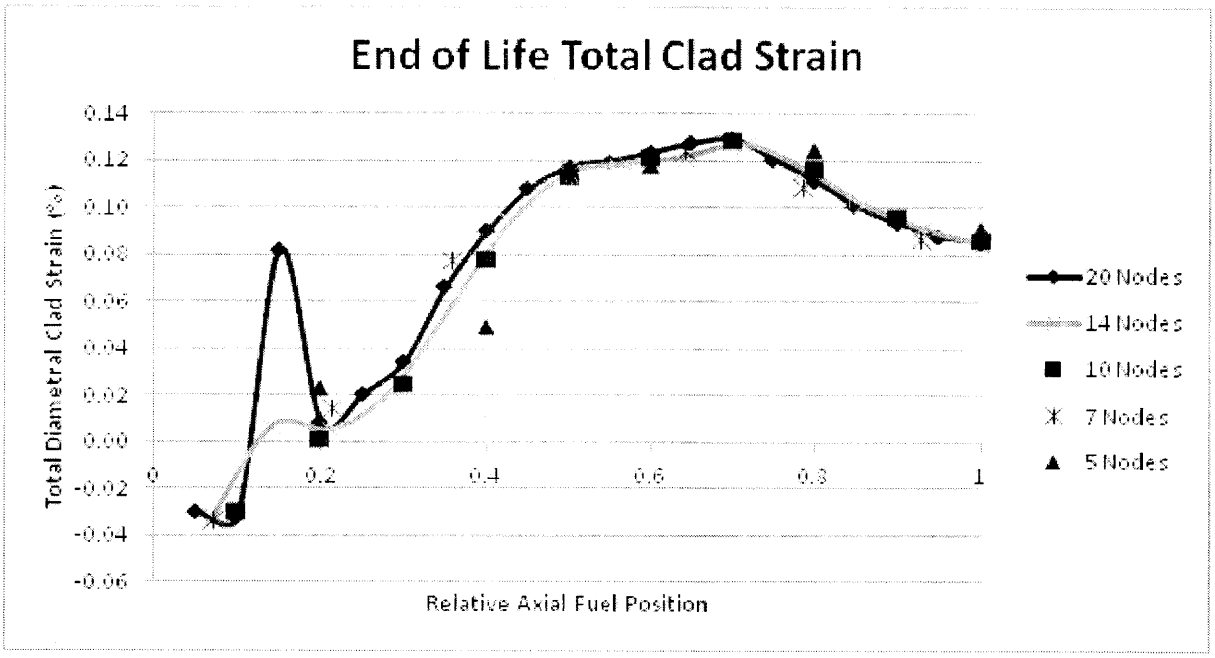

Figure 5-11- Axial clad strain profile predicted by FEAST plotted for various numbers of axial nodes.

For both of these metrics the RMS difference of the data can be calculated and used to determine the order of convergence. The formula for calculating the RMS difference can be found in Section 2.2.3 in Equation 2-15. The RMS formula becomes the absolute value of the

difference for the different nodalizations when applied to peak clad temperature since there is only one value. Figure 5-12 shows a plot of the RMS difference for both clad strain and peak clad temperature plotted against difference in node size.

The order of convergence can be determined by calculating the slope of the lines on Figure 5-12. A linear regression of the log-log plot yields the values calculated in Table 5-8. Peak clad temperature converges with an order of about 1, while total clad strain converges with order of approximately 1.5.

This analysis shows that FEAST converges as expected as the number of axial nodes increases. The exact node size that should be used will depend how valuable low solution error is compared to computational time. 10-15 centimeters is a reasonable limit for node size, as a coarser nodalization could produce peak clad temperature values with greater than 5 °C of error.

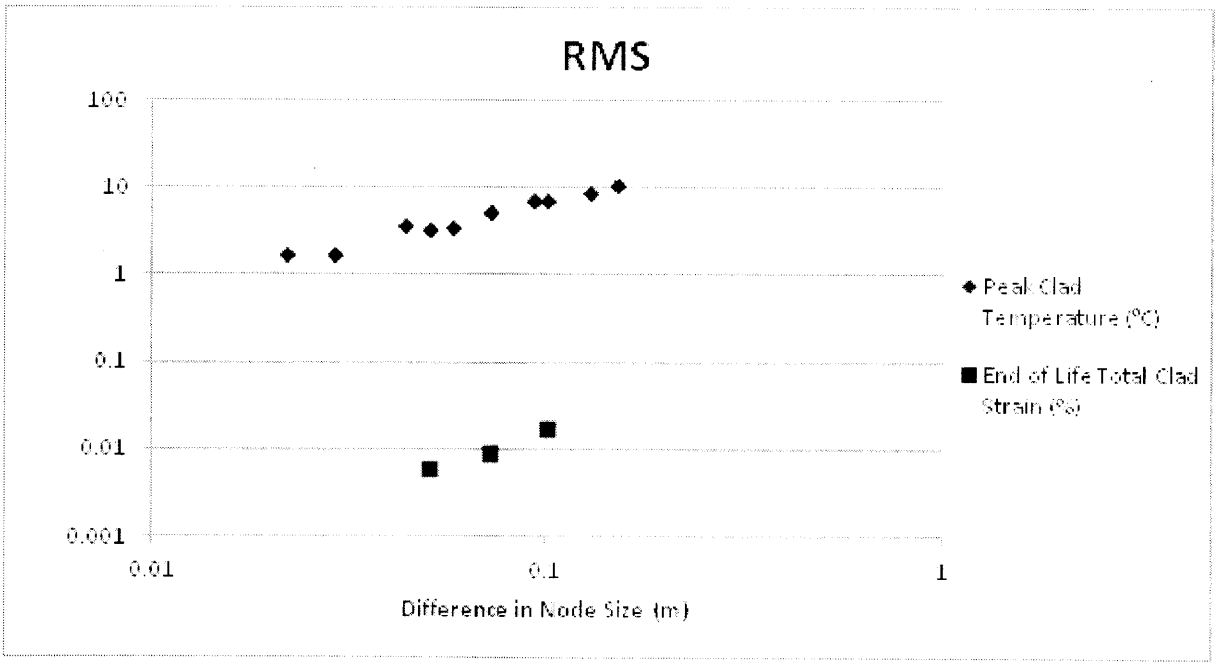

Figure 5-12- RMS difference of node size plotted on a log-log scale for peak clad temperature and end of life clad strain.

Table 5-8- Order of convergence based on node size for two performance metrics.

Performance Metric	Order of Convergence
Peak Clad Temperature	.997
Total Clad Strain	1.539

5.3. Hot Pin Versus Limiting Pin

When running CAFE to evaluate assembly performance, a decision must be made as to which pin or pins should be examined with FEAST. COBRA examines the behavior of the entire assembly; depending on location in the assembly every pin will experience different conditions. While the user would have the option to examine every single pin in the assembly this would prove extremely time consuming computationally due to the nature of FEAST (see the discussion in Section 4.3 regarding examining every pin for geometry changes). Certain pins must be selected that are representative of the assembly, by which the overall fuel performance of the assembly can be judged.

The generally accepted approach when selecting a pin to examine an assembly is to look at the hot pin. The theory is that if the hot pin meets the fuel performance criteria, then every other pin in the assembly will too. To test this practice, the behavior of various pins from a sample assembly was compared to the behavior of the hot pin. The assembly chosen is the EBR-II X425 assembly, which was discussed in Section 5.1.

This assembly is a logical choice for this analysis as the behavior of the hot pin is known to match the experiments well. The CAFE model was used to examine one pin from each ring of the assembly: pins 7, 19, 37, and 61. The results from these pins are then compared to the hot pin, pin 1. All the inputs for this run can be found in Section 5.1. Table 5-1 and Table 5-2 show the COBRA and FEAST input data and Figure 5-1 through Figure 5-3 show the burnup, power, and outlet temperature histories for the assembly. The input set up for this analysis highlights one of the strengths of CAFE: the only alteration from the previous input file used to examine the hot pin of the assembly necessary was to indicate additional fuel pins for examination.

The assembly was initially examined with 7 axial FEAST nodes. This produced some surprising and questionable results. Figure 5-13 shows the peak axial irradiation creep strain results when using 7 axial FEAST nodes.

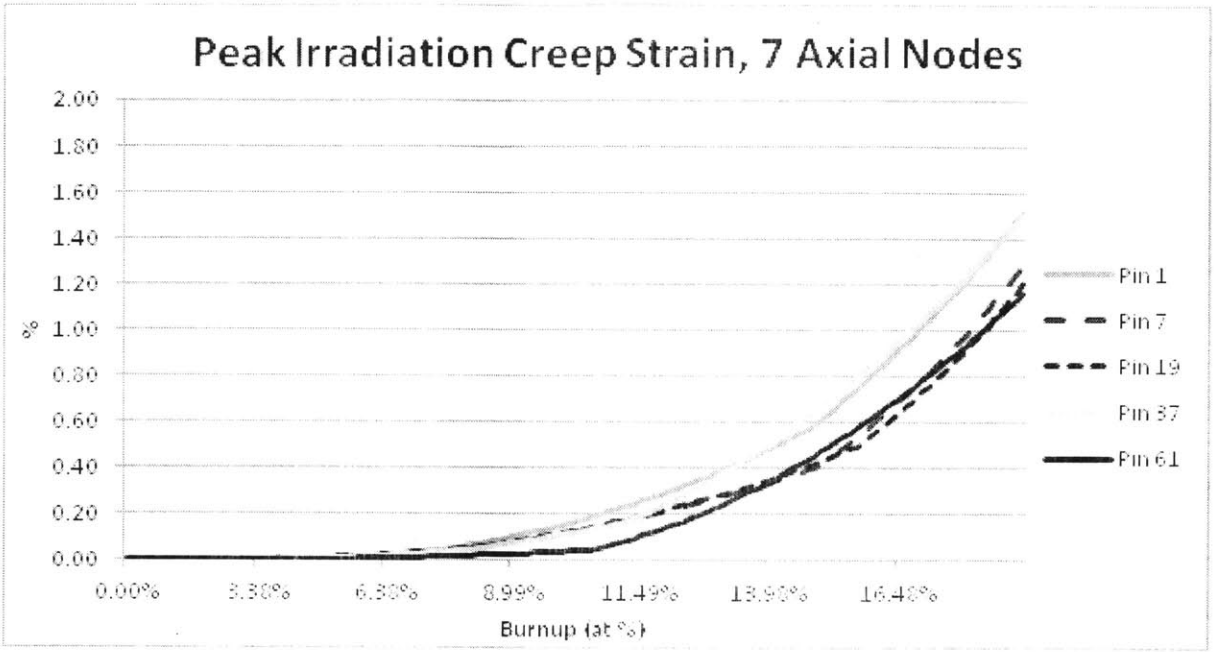

Figure 5-13- Peak irradiation creep strain history predicted by CAFE using 7 axial nodes for 5 different fuel pins for the EBR-II X425 assembly.

Of particular interest is pin 37, which is located near the periphery of the assembly, and thus will be much cooler than the interior pins, as shown in Figure 5-14. With only 7 nodes FEAST calculates that the irradiation creep strain behavior of pin 37 is very similar in magnitude to the hot pin and more severe than other pins more interior to the assembly.

This result prompted further examination of the assembly with more axial nodes to determine if this was an artifact of the calculation or actual behavior that should be expected. Figure 5-15 shows the peak irradiation creep strain for 13 nodes. This shows the more expected behavior where the creep strain is ordered from greatest to least based on how hot each fuel pin is. Table 5-9 shows a comparison of the peak irradiation creep strain for each pin for both 7 and 13 axial FEAST nodes. This data reinforces the conclusions drawn in the previous two sections that too coarse of an axial node length for FEAST will produce incorrect results.

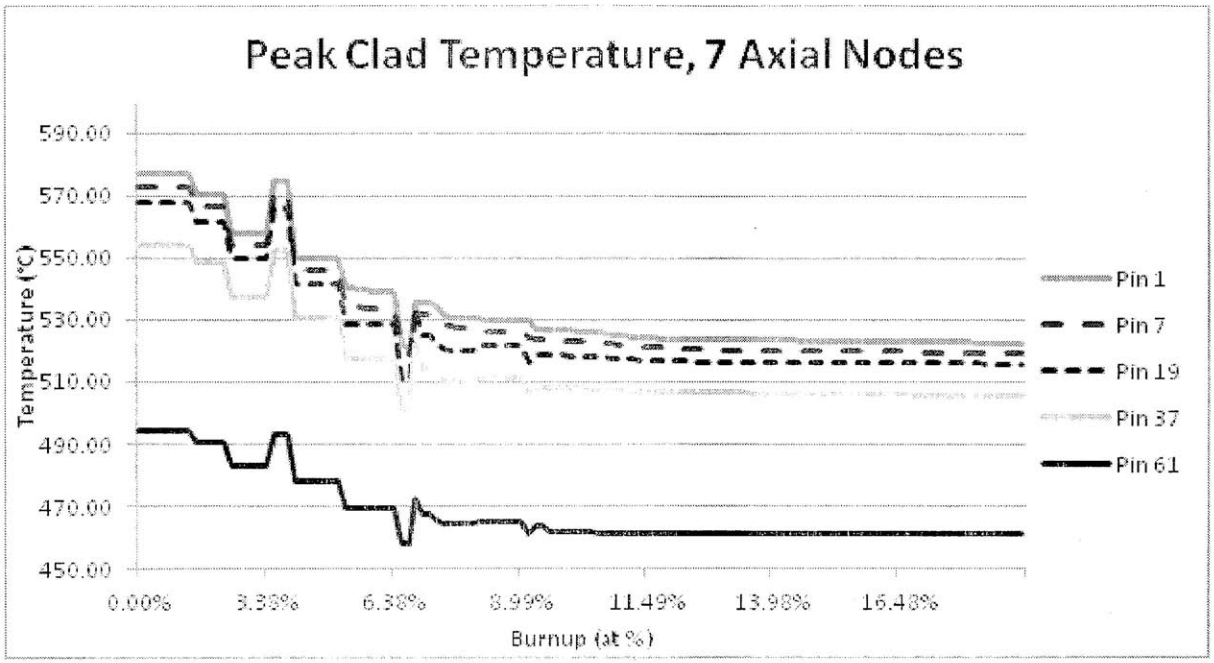

Figure 5-14- Peak clad temperature history predicted by CAFE using 7 axial nodes for 5 different fuel pins for the EBR-II X425 assembly.

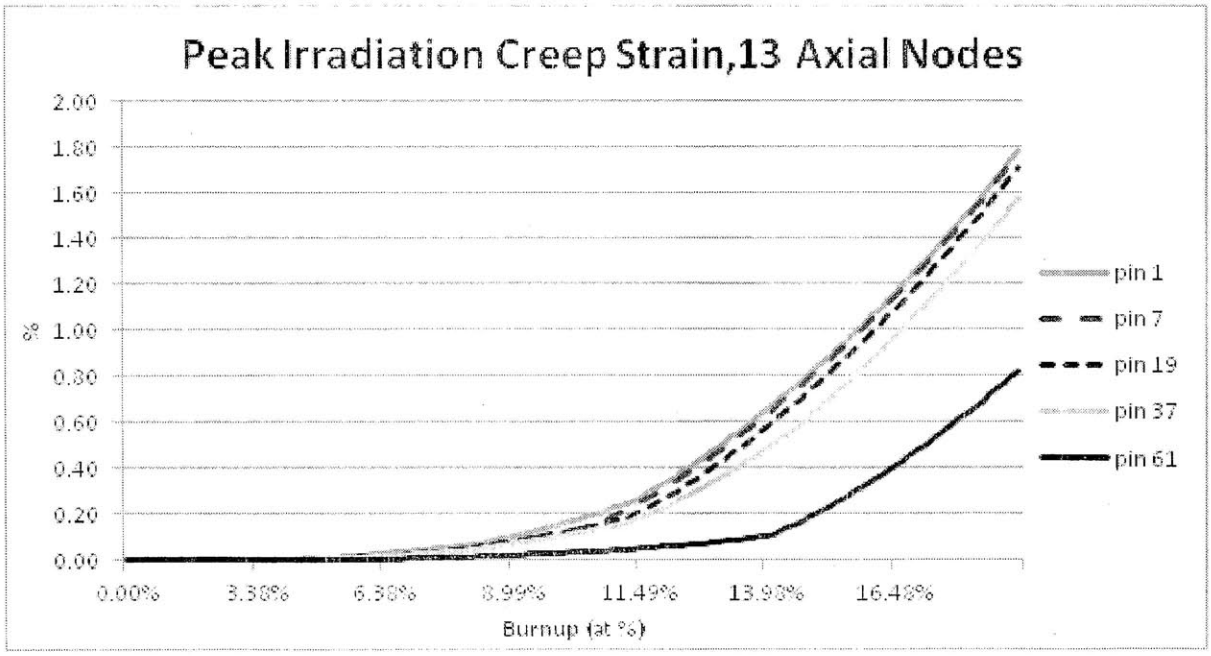

Figure 5-15- Peak irradiation clad strain history predicted by CAFE for EBR-II X425 fuel pins using a finer axial nodalization for FEAST of 13 nodes.

Table 5-9- Comparison of the peak irradiation creep strains predicted by CAFE for EBR-II X425 fuel pins using 7 and 13 axial nodes for FEAST.

	Peak Irradiation Creep Strain	
Pin	7 Nodes	13 Nodes
1	1.52	1.78
7	1.29	1.77
19	1.21	1.71
37	1.51	1.57
61	1.16	0.82

In section 5.1 the formula for determining irradiation creep strain is shown as Equation 5-1. One of the important terms in this equation is stress. The stress on the clad comes from the plenum pressure and the FCMI. The FCMI is a complicated phenomenon, but does not scale based on temperature like many other fuel performance metrics do. Lower fuel temperatures can result in higher FCMI due to higher fuel stiffness. Figure 5-16 shows the peak FCMI-driven stress predicted for each pin over the course of the burnup. At various times the fuel pins from the outer rings experience FCMI-driven stress equal to the stress of the inner pin. However, while the stress is similar, the temperature is lower in the peripheral pins which ultimately results in lower strain rates and strains. For this case all the pins are operated at the same power and are assumed to burn at the same rate, if the power levels and consequently the burnup history were different it would further complicate knowing which pin in the assembly will have the peak FCMI-driven stress.

Figure 5-17 and Figure 5-18 show the peak thermal creep strain and the peak clad wastage, respectively, for each pin examined. The results are as expected where the hotter pins exhibit higher values of strain and wastage. Most fuel performance metrics are indeed most critical for the hot pin, with FCMI being an interesting exception.

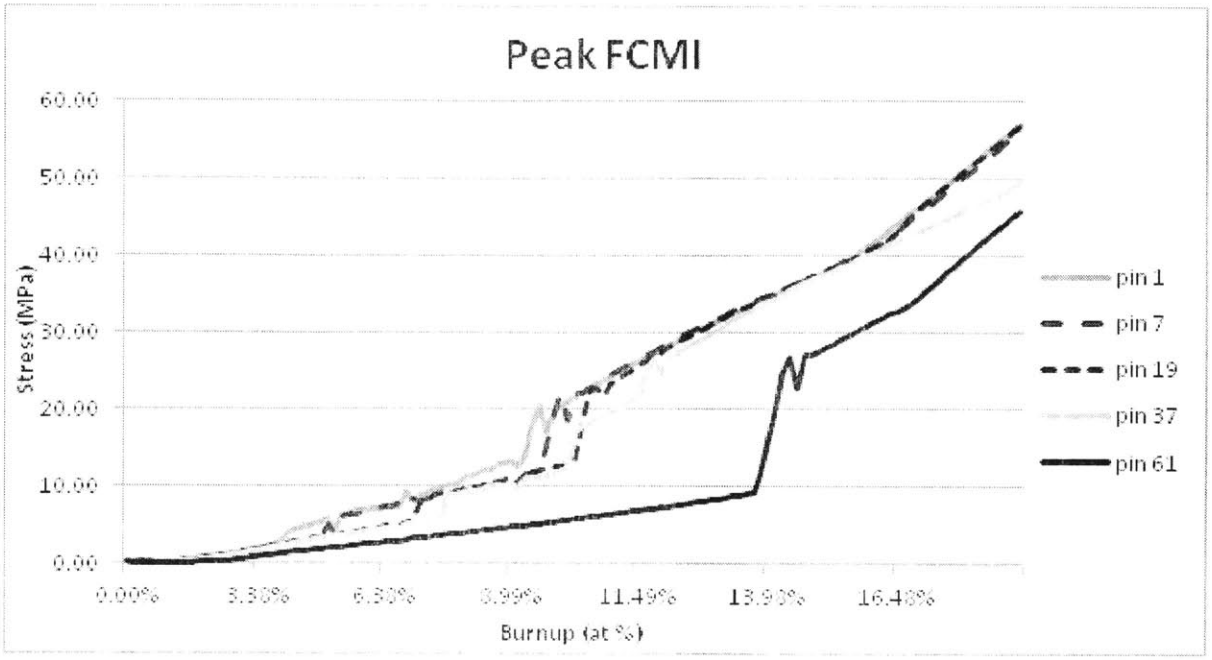

Figure 5-16- Peak FCMI history predicted by CAFE for EBR-II X425.

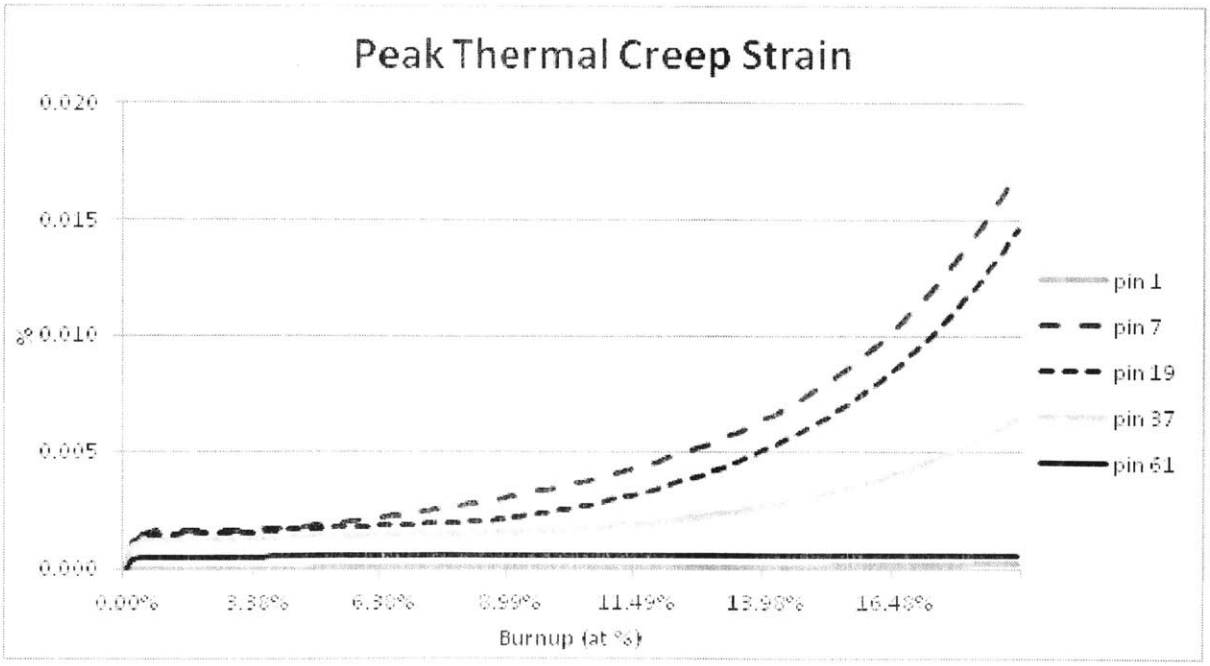

Figure 5-17- Peak thermal creep strain history predicted by CAFE for EBR-II X425.

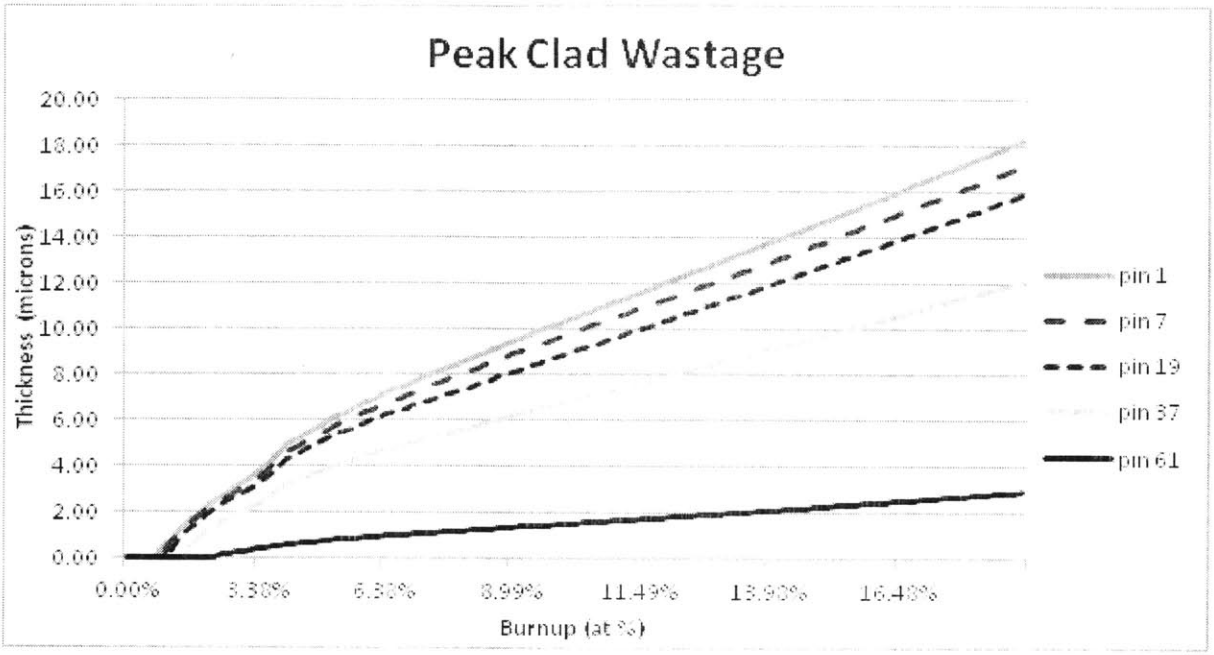

Figure 5-18- Peak clad wastage history predicted by CAFE for EBR-II X425.

5.4. Parametric Study of Fuel Pin Performance

The previous section showed while most fuel performance metrics will be most severe for the hot pin of an assembly, not all of them necessarily have to be. The goal of this section is to examine fuel pins parametrically while varying key geometric parameters and operating conditions to determine the corresponding failure mechanism likely to occur and the expected life of the pin for steady-state operation. The result will be a set of charts that can be used as a design guideline, and to help decide which pins in an assembly to analyze.

The first step was determining which failure (or in some cases limiting) mechanisms be would examined. The important limits considered for a fuel pin are as follows:

- Thermal Creep Strain – Damage caused to the clad by thermal creep.

- Irradiation Creep Strain – Damage caused to the clad by irradiation creep.

- Cumulative Damage Fraction (CDF)– A statistical measure of life of the clad based on time to rupture correlations as a function of temperature and stress. CDF is particularly useful for pins with a variable power history.

- Clad Wastage (FCCI) – Loss of clad thickness at the inner wall due to interaction with the fuel.

There are other failure mechanisms for fuel pins which are not examined here because the purpose of this study is to develop a guide for steady-state operation. For example, fuel melting was not considered because the most conservative fuel melting temperature (lowest solidus T on the phase diagram corresponding to no zirconium) is 920 °C, a temperature which should never occur during steady-state operation (74). CDF and creep strain are different representations of the same damage caused to the clad. Creep strain will be considered primarily over CDF in this study (all of the power histories for the study are constant so both metrics would have similar results.)

Next it was necessary to determine which operational parameters were likely to have the largest effect on each of the chosen fuel performance metrics. While clad type would have a large effect, the study was limited to HT9 as cladding material because it has the most desirable properties.

FCCI is known to exhibit a strong threshold behavior based on clad temperature. Furthermore, it will be affected by the fuel composition. For high plutonium fuels, below 650 °C it has little effect; however, above this temperature the clad becomes susceptible to it (75). Therefore, the important parameters to study for FCCI are peak clad temperature and fuel composition.

Figure 5-19 below shows several data points obtained from FEAST by running a sample pin at a range of coolant inlet temperatures, it exhibits the threshold behavior of FCCI. The sample pins were of a representative S-PRISM driver fuel geometry, which can be found in Table 5-2. The fuel composition is U-19Pu-10Zr. The x-axis of Figure 5-19 shows the peak clad temperature for each run, the y-axis shows the burnup that was achieved for that run. For all

the pins FEAST predicts that below 660 °C the pins will reach burnups of at least 6 at. %, a value determined by the creep strain limit. However, once the peak clad temperature exceeds 660 °C the achievable burnup plummets because of FCCI. Fuel compositions with no Pu exhibit similar behavior, but the threshold temperature is higher because of the lack of Pu raises the eutectic temperature.

While FCCI behavior is fairly straight-forward to study for different conditions, studying clad creep strain is significantly more challenging. Clad creep strain is strongly affected by clad temperature, clad stress, and neutron flux, which in turn depend on the following parameters: linear power (affecting both temperature and neutron flux), smear density and fuel composition (affecting FCMI and thus stress), pin size, and pin diameter-to-clad ratio (affecting stress). These effects were all considered by starting with base pin designs and operating conditions of different types and altering them slightly. Each of the fuel types and the corresponding parametric studies are discussed below.

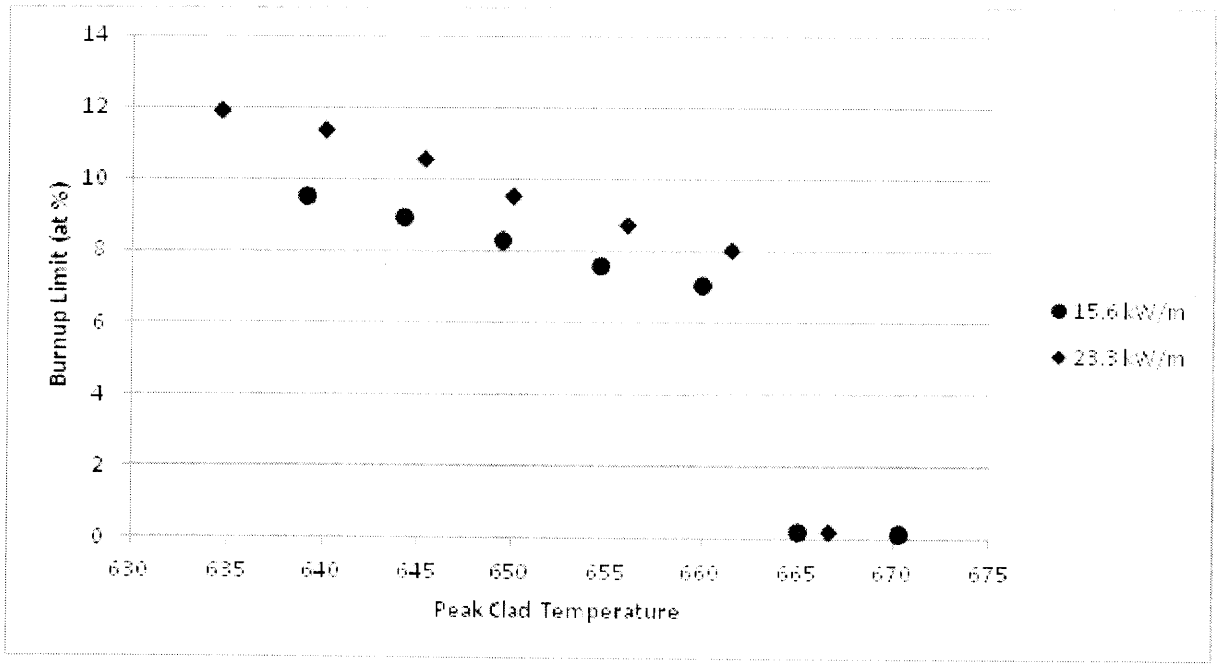

Figure 5-19- Predicted achievable burnup by FEAST versus clad temperature for U-19Pu-10Zr fuel for two different power levels. The sharp drop that occurs between 660 °C and 665 °C occurs because of FCCI.

5.4.1. S-PRISM Driver Fuel

To study typical SFR driver fuel the S-PRISM fuel design was once again selected, the details of which can be found in Table 5-2 in Section 5.1. The operating conditions and geometric parameters that were varied are shown in Table 5-10 below. Two parameters that were not varied are the pin diameter and the plenum to fuel ratio, this was done to keep the assembly geometry the same. Results for different pin diameters and plenum to fuel ratios can be found in Sections 5.4.2 and 5.4.3 for the other assembly geometries examined, blanket fuel and breed and burn fuel.

Table 5-10 – Parameters and different values explored in a parametric study of fuel pin performance.

Parameter	Values
Inlet Temperature	371-531 °C at 20 °C intervals
Power	15, 20, and 25 kW/m
Pu Content	0, 19 at. %
Smear Density	75, 80, and 85%
Clad Thickness (outer pin diameter held constant)	0.477 ,0.559, 0.67 mm

With the large number of parameters varied the study produced a very large amount of data, which is located in Appendix A. An overview of the data is presented in Table 5-11. This table shows a grid of the different combinations examined and what effect FEAST indicated was the most limiting for a range of peak clad temperatures along with what burnup can be expected for those conditions. The parameters in the left columns were study variables that could be set directly in FEAST. While peak clad temperature was a desired variable to examine, it had to be controlled indirectly through power and inlet temperature.

The thermal creep strain limit used for this table was 1%, which is a value used previously in the literature as a design limit (76). The total creep strain is defined as the sum of the irradiation creep strain and the thermal creep strain and the limit for the table is 3%, beyond which pins failure is expected (23)(65). All of the cases with Pu exhibit the behavior discussed

above where FCCI dominates above 665 °C and limits the burnup to almost zero. For cases with no Pu, FEAST predicts FCCI will not limit fuel performance until over 700 °C.

In some cases with lower clad temperatures the limits were never reached over the course of the 20 year run. In these cases the expected failure mechanism reported in Table 5-11 is that which is most significant at the end of the run.

One interesting result from this data is that a higher burnup can be achieved for a given peak clad temperature by using a higher power. This is due to the time-dependent nature of creep strain: the higher burnup occurs over a shorter amount of time and results in less creep strain. Figure 5-20 shows this behavior, for the base fuel having nominal clad thickness, and smear density and plutonium content of 75% and 19%, respectively. At a given clad temperature an increase in power will correspond to an increase in predicted achievable burnup.

Other notable observations from Table 5-11 are that increasing the clad thickness by 20% provides only a slight gain in predicated achievable burnup which diminishes as peak clad temperature rises. Furthermore increasing the smear density significantly limits the performance of the fuel, as expected.

Table 5-11- Overview of the results from the parametric study on fuel pins with the geometry of SPRSIM driver fuel, the full results can be found in Appendix A.

				500 °C PCT		550 °C PCT		600 °C PCT		650 °C PCT		700 °C PCT	
Linear Power	Pu	Clad Thickness	Smear Density	Limit Type	Burnup	Limit Type	Burnup	Limit Type	Burnup	Limit Type	Burnup	Limit Type	Burnup
kW/m	%	mm	%		Atom %		Atom %		Atom %		Atom %		Atom %
15	19	0.56	75	Total Strain	>30	Total Strain	>30	Therm Strain	18.0	Therm Strain	8.5	FCCI	0.1
15	0	0.56	75	Total Strain	>30	Total Strain	>30	Therm Strain	18.0	Therm Strain	8.5	Therm Strain	NA
20	19	0.56	75	Total Strain	>30	Total Strain	>30	Therm Strain	21.0	Therm Strain	9.5	FCCI	0.1
20	0	0.56	75	Total Strain	>30	Total Strain	>30	Therm Strain	21.0	Therm Strain	9.5	Therm Strain	4.5
25	19	0.56	75	Total Strain	>30	Total Strain	>30	Therm Strain	23.5	Therm Strain	11.0	FCCI	0.1
25	0	0.56	75	Total Strain	>30	Total Strain	>30	Therm Strain	23.5	Therm Strain	11.0	Therm Strain	5.0
15	19	0.49	75	Total Strain	>30	Therm Strain	28.5	Therm Strain	15.5	Therm Strain	6.5	FCCI	0.1
15	0	0.49	75	Total Strain	>30	Therm Strain	28.0	Therm Strain	15.0	Therm Strain	7.0	Therm Strain	NA
15	19	0.67	75	Total Strain	>30	Total Strain	>30	Therm Strain	23.0	Therm Strain	10.0	FCCI	0.1
15	0	0.67	75	Total Strain	>30	Total Strain	>30	Therm Strain	23.0	Therm Strain	10.0	Therm Strain	NA

Table 5-11 continued.

				500 °C PCT		550 °C PCT		600 °C PCT		650 °C PCT		700 °C PCT	
Linear Power	Pu	Clad Thickness	Smear Density	Limit Type	Burnup	Limit Type	Burnup	Limit Type	Burnup	Limit Type	Burnup	Limit Type	Burnup
kW/m	%	mm	%		Atom %		Atom %		Atom %		Atom %		Atom %
15	19	0.56	80	CDF	15.0	CDF	19.0	Therm Strain	17.5	Therm Strain	8.0	FCCI	0.1
15	0	0.56	80	CDF	15.0	CDF	17.0	Therm Strain	17.5	Therm Strain	8.0	Therm Strain	NA
15	19	0.56	85	Total Strain	10.5	Total Strain	10.0	Total Strain	9.5	Total Strain	3.5	FCCI	0.1
15	0	0.56	85	Total Strain	11.0	Total Strain	10.0	Total Strain	11.0	Total Strain	7.5	Therm Strain	NA

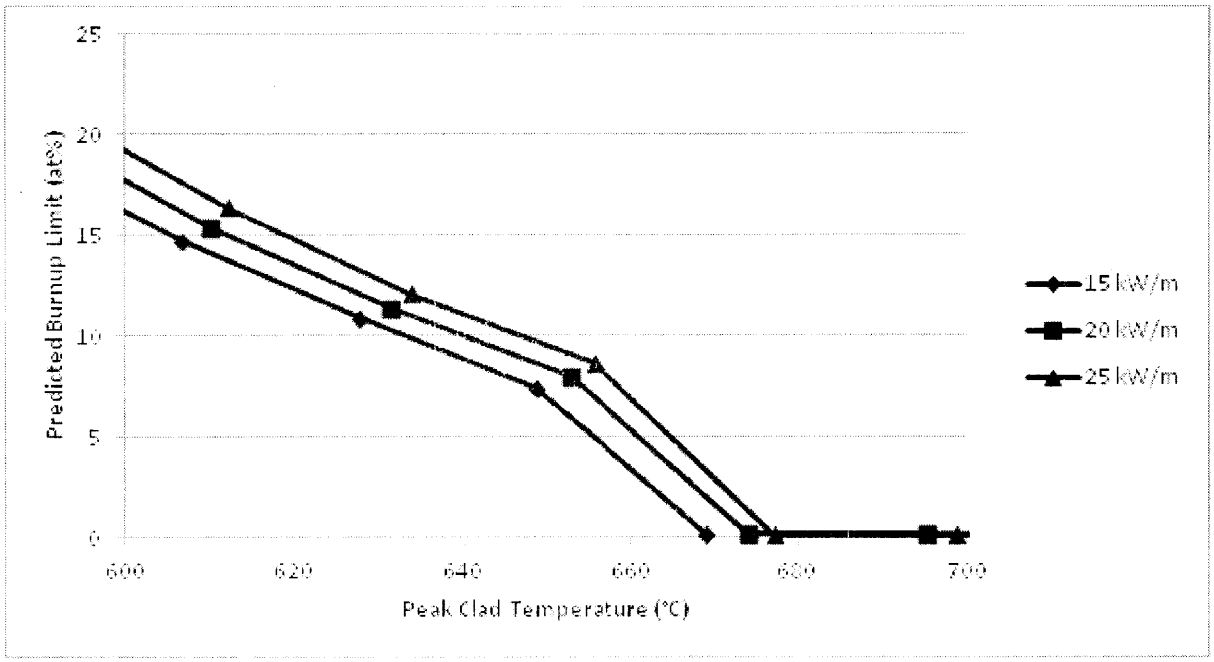

Figure 5-20- The FEAST predicted burnup limit for a fuel pin at three different power levels. As the power level increase the predicted burnup also increases for a constant clad temperature.

5.4.2. S-PRISM Radial Blanket

The second geometry examined parametrically also comes from the S-PRISM design: the radial blanket. The blanket pins have a significantly increased diameter and tighter pitch with respect to the driver fuel. The pin geometry is detailed in Table 5-12. Smear density and clad thickness are not varied for this case; the only parameters varied are plutonium content (0, 19 at%), power (10, 15 kW/m) and inlet temperature (same range as Table 5-10). Pu would not traditionally go into a blanket region, it is considered here as the interest is for theoretical pins of the given geometry. The full results are given in Appendix A and an overview of the data can be found in Table 5-13. The FEAST runs were again 20 years for this fuel, but due to the much lower volumetric power rate the pins had much lower burnups at the end of life. Once again FEAST predicts that increasing the linear power will allow for a higher achievable burnup for a given peak clad temperature.

Table 5-12- FEAST input data used to model S-PRISM blanket pins.

	Input Parameter	Sample Assembly
Geometry	Clad Outer Radius (mm)	6.005
	Clad Inner Radius (mm)	5.446
	Fuel Outer Radius (mm)	5.023
	Wire Wrap Radius (mm)	0.47
	Plenum to Fuel Ratio	1.2
	Axial Node Length	.145
Fuel Conditions	Zr weight fraction	10
	Pu weight fraction	0
	Initial Fill Gas Pressure (kPa)	84
Calculation Parameters	Time Periods in Rod History	2
	Number of Axial Nodes	7
	Time Step (seconds)	10
	Flux Conversion Factor	5.0

Table 5-13- Overview of the results from the parametric study on fuel pins with the geometry of S-PRISM blanket, the full results can be found in Appendix A.

				500 °C PCT		550 °C PCT		600 °C PCT		650 °C PCT	
Linear Power	Pu	Clad Thickness	Smear Density	Limit Type	Burnup	Limit Type	Burnup	Limit Type	Burnup	Limit Type	Burnup
kW/m	%	mm	%	Atom %		Atom %		Atom %		Atom %	
10	19	0.56	70	Total Strain	>10	Total Strain	>10	Therm Strain	4.5	NA	
10	0	0.56	70	Total Strain	>10	Total Strain	>10	Therm Strain	5.0	NA	
15	19	0.56	70	Total Strain	>10	Total Strain	>10	Therm Strain	5.5	Therm Strain	2.0
15	0	0.56	70	Total Strain	>10	Total Strain	>10	Therm Strain	6.0	Therm Strain	1.5

5.4.3. Tight Pitch Breed and Burn Fuel

The final geometry examined parametrically is breed and burn fuel that has a very tight pitch. The pin geometry is detailed in Figure 5-14. The variables examined for this fuel are power (10, 15, 20, and 25 kW/m) and fuel venting. Vented fuel pins are not sealed so do not build up plenum pressure due to fission gas. For the purposes of this simulation the pressure in the pins vents at 500 kPa so the plenum pressure will always be below 500 kPa. Also of note this pin type has a low smear density of only 63%. The FEAST runs were for 40 years for this fuel because the venting allows for a longer life and because it takes appreciable time to breed enough plutonium in blanket assemblies before the blanket becomes the driver.

The full results are given in Appendix A, an overview of the data can be found in Table 5-13. Not surprisingly, the vented pins could achieve significantly higher burnups than the unvented pins. In some cases, at lower peak clad temperatures, it was impossible to predict what the eventual failure mechanism would be because FEAST predicted so little damage to the clad at high burnup (20-30 at. %). For these cases a question mark is entered for the failure mechanism in Table 5-15. As was observed for previous geometries, in all cases for the breed and burn pins higher power allowed for a higher achievable burnup.

Table 5-14- FEAST input data used to model breed and burn fuel pins.

	Input Parameter	Sample Assembly
Geometry	Clad Outer Radius (mm)	5.22
	Clad Inner Radius (mm)	4.72
	Fuel Outer Radius (mm)	3.747
	Wire Wrap Radius (mm)	0.711
	Plenum to Fuel Ratio	0.72
	Axial Node Length	.125
Fuel Conditions	Zr weight fraction	5
	Pu weight fraction	0
	Initial Fill Gas Pressure (kPa)	84
Calculation Parameters	Time Periods in Rod History	2
	Number of Axial Nodes	20
	Time Step (seconds)	10
	Flux Conversion Factor	5.0

Table 5-15- Overview of the results from the parametric study on breed and burn fuel pins. Fuel Pin venting means the plenum pressure of the pin is vented so the pressure does not exceed 500 kPa.

				500 °C PCT		550 °C PCT		600 °C PCT		650 °C PCT		700 °C PCT	
Linear Power	Pu	Fuel Pin Venting	Smear Density	Limit Type	Burnup	Limit Type	Burnup	Limit Type	Burnup	Limit Type	Burnup	Limit Type	Burnup
kW/m	%		%		Atom %		Atom %		Atom %		Atom %		Atom %
10	0	No	63	Total Strain	>30	Therm Strain	17.0	Therm Strain	7.5	Therm Strain	3.0		
10	0	Yes	63	?	>30	?	>30	Therm Strain	20.5	Therm Strain	10.0		
15	0	No	63			Therm Strain	20.0	Therm Strain	10.0	Therm Strain	3.5	Therm Strain	2.0
15	0	Yes	63			Therm Strain	>30	Therm Strain	25.5	Therm Strain	11.0	Therm Strain	4.5
20	0	No	63			Therm Strain	22.0	Therm Strain	10.5	Therm Strain	4.5	Therm Strain	2.0
20	0	Yes	63			Therm Strain	>30	Therm Strain	27.5	Therm Strain	12.5	Therm Strain	6.0
25	0	No	63					Therm Strain	11.0	Therm Strain	4.5	Therm Strain	2.0
25	0	Yes	63					Therm Strain	29.0	Therm Strain	15.0	Therm Strain	6.0

Chapter 6. Conclusions

6.1. Conclusions

The major conclusions and takeaways from this thesis are listed below. The key original contributions are items 2, 4, and 7.

1) COBRA-IV-I-MIT is an updated version of COBRA that contains several new correlations for pressure drop, mixing and heat transfer. It was benchmarked with the available experimental data consistently producing less than 5% error. This compared favorably to the experimental uncertainty from the benchmarks, which, while hard to quantify, was similar in magnitude.

2) Azimuthal symmetry was an acceptable assumption for fuel performance models in regards to added clad stress. Finite element analysis with supporting hand calculations showed the added stress generated by limiting axial peaking functions is very low (~1%) and should not contribute significantly to creep strain. Clad temperature peaking can be caused by azimuthal effects however, affecting the creep in the clad. To account for this FEAST was modified to calculate clad creep performance metrics at an additional peak temperature if desired.

3) Under the assumptions used clad strains of up to 3% will not cause geometry changes that have a significant effect on the assembly thermal hydraulic behavior. Furthermore, there was no way to generate an accurate three-dimensional geometric evolution of the assembly with the available codes. Therefore, it was not necessary to model the deformed assembly geometry in COBRA, which makes one-way coupling between COBRA and FEAST acceptable. However, the deformed assembly geometry can still be modeled in COBRA if an accurate description of the behavior is available.

4) CAFE is a coupled thermal hydraulic fuel performance model that uses COBRA-IV-I-MIT and FEAST to predict assembly behavior. It was written in the Python language. It operates with a single input file and handles all the interaction with COBRA and FEAST.

5) No good sets of data were available for benchmarking a full fuel assembly performance code such as CAFE. COBRA and FEAST were each benchmarked independently and proved accurate. CAFE was compared to FEAST benchmarks and good agreement was established.

6) Using CAFE, a limitation on the FEAST node size was identified. Using FEAST node sizes greater than 10-15 cm can lead to very inaccurate results. CAFE was verified to ensure that solution convergence is achieved as the node size is reduced.

7) Having the ability to examine every fuel pin in an assembly design raised the question of which fuel pins should be looked at when resources are limited. A parametric study of fuel pin behavior was conducted with FEAST to determine expected failure mechanisms and achievable burnups for different pin geometries, and how the failure mechanism and burnups vary with parameters like peak clad temperature, power, and plutonium content. These results are useful in the preliminary design of SFR fuel rods and assemblies.

6.2. Future Work

Future work for this project would include any updates or improvements to COBRA or FEAST and further application and benchmarking of CAFE. Specific suggestions for future work are listed below:

1) The use of CFD to improve the correlations used in COBRA. COBRA-IV-I-MIT uses the most recent correlations found in the literature, however some of these correlations are 20-30 years old. The correlations are all based on the same data sets that are used to benchmark the code so it is no surprise that good agreement is found between the code and the limited experimental data. Short of conducting new experiments, CFD may be the best way to generate data to develop higher-fidelity correlations. CFD could be particularly useful to produce correlations for fringe regions where little experimental data exists, such as extremely tight fuel pitches (P/D<1.1).

2) Changing FEAST to allow for finer axial nodalization. The current limit in FEAST is 20 axial nodes. While this allows fine enough node sizes for fuel rods of 1-2 meters long, longer fuel lengths and very detailed examination are problematic.

3) Development of FEAST to allow for data input and output during a run or to allow for restart files. One of the limitations to two-way information passing is the computationally intensive nature of FEAST. Currently, FEAST requires all input data at the start of a run, meaning that for coupling it must be run to completion before COBRA can be updated and generate data for the new geometries produced. If FEAST could be paused or restarted, input and output data could be processed during a run, so that long FEAST runs could be broken down in to short segments of months or years in between which COBRA could be update and run.

4) Development of a three-dimensional mechanical analysis code to examine the interaction between the pin swelling, the wire wraps and the duct wall. Further considerations to examine for the duct wall would be dilation due to pressure difference and irradiation damage. A three-dimensional fuel performance model would be necessary for this analysis. Such a code would provide valuable insight into the swelling behavior of an SFR assembly with time.

5) Extension of FEAST into three dimensions. This is closely tied to the previous item, as a three-dimensional fuel rod model would likely be needed for such an analysis code. To accurately pass coolant information to a three-dimensional code a better implementation of azimuthal hot spot factor with correlations would be needed.

6) Further benchmarking on more complete sets of assembly performance data for CAFE. This item is limited to the lack of available data, but should fuel performance data become available for a full assembly with multiple pins a good benchmark for CAFE could be completed.

7) Application of CAFE to assembly design. Now that the tool has been developed and tested it can be used to test new assembly designs!

References

1. Deutch, John M., et al. *Update to the MIT 2003 Future of Nuclear Power.* Cambridge: Massachusetts Institute of Technology, 2009.

2. *A Technology Roadmap for Generation IV Nuclear Energy System: Ten Nations Preparing Today for Tomorrow's Energy Needs.* U.S. DOE Nuclear Energy Research Advisory Committee and the Generation IV International Forum, 2002.

3. Boardman, Charles E., Allen E. Dubberley, Douglas G. Carroll, Marvin Hui, Alan W. Fanning, and Walter Kwant. "A Description of the S-PIRSM Plant." *Proceedings of ICONE 8.* Baltimore, MD: ASME, 2000.

4. Dubberley, A. E., Yoshida, K., C. E. Boardman, and T. Wu. "SuperPRISM Oxide and Metal Fuel Core Designs." *Proceedings of ICONE 8.* Baltimore, MD: ASME, 2000.

5. Dubberley, Allen E., and Marvin Hui. "Optimizing the Size of the Super-PRISM Reactor." *Proceedings of ICONE 8.* Baltimore, MD: ASME, 2000.

6. Dubberley, A. E. "S-PRISM High Burnup Metal-Fuel Core Design." *Proceedings of ICAPP '03.* Cordoba, Spain: ICAPP, 2003.

7. Ellis, Tyler, et al. "Traveling-Wave Reactors: A Truly Sustainable and Full-Scale Resource for Global Energy Needs." *International Congress on Advances in Nuclear Power Plants 2010, ICAPP 2010.* San Diego, CA: American Nuclear Society, 2010. 546-558.

8. Ellis, T., R. Petroski, P. Hejzlar, and G. Zimmerman. "Traveling Wave: a Fast Reactor Fuel Cycle without Reprocessing." *Modern Power Systems* (Wilmington Publishing Ltd.) 31, no. 4 (2011): 39-41.

9. Hejzlar, Pavel. "Traveling Wave Reactor: Technology Development and Deployment." Karlsruhe, Germany, 2011.

10. International Atomic Energy Agency. *Fast Reactor Database Home.* 2006. http://www.iaea.org/inisnkm/nkm/aws/frdb/index.html# (accessed 2012).

11. Perry, W. H., and E. A. Clifton. "Eighteen Years of Operation with a Sodium-Cooled Reactor: EBR-II." *Transactions of the American Nuclear Society.* Scottsdale, AZ: American Nuclear Society, 1983. 40-41.

12. Newland, D. J., and J. J. Krupar. "Fast Flux Test Facility Operational Experience." *American Society of Mechanical Engineers (Paper).* Toronto, Ca: AMSE, 1984.

13. Mi, Xu. "Entering a New Era [China Experimental Fast Reactor Project]." *Nuclear Engineering International* (Wilmington Publishing Ltd.) 54, no. 665 (2009): 18-19.

14. Guidez, J., L. Martin, and C. Courtois. "Status of Phenix Operation and of Sodium Fast Reactors in the World." *International Congress on Advances in Nuclear Power Plants - ICAPP 2007.* Nice, France, 2007. 1991-1996.

15. Vendryes, G. A. "Superphenix- A Full-Scale Breeder Reactor." *Scientific American* 124, no. 22 (1977): 26-35.

16. Raj, Baldev. "Status of Sodiuim Cooled Fast Reactors with Closed Fuel Cycle in India." *International Congress on Advances in Nuclear Power Plants - ICAPP 2007.* Nice, France, 2007. 3251-3260.

17. Cheta, S. C., et al. "Current Status of Fast Reactors and Future Plans in India." *Asian Nuclear Prospects 2010, ANUP 2010.* Mamallapuram, India: Elsevier Ltd, 2010. 64-73.

18. Sakata, H. "Construction and Function Tests of Experimental Fast Reactor 'JOYO'." *Journal of the Atomic Energy Society of Japan* (Atomic Energy Society of Japan) 19, no. 10 (1977): 680-694.

19. Takenouchi, K. "Construction and Development of the Monju FBR." *Nuclear Europe* (Nuclear Europe) 9, no. 11-12 (1989): 24-25.

20. Korol'kov, A. S., G. I. Gadzhiev., V. N. Efimov, and V. N. Marashev. "Experience in Operating the BOR-60 Reactor." *Atomic Energy* (Kluwer Academic/Consultants Bureau) 91, no. 5 (2001): 907-912.

21. Oshkanov, N. N., et al. "30 Years of Experience in Operating the BN-600 Sodium-Cooled Fast Reactor." *Atomic Energy* (Kluwer/Plenum Publishers) 108, no. 4 (2010): 234-239.

22. Tang, Y. S., Jr., R. D. Coffield, and R. A. Markley. *Thermal Analysis of Liquid Metal Fast Breeder Reactors.* La Grange Park, IL: American Nuclear Society, 1978.

23. Karahan, Aydin. *Modeling of Thermo-Mechanical and Irradiation Behavior of Metallic and Oxide Fuels for Sodium Fast Reactors.* PhD Thesis, Cambridge, MA: Massachusetts Institute of Technology, 2009.

24. Lawson, A. C., et al. "Structure of the ζ-Phase Plutonium-Uranium." *Acta Crystallographica, Section B (Structural Science)* (Acta Crystallographica) B52, no. 1 (1996): 32-37.

25. Todreas, Neil E., and Mujid S. Kazimi. *Nuclear Systems I: Thermal Hydraulic Fundamentals.* New York: Taylor & Francis Group, 1990.

26. Todreas, Neil E., and Mujid S. Kazimi.. *Nuclear Systems II: Elements of Thermal Hydraulic Design.* New York: Hemisphere Publishing Corporation, 1990.

27. Fanning, T. H., W. D. Pointer, and J. W. Thomas. "Multi-Resolution Modeling of Subassembly Pin Bundles for Advanced Fast Reactor Safety Simulations." *International Conference on Mathematics, Computational Methods & Reactor Physics (M&C 2009).* Saratoga Springs, NY: American Nuclear Society, 2009.

28. Karahan, A., and J. Boungiorno. "A New Code for Predicting the Thermo-Mechanical and Irradiation Behavior of Metallic Fuels in Sodium Fast Feactors." *Journal of Nuclear Materials* (Elsevier Science B. V.) 396, no. 2-3 (2010): 283-293.

29. Karahan, A., J. Buongiorno, and M. S. Kazimi. "Development of a New Irradiation Performance Code for Metal Fuels." *Transactions of the American Nuclear Society.* Anaheim, CA: American Nuclear Society, 2008. 1033-1034.

30. Ohsima, H., H. Narita, and H. Ninokata. "Analysis of Thermal-Hydraulic Behavior in a Fast Reactor Fuel Subassembly with Porous Blockages." *Proceedings of the International Topical Meeting on Advanced Reactors Safety.* Orlando, FL: American Nuclear Society, 1997. 1157-1164.

31. Wheeler, C. L., C. W. Stewart, R. J. Cena, D. S. Rowe, and A. M. Sutey. "COBRA-IV-I: An Interim Version of COBRA for Thermal-Hydraulic Analysis of Rod Bundle Nuclear Fuel Elements and Cores." BNWL-1962, 1976.

32. Stewart, C. W., C. L. Wheeler, R. J. Cena, C. A. McMonagle, J. M. Cuta, and D. S. Trent. "COBRA-IV: The Model and the Method." BNWL-2214, 1977.

33. Stewart, C. W., et al. "Core Thermal Model: COBRA-IV Development and Applications." BNWL-2212, 1977.

34. Kim, Won-Seok, Young-Gyun Kim, and Young-Jin Kim. "A Subchannel Analysis Code MATRA-LMR for Wire Wrapped LMR Subassembly." *Annals of Nuclear Energy* (Elsevier Science Ltd.) 29 (2001): 303-321.

35. Memmott, Matthew J. *Thermal-Hydraulic Analysis of Innovative Fuel Configurations for the Sodium Fast Reactor.* Ph.D. Thesis, Cambridge, MA: Massachusetts Institute of Technology, 2005.

36. MacDougall, J., and J. Lillington. "The SABRE Code for Fuel Rod Cluster Thermohydraulics." *Nuclear Engineering and Design* 82 (1984): 171-190.

37. Yang, Sik Yang. "An LMR Core Thermal-Hydraulics Code Based on the ENERGY Model." *Journal of the Korean Nuclear Society* (Korean Nuclear Society) 29, no. 5 (1977): Korean Nuclear Society.

38. Khan, E. U., W. M. Rohsenow, A. A. Sonin, and N. E. Todreas. "A Porous Body Model for Prediciting Tempertature Distribution in Wire-Wrapped Fuel Rod Assemblies." *Nuclear Engineering and Design* 35, no. 1 (1975): 1-12.

39. Stewart, C. W. "VIPRE01: Thermal Hydraulic Code for Reactor." EPRI NP-2511-CCM-A, 1983.

40. Fontana, M. H., R. E. MacPherson, P. A. Gnadt, and L. F. Parsly. "Temperature Distribution in the Duct Wall and at the Exit of a 19-rod Simulated LMFBR Fuel Assembly (FFM Budle 2A)." *Nuclear Technology* 24 (1974): 176-200.

41. Wantland, J. L., P. P. Gnadt, R. E. MacPherson, M. H. Fontana, H. Hanus, and C. M. Smith. "The Effects of Duct Configuration on Flow and Temperature Structure in Sodium-Cooled 19-Rod Simulated LMFBR Fuel Bundles with Helical Wire-Wrap Spacers." *16th National Heat Transfer Conference.* St. Louis, MI, 1976.

42. Fontana, M. H., R. E. MacPherson, P. A. Gnadt, L. F. Parsly, and J. L. Wantland. *Temperature Distribution in a 19-Rod Simulated LMFBR Fuel Assembly in a Hexagonal Duct (Fuel Failure Mockup Bundle 2A) - Record of Experimental Data.* Oak Ridge, TN: Oak Ridge National Laboratory, 1973.

43. Schilichting, H. *Boundary Layer Theory, 4th Edition.* New York: McGraw Hill, 1960.

44. Novendstern, E. H. "Turbulent Flow Pressure Drop Model for Fuel Rod Assemblies Utilizing a Helical Wire-Wrap Spacer System." *Nuclear Engineering and Design* 22, no. 1 (1972): 19-27.

45. Cheng, Shih-Kuei, and Neil E. Todreas. "Hydrodynamic Models and Correlations for Bare and Wire-Wrapped Hexagonal Rod Bundles - Bundle Fricition Factors, Subchannel Friction Factors and Mixing Parameters." *Nuclear Engineering and Design* (North-Holland) 92 (1986): 227-251.

46. Cheng, Shih-Kuei. *Constitutive Correlations for Wire-Wrapped Subchannel Analysis Under Forced and Mixed Convection Conditions.* Ph.D Thesis, Nuclear Science and Engineering, Cambridge, MA: Massachusetts Institute of Technology, 1984.

47. Chun, Moon-Hyun, and Kyong-Won Seo. "An Experimental Study and Assessment of Existing Friction Factor Correlations for Wire-Wrapped Fuel Assemblies." *Annals of Nuclear Energy* (Elsevier Science Ltd.) 28 (2001): 1683-1695.

48. Rheme, K. "The Structure of Turbulence in Rod Bundles and the Implications on Natural Mixing between the Subchannels." *Int. J. Heat Mass Transfer* 35 (1992): 567-591.

49. Engel, F. C., R. A. Markley, and A. A. Bishop. "Laminar, Transition, and Turbulent Parallel Flow Pressure Drop Across Wire-Wrap-Spaced Rod Bundles." *Nuclear Science and Engineering* 69, no. 2 (1979): 290-296.

50. Ro, Tae Sun, and Neil E. Todreas. "Energy Transfer Mechanisms in LMR Rod Bundles Under Mixed Convection Conditions." *Nuclear Engineering and Design* (North-Holland) 108 (1988): 343-357.

51. Rehme, K. "Pressure Drop Correlations for Fuel Element Spacers." *Nuclear Technology* 17, no. 1 (1973): 15-23.

52. Mikityuk, Konstantin. "Heat Transfer to Liquid Metal: Review of Data and Correlations for Tube Bundles." *Nuclear Engineering and Design* (Elsevier B. V.) 239 (2009): 680-687.

53. Engel, F. C., B. Minushkin, R. J. Atkins, and R. A. Markley. "Characterization of Heat Transfer and Temperature Distributions in an Electrically Heated Model of an LMFBR Blanket Assembly." *Nuclear Engineering and Design* (North-Holland Company) 62 (1980): 335-347.

54. Namekawa, F., A. Ito, and K. Mawatari. "Bouyancy Effects on Wire-Wrapped Rod Bundle Heat Transfer in an LMFBR Fuel Assembly." *AIChE Symposium Series.* Niagra Falls, 1984. 128-133.

55. Nam, Cheol, Woan Whang, and Dong-Seong Sohn. "Statistical Failure Analysis of Metallic U-10Zr/HT9 Fast Reactor Fuel Pin by Considering the Weibull Distribution and Cumulative Damage Fraction." *Anna. Nucl. Energy* (Elsevier Science Ltd.) 25, no. 17 (1998): 1441-1453.

56. Nuclear Energy Agency. *PRS-0199 HEATING-7.21 - 7.3.* http://www.oecd-nea.org/tools/abstract/detail/psr-0199/ (accessed 2011).

57. ADINA R&D, Inc. "ADINA Theory and Modeling Guide Volume I: ADINA." Watertown, MA, 2009.

58. ADINA R&D, Inc. "ADINA Theory and Modeling Guide Volume II: ADINA Heat Transfer." Watertown, MA, 2009.

59. Leibowitz, L., and R. A. Blomquist. "Thermal Conductivity and Thermal Expansion of Stainless Steels D9 and HT9." *International Journal of Thermophysics* 9, no. 5 (1988): 873-883.

60. Leffler, Bela. "Stainless - Stainless Steels and their Properties." http://www.outokumpu.com/files/Group/HR/Documents/STAINLESS20.pdf, Outokumpu.

61. Chuang, M. C., R. E. Rothmann, M. J. Pechersky, and R. A. Markley. "Cladding Circumferential Hot Spot Factors for Fuel and Blanket Rods." *Nuclear Engineering and Design* (North-Holland Publishing Company) 35 (1975): 21-28.

62. Roark, Raymond J. *Roark's Formulas for Stress and Strain.* 6th. New York, NY: McGraw-Hill, Inc., 1989.

63. Lawrence, Norman. *Compaq Visual Fortran.* Digital press, 2002.

64. Ohmae, Kenichi, Akakizu Morino, Norboru Nakao, and Seizo Hirao. "Channel Deformation Analysis for Fast Reactor Fuel Assemblies Undergoing Swelling and Thermal Bowing." *Nuclear Engineering and Design* (North-Holland Publishing Company) 23 (1972): 309-320.

65. Pahl, R. G., C. E. Lahm, and S. L. Hayes. "Performance of HT9 Clad Metallic Fuel at High Temperature." *Journal of Nuclear Materials* (North-Holland) 204 (1993): 141-147.

66. Python Software Foundation.. *Python.* 2011. http://python.org/ (accessed 2011).

67. Python Software Foundation. *About Python.* 2011. http://www.python.org/about/ (accessed 2011).

68. Python Software Foundation.. *Python 2.6.7.* 2011. http://www.python.org/download/releases/2.6.7/ (accessed 2011).

69. Gazoni, Eric. *OpenPyXL - A Python Library to Read/Write Excel 2007 xlsx/xlsm Files.* 2011. http://packages.python.org/openpyxl/ (accessed 2011).

70. Pahl, R. G., D. L. Porter, D. C. Crawford, and L. C. Walters. "Irradiation Behavior of Metallic Fast Reactor Fuels." *Journal of Nuclear Materials* (North-Holland) 188 (1992): 3-9.

71. Lahm, C. E., J. F. Koenig, R. G. Pahl, D. L. Porter, and D. C. Crawford. "Experience with Advanced Driver Fuels in EBR-II." *Journal of Nuclear Materials* (North-Holland) 204 (1993): 119-123.

72. Crawford, D. C., S. L. Hayes, R. G. Pahl. "Large-Diameter, High-Plutonium Metallic Fuel Testing in EBR-II." *Transactions of the American Nuclear Society* 71. Washington, DC: American Nuclear Society, 1994. 178-179.

73. Pahl, R. G., R. S. Wisner, M. C. Billone, and G. L. Hofman. "Steady-State Irradiation Testing of U-Pu-Zr Fuel to >18 at.% Burnup." *Proceedings of the 1990 International Fast Reactor Safety Meeting.* Snowbird, UT: American Nuclear Society, 1990. 129-137.

74. Porter, Douglas L., and Conor B. Hilton. "Extending Sodium Fast Reactor Driver Fuel Use to Higher Temperatures." *Nuclear Technology* 173 (2010): 218-225.

75. Cohen, A. B., H. Tsai, and L. A. Neimark. "Fuel/Cladding Compatibility in U-19Pu-10Zr/HT9-Clad Fuel at Elevated Temperatures." *Journal of Nuclear Materials* (North-Holland) 204 (1993): 244-251.

76. Lee, Byoung Oon, J. S. Cheon, and C. B Lee. "Performance Limit Analysis of Metallic Fuel for Kalimer." *Global 2007*. Boise, Idaho, 397-403.

Appendix A: Fuel Pin Parametric Study Data

This appendix contains all the data from the fuel rod parametric studies discussed in Section 5.4. For each condition studied there are three tables: Thermal Creep Strain, Irradiation Creep Strain, and Total Creep Strain. These tables have strain values ranging from 0.1% to 3.0%. The burnup at which each strain value occurred is listed for nine different peak clad temperatures. If no value is listed it means the run terminated before that strain value was reached. The four ways for a run to terminate are: FCCI limit, CDF limit, Total Strain limit, or it reached full duration. To determine what caused a particular run to terminate refer to the column in the total creep strain table. If "FCCI" or "CDF" appears then the run ended before this level of strain was reached due to the FCCI limit or the CDF limit. If these letters do not appear but a burnup is given for 3.0% that is not the End of Life (EOL) burnup then the total creep strain limit was hit. Otherwise the run lasted the full duration. The EOL burnup listed on each table shows what the burnup would be for the pin if the run lasted the full duration. For some of the cases below the listed EOL burnup was not realized for any of the peak clad temperatures.

Index

S-PRISM Driver Fuel

Linear Power	15 kW/m	Clad Thickness	0.56 mm
Plutonium Content	19%	Smear Density	75%
Duration	20 years	EOL Burnup	30.7

Thermal Creep Strain

	501.60	522.66	543.71	564.76	585.77	606.74	627.69	648.62	668.98
0.10			29.65	20.96	14.28	9.66	6.59	4.12	
0.20				24.70	17.14	11.84	8.23	5.33	
0.30				26.84	18.82	13.19	9.24	6.13	
0.40				28.39	19.99	14.11	10.00	6.72	
0.50				29.57	20.92	14.87	10.58	7.18	
0.75					22.51	16.17	11.68	8.02	
1.00					23.60	17.05	12.39	8.65	
1.50					25.03	18.19	13.31	9.49	
2.00							13.90	10.04	
3.00									

Irradiation Creep Strain

	501.60	522.66	543.71	564.76	585.77	606.74	627.69	648.62	668.98
0.10	13.15	10.63	9.16	8.36	7.85	7.48	5.75	3.65	
0.20	15.08	12.85	11.42	10.54	10.37	9.91	7.73	5.17	
0.30	16.51	14.49	13.31	12.39	12.18	11.80	9.16	6.22	
0.40	17.85	15.96	14.95	13.99	13.78	13.19	10.25	7.06	
0.50	19.07	17.30	16.25	15.41	15.20	14.41	11.17	7.77	
0.75	21.42	19.99	19.11	18.48	18.27	16.72	12.98	9.11	
1.00	23.48	22.26	21.50	21.00	20.83	18.44			
1.50	26.80	25.66	25.24	25.07	25.07				
2.00	28.27	28.39	28.22	28.31					
3.00									

Total Creep Strain

	501.60	522.66	543.71	564.76	585.77	606.74	627.69	648.62	668.98
0.10	13.10	10.58	9.11	8.27	7.81	6.51	4.66	2.77	FCCI
0.20	15.08	12.85	11.38	10.50	10.25	8.48	6.17	3.91	
0.30	16.51	14.49	13.27	12.35	12.14	9.87	7.22	4.66	
0.40	17.85	15.96	14.95	13.94	13.73	10.92	8.02	5.25	
0.50	19.03	17.30	16.25	15.37	15.16	11.80	8.65	5.75	
0.75	21.42	19.99	19.07	18.40	17.56	13.48	9.91	6.68	
1.00	23.48	22.26	21.50	20.92	19.19	14.70	10.84	7.39	
1.50	26.75	25.66	25.24	25.03	21.55	16.34	12.10	8.40	
2.00	28.27	28.35	28.22	28.18	23.14	17.47	12.94	9.11	
3.00					25.16	18.82	13.99	10.08	

S-PRISM Driver Fuel

Linear Power	15 kW/m	Clad Thickness	0.56 mm
Plutonium Content	0%	Smear Density	75%
Duration	20 years	EOL Burnup	30.7

Thermal Creep Strain

	501.60	522.66	543.70	564.76	585.76	606.74	627.69	648.61	668.98
0.10			28.98	19.87	13.78	9.62	6.68	4.66	2.02
0.20				23.65	16.67	11.76	8.27	5.80	2.90
0.30				25.83	18.44	13.06	9.24	6.55	3.53
0.40				27.43	19.66	14.03	10.00	7.10	3.99
0.50				28.69	20.58	14.78	10.54	7.52	4.41
0.75					22.30	16.04	11.59	8.32	5.17
1.00					23.48	16.93	12.26	8.86	5.71
1.50					24.99	18.06	13.15	9.58	6.55
2.00							13.69	10.04	
3.00									

Irradiation Creep Strain

	501.60	522.66	543.70	564.76	585.76	606.74	627.69	648.61	668.98
0.10	13.15	10.63	9.07	8.15	7.64	7.27	5.96	4.37	1.93
0.20	14.83	12.77	11.21	10.33	9.91	9.62	7.90	5.75	2.90
0.30	16.17	14.36	13.02	12.10	11.76	11.47	9.24	6.72	3.65
0.40	17.47	15.79	14.57	13.61	13.36	13.10	10.33	7.52	4.28
0.50	18.65	17.09	15.88	14.99	14.74	14.32	11.21	8.19	4.83
0.75	20.16	19.66	18.61	17.93	17.72	16.63	12.89	9.41	5.92
1.00	21.55	21.88	20.71	20.41	20.20	18.35			6.76
1.50	24.15	25.03	24.23	24.49	24.07				
2.00	26.42	26.96	27.22	27.76					
3.00									

Total Creep Strain

	501.60	522.66	543.70	564.76	585.76	606.74	627.69	648.61	668.98
0.10	13.15	10.58	9.07	8.11	7.52	6.59	4.96	3.53	1.30
0.20	14.83	12.77	11.17	10.29	9.83	8.48	6.34	4.49	1.97
0.30	16.17	14.32	12.98	12.05	11.63	9.87	7.31	5.21	2.48
0.40	17.43	15.75	14.53	13.57	13.23	10.92	8.11	5.75	2.90
0.50	18.65	17.09	15.88	14.91	14.62	11.76	8.74	6.22	3.28
0.75	20.16	19.61	18.61	17.85	17.14	13.40	9.91	7.10	3.99
1.00	21.55	21.88	20.71	20.33	18.82	14.62	10.79	7.77	4.58
1.50	24.15	25.03	24.23	24.36	21.21	16.25	12.01	8.69	5.42
2.00	26.42	26.96	27.17	27.64	22.89	17.35	12.77	9.32	6.09
3.00					25.07	18.69	13.78	10.08	7.01

S-PRISM Driver Fuel

Linear Power	20 kW/m	Clad Thickness	0.56 mm
Plutonium Content	19%	Smear Density	75%
Duration	20 years	EOL Burnup	40.9

Thermal Creep Strain

	545.89	567.31	588.69	610.08	631.40	652.68	673.93	695.15	715.59
0.10		23.21	15.92	10.65	7.29	4.82			
0.20		27.08	18.84	12.89	8.97	6.11			
0.30		29.32	20.52	14.18	9.98	6.90			
0.40		30.89	21.75	15.19	10.76	7.51			
0.50		32.12	22.65	15.92	11.38	8.02			
0.75			24.22	17.21	12.45	8.91			
1.00			25.34	18.11	13.17	9.53			
1.50				19.23	14.13	10.32			
2.00									
3.00									

Irradiation Creep Strain

	545.89	567.31	588.69	610.08	631.40	652.68	673.93	695.15	715.59
0.10	9.98	9.19	8.75	7.79	5.83	3.92			
0.20	12.28	11.77	11.21	10.26	7.79	5.38			
0.30	14.18	13.51	13.34	12.00	9.19	6.45			
0.40	15.87	15.08	14.91	13.40	10.26	7.29			
0.50	17.38	16.48	16.20	14.58	11.21	7.96			
0.75	20.29	19.51	19.06	16.87	13.01	9.36			
1.00	22.59	21.98	21.53	18.67	14.35	10.37			
1.50	25.73	25.62	25.56						
2.00	28.03	28.48							
3.00									

Total Creep Strain

	545.89	567.31	588.69	610.08	631.40	652.68	673.93	695.15	715.59
0.10	9.98	9.14	8.69	6.90	4.88	3.20	FCCI	FCCI	FCCI
0.20	12.22	11.72	11.16	8.97	6.50	4.37			
0.30	14.13	13.51	13.29	10.43	7.57	5.16			
0.40	15.81	15.02	14.91	11.49	8.41	5.77			
0.50	17.32	16.43	16.20	12.39	9.08	6.28			
0.75	20.29	19.45	18.56	14.13	10.37	7.23			
1.00	22.59	21.92	20.29	15.36	11.32	7.96			
1.50	25.73	25.62	22.76	17.10	12.67	9.08			
2.00	28.03	28.48	24.39	18.28	13.57	9.81			
3.00	32.18	32.40	26.57	19.73	14.69	10.71			

S-PRISM Driver Fuel

Linear Power	20 kW/m	Clad Thickness	0.56 mm
Plutonium Content	0%	Smear Density	75%
Duration	20 years	EOL Burnup	40.9

Thermal Creep Strain

	545.89	567.31	588.69	610.08	631.40	652.68	673.92	695.14	715.59
0.10		22.37	15.25	10.65	7.34	4.99	2.41	1.74	0.90
0.20		26.29	18.28	12.89	9.03	6.22	3.36	2.47	1.51
0.30		28.59	20.07	14.24	10.04	7.01	3.98	2.97	1.91
0.40		30.22	21.30	15.19	10.76	7.62	4.48	3.31	2.24
0.50			22.31	15.92	11.32	8.07	4.88	3.59	2.47
0.75			23.99	17.21	12.33	8.91	5.61	4.20	2.92
1.00			25.23	18.05	13.01	9.47	6.17	4.60	3.31
1.50				19.17	13.90	10.20	6.95	5.21	3.81
2.00									
3.00									

Irradiation Creep Strain

	545.89	567.31	588.69	610.08	631.40	652.68	673.92	695.14	715.59
0.10	9.75	8.69	8.07	7.57	6.11	4.15	1.96	1.40	0.90
0.20	11.94	11.04	10.26	9.98	7.96	5.61	2.92	2.07	1.35
0.30	13.74	13.06	12.05	11.89	9.31	6.62	3.64	2.63	1.68
0.40	15.36	14.58	13.62	13.46	10.37	7.40	4.26	3.03	2.02
0.50	16.82	15.92	15.02	14.63	11.27	8.07	4.71	3.36	2.24
0.75	19.73	18.78	17.49	16.93	12.95	9.42	5.77	4.15	2.80
1.00	22.03	21.25	19.57	18.67	14.24	10.37	6.62	4.71	3.25
1.50	25.40	24.61	23.32						
2.00	27.53	27.13							
3.00									

Total Creep Strain

	545.89	567.31	588.69	610.08	631.40	652.68	673.92	695.14	715.59
0.10	9.70	8.63	7.96	7.01	5.21	3.42	1.46	1.01	0.50
0.20	11.94	10.99	10.26	9.03	6.67	4.54	2.19	1.57	0.90
0.30	13.74	13.01	12.05	10.43	7.74	5.33	2.69	1.96	1.18
0.40	15.31	14.58	13.57	11.55	8.52	5.89	3.14	2.30	1.40
0.50	16.76	15.87	14.97	12.45	9.14	6.39	3.53	2.52	1.63
0.75	19.68	18.78	17.49	14.13	10.37	7.34	4.26	3.08	2.02
1.00	22.03	21.19	19.57	15.36	11.32	8.07	4.82	3.53	2.35
1.50	25.40	24.61	22.31	17.10	12.56	9.08	5.66	4.15	2.86
2.00	27.53	27.13	24.11	18.22	13.40	9.75	6.34	4.65	3.25
3.00	30.78	31.51	26.52	19.68	14.41	10.65	7.23	5.38	3.87

S-PRISM Driver Fuel

Linear Power	25 kW/m	Clad Thickness	0.56 mm
Plutonium Content	19%	Smear Density	75%
Duration	20 years	EOL Burnup	51.1

Thermal Creep Strain

	590.34	612.08	633.81	655.48	677.13	698.70	720.23	741.72	762.28
0.10	17.73	11.84	8.06	5.54					
0.20	20.74	14.23	9.88	6.87					
0.30	22.57	15.63	11.00	7.71					
0.40	23.76	16.68	11.77	8.34					
0.50	24.74	17.38	12.40	8.83					
0.75	26.35	18.71	13.53	9.74					
1.00	27.54	19.62	14.23	10.30					
1.50		20.74	15.21	11.07					
2.00									
3.00									

Irradiation Creep Strain

	590.34	612.08	633.81	655.48	677.13	698.70	720.23	741.72	762.28
0.10	9.60	8.06	5.96	4.20					
0.20	12.47	10.65	7.99	5.68					
0.30	14.65	12.47	9.46	6.73					
0.40	16.26	13.95	10.58	7.57					
0.50	17.45	15.14	11.49	8.27					
0.75	20.11	17.52	13.38	9.67					
1.00	22.43	19.34	14.79	10.65					
1.50	26.07								
2.00	28.38								
3.00									

Total Creep Strain

	590.34	612.08	633.81	655.48	677.13	698.70	720.23	741.72	762.28
0.10	9.39	7.29	5.12	3.57	FCCI	FCCI	FCCI	FCCI	FCCI
0.20	12.33	9.53	6.87	4.77					
0.30	14.44	11.07	7.99	5.61					
0.40	15.98	12.26	8.90	6.31					
0.50	17.24	13.24	9.67	6.80					
0.75	19.69	15.07	11.00	7.85					
1.00	21.51	16.40	12.05	8.62					
1.50	24.18	18.29	13.46	9.67					
2.00	26.00	19.55	14.44	10.44					
3.00	28.45	21.09	15.63	11.35					

S-PRISM Driver Fuel

Linear Power	25 kW/m	Clad Thickness	0.56 mm
Plutonium Content	0%	Smear Density	75%
Duration	20 years	EOL Burnup	51.1

Thermal Creep Strain

	590.34	612.07	633.81	655.48	677.13	698.70	720.23	741.72	762.28
0.10	17.45	11.91	8.20	5.54	2.80	1.89			
0.20	20.67	14.23	9.95	6.87	3.78	2.73			
0.30	22.57	15.63	11.07	7.71	4.49	3.22			
0.40	23.83	16.61	11.84	8.34	4.98	3.57			
0.50	24.81	17.38	12.40	8.83	5.40	3.92			
0.75	26.56	18.64	13.38	9.67	6.17	4.49			
1.00	27.75	19.55	14.09	10.23	6.73	4.91			
1.50		20.67	14.93	10.93	7.50				
2.00									
3.00									

Irradiation Creep Strain

	590.34	612.07	633.81	655.48	677.13	698.70	720.23	741.72	762.28
0.10	8.48	7.99	6.31	4.27	1.96	1.40			
0.20	11.14	10.30	8.27	5.75	3.01	2.10			
0.30	12.96	12.19	9.67	6.80	3.71	2.59			
0.40	14.51	13.88	10.79	7.64	4.27	3.01			
0.50	15.91	15.14	11.70	8.34	4.84	3.36			
0.75	18.92	17.52	13.46	9.67	5.82	4.06			
1.00	21.51	19.34	14.79	10.65	6.66	4.70			
1.50	24.46								
2.00	26.35								
3.00									

Total Creep Strain

	590.34	612.07	633.81	655.48	677.13	698.70	720.23	741.72	762.28
0.10	8.41	7.36	5.54	3.64	1.47	0.98	FCCI	FCCI	FCCI
0.20	11.00	9.60	7.15	4.84	2.31	1.61			
0.30	12.96	11.14	8.27	5.68	2.87	2.03			
0.40	14.51	12.33	9.11	6.31	3.36	2.38			
0.50	15.91	13.32	9.81	6.80	3.78	2.66			
0.75	18.92	15.07	11.14	7.85	4.49	3.22			
1.00	21.37	16.40	12.12	8.62	5.12	3.64			
1.50	24.18	18.22	13.46	9.67	6.03	4.34			
2.00	26.07	19.48	14.30	10.37	6.66	4.84			
3.00	28.66	21.02	15.35	11.28	7.64	5.54			

S-PRISM Driver Fuel

Linear Power	15 kW/m	Clad Thickness	0.49 mm
Plutonium Content	19%	Smear Density	75%
Duration	20 years	EOL Burnup	28.6

Thermal Creep Strain

	499.23	520.29	541.33	562.37	583.37	604.34	625.28	646.19	666.54
0.10			24.95	17.62	12.08	8.08	5.53	2.82	
0.20				20.79	14.40	9.93	6.87	3.88	
0.30				22.60	15.81	11.02	7.73	4.59	
0.40				23.89	16.79	11.85	8.36	5.10	
0.50				24.91	17.58	12.44	8.87	5.53	
0.75				26.76	18.91	13.57	9.77	6.32	
1.00				27.97	19.85	14.32	10.36	6.87	
1.50					21.03	15.26	11.14	7.65	
2.00						15.89	11.65	8.16	
3.00									

Irradiation Creep Strain

	499.23	520.29	541.33	562.37	583.37	604.34	625.28	646.19	666.54
0.10	12.63	10.04	8.55	7.57	7.14	6.67	5.10	2.75	
0.20	14.32	11.89	10.36	9.53	9.10	8.67	6.83	4.04	
0.30	15.58	13.42	11.89	10.98	10.75	10.32	8.04	4.98	
0.40	16.60	14.55	13.26	12.28	12.12	11.57	8.98	5.73	
0.50	17.58	15.65	14.48	13.46	13.30	12.59	9.81	6.39	
0.75	19.77	18.09	16.99	16.05	15.85	14.63	11.34	7.65	
1.00	21.54	19.97	18.99	18.20	18.05				
1.50	24.52	23.19	22.48	21.81					
2.00	27.07	25.93	25.27	24.83					
3.00									

Total Creep Strain

	499.23	520.29	541.33	562.37	583.37	604.34	625.28	646.19	666.54
0.10	12.63	10.00	8.51	7.53	7.10	5.69	4.08	1.88	FCCI
0.20	14.28	11.89	10.32	9.49	9.02	7.34	5.34	2.79	
0.30	15.58	13.38	11.85	10.95	10.63	8.47	6.20	3.45	
0.40	16.60	14.55	13.22	12.24	12.04	9.38	6.87	3.96	
0.50	17.58	15.65	14.44	13.42	13.26	10.12	7.38	4.39	
0.75	19.77	18.05	16.95	15.97	15.14	11.49	8.43	5.22	
1.00	21.54	19.97	18.99	18.13	16.48	12.51	9.18	5.85	
1.50	24.52	23.19	22.44	21.73	18.40	13.89	10.24	6.75	
2.00	27.07	25.93	25.27	24.68	19.73	14.79	10.91	7.38	
3.00				28.13	21.38	15.93	11.77	8.28	

S-PRISM Driver Fuel

Linear Power	15 kW/m	Clad Thickness	0.49 mm
Plutonium Content	0%	Smear Density	75%
Duration	20 years	EOL Burnup	28.6

Thermal Creep Strain

	499.23	520.29	541.33	562.37	583.37	604.33	625.28	646.19	666.54
0.10			24.25	16.63	11.53	8.08	5.65	3.92	1.49
0.20			28.40	19.77	13.97	9.85	6.94	4.86	2.24
0.30				21.66	15.42	10.95	7.77	5.49	2.71
0.40				22.99	16.44	11.73	8.36	5.92	3.14
0.50				24.05	17.22	12.36	8.83	6.32	3.45
0.75				26.01	18.67	13.46	9.69	6.98	4.08
1.00				27.46	19.69	14.20	10.28	7.41	4.55
1.50					20.99	15.18	11.02	8.04	5.26
2.00						15.77	11.49	8.40	
3.00									

Irradiation Creep Strain

	499.23	520.29	541.33	562.37	583.37	604.33	625.28	646.19	666.54
0.10	12.79	10.08	8.55	7.49	6.90	6.43	5.34	3.88	1.61
0.20	14.28	11.85	10.24	9.38	8.79	8.43	6.94	5.06	2.43
0.30	15.34	13.26	11.65	10.79	10.28	10.00	8.12	5.92	3.10
0.40	16.32	14.40	12.95	12.00	11.61	11.34	9.06	6.59	3.61
0.50	17.26	15.46	14.12	13.14	12.79	12.55	9.81	7.18	4.08
0.75	19.38	17.77	16.60	15.61	15.34	14.55	11.30	8.24	5.02
1.00	20.52	19.62	18.52	17.73	17.46				
1.50	22.64	22.87	21.77	21.22	20.91				
2.00	24.60	25.62	24.40	24.17					
3.00									

Total Creep Strain

	499.23	520.29	541.33	562.37	583.37	604.33	625.28	646.19	666.54
0.10	12.75	10.08	8.47	7.41	6.75	5.81	4.35	3.14	1.02
0.20	14.24	11.81	10.20	9.30	8.71	7.38	5.49	3.92	1.53
0.30	15.30	13.26	11.61	10.75	10.20	8.47	6.32	4.47	1.96
0.40	16.32	14.40	12.91	11.97	11.49	9.38	6.94	4.94	2.31
0.50	17.22	15.42	14.08	13.10	12.63	10.08	7.45	5.34	2.59
0.75	19.38	17.77	16.56	15.54	14.71	11.46	8.43	6.04	3.22
1.00	20.52	19.62	18.52	17.65	16.09	12.44	9.18	6.59	3.69
1.50	22.64	22.83	21.77	21.15	18.13	13.81	10.16	7.38	4.43
2.00	24.60	25.62	24.40	24.01	19.54	14.71	10.83	7.89	4.98
3.00	28.21			27.58	21.30	15.81	11.61	8.51	5.77

S-PRISM Driver Fuel

Linear Power	15 kW/m	Clad Thickness	0.67 mm
Plutonium Content	19%	Smear Density	75%
Duration	20 years	EOL Burnup	33.0

Thermal Creep Strain

	504.04	525.11	546.16	567.22	588.24	609.22	630.19	651.12	671.50
0.10				24.12	16.49	11.20	7.63	4.88	
0.20				28.42	19.79	13.69	9.53	6.28	
0.30				30.90	21.77	15.27	10.75	7.18	
0.40				32.62	23.13	16.35	11.61	7.86	
0.50					24.21	17.21	12.29	8.40	
0.75					26.02	18.70	13.51	9.44	
1.00					27.29	19.70	14.37	10.16	
1.50						21.01	15.40	11.07	
2.00									
3.00									

Irradiation Creep Strain

	504.04	525.11	546.16	567.22	588.24	609.22	630.19	651.12	671.50
0.10	13.64	11.29	9.85	9.08	8.81	8.27	6.37	4.11	
0.20	15.77	13.78	12.60	11.70	11.47	11.16	8.58	5.78	
0.30	17.53	15.81	14.77	13.91	13.64	13.15	10.16	6.96	
0.40	19.11	17.53	16.44	15.77	15.50	14.73	11.43	7.91	
0.50	20.37	18.93	17.98	17.44	17.17	16.04	12.47	8.72	
0.75	23.18	21.96	21.23	20.83	20.69	18.61	14.46	10.25	
1.00	25.39	24.21	23.76	23.63	23.63	20.56	15.90	11.38	
1.50	27.01	27.74	27.78	27.96	27.60				
2.00	28.55	30.67		31.04					
3.00									

Total Creep Strain

	504.04	525.11	546.16	567.22	588.24	609.22	630.19	651.12	671.50
0.10	13.64	11.25	9.80	9.04	8.72	7.32	5.24	3.21	FCCI
0.20	15.77	13.78	12.56	11.66	11.43	9.58	7.00	4.52	
0.30	17.53	15.77	14.73	13.82	13.60	11.16	8.18	5.38	
0.40	19.11	17.53	16.44	15.72	15.45	12.42	9.08	6.05	
0.50	20.37	18.88	17.98	17.35	17.12	13.42	9.85	6.60	
0.75	23.13	21.96	21.23	20.78	19.83	15.36	11.29	7.72	
1.00	25.39	24.21	23.76	23.58	21.77	16.76	12.38	8.54	
1.50	27.01	27.74	27.78	27.92	24.48	18.70	13.82	9.71	
2.00	28.55	30.63	30.72	30.99	26.38	19.97	14.82	10.57	
3.00	31.53				28.78	21.59	16.08	11.66	

S-PRISM Driver Fuel

Linear Power	15 kW/m	Clad Thickness	0.67 mm
Plutonium Content	0%	Smear Density	75%
Duration	20 years	EOL Burnup	33.0

Thermal Creep Strain

	504.04	525.11	546.16	567.22	588.24	609.22	630.18	651.12	671.50
0.10				22.99	15.99	11.11	7.72	5.38	2.57
0.20				27.33	19.34	13.60	9.58	6.73	3.66
0.30				29.91	21.37	15.18	10.75	7.59	4.38
0.40				31.71	22.77	16.26	11.57	8.22	4.92
0.50					23.85	17.12	12.24	8.76	5.38
0.75					25.75	18.57	13.42	9.67	6.23
1.00					27.11	19.61	14.19	10.30	6.91
1.50						20.87		11.11	7.82
2.00									
3.00									

Irradiation Creep Strain

	504.04	525.11	546.16	567.22	588.24	609.22	630.18	651.12	671.50
0.10	13.64	11.25	9.71	8.94	8.36	8.09	6.60	4.79	2.21
0.20	15.54	13.60	12.29	11.43	11.11	10.80	8.76	6.32	3.34
0.30	17.26	15.54	14.41	13.51	13.24	13.01	10.25	7.45	4.20
0.40	18.79	17.26	16.04	15.27	15.04	14.68	11.47	8.36	4.92
0.50	20.24	18.61	17.53	16.90	16.62	15.99	12.47	9.13	5.51
0.75	22.95	21.64	20.33	20.28	20.06	18.57	14.41	10.53	6.73
1.00	24.67	23.81	22.68	23.04	22.86	20.46		11.57	7.68
1.50	26.52	26.25	26.61	27.47	26.92				
2.00	28.10	28.51	29.73	30.63					
3.00									

Total Creep Strain

	504.04	525.11	546.16	567.22	588.24	609.22	630.18	651.12	671.50
0.10	13.64	11.20	9.67	8.85	8.31	7.36	5.51	3.89	1.58
0.20	15.54	13.60	12.24	11.38	10.98	9.58	7.14	5.06	2.39
0.30	17.26	15.54	14.37	13.46	13.15	11.16	8.31	5.92	3.03
0.40	18.79	17.21	16.04	15.22	14.95	12.38	9.17	6.55	3.52
0.50	20.24	18.61	17.53	16.81	16.58	13.37	9.89	7.09	3.93
0.75	22.95	21.64	20.33	20.19	19.43	15.27	11.29	8.13	4.79
1.00	24.67	23.81	22.68	22.99	21.37	16.67	12.33	8.90	5.42
1.50	26.52	26.25	26.61	27.42	24.12	18.57	13.73	9.98	6.46
2.00	28.10	28.51	29.73	30.63	26.07	19.88	14.68	10.71	7.23
3.00	31.08	32.80			28.64	21.46	15.81	11.61	8.27

S-PRISM Driver Fuel

Linear Power	15 kW/m	Clad Thickness	0.56 mm
Plutonium Content	19%	Smear Density	80%
Duration	20 years	EOL Burnup	30.0

Thermal Creep Strain

	501.60	522.66	543.70	564.76	585.76	606.74	627.69	648.61	668.98
0.10				17.99	12.39	8.23	5.61	3.61	
0.20					15.09	10.39	7.21	4.74	
0.30					16.70	11.72	8.23	5.49	
0.40					17.80	12.66	8.98	6.08	
0.50					18.62	13.41	9.56	6.51	
0.75					20.15	14.70	10.62	7.33	
1.00					21.21	15.64	11.37	7.96	
1.50						16.93	12.43	8.78	
2.00						17.80	13.09	9.33	
3.00									

Irradiation Creep Strain

	501.60	522.66	543.70	564.76	585.76	606.74	627.69	648.61	668.98
0.10	12.39	11.56	9.72	10.11	9.88	9.64	8.27	5.72	
0.20	12.90	12.58	11.37	13.21	13.88	13.72	11.05	7.80	
0.30	13.25	12.97	12.74	14.62	16.54	16.11	12.90	9.17	
0.40	13.56	13.33	13.84	15.80	18.19	17.56			
0.50	13.80	13.64	14.74	16.70	19.40				
0.75	14.39	14.31	16.31	18.38	21.21				
1.00	14.90	14.93	17.29	19.48					
1.50									
2.00									
3.00									

Total Creep Strain

	501.60	522.66	543.70	564.76	585.76	606.74	627.69	648.61	668.98
0.10	12.39	11.48	9.72	9.96	9.45	6.78	4.82	3.10	FCCI
0.20	12.90	12.58	11.37	13.21	12.39	8.98	6.43	4.19	
0.30	13.25	12.97	12.74	14.62	14.23	10.43	7.45	4.98	
0.40	13.56	13.33	13.84	15.76	15.60	11.45	8.23	5.53	
0.50	13.80	13.64	14.74	16.70	16.66	12.27	8.86	6.00	
0.75	14.39	14.31	16.31	18.38	18.50	13.76	10.00	6.90	
1.00	14.90	14.93	17.29	19.44	19.79	14.82	10.82	7.53	
1.50	CDF	CDF	CDF	CDF	21.21	16.27	11.96	8.43	
2.00					CDF	17.25	12.74	9.02	
3.00						18.50	13.68	9.84	

S-PRISM Driver Fuel

Linear Power	15 kW/m	Clad Thickness	0.56 mm
Plutonium Content	0%	Smear Density	80%
Duration	20 years	EOL Burnup	27.1

Thermal Creep Strain

	501.59	522.65	543.70	564.75	585.76	606.73	627.69	648.61	668.97
0.10				17.05	11.68	8.00	5.49	3.72	1.33
0.20					14.46	10.23	7.17	4.98	2.04
0.30					16.11	11.56	8.19	5.76	2.55
0.40					17.25	12.54	8.98	6.31	2.98
0.50					18.15	13.29	9.56	6.78	3.33
0.75					19.79	14.62	10.62	7.64	4.04
1.00					20.97	15.56	11.37	8.23	4.55
1.50						16.85	12.35	9.02	5.37
2.00						17.68	12.97	9.53	5.96
3.00									

Irradiation Creep Strain

	501.59	522.65	543.70	564.75	585.76	606.73	627.69	648.61	668.97
0.10	12.47	11.21	10.43	8.90	9.56	9.49	8.27	6.04	2.86
0.20	12.74	11.88	11.41	11.13	13.41	13.52	11.05	8.07	4.35
0.30	12.97	12.35	12.11	12.90	15.64	16.07	12.86	9.41	5.45
0.40	13.21	12.66	12.70	14.31	17.17	17.91			6.35
0.50	13.44	12.97	13.17	15.44	18.34				
0.75	13.99	13.56	14.15	17.48	20.46				
1.00	14.54		14.90	18.85	21.87				
1.50									
2.00									
3.00									

Total Creep Strain

	501.59	522.65	543.70	564.75	585.76	606.73	627.69	648.61	668.97
0.10	12.47	11.21	10.31	8.86	8.74	6.59	4.70	3.21	1.10
0.20	12.74	11.88	11.41	11.13	11.72	8.82	6.35	4.43	1.72
0.30	12.97	12.31	12.11	12.90	13.60	10.27	7.41	5.21	2.23
0.40	13.21	12.66	12.70	14.31	14.97	11.33	8.23	5.80	2.63
0.50	13.44	12.97	13.17	15.40	16.07	12.15	8.86	6.27	2.98
0.75	13.99	13.56	14.15	17.44	17.99	13.64	10.00	7.17	3.65
1.00	14.54	CDF	14.90	18.82	19.36	14.70	10.82	7.80	4.19
1.50	CDF		CDF	CDF	21.32	16.15	11.96	8.70	4.98
2.00					CDF	17.17	12.66	9.25	5.61
3.00						18.38	13.56	9.96	6.51

S-PRISM Driver Fuel

Linear Power	15 kW/m	Clad Thickness	0.56 mm
Plutonium Content	19%	Smear Density	85%
Duration	20 years	EOL Burnup	27.1

Thermal Creep Strain

	501.59	522.65	543.70	564.75	585.76	606.73	627.68	648.61	668.97
0.10						5.68	4.19	1.15	
0.20						7.76	5.86	1.52	
0.30						8.98	6.86	1.71	
0.40							7.61	1.89	
0.50							8.20	2.00	
0.75							9.31	2.30	
1.00								2.56	
1.50								3.04	
2.00								3.49	
3.00									

Irradiation Creep Strain

	501.59	522.65	543.70	564.75	585.76	606.73	627.68	648.61	668.97
0.10	5.90	5.08	4.86	4.23	3.86	2.89	2.49	1.08	
0.20	6.09	5.49	5.27	4.60	4.38	3.41	3.19	1.71	
0.30	6.23	5.79	5.53	4.90	4.86	3.90	3.82	2.12	
0.40	6.42	6.05	5.75	5.16	5.31	4.30	4.23	2.45	
0.50	6.57	6.27	5.94	5.42	5.64	4.68	4.60	2.78	
0.75	6.98	6.72	6.38	5.97	6.12	5.45	5.42	3.60	
1.00	7.35	7.16	6.75	6.49	6.61	6.05	6.12		
1.50	8.13	7.98	7.50	7.42	7.53	7.12	7.35		
2.00	8.91	8.76	8.24	8.31	8.46	8.09	8.46		
3.00									

Total Creep Strain

	501.59	522.65	543.70	564.75	585.76	606.73	627.68	648.61	668.97
0.10	5.90	5.08	4.82	4.23	3.86	2.86	2.34	0.71	FCCI
0.20	6.09	5.49	5.27	4.60	4.38	3.38	3.12	1.04	
0.30	6.23	5.79	5.53	4.90	4.86	3.86	3.71	1.34	
0.40	6.42	6.05	5.75	5.16	5.31	4.27	4.16	1.56	
0.50	6.57	6.27	5.94	5.42	5.64	4.64	4.53	1.74	
0.75	6.98	6.72	6.38	5.97	6.12	5.42	5.31	2.00	
1.00	7.35	7.16	6.75	6.49	6.61	6.01	5.97	2.23	
1.50	8.13	7.98	7.50	7.42	7.53	7.05	7.05	2.60	
2.00	8.91	8.76	8.24	8.27	8.42	7.87	8.02	2.97	
3.00	10.43	10.35	9.72	9.98	10.28	9.50	9.72	3.67	

S-PRISM Driver Fuel

Linear Power	15 kW/m	Clad Thickness	0.56 mm
Plutonium Content	0%	Smear Density	85%
Duration	20 years	EOL Burnup	30.66

Thermal Creep Strain

	501.59	522.65	543.69	564.75	585.75	606.73	627.68	648.60	668.97
0.10					9.57	6.05	3.67	2.23	0.56
0.20						8.39	5.60	3.60	1.00
0.30						9.83	6.79	4.56	1.45
0.40						10.84	7.61	5.27	1.82
0.50							8.27	5.83	2.15
0.75							9.50	6.79	2.82
1.00							10.35	7.50	3.34
1.50							11.54	8.46	4.19
2.00									
3.00									

Irradiation Creep Strain

	501.59	522.65	543.69	564.75	585.75	606.73	627.68	648.60	668.97
0.10	5.60	5.31	4.49	4.38	3.56	3.56	3.34	2.34	0.71
0.20	5.97	5.57	4.90	4.71	3.90	4.23	3.97	3.71	1.19
0.30	6.23	5.79	5.23	4.97	4.19	4.56	4.53	4.79	1.82
0.40	6.49	5.97	5.49	5.20	4.49	4.90	5.05	5.64	2.34
0.50	6.72	6.16	5.75	5.38	4.79	5.20	5.49	6.38	2.78
0.75	7.20	6.57	6.38	5.86	5.45	5.90	6.57	7.79	3.71
1.00	7.61	6.94	6.90	6.27	6.12	6.57	7.46	8.87	4.53
1.50	8.42	7.64	7.61	7.12	7.31	7.83	9.02		
2.00	9.24	8.39	8.39	7.98	8.46	8.94	10.43		
3.00									

Total Creep Strain

	501.59	522.65	543.69	564.75	585.75	606.73	627.68	648.60	668.97
0.10	5.60	5.31	4.49	4.34	3.56	3.30	2.34	1.60	0.37
0.20	5.97	5.57	4.90	4.71	3.90	4.23	3.49	2.26	0.56
0.30	6.23	5.75	5.23	4.97	4.19	4.56	4.49	2.97	0.71
0.40	6.49	5.97	5.49	5.20	4.49	4.86	4.97	3.64	0.89
0.50	6.72	6.16	5.75	5.38	4.79	5.20	5.45	4.19	1.11
0.75	7.20	6.57	6.35	5.83	5.45	5.90	6.46	5.27	1.82
1.00	7.61	6.94	6.90	6.27	6.09	6.53	7.35	6.05	2.41
1.50	8.42	7.64	7.61	7.12	7.31	7.76	8.79	7.16	3.15
2.00	9.24	8.39	8.35	7.94	8.42	8.83	10.09	7.98	3.78
3.00	10.87	9.83	9.91	9.69	10.69	10.98	12.32	9.02	4.79

S-PRISM Radial Blanket

Linear Power	10 kW/m	Clad Thickness	0.56 mm
Plutonium Content	19%	Smear Density	70%
Duration	20 years	EOL Burnup	6.1

Thermal Creep Strain

	441.10	461.68	482.27	502.85	523.41	543.96	564.47	585.00	605.50
0.10							4.04	2.60	1.20
0.20							5.55	3.72	1.88
0.30								4.51	2.41
0.40								5.08	2.82
0.50								5.52	3.15
0.75									3.80
1.00									4.28
1.50									5.00
2.00									5.52
3.00									

Irradiation Creep Strain

	441.10	461.68	482.27	502.85	523.41	543.96	564.47	585.00	605.50
0.10		5.66	5.04	3.99	3.37	3.01	2.82	2.70	1.65
0.20		5.90	5.46	4.79	4.26	3.95	3.78	3.78	2.61
0.30			5.68	5.09	4.70	4.60	4.57	4.69	3.59
0.40			5.88	5.36	4.98	5.06	5.25	5.56	4.48
0.50			6.07	5.62	5.26	5.51	5.90		5.25
0.75					5.93				
1.00									
1.50									
2.00									
3.00									

Total Creep Strain

	441.10	461.68	482.27	502.85	523.41	543.96	564.47	585.00	605.50
0.10		5.66	5.03	3.98	3.35	2.96	2.64	2.11	1.02
0.20		5.90	5.46	4.78	4.24	3.91	3.70	2.92	1.57
0.30			5.68	5.08	4.70	4.58	4.51	3.64	2.04
0.40			5.88	5.36	4.97	5.04	5.15	4.21	2.43
0.50			6.07	5.61	5.25	5.48	5.78	4.68	2.77
0.75					5.91			5.57	3.41
1.00									3.90
1.50									4.64
2.00									5.19
3.00									6.00

S-PRISM Radial Blanket

Linear Power	10 kW/m	Clad Thickness	0.56 mm
Plutonium Content	0%	Smear Density	70%
Duration	20 years	EOL Burnup	6.1

Thermal Creep Strain

	441.10	461.68	482.27	502.85	523.41	543.95	564.47	585.00	605.50
0.10							3.88	2.45	1.66
0.20							5.36	3.42	2.22
0.30								4.21	2.75
0.40								4.80	3.21
0.50								5.26	3.59
0.75									4.29
1.00									4.80
1.50									5.51
2.00									6.02
3.00									

Irradiation Creep Strain

	441.10	461.68	482.27	502.85	523.41	543.95	564.47	585.00	605.50
0.10		5.66	4.87	3.97	3.31	2.96	2.77	2.67	2.56
0.20		5.93	5.14	4.66	4.21	3.86	3.73	3.77	3.86
0.30			5.37	4.90	4.71	4.51	4.53	4.68	4.91
0.40			5.59	5.11	4.96	4.94	5.19	5.54	5.79
0.50			5.79	5.32	5.21	5.36	5.82		
0.75				5.81	5.81				
1.00									
1.50									
2.00									
3.00									

Total Creep Strain

	441.10	461.68	482.27	502.85	523.41	543.95	564.47	585.00	605.50
0.10		5.66	4.87	3.95	3.28	2.91	2.58	2.05	1.52
0.20		5.93	5.13	4.66	4.19	3.83	3.59	2.75	1.97
0.30			5.37	4.89	4.71	4.49	4.41	3.38	2.39
0.40			5.58	5.11	4.96	4.91	5.10	3.95	2.79
0.50			5.78	5.31	5.20	5.33	5.71	4.42	3.16
0.75				5.81	5.80			5.32	3.87
1.00								6.00	4.40
1.50									5.16
2.00									5.70
3.00									

S-PRISM Radial Blanket

Linear Power	15 kW/m	Clad Thickness	0.56 mm
Plutonium Content	19%	Smear Density	70%
Duration	20 years	EOL Burnup	9.1

Thermal Creep Strain

	476.47	497.35	518.21	539.07	559.90	580.70	601.49	622.25	642.99
0.10				9.05	5.79	3.65	1.92	0.69	0.51
0.20					7.57	5.11	2.86	1.11	0.82
0.30					8.65	6.00	3.50	1.42	1.07
0.40						6.63	3.97	1.67	1.31
0.50						7.13	4.36	1.90	1.51
0.75						8.05	5.10	2.32	1.94
1.00						8.71	5.65	2.67	2.26
1.50							6.43	3.25	2.76
2.00							7.02		
3.00									

Irradiation Creep Strain

	476.47	497.35	518.21	539.07	559.90	580.70	601.49	622.25	642.99
0.10	5.50	4.81	3.90	3.34	3.01	2.82	1.87	0.99	0.94
0.20	5.72	5.52	4.76	4.27	3.90	3.70	2.69	1.64	1.59
0.30	5.92	5.82	5.00	4.66	4.36	4.09	3.16	2.17	2.16
0.40	6.12	5.99	5.22	4.94	4.61	4.46	3.56	2.72	2.70
0.50	6.30	6.15	5.42	5.19	4.85	4.82	3.95	3.25	
0.75	6.73	6.53	5.89	5.80	5.41	5.67	4.86		
1.00	7.13	6.91	6.31	6.40	5.96	6.48	5.72		
1.50	7.92	7.65	7.07	7.20	7.06	8.01	7.32		
2.00	8.68	8.40	7.85	7.98	8.16				
3.00									

Total Creep Strain

	476.47	497.35	518.21	539.07	559.90	580.70	601.49	622.25	642.99
0.10	5.50	4.80	3.87	3.31	2.97	2.60	1.01	0.45	0.44
0.20	5.72	5.51	4.75	4.26	3.87	3.61	1.54	0.62	0.59
0.30	5.92	5.82	5.00	4.66	4.36	4.07	2.16	0.80	0.74
0.40	6.11	5.99	5.22	4.92	4.60	4.44	2.86	0.97	0.87
0.50	6.30	6.15	5.42	5.19	4.84	4.79	3.49	1.15	1.02
0.75	6.73	6.53	5.89	5.80	5.40	5.62	4.46	1.60	1.37
1.00	7.13	6.91	6.30	6.38	5.95	6.42	5.04	1.95	1.72
1.50	7.92	7.65	7.07	7.18	7.03	7.91	5.89	2.47	2.17
2.00	8.68	8.40	7.83	7.98	8.11		6.51	2.90	2.49
3.00							7.42	3.62	3.04

S-PRISM Radial Blanket

Linear Power	15 kW/m	Clad Thickness	0.56 mm
Plutonium Content	0%	Smear Density	70%
Duration	20 years	EOL Burnup	9.1

Thermal Creep Strain

	476.47	497.35	518.21	539.07	559.90	580.70	601.49	622.25	642.99
0.10				8.83	5.46	3.34	2.14	1.49	0.25
0.20					7.20	4.66	2.97	1.96	0.40
0.30					8.26	5.56	3.67	2.41	0.55
0.40					9.02	6.22	4.22	2.81	0.75
0.50						6.73	4.66	3.16	0.95
0.75						7.68	5.45	3.80	1.36
1.00						8.38	6.02	4.26	1.70
1.50							6.82	4.90	2.21
2.00							7.40	5.35	2.62
3.00									

Irradiation Creep Strain

	476.47	497.35	518.21	539.07	559.90	580.70	601.49	622.25	642.99
0.10	5.52	4.86	3.90	3.32	3.00	2.76	2.62	2.44	0.90
0.20	5.80	5.16	4.87	4.21	3.89	3.60	3.49	3.49	1.64
0.30	6.05	5.36	5.19	4.45	4.42	4.06	4.12	4.26	2.24
0.40	6.27	5.55	5.37	4.66	4.65	4.41	4.66	5.02	2.75
0.50	6.47	5.74	5.54	4.87	4.85	4.75	5.19		
0.75	6.95	6.15	5.92	5.37	5.36	5.56	6.45		
1.00	7.38	6.52	6.30	5.87	5.89	6.35	7.65		
1.50	8.06	7.25	7.00	6.86	6.92	7.85			
2.00	8.70	7.95	7.70	7.87	8.00				
3.00									

Total Creep Strain

	476.47	497.35	518.21	539.07	559.90	580.70	601.49	622.25	642.99
0.10	5.52	4.84	3.87	3.30	2.92	2.47	1.84	1.36	0.24
0.20	5.80	5.16	4.86	4.21	3.82	3.36	2.44	1.72	0.35
0.30	6.05	5.36	5.17	4.45	4.42	4.04	3.00	2.09	0.47
0.40	6.27	5.55	5.36	4.66	4.64	4.37	3.50	2.42	0.61
0.50	6.47	5.72	5.54	4.86	4.85	4.71	3.92	2.74	0.77
0.75	6.95	6.15	5.92	5.36	5.35	5.50	4.77	3.39	1.16
1.00	7.38	6.52	6.30	5.86	5.86	6.27	5.39	3.86	1.47
1.50	8.06	7.23	7.00	6.85	6.88	7.72	6.26	4.55	1.97
2.00	8.70	7.95	7.68	7.85	7.95		6.88	5.04	2.36
3.00							7.75	5.69	2.99

Tight Pitch Breed and Burn Fuel

Linear Power	10 kW/m	Fuel Venting	No
Plutonium Content	0%	Smear Density	63%
Duration	40 years	EOL Burnup	21.4

Thermal Creep Strain

	496.31	517.51	538.70	559.83	580.95	602.04	623.07	644.09	665.07
0.10		19.81	13.44	9.04	6.06	4.10	2.38	1.68	1.16
0.20			15.39	10.55	7.20	4.92	2.84	2.02	1.43
0.30			16.54	11.48	7.91	5.44	3.13	2.24	1.61
0.40			17.38	12.16	8.44	5.85	3.36	2.41	1.73
0.50			18.01	12.68	8.86	6.19	3.54	2.56	1.84
0.75			19.18	13.69	9.65	6.82	3.89	2.82	2.05
1.00			20.03	14.42	10.25	7.28	4.15	3.03	2.19
1.50			21.25	15.49	11.12	7.99	4.52	3.32	2.43
2.00				16.25	11.76	8.51	4.78	3.54	2.60
3.00									

Irradiation Creep Strain

	496.30	517.51	538.69	559.82	580.94	602.03	623.06	644.08	665.05
0.10	13.14	11.67	10.59	9.76	9.08	7.83	5.05	3.70	2.62
0.20	16.50	14.83	13.57	12.61	11.91				
0.30	18.90	17.10	15.73	14.72					
0.40	20.85	19.02	17.52	16.44					
0.50	21.36	20.61	18.99						
0.75									
1.00									
1.50									
2.00									
3.00									

Total Creep Strain

	496.30	517.51	538.69	559.82	580.94	602.03	623.06	644.08	665.05
0.10	13.12	11.64	10.30	7.86	5.63	3.92	2.33	1.64	1.13
0.20	16.50	14.82	12.67	9.51	6.79	4.74	2.78	1.97	1.39
0.30	18.90	17.07	14.16	10.56	7.53	5.28	3.07	2.19	1.57
0.40	20.83	18.99	15.24	11.32	8.09	5.69	3.31	2.37	1.70
0.50		20.51	16.11	11.92	8.54	6.03	3.48	2.50	1.80
0.75			17.63	13.02	9.38	6.67	3.83	2.78	2.00
1.00			18.68	13.82	9.99	7.15	4.10	2.98	2.16
1.50			20.16	14.99	10.88	7.87	4.48	3.29	2.40
2.00			21.20	15.83	11.56	8.41	4.75	3.51	2.57
3.00				17.03	12.52	9.20	5.13	3.83	2.82

Tight Pitch Breed and Burn Fuel

Linear Power	10 kW/m	Fuel Venting	Yes
Plutonium Content	0%	Smear Density	63%
Duration	40 years	EOL Burnup	31.4

Thermal Creep Strain

	496.31	517.51	538.70	559.83	580.95	602.04	623.07	644.09	665.07
0.10						17.11	8.98	6.25	4.48
0.20						18.72	11.42	8.06	5.97
0.30						19.34	12.62	8.95	6.66
0.40						19.67	13.34	9.49	7.05
0.50						19.89	13.82	9.86	7.30
0.75						20.23	14.53	10.37	7.67
1.00						20.36	14.91	10.66	7.86
1.50						20.44	15.33	10.99	8.07
2.00						20.45	15.59	11.16	8.13
3.00									

Irradiation Creep Strain

	496.30	517.51	538.69	559.82	580.94	602.03	623.06	644.08	665.05
0.10							15.05	10.90	8.00
0.20									
0.30									
0.40									
0.50									
0.75									
1.00									
1.50									
2.00									
3.00									

Total Creep Strain

	496.30	517.51	538.69	559.82	580.94	602.03	623.06	644.08	665.05
0.10						16.19	8.22	5.75	4.07
0.20						18.30	10.84	7.67	5.65
0.30						19.09	12.19	8.66	6.42
0.40						19.50	13.00	9.27	6.88
0.50						19.76	13.55	9.67	7.17
0.75						20.14	14.35	10.25	7.58
1.00						20.33	14.79	10.58	7.81
1.50						20.42	15.26	10.93	8.05
2.00						20.45	15.53	11.13	8.13
3.00						20.48	15.89	11.34	8.18

Tight Pitch Breed and Burn Fuel

Linear Power	15 kW/m	Fuel Venting	No
Plutonium Content	0%	Smear Density	63%
Duration	40 years	EOL Burnup	32.0

Thermal Creep Strain

	565.47	587.25	608.97	630.64	652.29	673.81	695.32	716.76	738.17
0.10	10.62	7.07	4.74	2.81	1.93	1.32	0.81	0.11	0.00
0.20	12.40	8.38	5.68	3.31	2.30	1.60	1.10	0.61	0.02
0.30	13.47	9.22	6.30	3.62	2.52	1.78	1.25	0.81	0.29
0.40	14.24	9.81	6.76	3.86	2.70	1.91	1.36	0.92	0.46
0.50	14.86	10.29	7.11	4.04	2.85	2.02	1.45	1.03	0.57
0.75	15.95	11.19	7.81	4.41	3.12	2.24	1.62	1.18	0.77
1.00	16.74	11.85	8.34	4.67	3.34	2.39	1.73	1.32	0.88
1.50	17.86	12.79	9.08	5.05	3.62	2.61	1.91	1.49	1.05
2.00	18.67	13.49	9.63	5.31	3.84	2.79	2.04	1.60	1.18
3.00									

Irradiation Creep Strain

	565.45	587.23	608.95	630.62	652.27	673.79	695.30	716.73	738.12
0.10	10.91	10.14	8.21	5.13	3.62	2.52	1.76	1.27	0.83
0.20	14.07	13.14						1.67	1.16
0.30	16.43								
0.40	18.23								
0.50									
0.75									
1.00									
1.50									
2.00									
3.00									

Total Creep Strain

	565.45	587.23	608.95	630.62	652.27	673.79	695.30	716.73	738.12
0.10	9.04	6.47	4.48	2.70	1.87	1.27	0.75	0.09	0.00
0.20	10.99	7.83	5.42	3.20	2.24	1.56	1.05	0.57	0.02
0.30	12.22	8.71	6.06	3.53	2.46	1.73	1.21	0.77	0.26
0.40	13.12	9.35	6.52	3.77	2.66	1.87	1.32	0.88	0.44
0.50	13.82	9.85	6.89	3.97	2.79	1.97	1.40	0.97	0.53
0.75	15.12	10.82	7.61	4.32	3.07	2.19	1.58	1.14	0.72
1.00	16.02	11.50	8.14	4.61	3.27	2.35	1.69	1.27	0.83
1.50	17.27	12.51	8.91	4.98	3.58	2.57	1.87	1.45	1.01
2.00	18.15	13.23	9.48	5.24	3.80	2.74	2.02	1.58	1.14
3.00	19.42	14.26	10.31	5.64	4.10	2.98	2.19	1.73	1.32

Tight Pitch Breed and Burn Fuel

Linear Power	15 kW/m	Fuel Venting	Yes
Plutonium Content	0%	Smear Density	63%
Duration	40 years	EOL Burnup	32.0

Thermal Creep Strain

	565.47	587.25	608.97	630.64	652.29	673.81	695.32	716.76	738.17
0.10		26.88	18.08	9.96	6.49	3.84	2.35	0.11	0.00
0.20		28.94	19.70	12.46	8.45	5.33	3.25	1.80	0.02
0.30		29.73	20.32	13.65	9.41	6.14	3.84	2.26	0.29
0.40		30.17	20.63	14.33	9.96	6.67	4.28	2.68	
0.50		30.48	20.85	14.77	10.33	7.02	4.59	3.01	
0.75		30.98	21.17	15.43	10.86	7.55	5.09	3.55	
1.00		31.31	21.31	15.78	11.17	7.83	5.42	3.93	
1.50		31.44	21.37	16.17	11.48	8.16	5.79	4.23	
2.00			21.39	16.41	11.67	8.36	6.01	4.37	
3.00									

Irradiation Creep Strain

	565.45	587.23	608.95	630.62	652.27	673.79	695.30	716.73	738.12
0.10	28.59	27.23	21.33	15.27	10.82	7.33	4.81	3.20	
0.20							5.92	4.23	
0.30									
0.40									
0.50									
0.75									
1.00									
1.50									
2.00									
3.00									

Total Creep Strain

	565.45	587.23	608.95	630.62	652.27	673.79	695.30	716.73	738.12
0.10	28.33	24.27	16.94	8.91	5.79	3.40	2.08	0.09	0.00
0.20		27.74	19.18	11.70	7.90	4.89	2.98	1.43	0.02
0.30		29.03	20.01	13.08	8.97	5.77	3.58	2.04	0.26
0.40		29.69	20.43	13.91	9.63	6.34	4.02	2.44	FCCI
0.50		30.11	20.69	14.44	10.07	6.76	4.34	2.76	
0.75		30.72	21.09	15.23	10.71	7.37	4.92	3.36	
1.00		31.11	21.28	15.62	11.06	7.70	5.27	3.73	
1.50		31.42	21.37	16.08	11.41	8.07	5.68	4.17	
2.00		CDF	21.39	16.35	11.63	8.29	5.95	4.32	
3.00			CDF	16.68	11.85	8.47	6.12	4.45	

Tight Pitch Breed and Burn Fuel

Linear Power	20 kW/m	Fuel Venting	No
Plutonium Content	0%	Smear Density	63%
Duration	40 years	EOL Burnup	42.7

Thermal Creep Strain

	579.74	601.62	623.46	645.20	666.93	688.55	710.14	731.68	753.14
0.10	9.01	6.06	4.10	2.78	1.73	1.14	0.53	0.00	0.00
0.20	10.59	7.20	4.92	3.39	2.11	1.43	0.94	0.29	0.00
0.30	11.53	7.93	5.47	3.77	2.31	1.61	1.11	0.59	0.00
0.40	12.23	8.48	5.88	4.07	2.49	1.76	1.23	0.76	0.06
0.50	12.79	8.92	6.20	4.30	2.60	1.84	1.32		
0.75	13.81	9.71	6.82	4.80	2.87	2.05	1.46		
1.00	14.57	10.30	7.28	5.15	3.04	2.19	1.58		
1.50	15.62	11.15	7.96	5.68	3.31	2.40	1.76		
2.00	16.35	11.79	8.46	6.06	3.51	2.57	1.87		
3.00									

Irradiation Creep Strain

	579.72	601.60	623.44	645.18	666.90	688.52	710.09	731.61	753.03
0.10	10.53	9.13	6.99	5.00	3.04	2.11	1.46		0.67
0.20	13.63	11.85				2.66	1.87		
0.30	15.95								
0.40									
0.50									
0.75									
1.00									
1.50									
2.00									
3.00									

Total Creep Strain

	579.72	601.60	623.44	645.18	666.90	688.52	710.09	731.61	753.03
0.10	7.93	5.59	3.86	2.63	1.67	1.05	0.47	0.00	0.00
0.20	9.60	6.79	4.68	3.22	2.02	1.38	0.85	0.23	0.00
0.30	10.65	7.55	5.24	3.63	2.25	1.55	1.05	0.53	0.00
0.40	11.44	8.10	5.65	3.92	2.40	1.70	1.17	0.67	0.03
0.50	12.05	8.54	6.00	4.18	2.55	1.78	1.26	0.79	0.26
0.75	13.19	9.39	6.61	4.65	2.81	1.99	1.40	FCCI	0.53
1.00	13.98	10.01	7.11	5.00	2.98	2.14	1.52		0.67
1.50	15.16	10.91	7.81	5.56	3.28	2.37	1.70		FCCI
2.00	15.97	11.56	8.31	5.94	3.45	2.52	1.84		
3.00	17.12	12.52	9.07	6.55	3.74	2.75	2.02		

Tight Pitch Breed and Burn Fuel

Linear Power	20 kW/m	Fuel Venting	Yes
Plutonium Content	0%	Smear Density	63%
Duration	40 years	EOL Burnup	42.7

Thermal Creep Strain

	579.74	601.62	623.46	645.20	666.93	688.55	710.14	731.68	753.14
0.10	34.84	23.67	15.89	10.47	5.32	2.95	0.94	0.00	0.00
0.20	37.24	25.40	17.38	11.88	7.20	4.27	2.72	0.29	0.00
0.30	38.18	26.04	17.91	12.40	8.13	5.06	3.31		0.00
0.40	38.71	26.39	18.20	12.67	8.72	5.59	3.72		0.06
0.50	39.12	26.62	18.37	12.84	9.10	5.97	4.01		0.29
0.75	39.79	27.03	18.67	13.11	9.65	6.55	4.53		
1.00	40.23	27.24	18.75	13.19	9.95	6.90	4.86		
1.50	40.70	27.33	18.81	13.25	10.30	7.26	5.27		
2.00	40.75	27.36	18.84	13.28	10.47	7.49	5.47		
3.00									

Irradiation Creep Strain

	579.72	601.60	623.44	645.18	666.90	688.52	710.09	731.61	753.03
0.10	28.35	26.24	18.72	13.14	8.98	5.76	3.86		
0.20	35.90				10.44	7.14	4.97		
0.30	38.44						5.53		
0.40									
0.50									
0.75									
1.00									
1.50									
2.00									
3.00									

Total Creep Strain

	579.72	601.60	623.44	645.18	666.90	688.52	710.09	731.61	753.03
0.10	28.12	21.68	14.80	9.65	4.56	2.60	0.50	0.00	0.00
0.20	34.73	24.55	16.88	11.44	6.52	3.80	2.46	0.23	0.00
0.30	36.69	25.57	17.61	12.14	7.61	4.62	3.01	FCCI	0.00
0.40	37.68	26.07	17.99	12.49	8.31	5.21	3.39		0.03
0.50	38.33	26.39	18.23	12.73	8.75	5.62	3.72		0.26
0.75	39.26	26.86	18.58	13.02	9.45	6.32	4.30		FCCI
1.00	39.82	27.15	18.72	13.17	9.80	6.70	4.65		
1.50	40.58	27.30	18.78	13.25	10.18	7.14	5.12		
2.00	40.73	CDF	18.81	CDF	10.42	7.40	5.38		
3.00	CDF		CDF		CDF	7.64	5.56		

Tight Pitch Breed and Burn Fuel

Linear Power	25 kW/m	Fuel Venting	No
Plutonium Content	0%	Smear Density	63%
Duration	40 years	EOL Burnup	53.4

Thermal Creep Strain

	603.59	625.63	647.62	669.56	691.41	713.20	734.91	756.59	778.04
0.10	6.47	4.39	2.74	1.87	1.21	0.55	0.00	0.00	0.00
0.20	7.68	5.27	3.22	2.27	1.54	0.99	0.22	0.00	0.00
0.30	8.45	5.85	3.55	2.49	1.76	1.17	0.62	0.00	0.00
0.40	9.03	6.25	3.77	2.67	1.90	1.28		0.04	0.00
0.50	9.47	6.62	3.95	2.82	2.01	1.39		0.22	0.00
0.75	10.31	7.24	4.32	3.11	2.23	1.57		0.59	0.00
1.00	10.93	7.75	4.53	3.29	2.38	1.68			0.04
1.50	11.81	8.45	4.90	3.58	2.60	1.90			0.48
2.00	12.47	8.96	5.12	3.77	2.78	2.01			0.69
3.00									

Irradiation Creep Strain

	603.57	625.60	647.58	669.52	691.36	713.14	734.83	756.44	777.76
0.10	9.25	7.06	4.46	3.11	2.16	1.46		0.66	0.44
0.20	12.00	9.18		3.91	2.71	1.87			0.66
0.30									
0.40									
0.50									
0.75									
1.00									
1.50									
2.00									
3.00									

Total Creep Strain

	603.57	625.60	647.58	669.52	691.36	713.14	734.83	756.44	777.76
0.10	5.92	4.10	2.60	1.76	1.10	0.44	0.00	0.00	0.00
0.20	7.17	4.97	3.11	2.16	1.46	0.88	0.15	0.00	0.00
0.30	7.97	5.56	3.40	2.38	1.65	1.10	0.51	0.00	0.00
0.40	8.56	6.00	3.66	2.60	1.79	1.21	0.69	0.04	0.00
0.50	9.07	6.36	3.84	2.74	1.90	1.32	FCCI	0.18	0.00
0.75	9.95	7.02	4.21	3.00	2.12	1.50		0.51	0.00
1.00	10.61	7.53	4.46	3.22	2.30	1.65		0.69	0.04
1.50	11.52	8.27	4.83	3.51	2.52	1.83		FCCI	0.44
2.00	12.21	8.78	5.08	3.73	2.71	1.97			0.62
3.00	13.20	9.58	5.41	4.02	2.96	2.16			FCCI

Tight Pitch Breed and Burn Fuel

Linear Power	25 kW/m	Fuel Venting	Yes
Plutonium Content	0%	Smear Density	63%
Duration	40 years	EOL Burnup	53.4

Thermal Creep Strain

	603.59	625.63	647.62	669.56	691.41	713.20	734.91	756.59	778.04
0.10	25.42	17.04	10.28	5.49	3.07	0.88	0.00	0.00	0.00
0.20	27.06	18.47	12.62	7.50	4.53	2.78	0.22	0.00	0.00
0.30	27.68	18.98	13.60	8.52	5.41	3.44		0.00	0.00
0.40	28.01	19.27	14.15	9.14	5.96	3.88		0.04	0.00
0.50	28.23	19.42	14.48	9.55	6.36	4.21		0.22	0.00
0.75	28.64	19.71	14.96	10.13	6.99	4.75			0.00
1.00	28.82	19.78	15.25	10.42	7.31	5.12			0.04
1.50	28.89		15.54	10.79	7.68	5.52			
2.00			15.73	11.01	7.86	5.74			
3.00									

Irradiation Creep Strain

	603.57	625.60	647.58	669.52	691.36	713.14	734.83	756.44	777.76
0.10	27.43	19.53	14.08	8.96	5.71	3.77			
0.20				10.64	7.28	4.94			
0.30					7.94	5.60			
0.40									
0.50									
0.75									
1.00									
1.50									
2.00									
3.00									

Total Creep Strain

	603.57	625.60	647.58	669.52	691.36	713.14	734.83	756.44	777.76
0.10	23.11	15.76	8.78	4.61	2.63	0.44	0.00	0.00	0.00
0.20	26.11	17.92	11.67	6.66	3.91	2.49	0.15	0.00	0.00
0.30	27.14	18.69	12.98	7.83	4.83	3.04	FCCI	0.00	0.00
0.40	27.65	19.05	13.68	8.59	5.45	3.51		0.04	0.00
0.50	27.98	19.27	14.15	9.11	5.92	3.84		0.18	0.00
0.75	28.45	19.60	14.77	9.84	6.66	4.46		FCCI	0.00
1.00	28.74	19.75	15.10	10.24	7.09	4.86			0.04
1.50	CDF	19.82	15.47	10.68	7.53	5.34			FCCI
2.00		CDF	15.65	10.90	7.79	5.63			
3.00			CDF	CDF	CDF	CDF			

Appendix B: Sodium Properties

This appendix contains the sodium properties that were used in COBRA throughout the course of this work. COBRA uses all British units. All the values in British units are reported with the number of significant figures used (which is the number originally given with COBRA). Standard values on the tables below were converted from the British units and are rounded appropriately. Properties are for liquid sodium unless otherwise specified.

Pressure		Temperature		Specific Volume		Vapor Specific Volume	
psia	kPa	°F	°C	ft^3/lb	m^3/kg	ft^3/lb	m^3/kg
0	0	500	260.00	0.01801	1.12E-03		
0	0	550	287.78	0.01801	1.12E-03		
0	0	600	315.56	0.01828	1.14E-03		
0	0	650	343.33	0.01842	1.15E-03	409870.00	2.56E+04
0	0	700	371.11	0.01856	1.16E-03	178120.00	1.11E+04
0	0	750	398.89	0.0187	1.17E-03	83102.00	5.19E+03
0	0	800	426.67	0.01885	1.18E-03	41266.00	2.58E+03
0	0	840	448.89	0.01897	1.18E-03	24533.00	1.53E+03
0	0	880	471.11	0.01909	1.19E-03	15060.00	9.40E+02
0.1	0.69	920	493.33	0.01921	1.20E-03	9519.00	5.94E+02
0.1	0.69	940	504.44	0.01927	1.20E-03	7645.00	4.77E+02
0.1	0.69	960	515.56	0.01933	1.21E-03	6180.00	3.86E+02
0.1	0.69	980	526.67	0.0194	1.21E-03	5026.00	3.14E+02
0.2	1.38	1000	537.78	0.01946	1.21E-03	4111.00	2.57E+02
0.2	1.38	1020	548.89	0.01952	1.22E-03	3382.00	2.11E+02
0.2	1.38	1040	560.00	0.01959	1.22E-03	2798.00	1.75E+02
0.3	2.07	1060	571.11	0.01965	1.23E-03	2326.00	1.45E+02
0.4	2.76	1080	582.22	0.01971	1.23E-03	1944.00	1.21E+02
0.4	2.76	1100	593.33	0.01978	1.23E-03	1632.00	1.02E+02
0.5	3.45	1120	604.44	0.01985	1.24E-03	1376.00	8.59E+01
0.6	4.14	1140	615.56	0.01991	1.24E-03	1166.00	7.28E+01
0.7	4.83	1160	626.67	0.01998	1.25E-03	992.00	6.19E+01
0.9	6.21	1180	637.78	0.02005	1.25E-03	847.50	5.29E+01
1	6.89	1200	648.89	0.02011	1.26E-03	726.90	4.54E+01
2.1	14.48	1300	704.44	0.02046	1.28E-03	356.30	2.22E+01
4.2	28.96	1400	760.00	0.02082	1.30E-03	189.10	1.18E+01
7.8	53.78	1500	815.56	0.02119	1.32E-03	107.40	6.70E+00
13.4	92.39	1600	871.11	0.02157	1.35E-03	64.63	4.03E+00
14.8	102.04	1619	881.67	0.02165	1.35E-03	59.34	3.70E+00
124.2	856.33	2145	1173.89	0.02388	1.49E-03	8.52	5.32E-01

Pressure		Temperature		Enthalpy		Vapor Enthalpy	
psia	kPa	°F	°C	Btu/lb	J/kg	Btu/lb	J/kg
0	0	500	260.00	303.76	7.07E+05	2204.8	5.13E+06
0	0	550	287.78	319.44	7.43E+05	2212.9	5.15E+06
0	0	600	315.56	335.01	7.79E+05	2220.5	5.16E+06
0	0	650	343.33	350.49	8.15E+05	2227.6	5.18E+06
0	0	700	371.11	365.88	8.51E+05	2234.1	5.20E+06
0	0	750	398.89	381.19	8.87E+05	2240.2	5.21E+06
0	0	800	426.67	396.43	9.22E+05	2245.8	5.22E+06
0	0	840	448.89	408.58	9.50E+05	2249.9	5.23E+06
0	0	880	471.11	420.69	9.79E+05	2253.9	5.24E+06
0.1	0.69	920	493.33	432.77	1.01E+06	2257.6	5.25E+06
0.1	0.69	940	504.44	438.8	1.02E+06	2259.3	5.26E+06
0.1	0.69	960	515.56	444.83	1.03E+06	2261.1	5.26E+06
0.1	0.69	980	526.67	450.85	1.05E+06	2262.8	5.26E+06
0.2	1.38	1000	537.78	456.86	1.06E+06	2264.4	5.27E+06
0.2	1.38	1020	548.89	462.87	1.08E+06	2266.1	5.27E+06
0.2	1.38	1040	560.00	468.88	1.09E+06	2267.6	5.27E+06
0.3	2.07	1060	571.11	474.88	1.10E+06	2269.2	5.28E+06
0.4	2.76	1080	582.22	480.88	1.12E+06	2270.8	5.28E+06
0.4	2.76	1100	593.33	486.88	1.13E+06	2272.3	5.29E+06
0.5	3.45	1120	604.44	492.87	1.15E+06	2273.8	5.29E+06
0.6	4.14	1140	615.56	498.87	1.16E+06	2275.2	5.29E+06
0.7	4.83	1160	626.67	504.86	1.17E+06	2276.7	5.30E+06
0.9	6.21	1180	637.78	510.86	1.19E+06	2278.2	5.30E+06
1	6.89	1200	648.89	516.85	1.20E+06	2279.6	5.30E+06
2.1	14.48	1300	704.44	546.85	1.27E+06	2286.7	5.32E+06
4.2	28.96	1400	760.00	576.95	1.34E+06	2293.9	5.34E+06
7.8	53.78	1500	815.56	607.21	1.41E+06	2301.1	5.35E+06
13.4	92.39	1600	871.11	637.7	1.48E+06	2308.5	5.37E+06
14.8	102.04	1619	881.67	643.4	1.50E+06	2310.2	5.37E+06
124.2	856.33	2145	1173.89	810.92	1.89E+06	2351.7	5.47E+06

Pressure		Temperature		Viscosity		Thermal Conductivity		Surface Tension	
psia	kPa	°F	°C	lb/ft-hr	N-s/m2	Btu/(hr-ft-F)	W/m-k	lb_f/ft	N/m
0	0	500	260.00	0.9235	3.82E-04	45.43	78.57	0.01238	0.81
0	0	550	287.78	0.8591	3.55E-04	44.6	77.14	0.01219	0.80
0	0	600	315.56	0.8038	3.32E-04	43.79	75.74	0.012	0.78
0	0	650	343.33	0.7558	3.12E-04	42.98	74.34	0.01181	0.77
0	0	700	371.11	0.7138	2.95E-04	42.18	72.95	0.01162	0.76
0	0	750	398.89	0.6767	2.80E-04	41.39	71.59	0.01143	0.75
0	0	800	426.67	0.6437	2.66E-04	40.62	70.26	0.01124	0.73
0	0	840	448.89	0.6198	2.56E-04	40	69.18	0.01109	0.72
0	0	880	471.11	0.598	2.47E-04	39.39	68.13	0.01094	0.71
0.1	0.69	920	493.33	0.5778	2.39E-04	38.79	67.09	0.01078	0.70
0.1	0.69	940	504.44	0.5683	2.35E-04	38.5	66.59	0.01071	0.70
0.1	0.69	960	515.56	0.5592	2.31E-04	38.2	66.07	0.01063	0.69
0.1	0.69	980	526.67	0.5504	2.28E-04	37.91	65.57	0.01056	0.69
0.2	1.38	1000	537.78	0.5419	2.24E-04	37.61	65.05	0.01048	0.68
0.2	1.38	1020	548.89	0.5338	2.21E-04	37.42	64.72	0.0104	0.68
0.2	1.38	1040	560.00	0.5259	2.17E-04	37.03	64.05	0.01033	0.67
0.3	2.07	1060	571.11	0.5183	2.14E-04	36.74	63.54	0.01025	0.67
0.4	2.76	1080	582.22	0.511	2.11E-04	36.46	63.06	0.01018	0.66
0.4	2.76	1100	593.33	0.5004	2.07E-04	36.03	62.32	0.01006	0.66
0.5	3.45	1120	604.44	0.497	2.05E-04	35.89	62.07	0.01002	0.65
0.6	4.14	1140	615.56	0.4904	2.03E-04	35.61	61.59	0.00995	0.65
0.7	4.83	1160	626.67	0.484	2.00E-04	35.33	61.11	0.00987	0.64
0.9	6.21	1180	637.78	0.4778	1.98E-04	35.05	60.62	0.00979	0.64
1	6.89	1200	648.89	0.4717	1.95E-04	34.78	60.15	0.00972	0.63
2.1	14.48	1300	704.44	0.4442	1.84E-04	33.42	57.80	0.00934	0.61
4.2	28.96	1400	760.00	0.4204	1.74E-04	32.11	55.54	0.00896	0.59
7.8	53.78	1500	815.56	0.3995	1.65E-04	30.84	53.34	0.00858	0.56
13.4	92.39	1600	871.11	0.3811	1.58E-04	29.61	51.21	0.00819	0.53
14.8	102.04	1619	881.67	0.3779	1.56E-04	29.38	50.81	0.00812	0.53
124.2	856.33	2145	1173.89	0.3094	1.28E-04	23.64	40.89	0.00612	0.40

Appendix C: Input Files

This appendix contains a sampling of all the input files for COBRA and FEAST. Base input files were provided for each of the cases discussed in this thesis. For a detailed description of the input file for both codes consult Wheeler et al. (31) (COBRA) or Karahan (23) (FEAST). For each code, some changes made to the code required alterations to the input files. Those alterations are listed below.

COBRA Input File Modifications

-Setup.2 N5 LAMNF Pressure Drop Correlation

1=old cobra correlation

2= Cheng and Todreas Correlation

3= Novendstern

Setup 2.1 and 2.2 are filled with constants needed for the above correlations

-Setup.2 N6 Heat Transfer Correlation

0=Dittus Boelter

1=New Correlation-go to Setup2.3

For free form correlation enter constants as described

For Mikityuk correlation simply enter 1 on this line

-Setup.10 N1 Turbulent Mixing

0-3=options in manual

4=Rheme Correlation

FEAST Input File Modifications

- Supplemental input files were added for coolant temperature and heat transfer coefficient

- A case number was added as the first line of the input file after the title, this allows for FEAST to be run in a batch format.

-Tcout was removed from the main input file as it was redundant from the Coolant Temperature input file

- Dtpeak was added as the final option before the transient flag to allow for calculation of creep strains and CDF at a peak temperature

COBRA Input File for ORNL 19-Pin Assembly

```
99999
    1       ORNL
30
Sodium Properties Omitted-See Appendix B
23.64   .00612
    2    0    0    0    0    2    0
.1458.0363-.033.1430.0419-.044.1449.0067-.009.316 -.25
62.97216.9-190.44.40256.7-267.87.2638.59-55.1.316 -.25
    3    6
    0    0 .395    0  0.4  1.0 .920   1..925     0    1    0
    4   42   42               9
    7    1   60          2         9
       12.       .230       .056
    8   19   19    2    1                        9
9.250    0    00.17012.71    0    00.0159999.
    9    1
   40    0    0    0    0    0    0    0    0    0    0    0
   80       100
   10    0    0    1
  .01
2.
   11    1    0
     14.65       600.   0.0654  0.0085
   12    2    8    1
41 32 18 17 4  1  9  38
1
```

COBRA Input File for Toshiba 37-Pin Assembly

```
99999
    1       Toshiba
    1   32
Sodium Properties Omitted-See Appendix B
2    0    0    0    0    2    0
.1458.0363-.033.1430.0419-.044.1449.0067-.009.316 -.25
62.97216.9-190.44.40256.7-267.87.2638.59-55.1.316 -.25
    3   25
0.0000.0000.1300.0000.1310.6540.1460.7520.1620.8430.1770.925
0.1920.9990.2081.0620.2231.1140.2381.1560.2531.1860.2691.204
0.2841.2100.2991.2040.3141.1860.3301.1560.3451.1140.3601.062
0.3760.9990.3910.9250.4060.8430.4210.752.43570.654.43670.000
1.0000.000
    4   78   78              9

    7    1  114         2         9
       12.       .256       .052
    8   37   37    2    1                        9
9.250    0     00.17012.71    0    00.0159999.
    9
119.8    0  .10    0 .020    0    0    0    0    0    0    0
0
  240         30
   10    0    0    1
  .01
2.244
   11    1    0
     14.65    403.52    1.0826   0.02417
   12    0  14
65 42 43 18 17 4  5  6  1  8  7  26 27 56
```

COBRA Input File for WARD 61-Pin Assembly

```
99999
    1       WARD
    1   30
Sodium Properties Omitted-See Appendix B
    2    0    0    0    0    2    0
.1458.0363-.033.1430.0419-.044.1449.0067-.009.316 -.25
62.97216.9-190.44.40256.7-267.87.2638.59-55.1.316 -.25
    3  50
0.0000.0000.0900.0000.0910.3150.1010.3960.1100.4750.1200.553
0.1290.6290.1390.7020.1480.7740.1580.8420.1680.9070.1770.969
0.1871.0280.1961.0830.2061.1340.2161.1810.2251.2240.2351.263
0.2441.2970.2541.3260.2631.3510.2731.3700.2831.3850.2921.395
0.3021.4000.3111.4000.3211.3950.3301.3850.3401.3700.3501.351
0.3591.3260.3691.2970.3781.2630.3881.2240.3981.1810.4071.134
0.4171.0830.4261.0280.4360.9690.4450.9070.4550.8420.4650.774
0.4740.7020.4840.6290.4930.5530.5030.4750.5120.3960.5220.315
0.5230.0001.0000.000
    4  126  126               9
    7    1  186          2         9
   4.0       .519        .037
    8   61   61    2    1                          9
9.250    0    00.17012.71    0    00.0159999.
    9
104.4    0  .12    0 .012    0    0    0    0    0    0    0
0
  209       200
   10    0    0    1
 .01
3.64
   11    1    0
     14.65      605.2    0.8326   .04830
   12    0  18
 98 57 58 27 26  7  8  1  6  5  4 17 18 43 42 79 80111
```

COBRA Input File for KALIMER 271-Pin Assembly

```
99999
    1       KALIMER
    1   30
Sodium Properties Omitted-See Appendix B
    2    0    0    0    0    2    0
.1458.0363-.033.1430.0419-.044.1449.0067-.009.316 -.25
62.97216.9-190.44.40256.7-267.87.2638.59-55.1.316 -.25
    3    4
   0.   1..3120   1..3200   0.   1.   0.
    4  546  546              9
    7    1  816         2         9
   8.20866  .3019      .047244
    8  271  271    2    1                        9
9.250    0    00.17012.71    0    00.0159999.
    9    1
124.5    0    0    0    0    0    0    0    0    0    0    0
  250    0  100
   10    0    0    1
  .01
2.8
   11    1    1    0    0    0    0
    14.695     727.2     2.418     .1946
   12    0   22
5455224523542691941 31 82 44 19  4  1 10 29
611041612303094024965 42
```

COBRA Input File for ULOF Accident

```
99999
    1       ULOF Accident
    1   30
Sodium Properties Omitted-See Appendix B
    2    0    0    0    0    0   -1
.316 -.25      .316 -.25      .316  -.25     .316 -.25
    3   23
   0.   0..0277.2144.0555.3607.0833.5821.1111.8443.13881.099
.16661.307.19441.451.22221.544.25001.602.27771.615.30551.601
.33331.558.36111.475.38881.346.41661.157.4444.9106.4722.6344
0.500.3876.5277.2053.5555.1031.5577   0.   1.   0.
    4  546  546               9
    7    1  816          2         9
    19.685    .346456  .0413385
    8  271  271    2    1                          9
9.250    0    00.17012.71    0    00.0159999.
    9    1    4
172.212000    0    0    0    0    0    0    0    0    0    0
  219 2400 300
   10    0    0    1
  .01
.5
   11    1    0    0  601  601  601
    14.695       680.      5.098      .1779
0    1.00020   1.00140   1.00460   1.00680   1.008100  1.010
120  1.011140  1.013160  1.015180  1.016200  1.018220  1.019
240  1.021260  1.023280  1.024300  1.026320  1.028340  1.030
360  1.032380  1.034400  1.036420  1.037440  1.039460  1.042
480  1.044500  1.046520  1.048540  1.050560  1.052580  1.054
600  1.056620  1.058640  1.060660  1.063680  1.065700  1.067
720  1.069740  1.071760  1.073780  1.075800  1.077820  1.079
840  1.081860  1.083880  1.085900  1.087920  1.089940  1.090
960  1.092980  1.0941000 1.0961020 1.0981040 1.1001060 1.101
1080 1.1031100 1.1051120 1.1071140 1.1081160 1.1101180 1.112
1200 1.1131220 1.1151240 1.1171260 1.1181280 1.1201300 1.121
1320 1.1231340 1.1241360 1.1261380 1.1271400 1.1291420 1.130
1440 1.1321460 1.1331480 1.1341500 1.1361520 1.1371540 1.138
1560 1.1401580 1.1411600 1.1421620 1.1441640 1.1451660 1.146
1680 1.1471700 1.1491720 1.1501740 1.1511760 1.1521780 1.153
1800 1.1551820 1.1561840 1.1571860 1.1581880 1.1591900 1.160
1920 1.1611940 1.1621960 1.1631980 1.1642000 1.1652020 1.167
2040 1.1682060 1.1692080 1.1702100 1.1712120 1.1722140 1.173
2160 1.1742180 1.1742200 1.1752220 1.1762240 1.1772260 1.178
2280 1.1792300 1.1802320 1.1812340 1.1822360 1.1822380 1.183
2400 1.1842420 1.1852440 1.1862460 1.1872480 1.1872500 1.188
```

2520	1.1892540	1.1902560	1.1902580	1.1912600	1.1922620	1.193
2640	1.1932660	1.1942680	1.1952700	1.1952720	1.1962740	1.197
2760	1.1972780	1.1982800	1.1992820	1.1992840	1.2002860	1.201
2880	1.2012900	1.2022920	1.2032940	1.2032960	1.2042980	1.204
3000	1.2053020	1.2053040	1.2063060	1.2073080	1.2073100	1.208
3120	1.2083140	1.2093160	1.2093180	1.2103200	1.2103220	1.211
3240	1.2113260	1.2123280	1.2123300	1.2133320	1.2133340	1.214
3360	1.2143380	1.2153400	1.2153420	1.2163440	1.2163460	1.217
3480	1.2173500	1.2183520	1.2183540	1.2183560	1.2193580	1.219
3600	1.2203620	1.2203640	1.2203660	1.2213680	1.2213700	1.222
3720	1.2223740	1.2223760	1.2233780	1.2233800	1.2243820	1.224
3840	1.2243860	1.2253880	1.2253900	1.2253920	1.2263940	1.226
3960	1.2273980	1.2274000	1.2274020	1.2284040	1.2284060	1.228
4080	1.2294100	1.2294120	1.2294140	1.2304160	1.2304180	1.230
4200	1.2304220	1.2314240	1.2314260	1.2314280	1.2324300	1.232
4320	1.2324340	1.2334360	1.2334380	1.2334400	1.2334420	1.234
4440	1.2344460	1.2344480	1.2354500	1.2354520	1.2354540	1.235
4560	1.2364580	1.2364600	1.2364620	1.2364640	1.2374660	1.237
4680	1.2374700	1.2374720	1.2384740	1.2384760	1.2384780	1.238
4800	1.2394820	1.2394840	1.2394860	1.2394880	1.2404900	1.240
4920	1.2404940	1.2404960	1.2404980	1.2415000	1.2415020	1.241
5040	1.2415060	1.2425080	1.2425100	1.2425120	1.2425140	1.242
5160	1.2435180	1.2435200	1.2435220	1.2435240	1.2435260	1.244
5280	1.2445300	1.2445320	1.2445340	1.2445360	1.2455380	1.245
5400	1.2455420	1.2455440	1.2455460	1.2465480	1.2465500	1.246
5520	1.2465540	1.2465560	1.2465580	1.2475600	1.2475620	1.247
5640	1.2475660	1.2475680	1.2485700	1.2485720	1.2485740	1.248
5760	1.2485780	1.2485800	1.2495820	1.2495840	1.2495860	1.249
5880	1.2495900	1.2495920	1.2505940	1.2505960	1.2505980	1.250
6000	1.2506020	1.2506040	1.2506060	1.2516080	1.2516100	1.251
6120	1.2516140	1.2516160	1.2516180	1.2516200	1.2526220	1.252
6240	1.2526260	1.2526280	1.2526300	1.2526320	1.2526340	1.253
6360	1.2536380	1.2536400	1.2536420	1.2536440	1.2536460	1.253
6480	1.2546500	1.2546520	1.2546540	1.2546560	1.2546580	1.254
6600	1.2546620	1.2546640	1.2556660	1.2556680	1.2556700	1.255
6720	1.2556740	1.2556760	1.2556780	1.2556800	1.2566820	1.256
6840	1.2566860	1.2566880	1.2566900	1.2566920	1.2566940	1.256
6960	1.2576980	1.2577000	1.2577020	1.2577040	1.2577060	1.257
7080	1.2577100	1.2577120	1.2577140	1.2587160	1.2587180	1.258
7200	1.2587220	1.2587240	1.2587260	1.2587280	1.2587300	1.258
7320	1.2597340	1.2597360	1.2597380	1.2597400	1.2597420	1.259
7440	1.2597460	1.2597480	1.2597500	1.2597520	1.2607540	1.260
7560	1.2607580	1.2607600	1.2607620	1.2607640	1.2607660	1.260
7680	1.2607700	1.2607720	1.2607740	1.2617760	1.2617780	1.261
7800	1.2617820	1.2617840	1.2617860	1.2617880	1.2617900	1.261
7920	1.2617940	1.2617960	1.2627980	1.2628000	1.2628020	1.262
8040	1.2628060	1.2628080	1.2628100	1.2628120	1.2628140	1.262

8160 1.2628180 1.2638200 1.2638220 1.2638240 1.2638260 1.263
8280 1.2638300 1.2638320 1.2638340 1.2638360 1.2638380 1.263
8400 1.2638420 1.2638440 1.2648460 1.2648480 1.2648500 1.264
8520 1.2648540 1.2648560 1.2648580 1.2648600 1.2648620 1.264
8640 1.2648660 1.2648680 1.2648700 1.2658720 1.2658740 1.265
8760 1.2658780 1.2658800 1.2658820 1.2658840 1.2658860 1.265
8880 1.2658900 1.2658920 1.2658940 1.2658960 1.2658980 1.265
9000 1.2669020 1.2669040 1.2669060 1.2669080 1.2669100 1.266
9120 1.2669140 1.2669160 1.2669180 1.2669200 1.2669220 1.266
9240 1.2669260 1.2669280 1.2669300 1.2679320 1.2679340 1.267
9360 1.2679380 1.2679400 1.2679420 1.2679440 1.2679460 1.267
9480 1.2679500 1.2679520 1.2679540 1.2679560 1.2679580 1.267
9600 1.2679620 1.2689640 1.2689660 1.2689680 1.2689700 1.268
9720 1.2689740 1.2689760 1.2689780 1.2689800 1.2689820 1.268
9840 1.2689860 1.2689880 1.2689900 1.2689920 1.2689940 1.268
9960 1.2689980 1.268100001.269100201.269100401.269100601.269
100801.269101001.269101201.269101401.269101601.269101801.269
102001.269102201.269102401.269102601.269102801.269103001.269
103201.269103401.269103601.269103801.269104001.269104201.269
104401.269104601.269104801.269105001.269105201.269105401.269
105601.269105801.269106001.269106201.269106401.269106601.269
106801.269107001.268107201.268107401.268107601.268107801.268
108001.268108201.268108401.268108601.268108801.268109001.268
109201.268109401.267109601.267109801.267110001.267110201.267
110401.267110601.267110801.267111001.267111201.267111401.266
111601.266111801.266112001.266112201.266112401.266112601.266
112801.266113001.266113201.265113401.265113601.265113801.265
114001.265114201.265114401.265114601.265114801.264115001.264
115201.264115401.264115601.264115801.264116001.264116201.263
116401.263116601.263116801.263117001.263117201.263117401.263
117601.262117801.262118001.262118201.262118401.262118601.262
118801.262119001.261119201.261119401.261119601.261119801.261
120001.261
0 1.00020 0.26940 0.15060 0.10580 0.082100 0.068
120 0.059140 0.053160 0.048180 0.044200 0.042220 0.040
240 0.041260 0.041280 0.040300 0.039320 0.039340 0.039
360 0.039380 0.039400 0.039420 0.039440 0.039460 0.039
480 0.039500 0.039520 0.039540 0.039560 0.039580 0.038
600 0.038620 0.038640 0.038660 0.038680 0.037700 0.037
720 0.037740 0.037760 0.037780 0.037800 0.036820 0.036
840 0.036860 0.036880 0.036900 0.036920 0.036940 0.036
960 0.035980 0.0351000 0.0351020 0.0351040 0.0351060 0.035
1080 0.0351100 0.0351120 0.0341140 0.0341160 0.0341180 0.034
1200 0.0341220 0.0341240 0.0341260 0.0341280 0.0331300 0.033
1320 0.0331340 0.0331360 0.0331380 0.0331400 0.0331420 0.033
1440 0.0331460 0.0321480 0.0321500 0.0321520 0.0321540 0.032
1560 0.0321580 0.0321600 0.0321620 0.0321640 0.0311660 0.031

1680	0.0311700	0.0311720	0.0311740	0.0311760	0.0311780	0.031
1800	0.0311820	0.0311840	0.0311860	0.0301880	0.0301900	0.030
1920	0.0301940	0.0301960	0.0301980	0.0302000	0.0302020	0.030
2040	0.0302060	0.0302080	0.0302100	0.0292120	0.0292140	0.029
2160	0.0292180	0.0292200	0.0292220	0.0292240	0.0292260	0.029
2280	0.0292300	0.0292320	0.0292340	0.0292360	0.0282380	0.028
2400	0.0282420	0.0282440	0.0282460	0.0282480	0.0282500	0.028
2520	0.0282540	0.0282560	0.0282580	0.0282600	0.0282620	0.028
2640	0.0272660	0.0272680	0.0272700	0.0272720	0.0272740	0.027
2760	0.0272780	0.0272800	0.0272820	0.0272840	0.0272860	0.027
2880	0.0272900	0.0272920	0.0272940	0.0272960	0.0262980	0.026
3000	0.0263020	0.0263040	0.0263060	0.0263080	0.0263100	0.026
3120	0.0263140	0.0263160	0.0263180	0.0263200	0.0263220	0.026
3240	0.0263260	0.0263280	0.0263300	0.0263320	0.0263340	0.026
3360	0.0253380	0.0253400	0.0253420	0.0253440	0.0253460	0.025
3480	0.0253500	0.0253520	0.0253540	0.0253560	0.0253580	0.025
3600	0.0253620	0.0253640	0.0253660	0.0253680	0.0253700	0.025
3720	0.0253740	0.0253760	0.0253780	0.0253800	0.0253820	0.025
3840	0.0253860	0.0253880	0.0253900	0.0253920	0.0243940	0.024
3960	0.0243980	0.0244000	0.0244020	0.0244040	0.0244060	0.024
4080	0.0244100	0.0244120	0.0244140	0.0244160	0.0244180	0.024
4200	0.0244220	0.0244240	0.0244260	0.0244280	0.0244300	0.024
4320	0.0244340	0.0244360	0.0244380	0.0244400	0.0244420	0.024
4440	0.0244460	0.0244480	0.0244500	0.0244520	0.0244540	0.024
4560	0.0244580	0.0244600	0.0244620	0.0244640	0.0244660	0.024
4680	0.0244700	0.0244720	0.0244740	0.0244760	0.0244780	0.024
4800	0.0244820	0.0244840	0.0234860	0.0234880	0.0234900	0.023
4920	0.0234940	0.0234960	0.0234980	0.0235000	0.0235020	0.023
5040	0.0235060	0.0235080	0.0235100	0.0235120	0.0235140	0.023
5160	0.0235180	0.0235200	0.0235220	0.0235240	0.0235260	0.023
5280	0.0235300	0.0235320	0.0235340	0.0235360	0.0235380	0.023
5400	0.0235420	0.0235440	0.0235460	0.0235480	0.0235500	0.023
5520	0.0235540	0.0235560	0.0235580	0.0235600	0.0235620	0.023
5640	0.0235660	0.0235680	0.0235700	0.0235720	0.0235740	0.023
5760	0.0235780	0.0235800	0.0235820	0.0235840	0.0235860	0.023
5880	0.0235900	0.0235920	0.0235940	0.0235960	0.0235980	0.023
6000	0.0236020	0.0236040	0.0236060	0.0236080	0.0236100	0.023
6120	0.0236140	0.0236160	0.0236180	0.0236200	0.0236220	0.023
6240	0.0236260	0.0236280	0.0236300	0.0236320	0.0236340	0.023
6360	0.0236380	0.0236400	0.0236420	0.0236440	0.0236460	0.023
6480	0.0236500	0.0236520	0.0236540	0.0236560	0.0236580	0.023
6600	0.0236620	0.0236640	0.0236660	0.0236680	0.0226700	0.022
6720	0.0226740	0.0226760	0.0226780	0.0226800	0.0226820	0.022
6840	0.0226860	0.0226880	0.0226900	0.0226920	0.0226940	0.022
6960	0.0226980	0.0227000	0.0227020	0.0227040	0.0227060	0.022
7080	0.0227100	0.0227120	0.0227140	0.0227160	0.0227180	0.022
7200	0.0227220	0.0227240	0.0227260	0.0227280	0.0227300	0.022

7320 0.0227340 0.0227360 0.0227380 0.0227400 0.0227420 0.022
7440 0.0227460 0.0227480 0.0227500 0.0227520 0.0227540 0.022
7560 0.0227580 0.0227600 0.0227620 0.0227640 0.0227660 0.022
7680 0.0227700 0.0227720 0.0227740 0.0227760 0.0227780 0.022
7800 0.0227820 0.0227840 0.0227860 0.0227880 0.0227900 0.022
7920 0.0227940 0.0227960 0.0227980 0.0228000 0.0228020 0.022
8040 0.0228060 0.0228080 0.0228100 0.0228120 0.0228140 0.022
8160 0.0228180 0.0228200 0.0228220 0.0228240 0.0228260 0.022
8280 0.0228300 0.0228320 0.0228340 0.0228360 0.0228380 0.022
8400 0.0228420 0.0228440 0.0228460 0.0228480 0.0228500 0.022
8520 0.0228540 0.0228560 0.0228580 0.0228600 0.0228620 0.022
8640 0.0228660 0.0228680 0.0228700 0.0228720 0.0228740 0.022
8760 0.0228780 0.0228800 0.0228820 0.0228840 0.0228860 0.022
8880 0.0228900 0.0228920 0.0228940 0.0228960 0.0228980 0.022
9000 0.0229020 0.0229040 0.0229060 0.0229080 0.0229100 0.022
9120 0.0229140 0.0229160 0.0229180 0.0229200 0.0229220 0.022
9240 0.0229260 0.0229280 0.0229300 0.0229320 0.0229340 0.022
9360 0.0229380 0.0229400 0.0229420 0.0229440 0.0229460 0.022
9480 0.0229500 0.0229520 0.0229540 0.0229560 0.0229580 0.022
9600 0.0229620 0.0229640 0.0229660 0.0229680 0.0229700 0.022
9720 0.0229740 0.0229760 0.0229780 0.0229800 0.0229820 0.022
9840 0.0229860 0.0229880 0.0229900 0.0229920 0.0229940 0.022
9960 0.0229980 0.022100000.022100200.022100400.022100600.022
100800.022101000.022101200.022101400.022101600.022101800.022
102000.022102200.022102400.021102600.021102800.021103000.021
103200.021103400.021103600.021103800.021104000.021104200.021
104400.021104600.021104800.021105000.021105200.022105400.021
105600.021105800.021106000.021106200.022106400.021106600.021
106800.022107000.021107200.021107400.021107600.022107800.022
108000.022108200.022108400.022108600.022108800.021109000.021
109200.021109400.021109600.021109800.021110000.021110200.021
110400.021110600.021110800.021111000.021111200.021111400.021
111600.021111800.021112000.021112200.021112400.021112600.021
112800.021113000.021113200.021113400.021113600.021113800.021
114000.021114200.021114400.021114600.021114800.021115000.021
115200.021115400.021115600.021115800.021116000.021116200.021
116400.021116600.021116800.021117000.021117200.021117400.021
117600.021117800.021118000.021118200.021118400.021118600.021
118800.021119000.021119200.021119400.021119600.021119800.021
120000.021
0 1.00320 0.56840 0.33260 0.22280 0.160100 0.123
120 0.098140 0.082160 0.071180 0.062200 0.056220 0.052
240 0.049260 0.046280 0.045300 0.044320 0.044340 0.045
360 0.045380 0.045400 0.046420 0.046440 0.047460 0.047
480 0.047500 0.047520 0.046540 0.046560 0.045580 0.044
600 0.043620 0.043640 0.042660 0.041680 0.041700 0.040
720 0.040740 0.039760 0.039780 0.039800 0.038820 0.038

840	0.037860	0.037880	0.037900	0.036920	0.036940	0.036
960	0.035980	0.0351000	0.0341020	0.0341040	0.0341060	0.033
1080	0.0331100	0.0331120	0.0321140	0.0321160	0.0311180	0.031
1200	0.0311220	0.0311240	0.0301260	0.0301280	0.0301300	0.029
1320	0.0291340	0.0291360	0.0281380	0.0281400	0.0281420	0.028
1440	0.0271460	0.0271480	0.0271500	0.0271520	0.0261540	0.026
1560	0.0261580	0.0261600	0.0251620	0.0251640	0.0251660	0.025
1680	0.0241700	0.0241720	0.0241740	0.0241760	0.0231780	0.023
1800	0.0231820	0.0231840	0.0231860	0.0221880	0.0221900	0.022
1920	0.0221940	0.0221960	0.0221980	0.0212000	0.0212020	0.021
2040	0.0212060	0.0212080	0.0212100	0.0212120	0.0202140	0.020
2160	0.0202180	0.0202200	0.0202220	0.0202240	0.0192260	0.019
2280	0.0192300	0.0192320	0.0192340	0.0192360	0.0192380	0.018
2400	0.0182420	0.0182440	0.0182460	0.0182480	0.0182500	0.018
2520	0.0172540	0.0172560	0.0172580	0.0172600	0.0172620	0.017
2640	0.0172660	0.0172680	0.0162700	0.0162720	0.0162740	0.016
2760	0.0162780	0.0162800	0.0162820	0.0162840	0.0162860	0.015
2880	0.0152900	0.0152920	0.0152940	0.0152960	0.0152980	0.015
3000	0.0153020	0.0153040	0.0153060	0.0153080	0.0143100	0.014
3120	0.0143140	0.0143160	0.0143180	0.0143200	0.0143220	0.014
3240	0.0143260	0.0143280	0.0143300	0.0143320	0.0143340	0.013
3360	0.0133380	0.0133400	0.0133420	0.0133440	0.0133460	0.013
3480	0.0133500	0.0133520	0.0133540	0.0133560	0.0133580	0.013
3600	0.0133620	0.0133640	0.0133660	0.0133680	0.0133700	0.012
3720	0.0123740	0.0123760	0.0123780	0.0123800	0.0123820	0.012
3840	0.0123860	0.0123880	0.0123900	0.0123920	0.0123940	0.012
3960	0.0123980	0.0124000	0.0124020	0.0124040	0.0124060	0.012
4080	0.0124100	0.0124120	0.0124140	0.0124160	0.0124180	0.012
4200	0.0124220	0.0124240	0.0124260	0.0114280	0.0114300	0.011
4320	0.0114340	0.0114360	0.0114380	0.0114400	0.0114420	0.011
4440	0.0114460	0.0114480	0.0114500	0.0114520	0.0114540	0.011
4560	0.0114580	0.0114600	0.0114620	0.0114640	0.0114660	0.011
4680	0.0114700	0.0114720	0.0114740	0.0114760	0.0114780	0.011
4800	0.0114820	0.0114840	0.0114860	0.0114880	0.0114900	0.011
4920	0.0114940	0.0114960	0.0114980	0.0115000	0.0115020	0.011
5040	0.0115060	0.0115080	0.0115100	0.0115120	0.0115140	0.011
5160	0.0115180	0.0115200	0.0115220	0.0115240	0.0115260	0.011
5280	0.0115300	0.0115320	0.0115340	0.0115360	0.0105380	0.010
5400	0.0105420	0.0105440	0.0105460	0.0105480	0.0105500	0.010
5520	0.0105540	0.0105560	0.0105580	0.0105600	0.0105620	0.010
5640	0.0105660	0.0105680	0.0105700	0.0105720	0.0105740	0.010
5760	0.0105780	0.0105800	0.0105820	0.0105840	0.0105860	0.010
5880	0.0105900	0.0105920	0.0105940	0.0105960	0.0105980	0.010
6000	0.0106020	0.0106040	0.0106060	0.0106080	0.0106100	0.010
6120	0.0106140	0.0106160	0.0106180	0.0106200	0.0106220	0.010
6240	0.0106260	0.0106280	0.0106300	0.0106320	0.0106340	0.010
6360	0.0106380	0.0106400	0.0106420	0.0106440	0.0106460	0.010

6480 0.0106500 0.0106520 0.0106540 0.0106560 0.0106580 0.010
6600 0.0106620 0.0106640 0.0106660 0.0106680 0.0106700 0.010
6720 0.0106740 0.0106760 0.0106780 0.0106800 0.0106820 0.010
6840 0.0106860 0.0106880 0.0106900 0.0106920 0.0106940 0.010
6960 0.0106980 0.0107000 0.0107020 0.0107040 0.0107060 0.010
7080 0.0107100 0.0107120 0.0107140 0.0107160 0.0107180 0.010
7200 0.0107220 0.0107240 0.0107260 0.0107280 0.0107300 0.010
7320 0.0107340 0.0107360 0.0107380 0.0107400 0.0097420 0.009
7440 0.0097460 0.0097480 0.0097500 0.0097520 0.0097540 0.009
7560 0.0097580 0.0097600 0.0097620 0.0097640 0.0097660 0.009
7680 0.0097700 0.0097720 0.0097740 0.0097760 0.0097780 0.009
7800 0.0097820 0.0097840 0.0097860 0.0097880 0.0097900 0.009
7920 0.0097940 0.0097960 0.0097980 0.0098000 0.0098020 0.009
8040 0.0098060 0.0098080 0.0098100 0.0098120 0.0098140 0.009
8160 0.0098180 0.0098200 0.0098220 0.0098240 0.0098260 0.009
8280 0.0098300 0.0098320 0.0098340 0.0098360 0.0098380 0.009
8400 0.0098420 0.0098440 0.0098460 0.0098480 0.0098500 0.009
8520 0.0098540 0.0098560 0.0098580 0.0098600 0.0098620 0.009
8640 0.0098660 0.0098680 0.0098700 0.0098720 0.0098740 0.009
8760 0.0098780 0.0098800 0.0098820 0.0098840 0.0098860 0.009
8880 0.0098900 0.0098920 0.0098940 0.0098960 0.0098980 0.009
9000 0.0099020 0.0099040 0.0099060 0.0099080 0.0099100 0.009
9120 0.0099140 0.0099160 0.0099180 0.0099200 0.0099220 0.009
9240 0.0099260 0.0099280 0.0099300 0.0099320 0.0099340 0.009
9360 0.0099380 0.0099400 0.0099420 0.0099440 0.0099460 0.009
9480 0.0099500 0.0099520 0.0099540 0.0099560 0.0099580 0.009
9600 0.0099620 0.0099640 0.0099660 0.0099680 0.0099700 0.009
9720 0.0099740 0.0099760 0.0099780 0.0099800 0.0099820 0.009
9840 0.0099860 0.0099880 0.0099900 0.0099920 0.0099940 0.009
9960 0.0099980 0.009100000.009100200.009100400.009100600.009
100800.009101000.009101200.009101400.009101600.009101800.009
102000.009102200.009102400.009102600.009102800.009103000.009
103200.009103400.009103600.009103800.009104000.009104200.009
104400.009104600.009104800.009105000.009105200.009105400.009
105600.009105800.009106000.009106200.009106400.009106600.009
106800.009107000.009107200.009107400.009107600.009107800.009
108000.009108200.009108400.009108600.009108800.009109000.009
109200.009109400.008109600.008109800.008110000.008110200.008
110400.008110600.008110800.008111000.008111200.008111400.008
111600.008111800.008112000.008112200.008112400.008112600.008
112800.008113000.008113200.008113400.008113600.008113800.008
114000.008114200.008114400.008114600.008114800.008115000.008
115200.008115400.008115600.008115800.008116000.008116200.008
116400.008116600.008116800.008117000.008117200.008117400.008
117600.008117800.008118000.008118200.008118400.008118600.008
118800.008119000.008119200.008119400.008119600.008119800.008
120000.008

```
 12     0     3
1487541
```

COBRA Input File for UTOP Accident

```
99999
    1       UTOP Accident
    1   30
Sodium Properties Omitted-See Appendix B
    2    0    0    0    0    0   -1
.316 -.25       .316 -.25       .316  -.25      .316 -.25
    3   23
   0.   0..0277.2144.0555.3607.0833.5821.1111.8443.13881.099
.16661.307.19441.451.22221.544.25001.602.27771.615.30551.601
.33331.558.36111.475.38881.346.41661.157.4444.9106.4722.6344
0.500.3876.5277.2053.5555.1031.5577   0.   1.   0.
    4  546  546               9
    7    1  816          2          9
    19.685    .346456  .0413385
    8  271  271    2    1                          9
9.250    0     00.17012.71    0    00.0159999.
    9    1    3
172.2  300    3    0    0    0    0    0    0    0    0    0
  219  900  200
   10    0    0    0
  .01
   11    1    0    0  601  601  601
    14.695       680.      5.098      .1779
0    1.0000.5  1.0001    1.0001.5  1.0002    1.0002.5  1.000
3    1.0003.5  1.0004    1.0004.5  1.0005    1.0005.5  1.000
6    1.0006.5  1.0007    1.0007.5  1.0008    1.0008.5  1.000
9    1.0009.5  1.00010   1.00010.5 1.00011   1.00011.5 1.000
12   1.00012.5 1.00013   1.00013.5 1.00014   1.00014.5 1.000
15   1.00015.5 1.00016   1.00016.5 1.00017   1.00017.5 1.000
18   1.00018.5 1.00019   1.00019.5 1.00020   1.00020.5 1.000
21   1.00021.5 1.00022   1.00022.5 1.00023   1.00023.5 1.000
24   1.00024.5 1.00025   1.00025.5 1.00026   1.00026.5 1.000
27   1.00027.5 1.00028   1.00028.5 1.00029   1.00029.5 1.000
30   1.00030.5 1.00031   1.00031.5 1.00032   1.00032.5 1.000
33   1.00033.5 1.00034   1.00034.5 1.00035   1.00035.5 1.000
36   1.00036.5 1.00037   1.00037.5 1.00038   1.00038.5 1.000
39   1.00039.5 1.00040   1.00040.5 1.00041   1.00041.5 1.000
42   1.00042.5 1.00043   1.00043.5 1.00044   1.00044.5 1.000
45   1.00045.5 1.00046   1.00046.5 1.00047   1.00047.5 1.000
48   1.00048.5 1.00049   1.00049.5 1.00050   1.00050.5 1.000
51   1.00051.5 1.00052   1.00052.5 1.00053   1.00053.5 1.000
54   1.00054.5 1.00055   1.00055.5 1.00056   1.00056.5 1.000
57   1.00057.5 1.00058   1.00058.5 1.00059   1.00059.5 1.001
60   1.00160.5 1.00161   1.00161.5 1.00162   1.00162.5 1.001
63   1.00163.5 1.00164   1.00164.5 1.00165   1.00165.5 1.001
```

66 1.00166.5 1.00167 1.00167.5 1.00168 1.00168.5 1.002
69 1.00269.5 1.00270 1.00270.5 1.00271 1.00271.5 1.002
72 1.00272.5 1.00273 1.00273.5 1.00274 1.00274.5 1.002
75 1.00275.5 1.00376 1.00376.5 1.00377 1.00377.5 1.003
78 1.00378.5 1.00379 1.00379.5 1.00380 1.00380.5 1.003
81 1.00381.5 1.00382 1.00482.5 1.00483 1.00483.5 1.004
84 1.00484.5 1.00485 1.00485.5 1.00486 1.00486.5 1.004
87 1.00487.5 1.00588 1.00588.5 1.00589 1.00589.5 1.005
90 1.00590.5 1.00591 1.00591.5 1.00592 1.00592.5 1.006
93 1.00693.5 1.00694 1.00694.5 1.00695 1.00695.5 1.006
96 1.00696.5 1.00697 1.00697.5 1.00798 1.00798.5 1.007
99 1.00799.5 1.007100 1.007100.51.007101 1.007101.51.007
102 1.007102.51.008103 1.008103.51.008104 1.008104.51.008
105 1.008105.51.008106 1.008106.51.008107 1.009107.51.009
108 1.009108.51.009109 1.009109.51.009110 1.009110.51.009
111 1.009111.51.010112 1.010112.51.010113 1.010113.51.010
114 1.010114.51.010115 1.010115.51.011116 1.011116.51.011
117 1.011117.51.011118 1.011118.51.011119 1.011119.51.011
120 1.012120.51.012121 1.012121.51.012122 1.012122.51.012
123 1.012123.51.012124 1.013124.51.013125 1.013125.51.013
126 1.013126.51.013127 1.013127.51.013128 1.013128.51.014
129 1.014129.51.014130 1.014130.51.014131 1.014131.51.014
132 1.014132.51.015133 1.015133.51.015134 1.015134.51.015
135 1.015135.51.015136 1.015136.51.016137 1.016137.51.016
138 1.016138.51.016139 1.016139.51.016140 1.016140.51.017
141 1.017141.51.017142 1.017142.51.017143 1.017143.51.017
144 1.017144.51.017145 1.018145.51.018146 1.018146.51.018
147 1.018147.51.018148 1.018148.51.018149 1.019149.51.019
150 1.019150.51.019151 1.019151.51.019152 1.019152.51.019
153 1.020153.51.020154 1.020154.51.020155 1.020155.51.020
156 1.020156.51.020157 1.021157.51.021158 1.021158.51.021
159 1.021159.51.021160 1.021160.51.021161 1.021161.51.022
162 1.022162.51.022163 1.022163.51.022164 1.022164.51.022
165 1.022165.51.023166 1.023166.51.023167 1.023167.51.023
168 1.023168.51.023169 1.023169.51.024170 1.024170.51.024
171 1.024171.51.024172 1.024172.51.024173 1.024173.51.024
174 1.025174.51.025175 1.025175.51.025176 1.025176.51.025
177 1.025177.51.025178 1.026178.51.026179 1.026179.51.026
180 1.026180.51.026181 1.026181.51.026182 1.026182.51.027
183 1.027183.51.027184 1.027184.51.027185 1.027185.51.027
186 1.027186.51.027187 1.028187.51.028188 1.028188.51.028
189 1.028189.51.028190 1.028190.51.028191 1.028191.51.029
192 1.029192.51.029193 1.029193.51.029194 1.029194.51.029
195 1.029195.51.029196 1.030196.51.030197 1.030197.51.030
198 1.030198.51.030199 1.030199.51.030200 1.030200.51.031
201 1.031201.51.031202 1.031202.51.031203 1.031203.51.031
204 1.031204.51.031205 1.031205.51.032206 1.032206.51.032

```
207  1.032207.51.032208  1.032208.51.032209  1.032209.51.032
210  1.033210.51.033211  1.033211.51.033212  1.033212.51.033
213  1.033213.51.033214  1.033214.51.033215  1.034215.51.034
216  1.034216.51.034217  1.034217.51.034218  1.034218.51.034
219  1.034219.51.034220  1.034220.51.035221  1.035221.51.035
222  1.035222.51.035223  1.035223.51.035224  1.035224.51.035
225  1.035225.51.036226  1.036226.51.036227  1.036227.51.036
228  1.036228.51.036229  1.036229.51.036230  1.036230.51.036
231  1.037231.51.037232  1.037232.51.037233  1.037233.51.037
234  1.037234.51.037235  1.037235.51.037236  1.038236.51.038
237  1.038237.51.038238  1.038238.51.038239  1.038239.51.038
240  1.038240.51.038241  1.038241.51.038242  1.039242.51.039
243  1.039243.51.039244  1.039244.51.039245  1.039245.51.039
246  1.039246.51.039247  1.039247.51.039248  1.040248.51.040
249  1.040249.51.040250  1.040250.51.040251  1.040251.51.040
252  1.040252.51.040253  1.040253.51.040254  1.041254.51.041
255  1.041255.51.041256  1.041256.51.041257  1.041257.51.041
258  1.041258.51.041259  1.041259.51.041260  1.041260.51.042
261  1.042261.51.042262  1.042262.51.042263  1.042263.51.042
264  1.042264.51.042265  1.042265.51.042266  1.042266.51.042
267  1.043267.51.043268  1.043268.51.043269  1.043269.51.043
270  1.043270.51.043271  1.043271.51.043272  1.043272.51.043
273  1.043273.51.043274  1.044274.51.044275  1.044275.51.044
276  1.044276.51.044277  1.044277.51.044278  1.044278.51.044
279  1.044279.51.044280  1.044280.51.044281  1.045281.51.045
282  1.045282.51.045283  1.045283.51.045284  1.045284.51.045
285  1.045285.51.045286  1.045286.51.045287  1.045287.51.045
288  1.045288.51.045289  1.046289.51.046290  1.046290.51.046
291  1.046291.51.046292  1.046292.51.046293  1.046293.51.046
294  1.046294.51.046295  1.046295.51.046296  1.046296.51.046
297  1.047297.51.047298  1.047298.51.047299  1.047299.51.047
300  1.047
0    1.0000.5  1.0001    1.0001.5  1.0002    1.0002.5  1.000
3    1.0003.5  1.0004    1.0004.5  1.0005    1.0005.5  1.000
6    1.0006.5  1.0007    1.0007.5  1.0008    1.0008.5  1.000
9    1.0009.5  1.00010   1.00010.5 1.00011   1.00011.5 1.000
12   1.00012.5 1.00013   1.00013.5 1.00014   1.00014.5 1.000
15   1.00015.5 1.00016   1.00016.5 1.00017   1.00017.5 1.000
18   1.00018.5 1.00019   1.00019.5 1.00020   1.00020.5 1.000
21   1.00021.5 1.00022   1.00022.5 1.00023   1.00023.5 1.000
24   1.00024.5 1.00025   1.00025.5 1.00026   1.00026.5 1.000
27   1.00027.5 1.00028   1.00028.5 1.00029   1.00029.5 1.000
30   1.00030.5 1.00031   1.00031.5 1.00032   1.00032.5 1.000
33   1.00033.5 1.00034   1.00034.5 1.00035   1.00035.5 1.000
36   1.00036.5 1.00037   1.00037.5 1.00038   1.00038.5 1.000
39   1.00039.5 1.00040   1.00040.5 1.00041   1.00041.5 1.000
42   1.00042.5 1.00043   1.00043.5 1.00044   1.00044.5 1.000
```

45 1.00045.5 1.00046 1.00046.5 1.00047 1.00047.5 1.000
48 1.00048.5 1.00049 1.00049.5 1.00050 1.00050.5 1.000
51 1.00051.5 1.00052 1.00052.5 1.00053 1.00053.5 1.000
54 1.00054.5 1.00055 1.00055.5 1.00056 1.00056.5 1.000
57 1.00057.5 1.00058 1.00058.5 1.00059 1.00059.5 1.000
60 1.00060.5 1.00061 1.00061.5 1.00062 1.00062.5 1.000
63 1.00063.5 1.00064 1.00064.5 1.00065 1.00065.5 1.000
66 1.00066.5 1.00067 1.00067.5 1.00068 1.00068.5 1.000
69 1.00069.5 1.00070 1.00070.5 1.00071 1.00071.5 1.000
72 1.00072.5 1.00073 1.00073.5 1.00074 1.00074.5 1.000
75 1.00075.5 1.00076 1.00076.5 1.00077 1.00077.5 1.000
78 1.00078.5 1.00079 1.00079.5 1.00080 1.00080.5 1.000
81 1.00081.5 1.00082 1.00082.5 1.00083 1.00083.5 1.000
84 1.00084.5 1.00085 1.00085.5 1.00086 1.00086.5 1.000
87 1.00087.5 1.00088 1.00088.5 1.00089 1.00089.5 1.000
90 1.00090.5 1.00091 1.00091.5 1.00092 1.00092.5 1.000
93 1.00093.5 1.00094 1.00094.5 1.00095 1.00095.5 1.000
96 1.00096.5 1.00097 1.00097.5 1.00098 1.00098.5 1.000
99 1.00099.5 1.000100 1.000100.51.000101 1.000101.51.000
102 1.000102.51.000103 1.000103.51.000104 1.000104.51.000
105 1.000105.51.000106 1.000106.51.000107 1.000107.51.000
108 1.000108.51.000109 1.000109.51.000110 1.000110.51.000
111 1.000111.51.000112 1.000112.51.000113 1.001113.51.001
114 1.001114.51.001115 1.001115.51.001116 1.001116.51.001
117 1.001117.51.001118 1.001118.51.001119 1.001119.51.001
120 1.001120.51.001121 1.001121.51.001122 1.001122.51.001
123 1.001123.51.001124 1.001124.51.001125 1.001125.51.001
126 1.001126.51.001127 1.001127.51.001128 1.001128.51.001
129 1.001129.51.001130 1.001130.51.001131 1.001131.51.001
132 1.001132.51.001133 1.001133.51.001134 1.001134.51.001
135 1.001135.51.001136 1.001136.51.001137 1.001137.51.001
138 1.001138.51.001139 1.001139.51.001140 1.001140.51.001
141 1.001141.51.001142 1.001142.51.001143 1.001143.51.001
144 1.001144.51.001145 1.001145.51.001146 1.001146.51.001
147 1.001147.51.001148 1.001148.51.001149 1.001149.51.001
150 1.001150.51.001151 1.001151.51.001152 1.001152.51.001
153 1.001153.51.001154 1.001154.51.001155 1.001155.51.001
156 1.001156.51.001157 1.001157.51.001158 1.001158.51.001
159 1.001159.51.001160 1.001160.51.001161 1.001161.51.001
162 1.001162.51.001163 1.001163.51.001164 1.001164.51.001
165 1.001165.51.001166 1.001166.51.001167 1.001167.51.001
168 1.001168.51.001169 1.001169.51.001170 1.001170.51.001
171 1.001171.51.001172 1.001172.51.001173 1.001173.51.001
174 1.001174.51.001175 1.001175.51.001176 1.001176.51.001
177 1.001177.51.001178 1.001178.51.001179 1.001179.51.001
180 1.001180.51.001181 1.001181.51.001182 1.001182.51.001
183 1.001183.51.001184 1.001184.51.001185 1.001185.51.001

```
186  1.001186.51.001187  1.001187.51.001188  1.001188.51.001
189  1.001189.51.001190  1.001190.51.001191  1.001191.51.001
192  1.001192.51.001193  1.001193.51.001194  1.001194.51.001
195  1.001195.51.001196  1.001196.51.001197  1.001197.51.001
198  1.001198.51.001199  1.001199.51.001200  1.001200.51.001
201  1.001201.51.001202  1.001202.51.001203  1.001203.51.001
204  1.001204.51.001205  1.001205.51.001206  1.001206.51.001
207  1.001207.51.001208  1.001208.51.001209  1.001209.51.001
210  1.001210.51.001211  1.001211.51.001212  1.001212.51.001
213  1.001213.51.001214  1.001214.51.001215  1.001215.51.001
216  1.001216.51.001217  1.001217.51.001218  1.001218.51.001
219  1.001219.51.001220  1.001220.51.001221  1.001221.51.001
222  1.001222.51.001223  1.001223.51.001224  1.001224.51.001
225  1.001225.51.001226  1.001226.51.001227  1.001227.51.001
228  1.001228.51.001229  1.001229.51.001230  1.001230.51.001
231  1.001231.51.001232  1.001232.51.001233  1.001233.51.001
234  1.001234.51.001235  1.001235.51.001236  1.001236.51.001
237  1.001237.51.001238  1.001238.51.001239  1.001239.51.001
240  1.001240.51.001241  1.001241.51.001242  1.001242.51.001
243  1.001243.51.001244  1.001244.51.001245  1.001245.51.001
246  1.001246.51.001247  1.001247.51.001248  1.001248.51.001
249  1.001249.51.001250  1.001250.51.001251  1.001251.51.001
252  1.001252.51.001253  1.001253.51.001254  1.001254.51.001
255  1.001255.51.001256  1.001256.51.001257  1.001257.51.001
258  1.001258.51.001259  1.001259.51.001260  1.001260.51.001
261  1.001261.51.001262  1.001262.51.001263  1.001263.51.001
264  1.001264.51.001265  1.001265.51.001266  1.001266.51.001
267  1.001267.51.001268  1.001268.51.001269  1.001269.51.001
270  1.001270.51.001271  1.001271.51.001272  1.001272.51.001
273  1.001273.51.001274  1.001274.51.001275  1.001275.51.001
276  1.001276.51.001277  1.001277.51.001278  1.001278.51.001
279  1.001279.51.001280  1.001280.51.001281  1.001281.51.001
282  1.001282.51.001283  1.001283.51.001284  1.001284.51.001
285  1.001285.51.001286  1.001286.51.001287  1.001287.51.001
288  1.001288.51.001289  1.001289.51.001290  1.001290.51.001
291  1.001291.51.001292  1.001292.51.001293  1.001293.51.001
294  1.001294.51.001295  1.001295.51.001296  1.001296.51.001
297  1.001297.51.001298  1.001298.51.001299  1.001299.51.001
300  1.001
0    1.0000.5  1.0031    1.0061.5  1.0102    1.0142.5  1.018
3    1.0223.5  1.0264    1.0314.5  1.0355    1.0395.5  1.044
6    1.0486.5  1.0537    1.0577.5  1.0628    1.0668.5  1.071
9    1.0769.5  1.08110   1.08610.5 1.09011   1.09511.5 1.100
12   1.10512.5 1.11113   1.11613.5 1.12114   1.12614.5 1.131
15   1.13715.5 1.14216   1.14716.5 1.15317   1.15817.5 1.163
18   1.16918.5 1.17419   1.18019.5 1.18520   1.19120.5 1.193
21   1.19421.5 1.19522   1.19522.5 1.19623   1.19623.5 1.196
```

24	1.19724.5 1.19725	1.19825.5 1.19826	1.19926.5 1.199
27	1.20027.5 1.20028	1.20128.5 1.20129	1.20229.5 1.202
30	1.20330.5 1.20331	1.20331.5 1.20332	1.20432.5 1.204
33	1.20433.5 1.20434	1.20434.5 1.20435	1.20435.5 1.204
36	1.20536.5 1.20537	1.20537.5 1.20538	1.20538.5 1.205
39	1.20539.5 1.20540	1.20540.5 1.20541	1.20541.5 1.205
42	1.20542.5 1.20443	1.20443.5 1.20444	1.20444.5 1.204
45	1.20445.5 1.20446	1.20446.5 1.20447	1.20447.5 1.204
48	1.20348.5 1.20349	1.20349.5 1.20350	1.20350.5 1.203
51	1.20351.5 1.20252	1.20252.5 1.20253	1.20253.5 1.202
54	1.20254.5 1.20155	1.20155.5 1.20156	1.20156.5 1.201
57	1.20157.5 1.20058	1.20058.5 1.20059	1.20059.5 1.200
60	1.19960.5 1.19961	1.19961.5 1.19962	1.19962.5 1.198
63	1.19863.5 1.19864	1.19864.5 1.19865	1.19765.5 1.197
66	1.19766.5 1.19767	1.19667.5 1.19668	1.19668.5 1.196
69	1.19569.5 1.19570	1.19570.5 1.19571	1.19471.5 1.194
72	1.19472.5 1.19473	1.19373.5 1.19374	1.19374.5 1.193
75	1.19275.5 1.19276	1.19276.5 1.19277	1.19177.5 1.191
78	1.19178.5 1.19179	1.19079.5 1.19080	1.19080.5 1.189
81	1.18981.5 1.18982	1.18982.5 1.18883	1.18883.5 1.188
84	1.18784.5 1.18785	1.18785.5 1.18786	1.18686.5 1.186
87	1.18687.5 1.18588	1.18588.5 1.18589	1.18589.5 1.184
90	1.18490.5 1.18491	1.18391.5 1.18392	1.18392.5 1.182
93	1.18293.5 1.18294	1.18194.5 1.18195	1.18195.5 1.180
96	1.18096.5 1.18097	1.18097.5 1.17998	1.17998.5 1.179
99	1.17899.5 1.178100	1.178100.51.177101	1.177101.51.177
102	1.176102.51.176103	1.176103.51.175104	1.175104.51.175
105	1.174105.51.174106	1.174106.51.173107	1.173107.51.172
108	1.172108.51.172109	1.171109.51.171110	1.171110.51.170
111	1.170111.51.170112	1.169112.51.169113	1.169113.51.168
114	1.168114.51.168115	1.167115.51.167116	1.167116.51.166
117	1.166117.51.165118	1.165118.51.165119	1.164119.51.164
120	1.164120.51.163121	1.163121.51.163122	1.162122.51.162
123	1.161123.51.161124	1.161124.51.160125	1.160125.51.160
126	1.159126.51.159127	1.158127.51.158128	1.158128.51.157
129	1.157129.51.157130	1.156130.51.156131	1.156131.51.155
132	1.155132.51.154133	1.154133.51.154134	1.153134.51.153
135	1.153135.51.152136	1.152136.51.151137	1.151137.51.151
138	1.150138.51.150139	1.149139.51.149140	1.149140.51.148
141	1.148141.51.148142	1.147142.51.147143	1.146143.51.146
144	1.146144.51.145145	1.145145.51.145146	1.144146.51.144
147	1.143147.51.143148	1.143148.51.142149	1.142149.51.142
150	1.141150.51.141151	1.140151.51.140152	1.140152.51.139
153	1.139153.51.138154	1.138154.51.138155	1.137155.51.137
156	1.137156.51.136157	1.136157.51.135158	1.135158.51.135
159	1.134159.51.134160	1.134160.51.133161	1.133161.51.132
162	1.132162.51.132163	1.131163.51.131164	1.131164.51.130

```
165  1.130165.51.129166  1.129166.51.129167  1.128167.51.128
168  1.127168.51.127169  1.127169.51.126170  1.126170.51.126
171  1.125171.51.125172  1.124172.51.124173  1.124173.51.123
174  1.123174.51.123175  1.122175.51.122176  1.122176.51.121
177  1.121177.51.120178  1.120178.51.120179  1.119179.51.119
180  1.119180.51.118181  1.118181.51.117182  1.117182.51.117
183  1.116183.51.116184  1.116184.51.115185  1.115185.51.115
186  1.114186.51.114187  1.113187.51.113188  1.113188.51.112
189  1.112189.51.112190  1.111190.51.111191  1.111191.51.110
192  1.110192.51.109193  1.109193.51.109194  1.108194.51.108
195  1.108195.51.107196  1.107196.51.107197  1.106197.51.106
198  1.106198.51.105199  1.105199.51.105200  1.104200.51.104
201  1.104201.51.103202  1.103202.51.102203  1.102203.51.102
204  1.101204.51.101205  1.101205.51.100206  1.100206.51.100
207  1.099207.51.099208  1.099208.51.098209  1.098209.51.098
210  1.097210.51.097211  1.097211.51.096212  1.096212.51.096
213  1.095213.51.095214  1.095214.51.094215  1.094215.51.094
216  1.093216.51.093217  1.093217.51.092218  1.092218.51.092
219  1.091219.51.091220  1.091220.51.090221  1.090221.51.090
222  1.090222.51.089223  1.089223.51.089224  1.088224.51.088
225  1.088225.51.087226  1.087226.51.087227  1.086227.51.086
228  1.086228.51.085229  1.085229.51.085230  1.084230.51.084
231  1.084231.51.084232  1.083232.51.083233  1.083233.51.082
234  1.082234.51.082235  1.081235.51.081236  1.081236.51.081
237  1.080237.51.080238  1.080238.51.079239  1.079239.51.079
240  1.078240.51.078241  1.078241.51.078242  1.077242.51.077
243  1.077243.51.076244  1.076244.51.076245  1.076245.51.075
246  1.075246.51.075247  1.074247.51.074248  1.074248.51.074
249  1.073249.51.073250  1.073250.51.072251  1.072251.51.072
252  1.072252.51.071253  1.071253.51.071254  1.071254.51.070
255  1.070255.51.070256  1.069256.51.069257  1.069257.51.069
258  1.068258.51.068259  1.068259.51.068260  1.067260.51.067
261  1.067261.51.067262  1.066262.51.066263  1.066263.51.066
264  1.065264.51.065265  1.065265.51.065266  1.064266.51.064
267  1.064267.51.064268  1.063268.51.063269  1.063269.51.063
270  1.062270.51.062271  1.062271.51.062272  1.061272.51.061
273  1.061273.51.061274  1.060274.51.060275  1.060275.51.060
276  1.059276.51.059277  1.059277.51.059278  1.058278.51.058
279  1.058279.51.058280  1.058280.51.057281  1.057281.51.057
282  1.057282.51.056283  1.056283.51.056284  1.056284.51.055
285  1.055285.51.055286  1.055286.51.055287  1.054287.51.054
288  1.054288.51.054289  1.053289.51.053290  1.053290.51.053
291  1.053291.51.052292  1.052292.51.052293  1.052293.51.052
294  1.051294.51.051295  1.051295.51.051296  1.051296.51.050
297  1.050297.51.050298  1.050298.51.050299  1.049299.51.049
300  1.049
   12    0    3
```

1487541

COBRA Input File for EBR-II X425

```
99999
    1     EBR-II X425
    1   30
Sodium Properties Omitted-See Appendix B
    2    0    0    0    0    2    1
.1458.0363-.033.1430.0419-.044.1449.0067-.009.316 -.25
62.97216.9-190.44.40256.7-267.87.2638.59-55.1.316 -.25
 1.66  0.3  0.3  0.0
    3   11
  0.0  0.00.039  0.0 0.040.5610.1230.6680.2060.715 0.290.715
0.3730.6680.4560.579 0.540.4140.540  0.0  1.0  0.0
    4  126  126              9
    7    1  186         2         9
       6.0  0.229921  0.042125
    8   61   61    2    1                         9
9.250    0    00.37012.71    0    00.015  36.
    9
 29.5    0    0    0    0    0    0    0    0    0    0    0
0.6
   50       100
   10    0    0    1
 0.01
2.149
   11    1    0
  14.69595     698.0  3.214209  0.692642
   12    2    1    5
1
  1  7 19 37 61
```

COBRA Input File for S-PRISM

```
99999
    1      s-prism
    1   30
Sodium Properties Omitted-See Appendix B
    2    0    0    0    0    2    1
.1458.0363-.033.1430.0419-.044.1449.0067-.009.316 -.25
62.97216.9-190.44.40256.7-267.87.2638.59-55.1.316 -.25
1
    3   15
  0.0  0.0 0.25  0.0 0.250.7070.2750.807  0.30.8910.3250.951
 0.350.9880.375  1.0  0.40.9880.4250.951 0.450.8910.4570.807
  0.50.707  0.5  0.0  1.0  0.0
    4  546  546              9
    7    1  816         2         9
       8.0     0.293     0.056
    8  271  271    2    1                          9
9.250    0    00.37012.71    0    00.015  36.
    9
160.2    0    0    0    0    0    0    0    0    0    0    0
.6
  160        100
   10    0    0    1
 0.01
2.107
   11    1    0
  14.69595     699.8  2.542167  0.257257
   12    2    1    1
1
  1
```

FEAST Input File for EBR-II X425

```
    "FEAST-M: metal fuel code"
    61
    im= 50
    na= 13
    dt= 10.0
    ptof= 1.0
    rfo= 2.16e-03,2.16e-03,2.16e-03,2.16e-03,2.16e-03,2.16e-
03,2.16e-03,2.16e-03,2.16e-03,2.16e-03,2.16e-03,2.16e-03,2.16e-
03
    rci= 2.539e-03
    rco= 2.92e-03
    rw= 0.535e-03
    xpu= 0.19
    xzr= 0.10
    fgpav= 84000.0
    bonds= 0.00635
    lfu=
.02638,.02638,.02638,.02638,.02638,.02638,.02638,.02638,.02638,.
02638,.02638,.02638,.02638
    pco= 100000.0
    tcin= 370.0
    time=
0.000E+00,0.198E+00,0.198E+00,0.329E+00,0.329E+00,0.344E+00,
0.344E+00,0.512E+00,0.512E+00,0.598E+00,0.598E+00,0.775E+00,0.77
5E+00,0.775E+00,0.775E+00,0.938E+00,0.938E+00,0.101E+01,0.101E+0
1,0.105E+01,0.105E+01,0.105E+01,0.105E+01,0.107E+01,0.107E+01,0.
114E+01,0.114E+01,0.116E+01,0.116E+01,0.125E+01,0.125E+01,0.131E
+01,0.131E+01,0.150E+01,0.150E+01,0.152E+01,0.153E+01,0.152E+01,
0.152E+01,0.158E+01,0.158E+01,0.158E+01,0.158E+01,0.176E+01,0.17
6E+01,0.176E+01,0.176E+01,0.190E+01,
    0.190E+01,0.344E+01
    dos= 5.02
    tfre= 10.0
    pres= 3.0e+11,3.0e+5,10.0
    dtpeak= 0
    tr= 0
```

Feast Input File for S-PRISM Driver Fuel

```
    "FEAST-M: metal fuel code"
    0
    im= 2
    na= 7
    dt= 10.0
    ptof= 2.0
    rfo= 2.738e-03,2.738e-03,2.738e-03,2.738e-03,2.738e-
03,2.738e-03,2.738e-03
    rci= 3.1613e-03
    rco= 3.72e-03
    rw= 0.711e-03
    xpu= 0.19
    xzr= 0.10
    fgpav= 0.84E5
    bonds= 6.35e-03
    lfu= .145,.145,.145,.145,.145,.145,.145
    pco= 1.0e5
    tcin= 371.0
    time= 0.000E+00,20.E+00
    dos= 5.0
    tfre= 10.0
    pres= 3.0e+11,3.0e+5,10.0
    dtpeak= 0
    tr= 0
```

Feast Input File for Parametric Study of Radial Blanket

```
    "FEAST-M: metal fuel code"
    0
    im= 2
    na= 7
    dt= 10.0
    ptof= 1.2
    rfo= 5.023e-03,5.023e-03,5.023e-03,5.023e-03,5.023e-
03,5.023e-03,5.023e-03,
    rci= 5.446e-03
    rco= 6.005e-03
    rw= 0.47e-03
    xpu= 0.19
    xzr= 0.10
    fgpav= 0.84E5
    bonds= 6.35e-03
    lfu= .145,.145,.145,.145,.145,.145,.145
    pco= 1.0e5
    tcin= 371.0
    time= 0.000E+00,20.E+00
    dos= 5.0
    tfre= 10.0
    pres= 3.0e+11,3.0e+5,10.0
    dtpeak= 0
    tr= 0
```

Feast Input File for Parametric Study of Tight Pitch Breed and Burn Fuel

```
    "FEAST-M: metal fuel code"
    0
    im= 2
    na= 20
    dt= 10.0
    ptof= 0.72
    rfo= 3.747e-03,3.747e-03,3.747e-03,3.747e-03,3.747e-
03,3.747e-03,3.747e-03, 3.747e-03,3.747e-03,3.747e-03,3.747e-
03,3.747e-03,3.747e-03,3.747e-03, 3.747e-03,3.747e-03,3.747e-
03,3.747e-03,3.747e-03,3.747e-03
    rci= 4.72e-03
    rco= 5.22e-03
    rw= 0.711e-03
    xpu= 0.0
    xzr= 0.05
    fgpav= 0.84E5
    bonds= 6.35e-03
    lfu= .125, .125, .125, .125, .125, .125, .125, .125, .125,
.125, .125, .125, .125, .125, .125, .125, .125, .125, .125, .125
    pco= 1.0e5
    tcin= 360.0
    time= 0.000E+00,40.E+00
    dos= 5.0
    tfre= 10.0
    pres= 3.0e+11,3.0e+5,10.0
    dtpeak= 0
    tr= 0
```